



2016

Cryogenic Processing of *Al 7050-T7451* Alloy for Improved Surface Integrity

Bo Huang

University of Kentucky, hhbb123abc@gmail.com

Digital Object Identifier: <http://dx.doi.org/10.13023/ETD.2016.162>

[Click here to let us know how access to this document benefits you.](#)

Recommended Citation

Huang, Bo, "Cryogenic Processing of *Al 7050-T7451* Alloy for Improved Surface Integrity" (2016). *Theses and Dissertations--Mechanical Engineering*. 78.

https://uknowledge.uky.edu/me_etds/78

This Doctoral Dissertation is brought to you for free and open access by the Mechanical Engineering at UKnowledge. It has been accepted for inclusion in Theses and Dissertations--Mechanical Engineering by an authorized administrator of UKnowledge. For more information, please contact UKnowledge@lsv.uky.edu.

STUDENT AGREEMENT:

I represent that my thesis or dissertation and abstract are my original work. Proper attribution has been given to all outside sources. I understand that I am solely responsible for obtaining any needed copyright permissions. I have obtained needed written permission statement(s) from the owner(s) of each third-party copyrighted matter to be included in my work, allowing electronic distribution (if such use is not permitted by the fair use doctrine) which will be submitted to UKnowledge as Additional File.

I hereby grant to The University of Kentucky and its agents the irrevocable, non-exclusive, and royalty-free license to archive and make accessible my work in whole or in part in all forms of media, now or hereafter known. I agree that the document mentioned above may be made available immediately for worldwide access unless an embargo applies.

I retain all other ownership rights to the copyright of my work. I also retain the right to use in future works (such as articles or books) all or part of my work. I understand that I am free to register the copyright to my work.

REVIEW, APPROVAL AND ACCEPTANCE

The document mentioned above has been reviewed and accepted by the student's advisor, on behalf of the advisory committee, and by the Director of Graduate Studies (DGS), on behalf of the program; we verify that this is the final, approved version of the student's thesis including all changes required by the advisory committee. The undersigned agree to abide by the statements above.

Bo Huang, Student

Dr. Ibrahim S. Jawahir, Major Professor

Dr. Haluk E. Karaca, Director of Graduate Studies

**CRYOGENIC PROCESSING OF *AL 7050-T7451* ALLOY FOR
IMPROVED SURFACE INTEGRITY**

DISSERTATION

A dissertation submitted in partial fulfillment of
the requirements for the degree of Doctor of
Philosophy in the College of Engineering at the
University of Kentucky

By

Bo Huang

Director: Dr. I.S. Jawahir, Professor of Mechanical Engineering

Lexington, Kentucky

2016

Copyright © Bo Huang 2016

ABSTRACT OF DISSERTATION

CRYOGENIC PROCESSING OF *AL 7050-T7451* ALLOY FOR IMPROVED SURFACE INTEGRITY

Al 7050-T7451 alloy with good combinations of strength, stress corrosion cracking resistance and toughness, is used broadly in the aerospace/aviation industry for fatigue-critical airframe structural components. However, it is also considered as a highly anisotropic alloy as the crack growth behavior along the short transverse direction is very different from the one in the long transverse direction, due to the inhomogeneous microstructure with the elongated grains distributed in the work material used in the sheet/plate applications. Further processes on these materials are needed to improve its mechanical and material properties and broaden its applications.

The material with ultra-fine or nano grains exhibits improved wear and corrosion resistance, higher hardness and better fatigue life, compared to the one with coarse grains. In recent times, the development of novel processing technologies has gained great attention in the research community to enhance the properties of the materials employed in the aerospace, biomedical, precision instrument, automotive, nuclear/power industries. These novel processing technologies modify the microstructure of this alloy and improve the properties.

The aim of this dissertation is to investigate the effects of cryogenic processes, including friction stir processing (FSP), machining and burnishing, on *Al 7050-T7451* alloy to solve the inhomogeneity issue and improve its surface integrity. FSP is applied to modify the microstructure of *Al 7050-T7451* alloy for achieving more homogeneous structure with

near ultra-fine grains (UFG) which were less than 2 μm , particularly in cryogenic FSP with liquid nitrogen as the coolant. Approximately 10% increase could be observed from the hardness measurement from the samples processed by cryogenic FSP, in contrast to dry FSP. Also, the texture change from $Al(200)$ to $Al(111)$ could be achieved in all the samples processed by dry and cryogenic FSP.

Cryogenic machining and burnishing processes were also applied to enhance the surface integrity of the manufactured components with near-UFG structure. The highest cutting temperature was reduced by up to 44.7% due to the rapid cooling effect of liquid nitrogen in cryogenic machining, compared with dry machining. Nano grains were produced in the refined layers induced by cryogenic burnishing. And, up to 35.4% hardness increase was obtained within the layer depth of 200 μm in the cryogenically-burnished surface.

A numerical finite element method (FEM) model was developed for predicting the process performance in burnishing. Less than 10% difference between the experimental and predicted burnishing forces was achieved in the simulation of cryogenic burnishing, and reasonable predictions were also achieved for temperatures, severe plastic deformation (SPD) layers.

KEYWORDS: Cryogenic Friction Stir Processing, Cryogenic Machining, Cryogenic Burnishing, Surface Integrity, Hardness, Microstructure

Bo Huang

April 13, 2016

**CRYOGENIC PROCESSING OF *AL 7050-T7451* ALLOY FOR
IMPROVED SURFACE INTEGRITY**

By

Bo Huang

I.S. Jawahir

Director of Dissertation

H.E. Karaca

Director of Graduate Studies

April 28, 2016

ACKNOWLEDGMENTS

I want to thank my advisor Professor Jawahir for his patient guidance in my research work. He not only teaches me on how to be a good PhD student from the research point of view, but also guides me to be a better person in life. Being serious at work and keep thinking are two of the most important lessons that I learned from Professor Jawahir. I will benefit from the experience of working for him in my future career.

My wife Ying Sun is the important person in my life. She greatly supported my study when I pursued my PhD by taking good care of the household work and easing the life pressure from me. She gave birth to our beloved son Matthew in 2013 and spent most of her time to take care of the baby while balancing her course and research work for her PhD study. Her great contribution to our family is highly appreciated.

I also would like to thank Dr. Kaynak, he gave me a lot of tutorials on how to use the facilities and equipment in our labs. Without his kind help, my research from my experimental parts would not go smoothly. Mr. Charles Arvin and Mrs. Heather-Michele Adkins are appreciated for their kind-hearted supports in operating of experiments and ordering work materials, respectively. My formal colleague Dr. Lu was very nice to help me and Ying when we came to Lexington, he picked us in the airport and gave us rides to grocery shopping before we purchased our own vehicle. His advice in our research was very helpful to solve the problems that we encountered.

The friendship from Mr. Francis Almeida and his wife Calor is a great treasure for me during our stay in Lexington. I learned very important life principles of being positive and optimistic from them. I am very appreciative of Professor Dillon who is an emeritus

professor with great passion in research, even after the retirement. His advice for my theoretical work is very helpful to modify my numerical model, and his gentle care and kindness, including social support is greatly appreciated.

Finally, I want to thank my parents sincerely. Without their continuous support, I cannot pursue my dream and do my PhD in the US. I really appreciate their countless efforts to bring me up and supply everything I need through the thirty years during which I grew up from one little kid to a father.

TABLE OF CONTENTS

ACKNOWLEDGMENTS.....	iii
TABLE OF CONTENTS.....	v
LIST OF TABLES.....	ix
LIST OF FIGURES.....	x
CHAPTER 1 INTRODUCTION.....	1
1.1 Introduction.....	1
1.2 Overview of the dissertation.....	4
CHAPTER 2 LITERATURE REVIEW.....	7
2.1 Applications of <i>Al 7050-T7451</i> alloy.....	7
2.2 Applications of materials with ultra-fine grained structure.....	10
2.3 Friction stir processing.....	14
2.3.1 Friction stir processing of aluminum alloys.....	16
2.3.2 Friction stir processing of <i>Al 7050-T7451</i> alloy.....	27
2.4 Machining of <i>Al 7050-T7451</i> alloy.....	33
2.5 Burnishing of Aluminum alloys.....	38
2.6 Cryogenic processing.....	42
2.6.1 Cryogenic machining.....	42

2.6.2	Cryogenic burnishing.....	48
2.7	Burnishing model.....	52
CHAPTER 3 MICROSTRUCTURE REFINEMENT OF <i>Al 7050-T7451</i> ALLOYS		
ACHIEVED BY FRICTION STIR PROCESSING.....		
3.1	Introduction.....	57
3.2	Experimental work.....	59
3.2.1	Work material.....	59
3.2.2	FSP experiments.....	59
3.2.3	Measurements of surface integrity characteristics.....	64
3.3	Experimental results and discussion.....	65
3.3.1	Microstructure.....	65
3.3.2	Hardness.....	79
3.3.3	XRD measurements.....	86
3.4	Chapter conclusion.....	88
CHAPTER 4 IMPROVED SURFACE INTEGRITY FROM CRYOGENIC		
MACHINING OF <i>Al 7050-T7451</i> ALLOY WITH NEAR-UFG		
STRUCTURE.....		
4.1	Introduction.....	90
4.2	Experimental work.....	92
4.3	Experimental results and discussion.....	94

4.3.1	Cutting force components.....	94
4.3.2	Cutting temperature.....	96
4.3.3	Microstructure.....	98
4.3.4	Hardness.....	101
4.3.5	Chip microstructure.....	106
4.3.6	Chip hardness.....	124
4.4	Chapter conclusion.....	126
CHAPTER 5 SURFACE AND SUB-SURFACE MODIFICATION BY CRYOGENIC		
BURNISHING OF <i>Al 7050-T7451</i> ALLOY WITH NEAR-UFG		
	STRUCTURE.....	129
5.1	Introduction.....	129
5.2	Experimental work.....	132
5.3	Experimental results and discussion.....	135
5.3.1	Burnishing forces.....	135
5.3.2	Burnishing temperatures.....	138
5.3.3	Microstructure.....	140
5.3.4	Hardness.....	148
5.4	Chapter conclusion.....	154

CHAPTER 6 FINITE ELEMENT MODELING OF SURFACE LAYER

MODIFICATION INDUCED BY CRYOGENIC BURNISHING.....	157
6.1 Introduction.....	157
6.2 Modeling setup.....	158
6.2.1 Numerical setup of work material and burnishing tool.....	158
6.2.2 Material properties of work material and burnishing tool.....	159
6.2.3 Boundary conditions.....	162
6.2.4 Model of material flow stress.....	163
6.3 Calibration and validation of burnishing model by comparing the predicted radial burnishing forces and temperatures with the experimental results....	167
6.4 Prediction of depth of SPD layer induced by cryogenic burnishing.....	179
6.5 Chapter conclusion.....	188
CHAPTER 7 CONCLUSIONS AND FUTURE WORK.....	191
7.1 Conclusions.....	191
7.2 Future work.....	194
REFERENCES	196
VITA.....	211

LIST OF TABLES

Table 3.1: Chemical composition of <i>Al 7050-T7451</i> alloy (in wt. %) used in the experimental work.....	59
Table 3.2: (a) The rotational speeds and feed rates selected from the literature.....	62
Table 3.2: (b) Statistical classification of rotation speeds and feed rates.....	63
Table 3.3: FSP experimental matrix.....	63
Table 4.1: Experimental matrix regarding machining of <i>Al 7050-T7451</i> alloys with near-UFG structure.....	94
Table 5.1: Burnishing experimental matrix of <i>Al 7050-T7451</i> alloys with near-UFG structure.....	134
Table 6.1: Thermal and mechanical properties of uncoated carbide (Yang, 2012).....	160
Table 6.2: Thermal conductivity of <i>Al 7050-T7451</i> alloy at various temperatures (Hamilton et al., 2009).....	160
Table 6.3: Specific heat capacity of <i>Al 7050-T7451</i> alloy at various temperatures (Hamilton et al., 2009).....	161
Table 6.4: Thermal and mechanical properties of <i>Al 7050-T7451</i> alloy (Hamilton et al., 2009).....	161

LIST OF FIGURES

Figure 1.1: Flow chart of the dissertation overview.....	6
Figure 2.1: (a) Airbus A380 in flight; and (b) View of the internal face of a starboard wing skin panel made of <i>Al 7050-T7451</i> alloy (Atkins Ltd, 2012).....	8
Figure 2.2: Components made of <i>Al 7050-T7451</i> alloys: (a) Fuselage frame; and (b) Front fitting for aircrafts (OTTO FUCHS KG, 2012).....	8
Figure 2.3: <i>F-35</i> aircrafts: (a) Bulkhead components made of 7 series aluminum alloys (Bacon, 2014); and (b) <i>F-35</i> in flight (Wikipedia, 2011).....	8
Figure 2.4: (a) Medical devices applicator; and (b) Oncology needles with UFG structures (Tikhonovsky, 2011).....	11
Figure 2.5: The example of UFG steel applications (Ponge, 2011).....	12
Figure 2.6: <i>F-15E</i> aircraft fuselage: (a) conventional assembly; and (b) Superplastic forming structure (Salishchev et al., 2001).....	12
Figure 2.7: The working illustration of FSW/FSP (Friction stir Link, 2011).....	15
Figure 2.8: Influence of FSP on fatigue properties of <i>A356</i> alloy (Sharma et al., 2004).....	17
Figure 2.9: Tensile properties of <i>AZ91D</i> magnesium alloy (YS: yield strength, UTS: ultimate tensile strength, El.: elongation) (Feng and Ma, 2007).....	18
Figure 2.10: Micrographs of (a) cast <i>A356</i> alloy; (b) FSPed <i>A356</i> alloy; and (c) bright field TEM micrograph of FSPed <i>A356</i> alloy (Ma et al., 2004).....	19

Figure 2.11: Schematic illustrations of friction stir process in fabricating the AZ31/nanoparticles composites: (a) cutting groove and inserting nanoparticles and (b) conducting multiple FSP to fabricate composites (Azizieh et al., 2010).....	20
Figure 2.12: Microhardness values of FSPed specimens (a) without SiC particles and (b) with SiC particles in different traverse speeds (Barmouz et al., 2011).....	21
Figure 2.13: SEM micrographs showing particle distribution in (a) 4.2 wt pct SiC layer of functional graded (FG) material; (b) 10 wt pct layer of FG material; (c) 18 wt pct layer; and (d) Homogeneous nano-composite (the higher magnification images were added at upper right of each image) (Salehi et al., 2014).....	22
Figure 2.14: (a) Optical; and (b) SEM micrographs showing perfect bonding between surface composite and aluminum alloy substrate (Shafiei-Zarghani et al., 2009).....	23
Figure 2.15: TEM micrographs of the composite material in the stir zone after 2 FSP passes, showing (a) carbon nanotubes introduced by two-pass FSP are indicated with arrows; and (b) circular carbon structures (Izadi et al., 2012).....	24
Figure 2.16: Typical macrograph of multi-pass friction stir processed sample showing nugget and transitional zones of twelve-pass labeled as A, B, C, D, E, F, G, H, I, J, K, and L (Ramesh, et al., 2012).....	25

Figure 2.17: Submerged friction stir processing and the tool: (a) schematic drawing of FSP; (b) set up of submerged friction stir processing; and (c) the tool (Feng et al., 2013).....	26
Figure 2.18: (a) Macro image of FSPed <i>Al 7075</i> alloy after four passes; (b) TEM micrographs showing grain structures in the middle layer of Pass 1; (c) overlap between Pass 1 and Pass 2; and (d) Pass 2 of the processing nugget as indicated by the regions 1–3 (Su et al., 2005).....	27
Figure 2.19: (a) Micro-hardness trends for in-air, under-water, sub-ambient welds made at 800 rpm, 6.8mm/s and (b) Micro-hardness distribution for 200 rpm, 2.54 mm/s weld for in-air and under-water (Upadhyay et al., 2010).....	28
Figure 2.20: Average nugget grain size vs. peak probe temperature for different welding speeds. The arrows show equivalent welds done in air and under water (Upadhyay et al., 2010).....	28
Figure 2.21: (a) Optical macrophotograph showing the weld nugget and the TMAZ in the FSW weld of <i>7050-T7451</i> alloy; Higher magnification optical micrographs: (b) fine grain size in the weld nugget; and (c) bent grains in the TMAZ (Jata et al., 2000).....	29
Figure 2.22: Through thickness longitudinal residual stress (Brown et al., 2010).....	30
Figure 2.23: TEM micrographs of FSP plunge and extract tested <i>Al 7050</i> alloy by isopropyl alcohol/dry ice cooling: (a) 200 rpm tool rotational speed;	

(b) 300 rpm rotation speed; and (c) 500 rpm rotational speed. Arrows indicate recrystallized grains in contrast (Rhodes et al., 2003).....	31
Figure 2.24: Grain growth behavior in FSPed <i>Al 7050</i> at 350, 400, and 450°C (Rhodes et al., 2003).	32
Figure 2.25: Cross-sectional SEM of <i>Al 7050-T7451</i> alloy (1627 m/min, 0.2 mm/tooth, 1 mm) (Guo et al., 2006).....	34
Figure 2.26: Tool-life under MQL technique (Bork et al., 2015).....	35
Figure 2.27: Chip morphology according to the process parameters (Bork et al., 2015).....	35
Figure 2.28: SEM images acquired on different <i>TiN</i> covered inserts after dry turning 175 mm of <i>Al 7050</i> alloy bars at: (a) $V = 43$ m/min; and (b) $V = 64$ m/min (Sánchez et al., 2005).....	37
Figure 2.29: The schematics of burnishing process: (a) ball burnishing; and (b) roller burnishing (Substech, 2013).....	39
Figure 2.30: Residual stress distributions produced by end milling and LPB in <i>Al 7075-T6</i> alloy (Prevéy and Cammett, 2004).....	41
Figure 2.31: High cycle fatigue results for salt fog pitted and active corrosion fatigue of machined <i>Al 7075-T6</i> alloy with and without LPB processing prior to exposure to corrosion (Prevéy and Cammett, 2004).....	41
Figure 2.32: A schematic of the economical cryogenic machining approach (Hong et al., 2001).....	43

Figure 2.33: Measured and predicted tool temperature (Hong et al., 2001b).....	44
Figure 2.34: (a) Images of notch wear progression at the main cutting edge of the cutting tools; (b) Images of flank wear progression at the nose region of the cutting tool (Kaynak et al., 2013).....	45
Figure 2.35: Residual stresses after machining using cutting tools with different edge radii and cooling conditions in circumferential and axial directions (Pu et al., 2012).....	47
Figure 2.36: Microstructure of the surface after burnishing under different conditions: (a) dry burnishing, depth of penetration (DoP) = 0.127 mm; (b) cryogenic burnishing, DoP = 0.127 mm; (c) dry burnishing, DoP = 0.254 mm; and (d) cryogenic burnishing, DoP = 0.254 mm (Yang et al., 2013).....	49
Figure 2.37: Hardness variation with depth below the burnished surface (Yang et al., 2013).....	50
Figure 2.38: 3-D topographic profiles of the tool-wear zone: (a) dry, 0.15 mm DoP; (b) cryogenic, 0.15 mm DoP; (c) dry, 0.21 mm DoP; and (d) cryogenic, 0.21 mm DoP. (14.3 mm tool diameter, 100 m/min burnishing speed) (Yang et al., 2015).....	50
Figure 2.39: Typical microstructures at different depths from the surface, marked by <i>h1-h6</i> (Pu et al., 2011).....	51

Figure 2.40: Model of smoothing slide burnishing with a ball-tipped tool: P is the burnishing force (burnishing pressure, tool pressure force), f is the feed, n is the rotational speed, R_z is the surface roughness before burnishing, R_{z_b} represents the surface roughness after burnishing, r_d is the radius of tool tip rounding, u is the tool indentation, RS_m is the mean spacing of profile irregularities before burnishing (Korzynski, 2009)..... 53

Figure 2.41: Verification of the roller burnishing FE model (Klocke et al., 2011)..... 55

Figure 3.1: Equipment used in the FSP experiments: (a) Hass CNC machine tool VF-2; (b) ICEFLY[®] coolant delivery system; (c) FSP tool; and (d) Clamping system..... 60

Figure 3.2: (a) Illustration of multi-pass FSP; and (b) Experimental setup of cryogenic FSP..... 61

Figure 3.3: Measurement locations highlighted by Green rectangulars used for measuring the grain size for each processed material samples..... 65

Figure: 3.4: Microstructure images of the work material processed by dry FSP under the rotational speed of 19.2 m/min and feed rate of 101.6 mm/min at the positions of approximately 0 mm, 0.75 mm, 1.5 mm, 2.25 mm and 3 mm along the orientation of the plate thickness..... 66

Figure: 3.5: Microstructure images of the work material processed by cryogenic FSP under the rotational speed of 19.2 m/min and feed rate of 101.6 mm/min at the positions of approximately 0 mm, 0.75 mm, 1.5 mm, 2.25 mm and

3 mm along the orientation of the plate thickness.....	67
Figure: 3.6: Microstructure images of the work material processed by dry FSP under the rotational speed of 24 m/min and feed rate of 101.6 mm/min at the positions of 0 mm, 0.75 mm, 1.5 mm, 2.25 mm and 3 mm along the orientation of the plate thickness.....	68
Figure: 3.7: Microstructure images of the work material processed by cryogenic FSP under the rotational speed of 24 m/min and feed rate of 101.6 mm/min at the positions of approximately 0 mm, 0.75 mm, 1.5 mm, 2.25 mm and 3 mm along the orientation of the plate thickness.....	69
Figure: 3.8: Microstructure images of the work material processed by dry FSP under the rotational speed of 28.8 m/min and feed rate of 101.6 mm/min at the positions of 0 mm, 0.75 mm, 1.5 mm, 2.25 mm and 3 mm along the orientation of the plate thickness.....	70
Figure: 3.9: Microstructure images of the work material processed by cryogenic FSP under the rotational speed of 28.8 m/min and feed rate of 101.6 mm/min at the positions of 0 mm, 0.75 mm, 1.5 mm, 2.25 mm and 3 mm along the orientation of the plate thickness.....	71
Figure: 3.10: Microstructure images of the work material processed by dry FSP under the rotational speed of 48 m/min and feed rate of 101.6 mm/min at the positions of 0 mm, 0.75 mm, 1.5 mm, 2.25 mm and 3 mm along the orientation of the plate thickness.....	72

Figure: 3.11: Microstructure images of the work material processed by cryogenic FSP under the rotational speed of 48 m/min and feed rate of 101.6 mm/min at the positions of 0 mm, 0.75 mm, 1.5 mm, 2.25 mm and 3 mm along the orientation of the plate thickness.....	73
Figure 3.12: The microstructure image of the as-received material.....	74
Figure 3.13: Grain size distributions among the samples processed by dry and cryogenic FSP at four different rotational speeds of 19.2, 24, 28.8, and 48 m/min: (a) dry, 19.2 m/min; (b) dry, 24 m/min; (c) dry, 28.8 m/min; (d) dry, 48 m/min, (e) cryogenic, 19.2 m/min; (f) cryogenic, 24 m/min; (g) cryogenic, 28.8 m/min; and (h) cryogenic, 48 m/min.....	77
Figure 3.14: Grain size distributions among the samples processed by dry and cryogenic FSP at four different rotation speeds of 19.2, 24, 28.8, and 48 m/min: (a) dry, 19.2 m/min; (b) dry, 24 m/min; (c) dry, 28.8 m/min; (d) dry, 48 m/min; (e) cryogenic, 19.2 m/min; (f) cryogenic, 24 m/min; (g) cryogenic, 28.8 m/min; and (h) cryogenic, 48 m/min.....	78
Figure 3.15: Grain size variation in dry and cryogenic FSP at four different speeds: 19.2, 24, 28.8, 48 m/min.....	79
Figure 3.16: Detailed hardness distributions among the samples processed by dry and cryogenic FSP at four different rotation speeds of 19.2, 24, 28.8, and 48 m/min: (a) dry, 19.2 m/min; (b) dry, 24 m/min; (c) dry, 28.8 m/min; (d) dry, 48 m/min; (e) cryogenic, 19.2 m/min; (f) cryogenic, 24 m/min;	

(g) cryogenic, 28.8 m/min; and (h) cryogenic, 48 m/min..... 82

Figure 3.17: Hardness distributions among the samples processed by dry and

cryogenic FSP at four different rotation speeds of 19.2, 24, 28.8, and 48 m/min: (a) dry, 19.2 m/min; (b) dry, 24 m/min; (c) dry, 28.8 m/min;

(d) dry, 48 m/min; (e) cryogenic, 19.2 m/min; (f) cryogenic, 24 m/min;

(g) cryogenic, 28.8 m/min; and (h) cryogenic, 48 m/min..... 84

Figure 3.18: Hardness variation in dry and cryogenic FSP at four different speeds..... 86

Figure 3.19: (a) XRD plot ranging from 35° to 80°; (b) XRD distribution of *Al (111)*;

and (c) XRD distribution of *Al (200)*..... 88

Figure 4.1: Experimental setup: (a) Mazak Quick Turn-10 Turning Center and

cryogenic coolant delivery system; and (b) detailed illustration of

cryogenic machining of *Al 7050-T7451* disc with near-UFG structure..... 94

Figure 4.2: The cutting and thrust force components measured from the experiments

of dry and cryogenic machining of *Al 7050-T7451* alloys with near-UFG

structure..... 96

Figure 4.3: (a) Image example of temperature distribution obtained by infrared camera;

and (b) Highest temperature achieved in dry and cryogenic machining in the

work material-tool contact area..... 97

Figure 4.4: Microstructures of the machined surface layers produced by dry and

cryogenic machining of *Al 7050-7451* alloys with near-UFG structure at

four different cutting speeds: 50, 100, 200 and 300 m/min.....	99
Figure 4.5: Grain size distributions in the machined surface layers from (a) cryogenic; and (b) dry machining of <i>Al 7050-T7451</i> alloys with near-UFG structure at four different cutting speeds.....	101
Figure 4.6: Hardness distribution in the machined surface layers with the comparison of dry and cryogenic machining of <i>Al 7050-T7451</i> alloy with near-UFG structure: (a) $V = 50$ m/min; (b) $V = 100$ m/min; (c) $V = 200$ m/min; and (d) $V = 300$ m/min.....	104
Figure 4.7: Chip morphology and microstructure in dry and cryogenic machining of <i>Al 7050-T7451</i> alloy with near-UFG structure under four cutting speeds..	122
Figure 4.8: Grain size distributions in the three zones of chips produced by dry and cryogenic machining of <i>Al 7050-T7451</i> alloy with near-UFG structure...	123
Figure 4.9: Chip hardness measurement in dry and cryogenic machining.....	125
Figure 5.1: Experimental setup for orthogonal cryogenic burnishing.....	135
Figure 5.2: Radial and tangential burnishing forces under four different depths of penetration: (a) at the burnishing speed of 25 m/min; (b) at the burnishing speed of 50 m/min; and (c) at the burnishing speed of 100 m/min.....	137
Figure 5.3: (a) The infrared image of temperature measurement (dry burnishing under the depth of penetration of 0.2 mm and burnishing speed of 25 m/min); and (b) The highest temperatures measured in dry burnishing at three different burnishing speeds of 25, 50 and 100 m/min and four different	

depths of penetration of 0.05, 0.1, 0.15 and 0.2 mm..... 139

Figure 5.4: The microstructure of *Al 7050-T7451* alloy with near-UFG structure processed by cryogenic burnishing at the depth of penetration of 0.2 mm and burnishing speed of 25 m/min: (a) AFM image (measured from the refined layer denoted by the black rectangular box); (b) the microstructure of the burnished surface and sub-surface generated by cryogenic burnishing; and (c) the microstructure of the burnished surface and sub-surface generated by dry burnishing..... 141

Figure 5.5: The microstructures of *Al 7050-T7451* alloys with near-UFG structure processed by cryogenic burnishing under the depths of penetration of 0.05, 0.1, 0.15, 0.2 mm and burnishing speeds of 25, 50, 100 m/min..... 147

Figure 5.6: The depths of refined layers of *Al 7050-T7451* alloys with near-UFG structure processed by cryogenic burnishing under the depths of penetration of 0.05, 0.1, 0.15, 0.2 mm and burnishing speeds of 25, 50, 100 m/min..... 147

Figure 5.7: The hardness distributions of *Al 7050-T7451* alloys with near-UFG structure processed by dry and cryogenic burnishing at the depths of penetration of 0.05, 0.1, 0.15, 0.2 mm and burnishing speeds of 25, 50, 100 m/min..... 153

Figure 5.8: Hardness increase of *Al 7050-T7451* alloys with near-UFG structure processed by dry and cryogenic burnishing at the depths of penetration of 0.05, 0.1, 0.15, 0.2 mm and burnishing speeds of 25, 50, 100 m/min:

(a) cryogenic burnishing; and (b) dry burnishing.....	154
Figure 6.1: The boundary conditions of FEM-based numerical model.....	163
Figure 6.2: The flow stress curve in the case of dynamic recovery and dynamic recrystallization (Sarkar et al., 2011).....	164
Figure 6.3: Calibration of the numerical burnishing model.....	168
Figure 6.4: The calibration between predicted and experimental results to determine the material constants of <i>A</i> and <i>B</i> used in the modified Johnson-Cook material model (dry burnishing, under the burnishing speed of 50 m/min and the depth of penetration of 0.2 mm).....	169
Figure 6.5: The calibration between predicted and experimental results to determine the friction coefficient used in the shear friction model (dry burnishing, under the burnishing speed of 50 m/min and the depth of penetration of 0.2 mm).....	169
Figure 6.6: Comparison between predicted and experimental radial forces in dry burnishing: (a) burnishing speed of 25 m/min; (b) burnishing speed of 50 m/min; and (c) burnishing speed of 100 m/min.....	172
Figure 6.7: Comparison between predicted and experimental radial forces in cryogenic burnishing: (a) burnishing speed of 25 m/min; (b) burnishing speed of 50 m/min; and (c) burnishing speed of 100 m/min.....	173

Figure 6.8: Comparison between predicted and experimental tangential forces in dry burnishing: (a) burnishing speed of 25 m/min; (b) burnishing speed of 50 m/min; and (c) burnishing speed of 100 m/min.....	175
Figure 6.9: Comparison between predicted and experimental tangential forces in cryogenic burnishing: (a) burnishing speed of 25 m/min; (b) burnishing speed of 50 m/min; and (c) burnishing speed of 100 m/min.....	176
Figure 6.10: Comparison between predicted and experimental highest temperatures in dry burnishing: (a) burnishing speed of 25 m/min; (b) burnishing speed of 50 m/min; and (c) burnishing speed of 100 m/min.....	179
Figure 6.11: Calibration of the recrystallized grain size model.....	181
Figure 6.12: Simulation images of SPD layers induced by cryogenic burnishing and the comparison with the corresponding microstructure images: (a) burnishing speed of 25 m/min; (b) burnishing speed of 50 m/min; and (c) burnishing speed of 100 m/min.....	187
Figure 6.13: Comparison between the predicted and measured SPD layers induced by cryogenic burnishing by showing the error bars: (a) burnishing speed of 25 m/min; (b) burnishing speed of 50 m/min; and (c) burnishing speed of 100 m/min.....	188

CHAPTER 1

INTRODUCTION

1.1 Introduction

As one of the high-strength aluminum alloys with excellent corrosion resistance and mechanical properties, *Al 7050-T7451* alloy has been heavily used in the aerospace/aviation applications, for components such as fuselage frames, wing skins, bulkhead etc., where fatigue-critical properties are needed. Due to its advanced mechanical and material properties, *Al 7050-T7451* alloy becomes a preferred selection when the best possible combination of toughness, strength, stress corrosion cracking resistance is required for the utilization of aluminum alloys.

The addition of the chemical element of zirconium can reduce the sensitivity of this aluminum alloys to quenching, thus resulting in high strength for thick plates made of *Al 7050-T7451* alloy. The difference of this subtle addition makes *Al 7050* alloy superior to *Al 7075* alloy. However, the shortcoming of *Al 7050-T7451* alloy is also apparent, it is a highly anisotropic alloy in which the crack growth behavior along the short transverse direction is very different from the one in the long transverse direction. This drawback limits the application of *Al 7050-T7451* alloy, and this critical problem needs to be solved in order to broaden its application.

A new methodology for modifying the properties of this material is presented in the dissertation. In the past, many technologies have been developed to produce ultra-fine grained materials by inducing severe plastic deformation (SPD), for example, equal

channel angular pressing, high pressure torsion, twist extrusion, multi-directional forging, multi-axis restrain deformation etc. All of these methodologies aim at refining the grains with equiaxed structure in the ultra-fine grain size level (less than 1 μm), while improving the mechanical properties without significantly altering the overall dimensions of the processed work materials.

As one of the novel methods emerging in the past two decades, friction stir processing takes advantage of the stir and friction actions to induce severe plastic deformation associated with dynamic recrystallization of the processed materials for the purpose of grain refinement. This technology is used to process the as-received *Al 7050-T7451* alloy with coarse grains (more than 50 μm) with highly inhomogeneous structure in which the grains are elongated in the direction of rolling process. In the study presented in the dissertation, friction stir processing is employed to modify the microstructure of the as-received work material in order to achieve a more homogeneous material with near ultra-fine grained structure. The application of *Al 7050-T7451* alloy is expected to become wider as a result of the modification introduced by this methodology.

Further machining processes are indispensable to satisfy the need of desired dimensions with high accuracy and obtain good surface integrity characteristics influencing the performance of the manufactured components, such as surface roughness, hardness, wear/corrosion resistance, residual stresses, etc. In this study, friction stir processing cannot be the final process for the processed materials as accurate dimension and acceptable surface integrity need to be met. Therefore, machining of *Al 7050-T7451*

alloy with ultra-fine grained structure obtained through friction stir processing is also studied.

Cryogenic machining, using liquid nitrogen as the coolant during the machining process, is applied to achieve the dimension accuracy while improving the surface integrity characteristics, including improved surface roughness, enhanced microhardness, refined microstructure, induced compressive residual stresses and improved wear/corrosion resistance etc. Cryogenic machining of *Al 7050-T7451* alloy with near ultra-fine structure is investigated, following the research of friction stir processing. Very few researchers have studied the machining effects on materials with ultra-fine grained structure, especially with cryogenic cooling. Thus, the research conducted for this topic is very interesting and could significantly contribute to the present knowledge in the machining and applications. The combining effects of friction stir processing and cryogenic machining are the key points affecting the surface integrity of *Al 7050-T7451* alloy.

Furthermore, a burnishing process is used to further modify the surface integrity of *Al 7050-T7451* alloy to a greater degree. As a chipless post-machining process, burnishing is commonly performed on manufactured components for altering surface integrity. More severe plastic deformation is induced when the surface of the work material is compressed by a roller or ball burnishing tool made of hardened material. The tool marks/scratches, pits or porosity on the surface of the manufactured components can be eliminated by burnishing process while increased hardness, and improved surface roughness, refined surface layers and improved wear/corrosion resistance, etc., could

be achieved. In order to enhance the surface integrity characteristics of *Al 7050-T7451* alloy in aerospace applications, particularly for use in the critical structural components, cryogenic burnishing of *Al 7050-T7451* alloy is investigated to study the burnishing effects on *Al 7050-T7451* alloys with near ultra-fine grained structure obtained by friction stir processing under cryogenic condition.

Liquid nitrogen is applied to the contact area between the burnishing tool and work material to take away the heat within a relatively short time. The recrystallized grains produced by the dynamic recrystallization induced by cryogenic burnishing, are constrained to grow. Therefore, a refined layer with nano-grains is obtained, and higher hardness is achieved in this refined layer will benefit of enhanced the wear/corrosion resistance.

In general, new experimental methodologies have been developed for a series of successive operations: friction stir processing, cryogenic machining and cryogenic burnishing, to improve the surface integrity characteristics of *Al 7050-T7451* alloy step by step as shown in Figure 1.1. The detailed research content is also discussed in the next section.

1.2 Overview of the dissertation

In Chapter two, the applications of *Al 7050-T7451* alloys and ultra-fine grained materials are summarized, while the limits of its application are shown to specify the motivation of the research conducted and presented in this dissertation. Literature reviews provide a fundamental understanding of friction stir processing, cryogenic

machining and burnishing processes. Past research regarding friction stir processing and machining of *Al 7050-T7451* alloys is reviewed to enable guidance for the setup of the experimental design and output parameter analysis.

Friction stir processing is performed to modify the microstructure of *Al 7050-T7451* alloy in Chapter three, where it is shown that more homogeneous materials with near ultra-fine grained structure are acquired through friction stir processing. Grain size is measured in 45 spots distributed in the cross-section cut from the processed plate in order to identify the uniformity of each sample processed under dry and cryogenic friction stir processing at four different rotational speeds. Similarly, the measurement of hardness also provides another way to evaluate the homogeneity of the processed materials. The X-ray diffraction measurement is used to investigate texture change induced by friction stir processing.

In Chapter four, microstructure and hardness are studied as the surface integrity characteristics when cryogenic machining is used to further process the *Al 7050-T7451* alloy with near ultra-fine grained structure achieved by friction stir processing. The measurements and analysis of cutting forces, temperatures, chip microstructure and hardness also provide a better understanding of machining of ultra-fine grained materials.

In Chapter five, burnishing forces, temperatures, microstructure (depth of refined layers) and hardness in the burnished surface and sub-surface are measured and analyzed to demonstrate the burnishing effects induced by dry and cryogenic burnishing under three different burnishing speeds and four depths of penetration. A numerical

model based on finite element method is developed and presented in Chapter six. By means of calibration and validation through burnishing forces and temperatures, this numerical model is used to predict the depth of SPD layer produced by cryogenic burnishing.

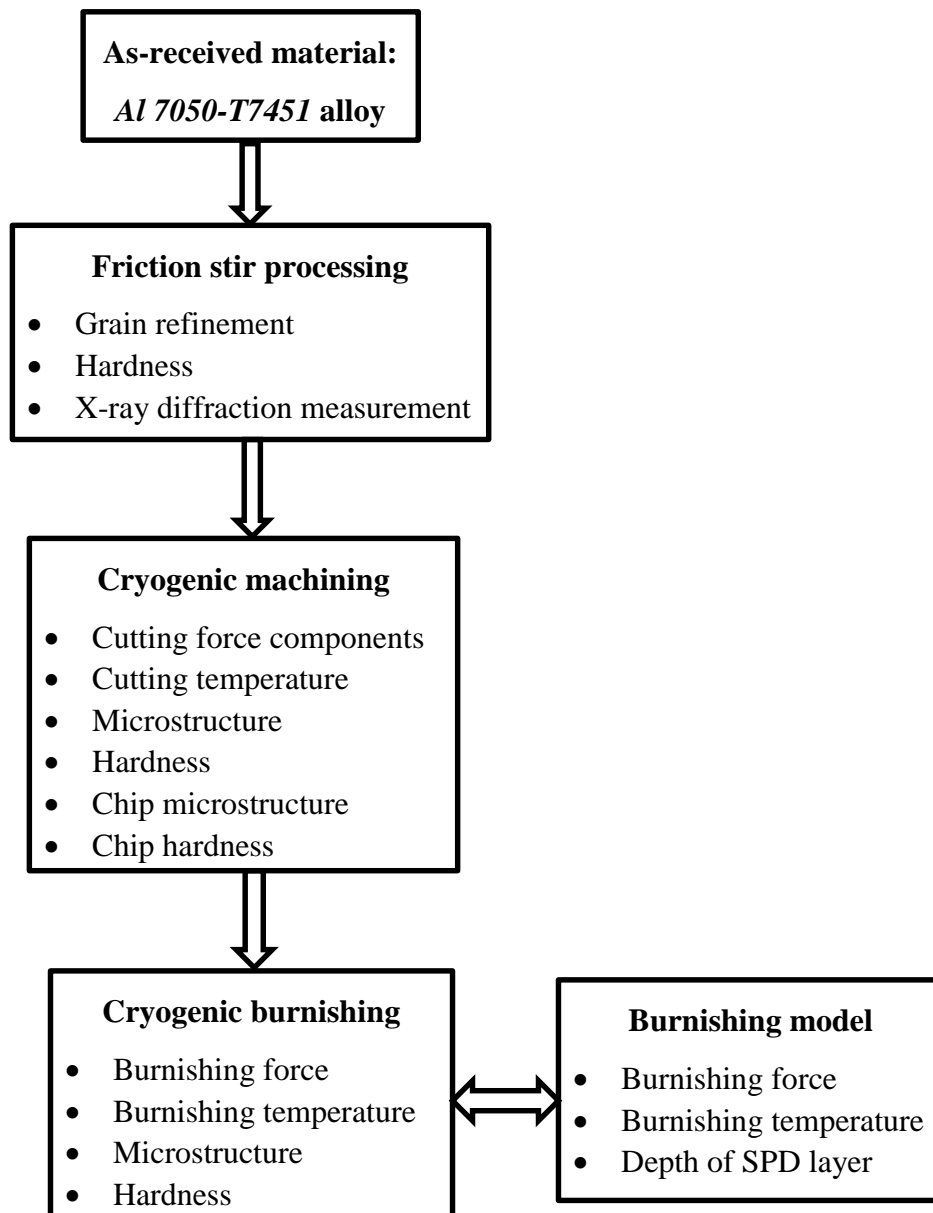


Figure 1.1: Flow chart of the dissertation overview.

CHAPTER 2

LITERATURE REVIEW

2.1 Applications of *Al 7050-T7451* alloy

Al 7050-T7451 alloy is one of the high-strength *Al-Zn-Mg-Cu-Zr* alloys developed to optimize the corrosion resistance and mechanical properties (Jata et al., 2000). In the early 1970s, this alloy was designed and introduced as an advanced aerospace alloy with high weight content of zinc and copper. *Al 7050-T7451* alloy is a premier choice for the aerospace applications with the requirements of the best possible combination of strength, stress corrosion cracking resistance and toughness (Alcoa, 2012; Hill and Panontin, 2002; Luong and Hill, 2010).

The widespread applications of this aluminum alloy used by aircraft manufacturers primarily include fatigue-critical airframe structural components for both military and civil aircrafts (Luong and Hill, 2010; Magnusen et al., 1997). The specific applications of *Al 7050-T7451* alloy are the bulkheads of RAAFF/A-18 aircrafts (Sharp and Clark, 2001). Other plate applications in the aerospace industry include the components of fuselage frames, wing skins, etc., assembled in Boeing 777 commercial airliner, the F/A-18 Hornet and F-22 Raptor military aircrafts (Clark and Johnson, 2003). Typical applications of *Al 7050-T7451* alloy are shown in Figures 2.1 to 2.3.



Figure 2.1: (a) Airbus A380 in flight; and (b) View of the internal face of a starboard wing skin panel made of Al 7050-T7451 alloy (Atkins Ltd, 2012).

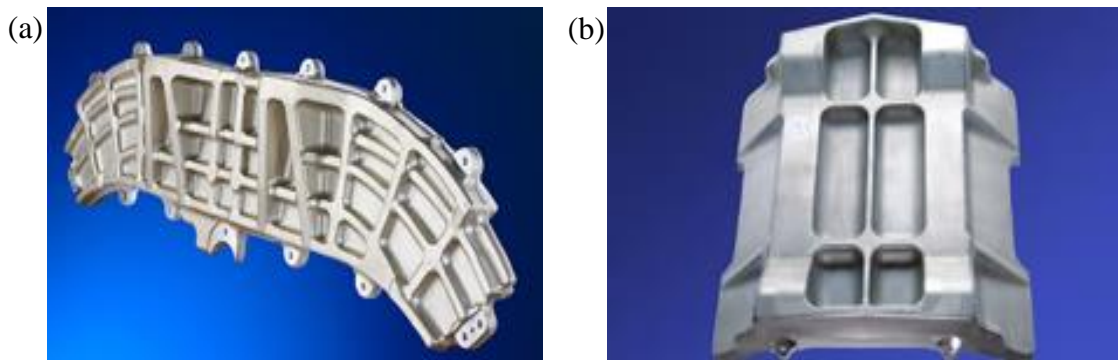


Figure 2.2: Components made of Al 7050-T7451 alloys: (a) Fuselage frame; and (b) Front fitting for aircrafts (OTTO FUCHS KG, 2012).

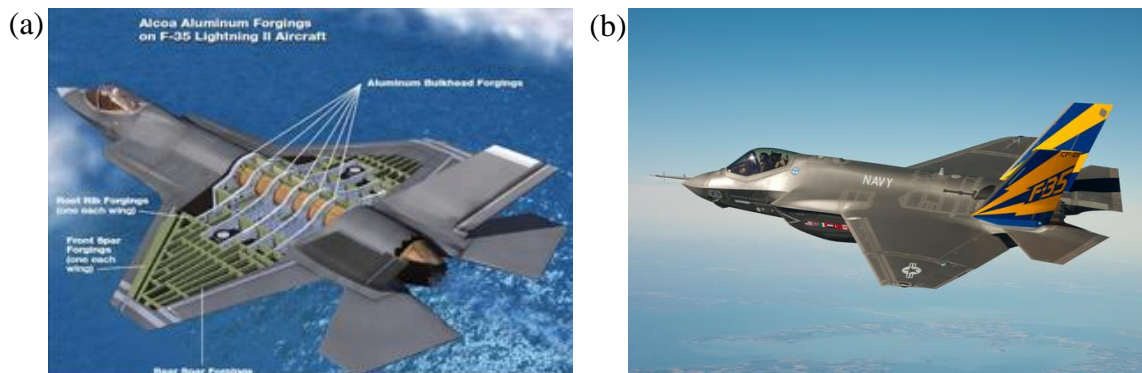


Figure 2.3: *F-35* aircrafts: (a) Bulkhead components made of 7 series aluminum alloys (Bacon, 2014); and (b) *F-35* in flight (Wikipedia, 2011).

The chemical compositions of Al 7050-T7451 alloy in weight percent varies slightly for the Al-Zn-Mg-Cu-Zr alloy. According to the literature reviews, the compositions consist of Zn (6.06%-6.2%), Mg (1.9%-2.25%), Cu (2.19%-2.6%), Zr (0.09%-0.15%), Fe (0.08%-0.15%), Si (0.05%-0.15%), Mn (0.1%), Cr (0.03% to 0.04%), Ti (0.04% to

0.06%) and others (0.01%) balanced with the rest by *Al* (Jata et al., 2000; Luong and Hill, 2010; Bao and Zhang, 2010; Schubbe, 2009; Carvalho and Voorwald, 2009). Furthermore, the heat treatment conditions of *T7451* include heat-treating, quenching and overaging (Lyman, 1967). The details of this particular heat treatment are heat-treating at 477 °C for 30 minutes, water quenching, aging at 121°C for 2 hours, and then aging at 163°C for 21 hours followed by 2% stretching (Yan and Reynolds, 2009). Processed by this specific heat treatment, *Al 7050-T7451* alloy is an over-aged plate material with improved fracture toughness and minimal loss of tensile strength (Mueller, 1985).

As the substitution of *Al 7075* alloy, a critical difference between *Al 7050* and *Al 7075* is the addition of zirconium instead of chromium for the purpose of inhibiting recrystallization. Although both of these two aluminum alloys have approximately the same tensile strengths, the fracture toughness of *Al 7050-T7451* alloy is more superior to *Al 7075* (Clark and Johnson, 2003). Due to the use of zirconium, it reduces the sensitivity of the alloys to quenching that leads to high strength in thick sections (Hill and Panontin, 2002).

The mechanical properties of *Al 7050-T7451* alloy are summarized as follows. The yield stress of this aluminum alloy is within the range from 429 MPa to 470 MPa, and the ultimate tensile strength is in the range of 502 to 520 MPa. The elongation is between 9% and 12%, while the elastic modulus is within a range from 65 GPa to 71.7 GPa (Carvalho and Voorwald, 2007; Bao and Zhang, 2010; Military handbook, 1994). Nevertheless, *Al 7050-T7451* alloy is considered to be a highly anisotropic alloy that

will limit its application. It was found that the crack growth behavior along the short transverse direction (L-S) was very different from the one along the long transverse direction (L-T) (Bao and Zhang, 2010; Schubbe, 2009). Thus, further modifications and processing would be needed to extend the applications of *Al 7050-T7451* alloy.

2.2 Applications of materials with ultra-fine grained structure

In the last two decades, the processing and manufacturing of the ultra-fine grained (UFG) and nanocrystalline materials have gained great attentions in the research communities and industries due to the advanced and improved properties of these materials and the development of novel processing technologies (Sanusi et al., 2012; Gleiter, 2001). UFG materials are employed in the industries with nuclear/power, aerospace, automotive and biomedical applications, and for precision instruments, micro-electromechanical systems (Kim and Sa, 2006; Valiev et al., 2008; Qiao et al., 2010).

For the biomedical applications, UFG tantalum, titanium and stainless steel are used to produce the medical implants and instruments in the form of the foils, wires and thin-walled tubes. The typical examples of biomedical applications are long-sized oncology needles and drug eluting stents due to the characteristics of biological compatibility, high strength and ductility provided by UFG materials (Tikhonovsky, 2011), as shown in Figure 2.4. Vehicle bodies made of high strength steels with dual or multi phases, such as transformation-induced plasticity (TRIP) steel, are more preferable and prevalent in the automotive industry from the beneficial perspectives of lightweight and crash

resistance (Ponge, 2011). More fractions of dual phase steel and Trip-steel are employed in the car bodies as shown in Figure 2.5.

Furthermore, Superplastic forming of UFG materials is performed to produce the fuselages of aircrafts to eliminate the part numbers and fasteners. Approximately 726 parts and 10,000 fasteners were eliminated in the manufacturing of F-15E fighter fuselage with the help of superplastic forming and diffusion bonding (Salishchev et al., 2001), Figure 2.6 shows the comparison of fuselages manufactured with and without the technology of superplastic forming.

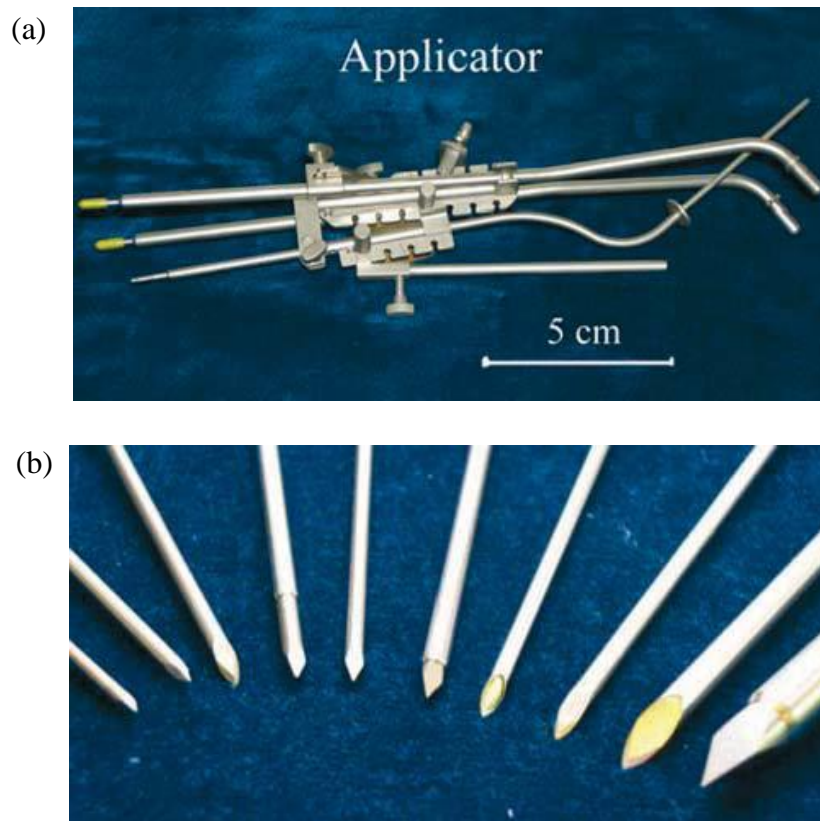


Figure 2.4: (a) Medical devices applicator and (b) Oncology needles with UFG structures (Tikhonovsky, 2011).

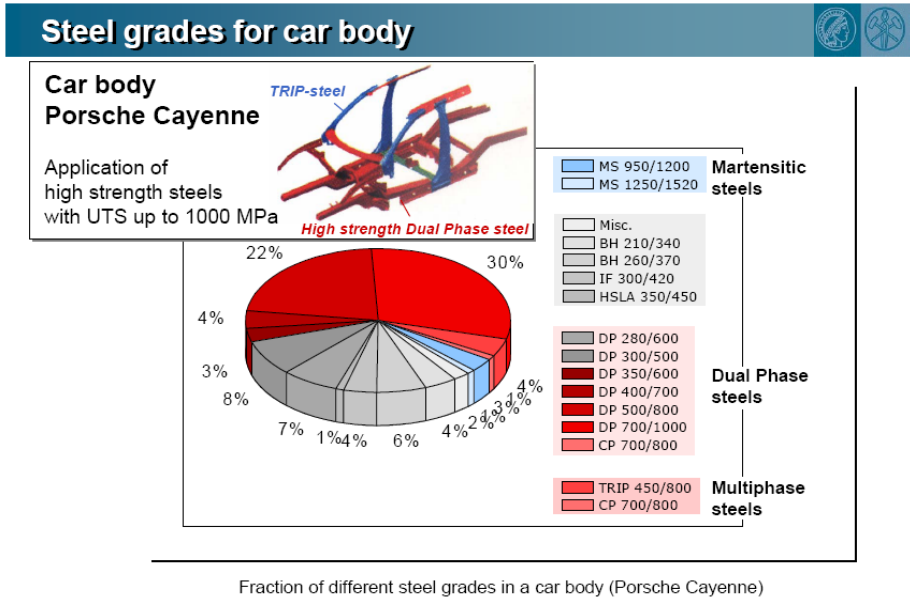


Figure 2.5: The example of UFG steel applications (Ponge, 2011).

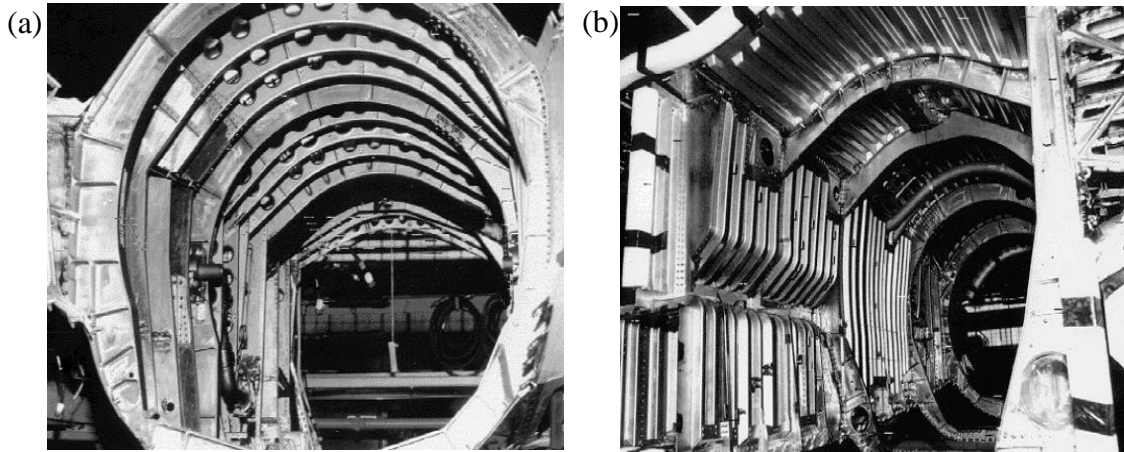


Figure 2.6: *F-15E* aircraft fuselage: (a) conventional assembly and (b) Superplastic forming structure (Salishchev et al., 2001).

The common definition of UFG is related to the small grains with the average grain size of less than 1 μm , and larger than 100 nm. Extremely homogeneous and equiaxed microstructures are also achieved in the UFG materials within which the majority of the grain boundaries with high angles of orientation are induced (Valiev, 2004). Due to these particular characteristics, some extraordinary mechanical properties can be obtained in UFG materials such as, high hardness, enhanced toughness, high yield

stress, improved ductility at increased strain-rates, good wear resistance, etc. (Gleiter, 2001; Valiev, 2003; Langdon, 2011; Gao et al., 2012).

Compared with coarse-grained materials, UFG materials possess superior mechanical properties, such as a combination of high strength and good ductility, superplasticity, higher elongation and yield strength (Gao et al., 2012; Lloyd et al., 1980; Saunders et al., 1997) in the potential structural applications. For example, the strength of *Al 5083* with the UFG structure was approximately 30% higher than the one with the coarse-grained materials (Topping et al., 2012).

In order to obtain UFG materials with excellent material and mechanical properties, SPD-based methods have been developed to fabricate UFG materials from coarse grained materials. The typical SPD methods are high pressure torsion, equal channel angular pressing, multi-axis restrain deformation, twist extrusion, cyclic extrusion compression, multi-directional forging, etc. (Sergueeva et al., 2002; Valiev et al., 2000; Chen et al., 2001; Richert, 1997). The principal mechanism of most SPD methods depends on metal forming procedures by imposing high strains on the materials that will result in exceptional grain refinement, without changing the overall dimensions of the work materials significantly. Attributing to the special design of tool geometries, free flow of the materials can be prevented, and therefore, a very high hydrostatic pressure is induced, which is essential to introduce high strains and great densities of lattice defects for grain refinement (Valiev et al., 2006).

For the *Al 7050-T7451* alloy and other aluminum alloys with specific mechanical properties, a novel SPD method with simplified experimental setup and effective

processing mechanism is used to process the coarse-grained materials for the purpose of obtaining the UFG materials with more homogeneous microstructure and hardness.

2.3 Friction stir processing

Friction stir welding (FSW) was invented by the Welding Institute as a reliable and efficient joining technology with the consideration of friendly environment (Thomas et al., 1995). A highly plastically-deformed area is produced through the stir action of the tool as it rotates and travels along the length direction of the abutting plates required to be welded. Based on the same principle of FSW, friction stir processing (FSP) has been developed as a novel solid state processing method to modify coarse materials in order to obtain the nano-structured or UFG materials.

The working mechanism of FSP is relatively simple, making it very convenient to be applied in the industries. A rotating tool consisting of a pin and a shoulder is plugged into the work material, and then traversed along the desired path while in the entire process, the tool shoulder contacts with the surface of the processed material imposed by a sufficient downward force. Figure 2.7 shows an illustration of the working mechanism of FSW/FSP. Due to the friction heat generated between the tool shoulder and the work material, the temperature of the processed material raises up, however it does not reach the melting temperature. Combined with the high temperature, severe plastic deformation occurs because of the stir action of the pin toward the softened work material, leading to dynamic recrystallization (DRX) as the conditions of strain, strain-rate and temperature have been met for the material. A significant microstructure

modification is achieved and nano or ultra-fine grains with equiaxed structure and high-angle grain boundaries are produced.

The mechanical and physical properties of the work materials can be improved due to the microstructure modification and grain refinement introduced by FSP. Therefore, it has been used in the typical applications, such as grain refinement of casting parts, formation of intermetallics, fabrication of metal matrix composite, superplasticity improvement, synthesizing in-situ composite, production of surface composite layers, improving the electrical conductivity, enhancing the corrosion resistance of the processed material, etc. (Ma et al., 2006a; Hsu et al., 2005; Ma et al., 2006b; Wang et al., 2009; Morisada et al., 2006; Santos et al., 2011; Shafiei-Zarghani et al., 2009).

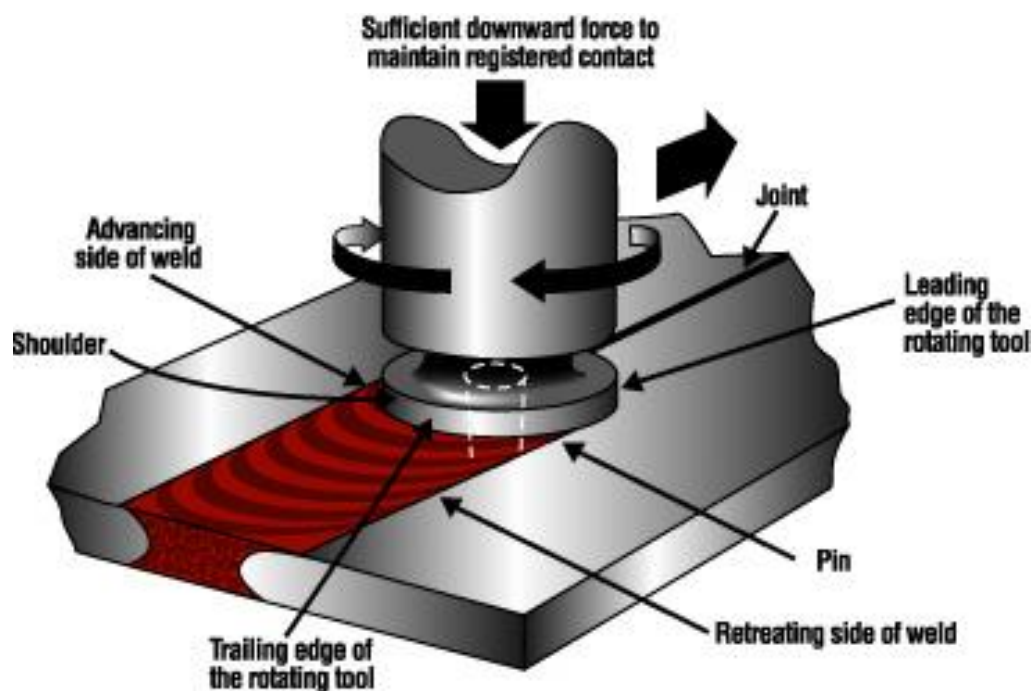


Figure 2.7: The working illustration of FSW/FSP (Friction stir Link, 2011).

2.3.1 Friction stir processing of aluminum alloys

Review of past work regarding FSP of aluminum alloys is very critical for planning new experimental work of FSP of *Al 7050-T7451* alloys to enhance its mechanical properties and solve the problem of inhomogeneity by introducing grain refinement. Research from the FSW/FSP community have been reviewed to know the details of the research areas being focused and the modifications achieved among the processed materials, especially aluminum alloys. The explicit research areas have been discussed as follows based on the applications of FSP and the corresponding types of aluminum alloys with specific properties.

As-cast aluminum alloys are commonly used in automotive and aircraft industries due to their mechanical properties, such as fatigue life, ductility and wear resistance. However, the shortcomings are also evident in limiting their applications. For example, *A356* alloy's drawbacks include the high porosity, coarse and acicular *Si* particles distributed non-uniformly and the dendritic structure etc. (Elmadagli et al., 2007; Lashgari et al., 2010; Seniw et al., 2000; Zhang et al., 1999). Thus, it is necessary to utilize an effective modification technology to eliminate the porosity and refine the large *Si* particles distributed uniformly in the bulk *Al* matrix.

In the latest two decades, FSP has been used as a solid method to modify as-cast aluminum alloys. Sharma et al. (2004) studied the effects of FSP on *A356* alloy, and they found that the fatigue life was enhanced by FSP attributing to the elimination of casting defects, the microstructure refinement and homogenization. FSP provided the advantages to break the coarse *Si* particles and distribute them uniformly in the bulk *Al*

matrix. The fatigue stress was improved by more than 80% in the processed area as shown in Figure 2.8, benefiting the reduction of crack growth rate. A similar phenomenon was observed by Nakata et al. (2006), where the hardness of the FSPed die-casting aluminum alloys was increased by 20 HV compared to the bulk material, in the meantime, the tensile strength of the FSPed samples was improved by 70% because of the elimination of cold flakes existing in the as-received materials and the uniform distribution of finer *Si* particles induced by FSP.

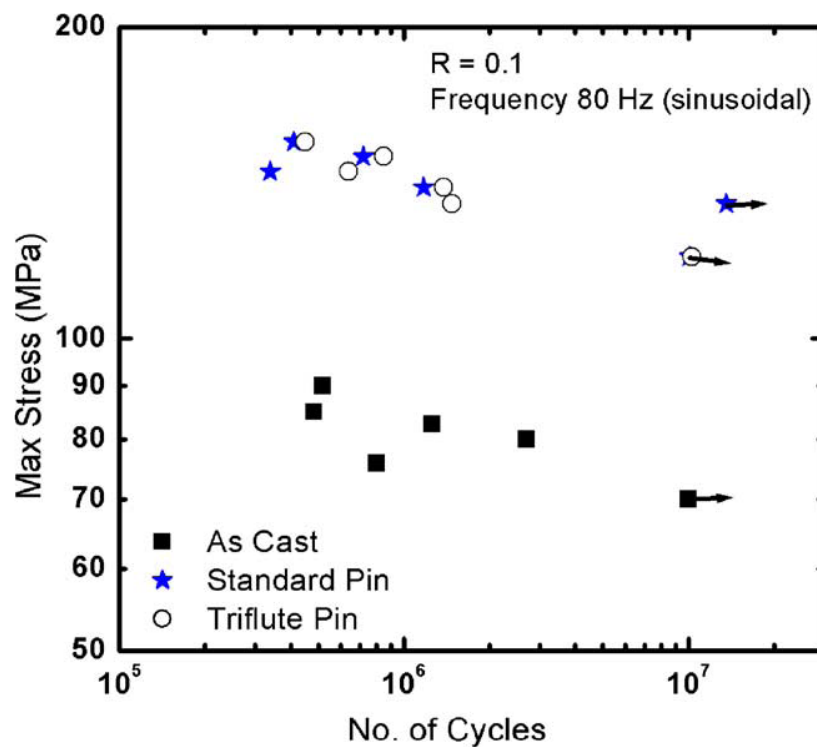


Figure 2.8: Influence of FSP on fatigue properties of *Al 356* alloy (Sharma et al., 2004).

It was also reported by Ma et al. (2006c) that the yield stress and ultimate tensile strength of *Al 356* alloy were improved substantially by two-pass FSP with 100% overlapping due to a further refinement of *Si* particles and a better porosity elimination. The mechanical properties of cast *AZ91* alloy were enhanced, including the increased

tensile strength and decreased ductility by FSP (Feng and Ma, 2007) due to the breakup and dissolution of the coarse particles and the grain refinement. The details of the strength improvement and microstructure of the processed materials are shown in Figures 2.9 and 2.10.

The microstructure, hardness and tribological behavior of FSPed *A356* alloy were evaluated by Alidokht et al. (2012). In their research, the grain size was refined to 1 μm while the size and aspect ratio of the *Si* particles were 3.3 μm and 1, respectively. The hardness of the processed material was also higher than the base material. Superior wear resistance was obtained in the FSPed material surface because of the load-bearing effect of finer *Si* particles, and more pronounced wear rate was achieved when using a high rotation speed for the FSP tool.

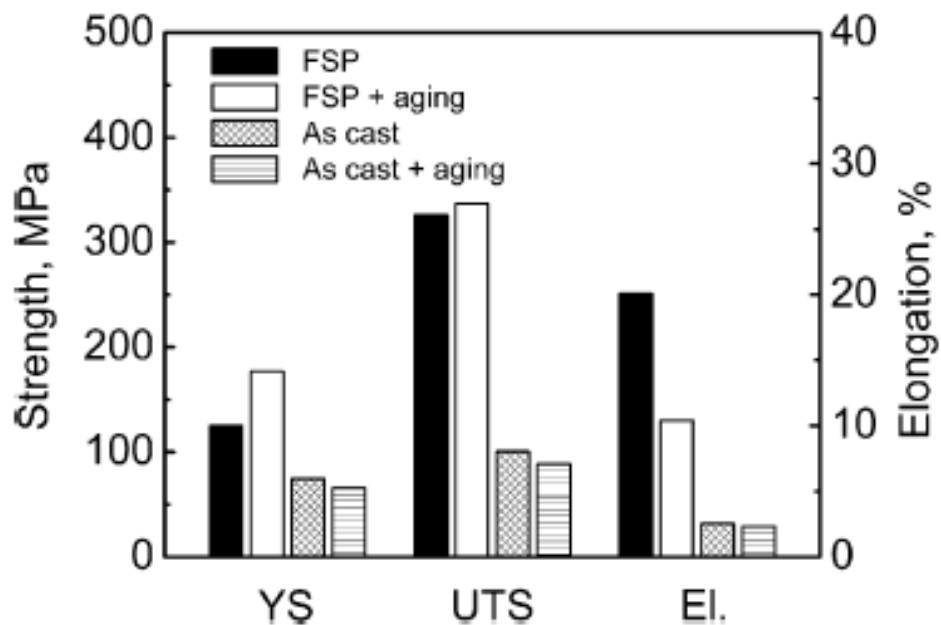


Figure 2.9: Tensile properties of *AZ91D* magnesium alloy (YS: yield strength, UTS: ultimate tensile strength, El.: elongation) (Feng and Ma, 2007).

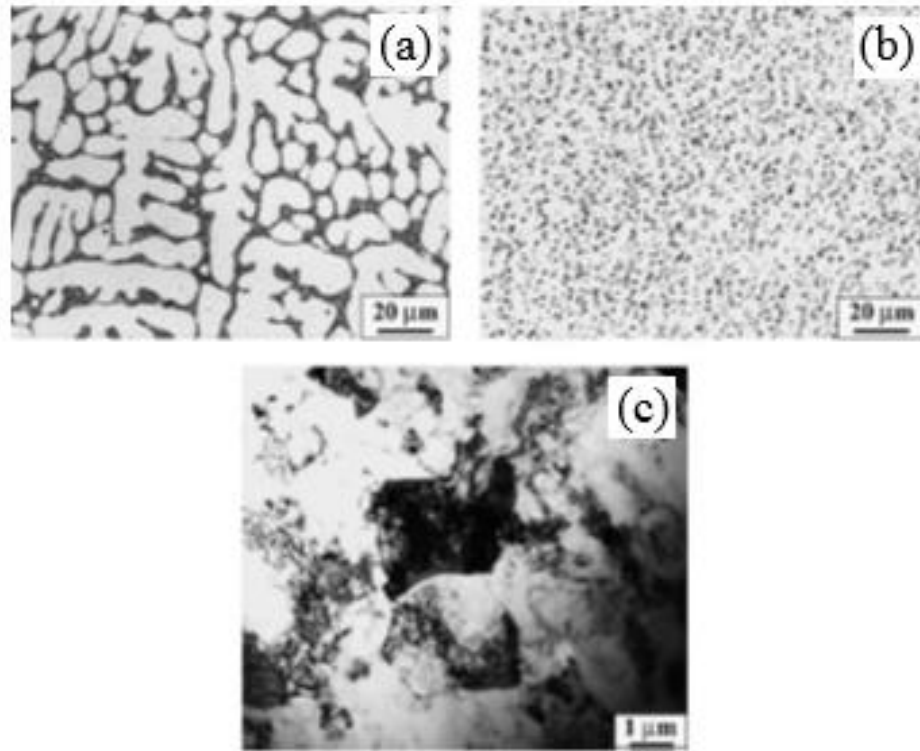


Figure 2.10: Micrographs of (a) cast A356 alloy; (b) FSPed A356 alloy; and (c) bright field TEM micrograph of FSPed A356 alloy (Ma et al., 2004).

Obtaining superplasticity will facilitate the manufacturing of complex components made of aluminum alloys with the aerospace applications, such as fuselage panels, structural parts and tanks, etc. FSP has been utilized as an effective method to process the aluminum alloys to achieve the desired property of superplasticity. The elongation of 1250% was acquired in the FSPed *Al 7075* sample whose grain size was refined to 3.8 μm, whereas under different processing parameters, the grain size was reduced to 7.5 μm by FSP, and the corresponding elongation became 1042% (Ma et al., 2002). Similarly, Charit et al. (2003) also demonstrated that a maximum elongation of 525% was achieved in the FSPed *Al 2024* alloy. For the FSPed cast A356 alloy, a maximum elongation of 650% was obtained in contrast to the non-superplastic base material (Ma et al., 2004). Moreover, the average grain size was between 1.49 μm and 2.58 μm

refined by FSP for *Al 5083* alloy (García-Bernal et al., 2009). These researchers found that the maximum elongation of 810% could be achieved when the rotational and traverse speeds were selected as 400 rpm and 0.42 mm/s, respectively.

As a more advanced methodology, FSP is used to fabricate metal composites by introducing phases into the metal matrix. The enhancement of the bulk composites is achieved through grain refinement and grain boundary pinning (Lee et al., 2006). Azizieh et al. (2010) reported that Magnesium alloy *AZ31* composites with nano- Al_2O_3 particles were fabricated by FSP, better particle distribution was available with the increase of rotation speed of the FSP tool. Compared with the as-received materials, the hardness of the formed composites was increased by 200%. In their FSP experiments, the groove was cut in the work material and the nanoparticles were inserted into the groove for the preparation of FSP. Then, the FSP tool traversed through the groove, and the stir zone with nanopowder could be formed as shown in Figure 2.11.

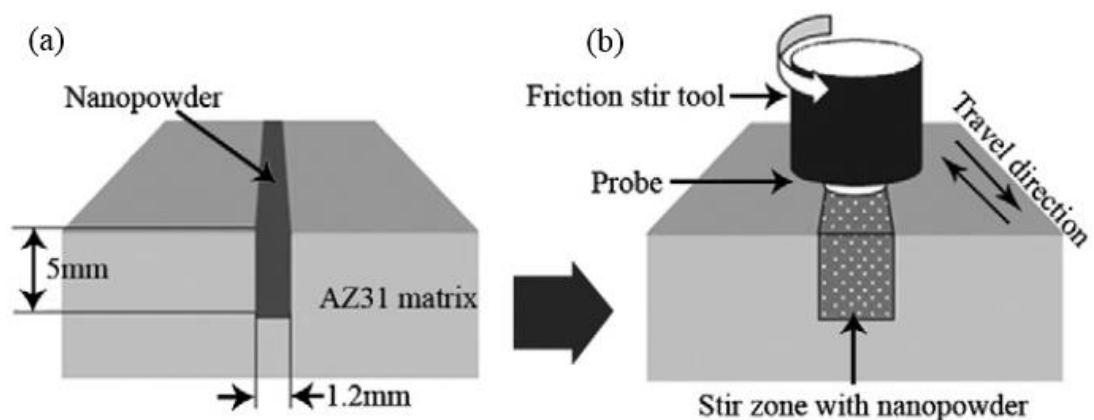


Figure 2.11: Schematic illustrations of friction stir process in fabricating the *AZ31*/nanoparticles composites: (a) cutting groove and inserting nanoparticles and (b) conducting multiple FSP to fabricate composites (Azizieh et al., 2010).

FSP was used to reinforce pure copper with *SiC* particles for improving its wear resistance (Barmouz et al., 2011). Also, higher hardness was found in the stir zones of the copper composites especially when the rotation speeds were chosen to be 40 and 80 mm/min as shown in Figure 2.12.

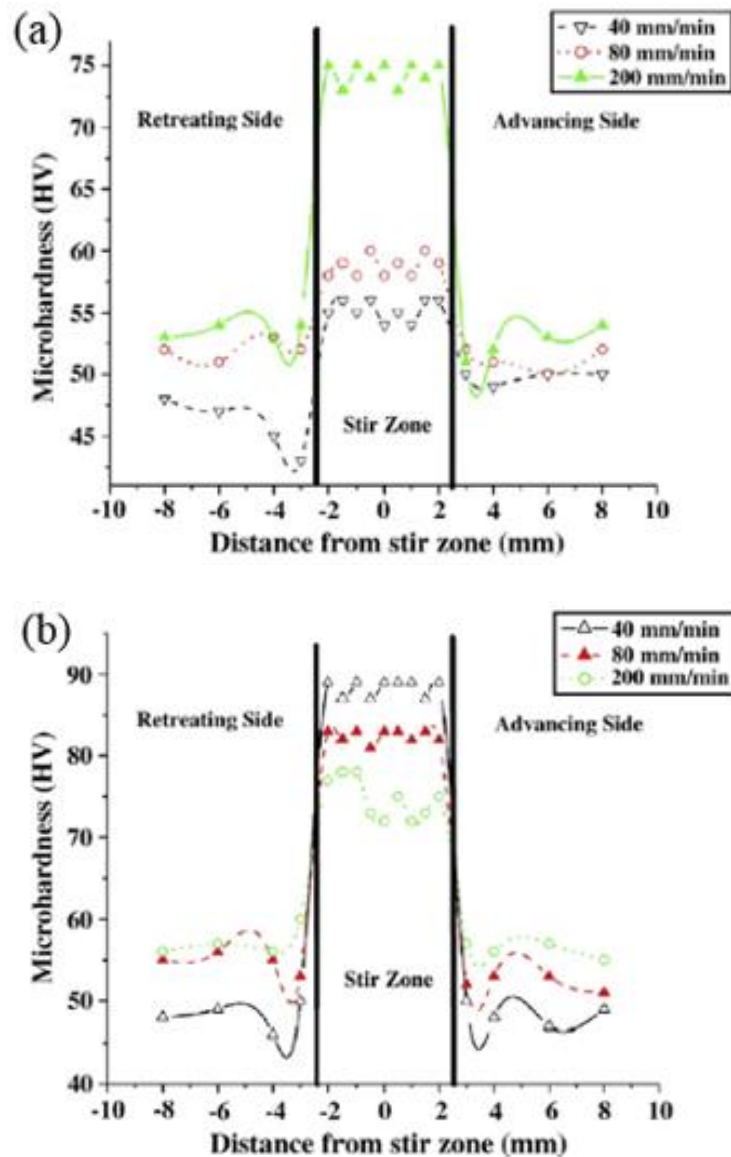


Figure 2.12: Microhardness values of FSPed specimens (a) without *SiC* particles and (b) with *SiC* particles in different traverse speeds (Barmouz et al., 2011).

The investigation of *Al 6061* composites with *SiC* nanoparticles was carried out by Salehi et al. (2014), they observed that the ultimate tensile strength, work fracture and

strain at maximum stress were enhanced by 44%, 492% and 244%, respectively, due to the homogeneous microstructure with nanoparticles produced by FSP. The detailed distributions of SiC particles are shown in Figure 2.13.

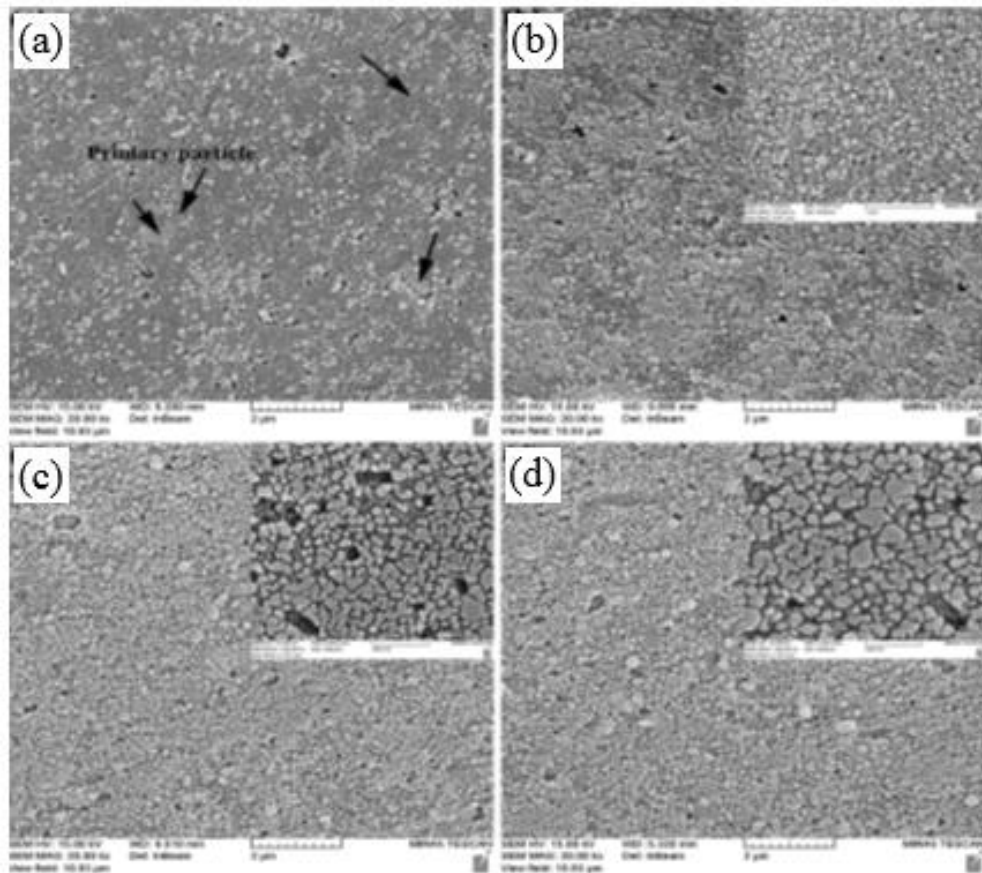


Figure 2.13: SEM micrographs showing particle distribution in (a) 4.2 wt pct SiC layer of functional graded (FG) material; (b) 10 wt pct layer of FG material; (c) 18 wt pct layer; and (d) Homogeneous nano-composite (the higher magnification images were added at upper right of each image) (Salehi et al., 2014).

Furthermore, the microstructure, hardness and tribological behavior of Al/Al_2O_3 nano-composites produced by FSP were studied by Shafiei-Zarghani et al. (2009). More homogeneous distribution of Al_2O_3 particles was observed when increasing the numbers of FSP passes as shown in Figure 2.14, and the nano-composite layer was formed by four-pass FSP.

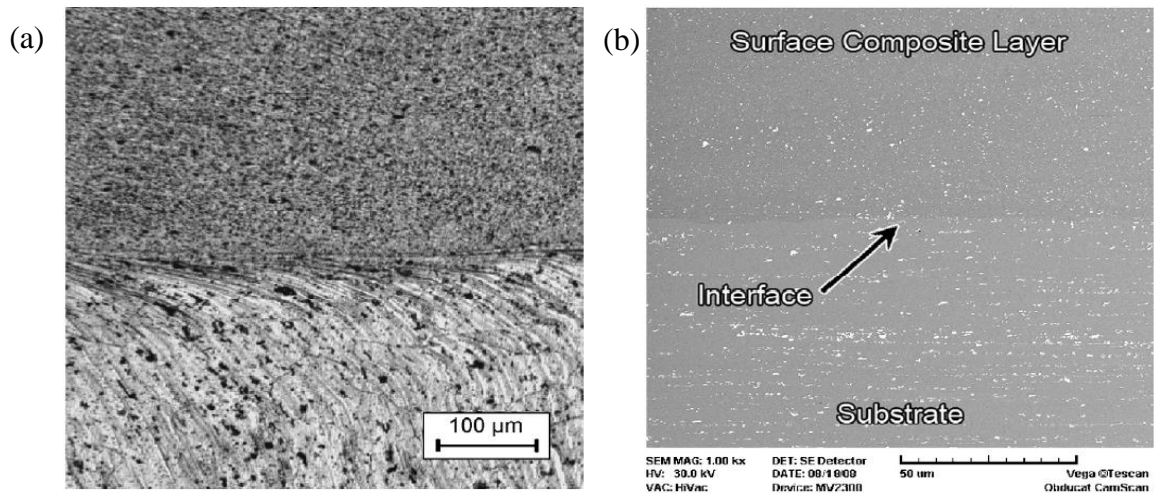


Figure 2.14: (a) Optical and (b) SEM micrographs showing perfect bonding between surface composite and aluminum alloy substrate (Shafiei-Zarghani et al., 2009).

As one of the effective reinforcing materials of metal matrix composite, carbon nanotubes are produced by different processing techniques to enhance the mechanical properties of the composite materials. However, a critical problem needs to be solved to expand the applications of carbon nanotubes due to its inhomogeneous distribution when it is introduced to metals by different production techniques (Zhong et al., 2003; Xu et al., 1999).

Izadi et al. (2012) investigated the fabrication of metal matrix composites with the base of *Al 5059*, in which multi-walled carbon nanotubes were uniformly distributed through two or three-pass FSP as shown in Figure 2.15, and such nano-structure reinforcements possessed high volume percentage. The hardness of the composite materials was enhanced by two times attributing to the reinforcing carbon nanotubes and grain refinement. Similarly, the mechanical strengths of *Al 2009* with carbon nanotubes induced by three-pass FSP were significantly improved because of the uniformly-distributed carbon nanotubes and refined grains (Liu et al., 2014).

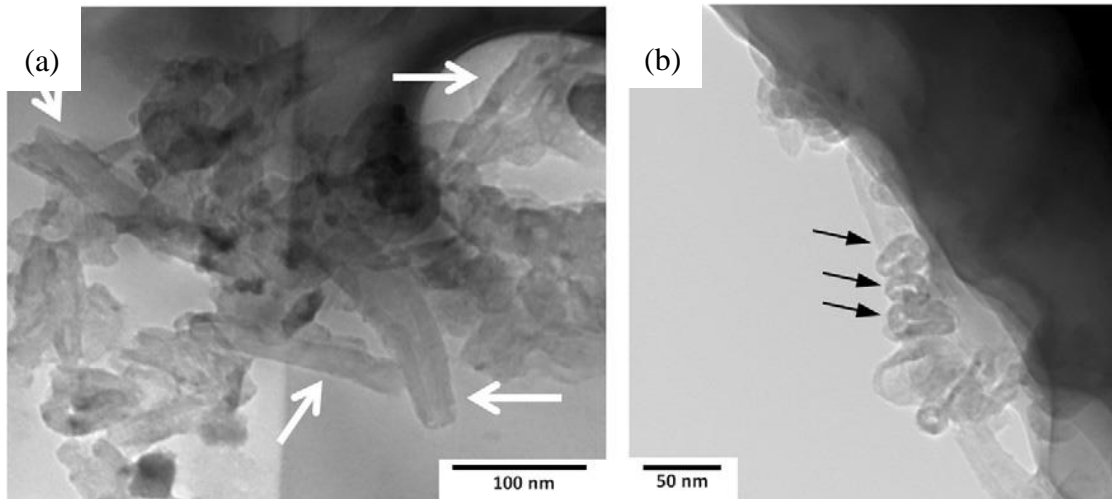


Figure 2.15: TEM micrographs of the composite material in the stir zone after 2 FSP passes, showing (a) carbon nanotubes introduced by two-pass FSP are indicated with arrows; and (b) circular carbon structures (Izadi et al., 2012).

Nevertheless, a single-pass FSP is not appropriate in the practical applications in which large areas of materials are required. Multi-pass FSP has to be carried out in order to address this problem. Since the variation exists between the stir zone and transition zone in terms of grain size and hardness, overlapping passes need to be used to solve this inhomogeneous issue. Ramesh et al. (2012) found that the material hardness of single-pass FSP was higher than the one of multi-pass FSP. However, the yield and tensile strength of the material processed by multi-pass FSP were comparable to the bulk material when a high transverse speed of 150 mm/min was used. The cross section of the processed material is shown in Figure 2.16.

The size, aspect ratio and distribution of *Si* particles were not influenced by overlapping multi-pass FSP, reported by Ma et al. (2006d) when they investigated the effects of FSP on A356 alloy. The tensile strength of the as-cast aluminum alloy processed by five-pass FSP was very comparable to the one of single-pass FSP. Hsu et al. (2005) also

demonstrated that multi-pass FSP could be a potential technique to produce refined materials with a large volume. Higher Young's modulus, good yield strength about 450 MPa, ultimate tensile strength approximately 650 MPa were also acquired for $Al-Al_2Cu$ composites fabricated by multi-pass FSP (Hsu et al., 2005).

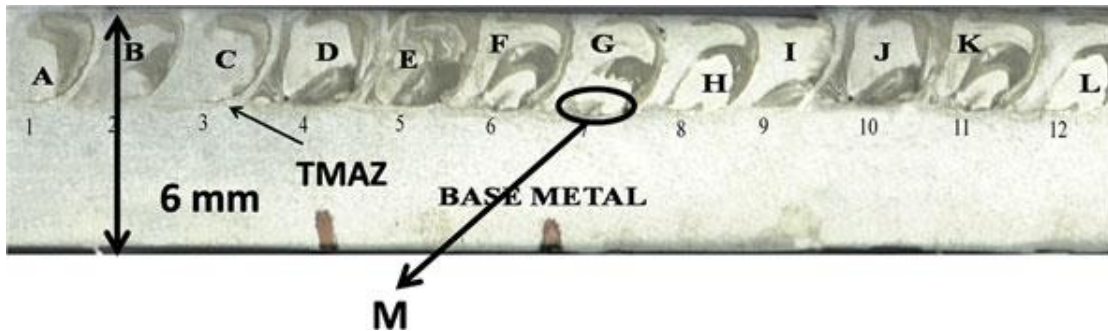


Figure 2.16: Typical macrograph of multi-pass friction stir processed sample showing nugget and transitional zones of twelve-pass labeled as A, B, C, D, E, F, G, H, I, J, K, and L (Ramesh et al., 2012).

On the other hand, cooling conditions used in FSP are also very important to homogenize the microstructure and control the grain size in a relatively small level after DRX occurs. Feng et al. (2013) investigated the effects of cooling method by which the work materials were submerged in the water during FSP of $Al\ 2219$. They found that as the rotational speed decreased, ultra-fine grains were formed in the stir zone when the material was submerged in the water as shown in Figure 2.17. However, the softening was observed in the stir zone under all conditions. In a similar case, the grain size of less than 100 nm was achieved in the materials processed by FSP due to the slower recrystallization kinetics resulted by the cooling condition of water submerging (Hofmann et al., 2005).

A mixture of water, methanol and dry ice was used by Su et al. (2005) as the coolant during FSP of *Al 7075*. Refined grains of 100 to 400 nm could be obtained by multi-pass FSP while the coolant was applied in the spots where the FSP tool just went through. The detailed experimental results are shown in Figure 2.18. They claimed that multi-pass FSP with a proper cooling method could be a potential technique to fabricate large-size UFG materials.

Considering all the reviewed literatures regarding FSP of aluminum alloys from different perspectives, multi-pass FSP will be the appropriate option to produce the materials with UFG structure in large size combined with the effective cooling methods in order to make sure the microstructure of the processed material is homogeneous in the meantime the hardness is not significantly influenced by the friction and stir actions inducing the thermal softening effect. In the following section, the literature review concerning FSP of *Al 7050-T7451* alloys will be presented and discussed to establish the state-of-the-art. The contributions from the reviewed papers will be summarized, and then the objectives and improvements in the corresponding research areas in the dissertation are presented.

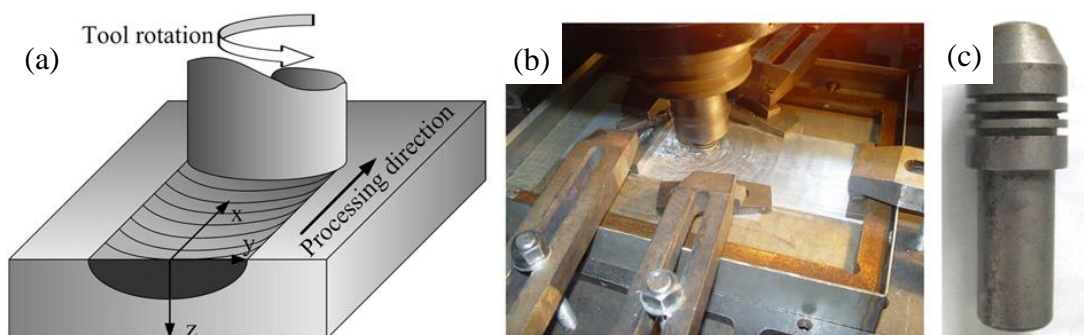


Figure 2.17: Submerged friction stir processing and the tool: (a) schematic drawing of FSP; (b) set up of submerged friction stir processing; and (c) the tool (Feng et al., 2013).

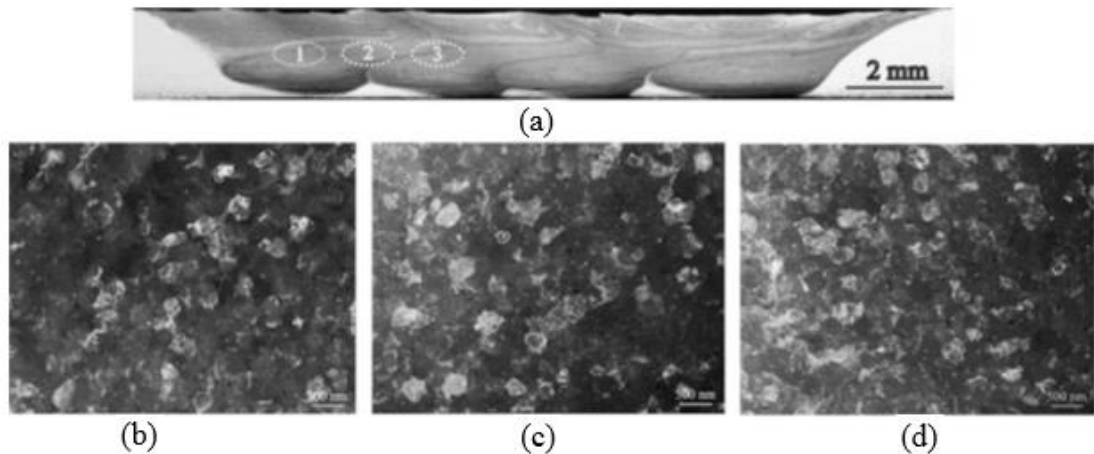


Figure 2.18: (a) Macro image of FSPed *Al 7075* alloy after four passes; (b) TEM micrographs showing grain structures in the middle layer of Pass 1; (c) overlap between Pass 1 and Pass 2; and (d) Pass 2 of the processing nugget as indicated by the regions 1-3 (Su et al., 2005).

2.3.2 Friction stir processing of *Al 7050-T7451* alloy

In this section, past research concerning FSP of *Al 7050-T7451* alloys has been summarized to know the major areas being focused by previous researchers. FSW, considered as a single-pass FSP, has been investigated broadly to process *Al 7050-T7451* alloys. The effects of FSW on the hardness of the processed materials with different tempers were studied. Yan et al. (2009) found that a higher and more uniform hardness distribution was achieved in the *Al 7050* alloy with *W* temper processed by FSW, compared with the hardness of the materials with the tempers of *T6* and *T7*. Hardness became higher when using a faster welding speed (Reynolds et al., 2005).

Upadhyay et al. (2010) studied the effects of various cooling methods on FSP of *Al 7050* alloy. Reduced processing temperature, decreased grain size in the stir zone and higher hardness were observed when the processed materials was submerged in water, while the transverse tensile strength was also enhanced in the under-water condition. It was very interesting that the authors used a special coolant that was a mixture of 50%

ethylene glycol, 50% water and 30 lb of dry ice keeping its temperature steady at approximately -25 degree in Celsius. However, it did not provide more benefits compared to FSW under-water. The detailed hardness and grain size comparisons among in-air, sub-ambient and under-water are presented in Figures 2.19 and 2.20.

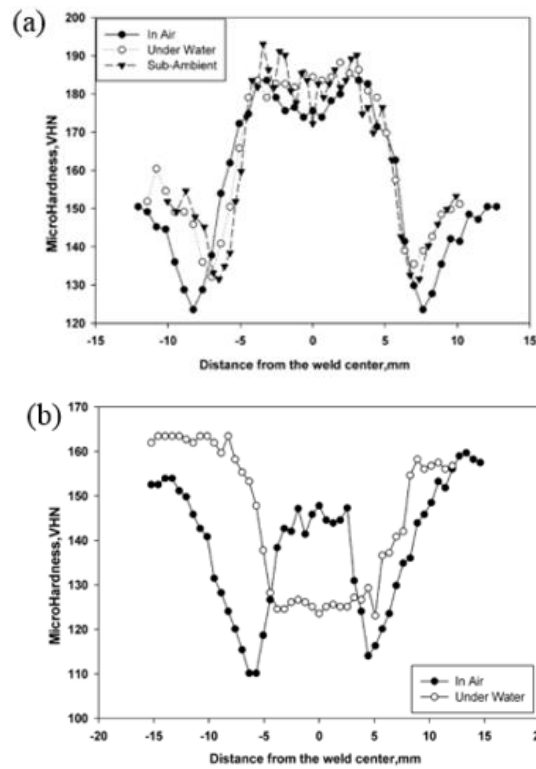


Figure 2.19: (a) Micro-hardness trends for in-air, under-water, sub-ambient welds made at 800 rpm, 6.8mm/s; and (b) Micro-hardness distribution for 200 rpm, 2.54 mm/s weld for in-air and under-water (Upadhyay et al., 2010).

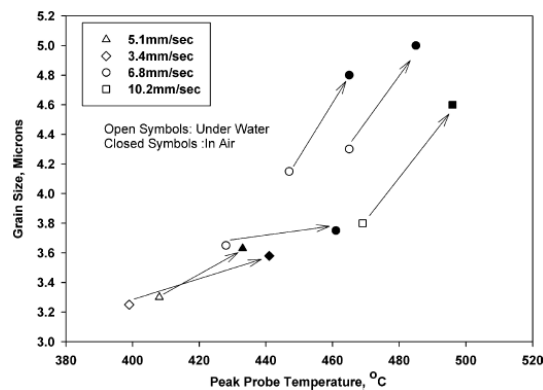


Figure 2.20: Average nugget grain size vs. peak probe temperature for different welding speeds. The arrows show equivalent welds done in air and under water (Upadhyay et al., 2010).

Moreover, the tensile strength of *Al 7050-T7651* alloy welded by FSW was continuously increased as the range of aging times changed, it was improved up to 24% (Fuller et al., 2010). Grain size is one of the most important factors investigated by the researchers. The grain size of about 1.5 μm was found in the stir zone formed by FSW of *Al 7050-T7451* alloys (Jata et al., 2000). Nonetheless, the non-uniform microstructure in the stir zone and thermal-mechanical affected zone (TMAZ) was also observed as shown in Figure 2.21. It is a very serious issue that needs to be resolved in multi-pass FSP, when it is used to process the work materials in a large scale.

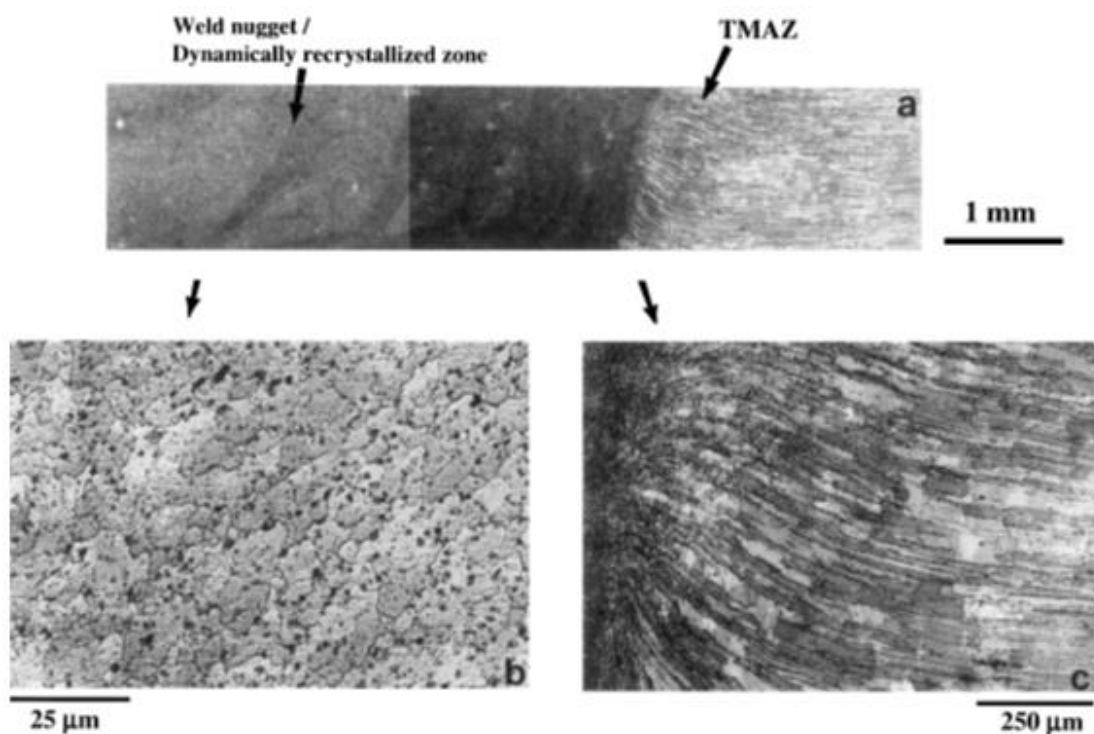


Figure 2.21: (a) Optical macrophotograph showing the weld nugget and the TMAZ in the FSW weld of *7050-T7451* alloy; Higher magnification optical micrographs: (b) fine grain size in the weld nugget; and (c) bent grains in the TMAZ (Jata et al., 2000).

Lower residual stresses measured in the stir zone, heat affected zone (HAZ) and TMAZ created by FSW were lower than the one measured in the welding zone formed by fusion welding (Prime et al., 2006; John et al., 2003). In the case of multi-pass welding, Brown et al. (2009) observed that the residual stresses became lower when more passes were used in FSW as shown in Figure 2.22.

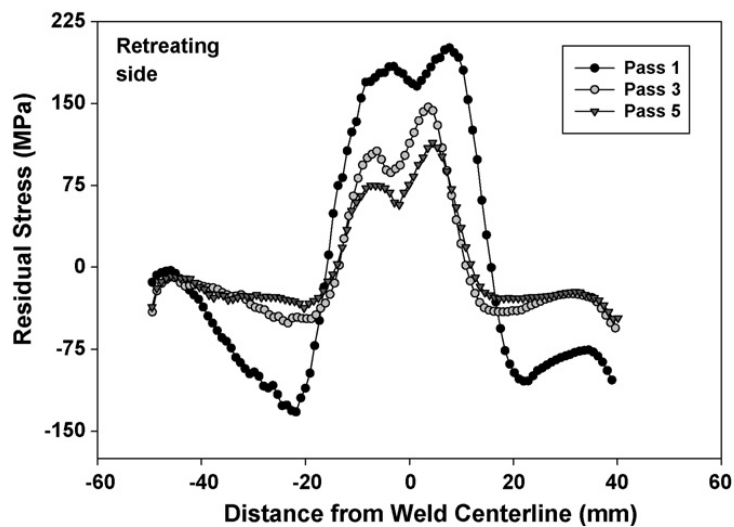


Figure 2.22: Through thickness longitudinal residual stress (Brown et al., 2010).

Modeling work was also conducted by Kamp et al. (2009) to predict the yield stress and hardness of *Al 7050-T7* alloy processed by FSW, by using the process model combining thermal, microstructural and yield strength models. A difference between 5 and 20% was found among the measured data and predicted values. Additionally, three different aluminum alloys was used to test the FSW model developed by Long et al. (2007). They found that the material flow stress was not very consistent regardless of the sticking contact or fully solid state processing at some rotational speeds.

In the case of FSP of *Al 7050-T7451* alloy, Rhodes et al. (2003) studied the evolution of fine-grained structure after FSP. They used a mixture of dry ice and isopropyl alcohol as the coolant to flood onto the upper surface of the processed plate before and during the plunge for the purpose of freezing the materials to maintain the initial microstructure. The initial grains with the size of 25 to 100 nm grew larger to the level of 2 to 5 μm after heating, and during the time from 1 to 4 minutes at the approximate temperatures from 350°C to 450°C, heat was generated by FSP when using different rotational speeds. The details of the initial grains and the grain growth at different temperatures are shown in Figures 2.23 and 2.24, respectively.

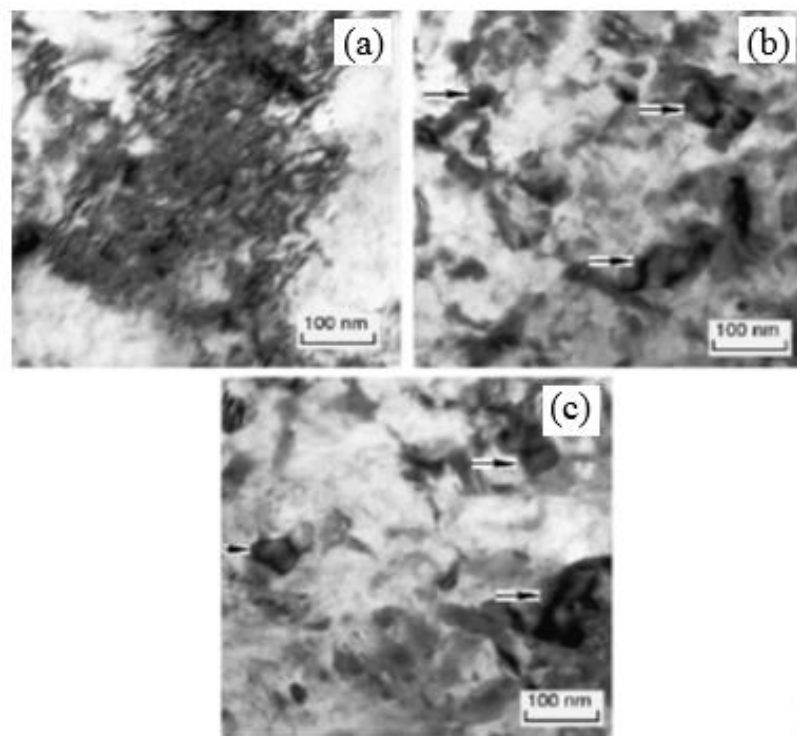


Figure 2.23: TEM micrographs of FSP plunge and extract tested *Al 7050* alloy by isopropyl alcohol/dry ice cooling: (a) 200 rpm tool rotational speed; (b) 300 rpm rotation speed; and (c) 500 rpm rotational speed. Arrows indicate recrystallized grains in contrast (Rhodes et al., 2003).

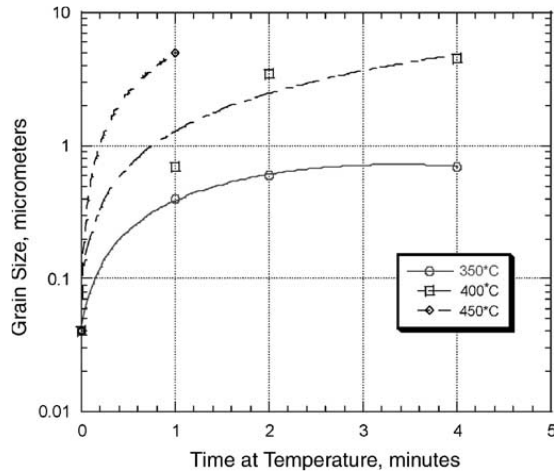


Figure 2.24: Grain growth behavior in FSPed *Al 7050* at 350, 400, and 450°C (Rhodes et al., 2003).

Miles et al. (2006) investigated the bending limit of *Al 7050* and *Al 6061* alloys, and they demonstrated that the bending limit was significantly improved by FSP used to modify the surface. A finite element method (FEM)-based model was also developed to predict the bending limit by adopting the criteria of Latham and Cockcroft and Von Mises.

The literature review about FSW/FSP of *Al 7050-T7451* alloys is very helpful to understand the state-of-the-art knowledge and find the potential gap for further improvement. More homogeneous structure and mechanical properties of the processed materials are needed in terms of grain size, hardness, microstructures, tensile/yield stress, etc. In addition, further machining or other processing technologies would be needed to shape or form the materials processed by FSP in order to produce the manufactured components with the desired dimensions and obtain the superior surface integrity with excellent hardness, more compressive residual stress, better corrosion/wear resistance.

2.4 Machining of *Al 7050-T7451* alloy

For *Al 7050-T7451* alloys, turning and milling processes are reviewed to summarize the research conducted by the academic and industry communities. This analysis can offer guidance for the dissertation study regarding machining of *Al 7050-T7451* alloys. Though the literature review was focused on the as-received materials with coarse grains, it is also helpful to initiate new studies of machining of *Al 7050-T7451* alloys with UFG structure processed by FSP.

Li et al. (2012) measured the residual stresses on the milled surface of *Al 7050-T7451* alloy, they found that compressive residual stress was generated at various cutting speeds and feed rates. Also, Tang et al. (2009) studied the dominant factor determining the layer thickness of residual stresses induced by milling of *Al 7050-T7451* alloy, and they reported that the mechanical load of high-speed milling using the worn tool played an important role. Moreover, the compressive residual stresses depth from 35 μm to 40 μm was acquired in the sub-surface of milled *Al 7050-T7451* alloys (Guo et al., 2006). Within this milling-induced layer, the microhardness was enhanced by 30% compared to the bulk material while this strain hardening layer also exhibited etching resistance and possessed less voids and secondary phase particles as shown in Figure 2.25.

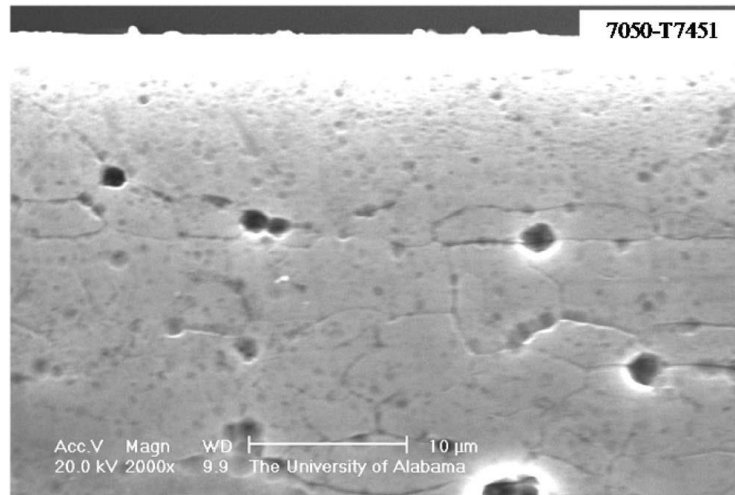


Figure 2.25: Cross-sectional SEM of *Al 7050-T7451* alloy (1627 m/min, 0.2 mm/tooth, 1 mm) (Guo et al., 2006).

Machining of *Al 7050-T7451* alloys was evaluated in terms of cutting forces, chip morphology, cutting temperature, surface roughness and etc. In micro-cutting of this aerospace-based aluminum alloy, Zhou et al. (2010a) investigated the effects of cutting speed and undeformed chip thickness on the cutting force ratio, chip morphology, effective shear and rake angle. They observed that continuous chips were always formed in the range from 1 to 200 μm when selecting undeformed chip thickness. The shear angle increased while the cutting ratio (cutting force/thrust force) decreased along with the increase of undeformed chip thickness. Radial force increased as the depth/width of milling or feed rate increased, while it decreased slightly when increasing the milling speed, however, the feed and tangential forces were found to be less affected by these milling parameters (Tang et al., 2012).

Bork et al. (2015) used three cutting fluids including jatropha, canola vegetable oils and a semisynthetic oil in milling of *Al 7050-T7451* alloys with the method of minimum quantity lubrication (MQL). Cutting force, surface roughness, flank wear and tool-life

were measured and studied, in which jatropha cutting fluid showed better results in terms of cutting length compared with the canola and semisynthetic oils. Less cutting force was measured in the case of MQL compared to flood cooling as less heat was taken away by MQL milling and the materials were easy to remove. The details of tool-life comparison when using the three cutting fluids and the distributions of chip morphologies are shown in Figures 2.26 and 2.27, respectively.

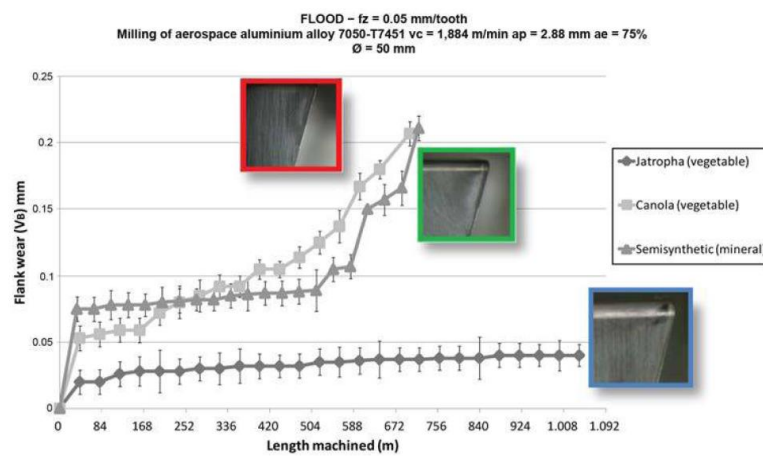


Figure 2.26: Tool-life under MQL technique (Bork et al., 2015).

Aluminum alloy 7050-T7451 / $v_c = 1,884$ mm/min / $a_p = 2.88$ mm / $a_e = 75\%$ / $\varnothing = 50$ mm						
Technique	f_z (mm/tooth)	Jatropha (vegetable)	Canola (vegetable)	Semisynthetic (mineral)		
Flood	0.05					
	0.15					
	0.30					
	0.05					
MQL	0.05					
	0.15					
	0.30					
	0.05					

Figure 2.27: Chip morphology according to the process parameters (Bork et al., 2015).

Mamedov et al. (2013) predicted the force and deflection by using their analytical model considering the ploughing force component and elastic recovery. The model was validated by micro end milling of *Al 7050* alloy with the help of laser displacement sensors and micro dynamometer.

Predictive models for machining of *Al 7050-T7451* alloys were developed by researchers in order to predict the cutting force, cutting temperature, effective strain, stress, etc. Zhou et al. (2010b) used a FEM model to simulate the cutting temperature and plastic strain distribution by employing the flow stress as the function of strain, strain-rate and temperature. A material constitutive model with Johnson-Cook equation was established by using the quick-stop equipment and, measurements of cutting force and temperature (Fu et al., 2010a). The predictions of effective strain, strain-rate and temperature under various cutting speeds were made, and good accuracy was obtained in this FEM-based model.

Fu et al. (2010b) also developed a model to predict surface roughness by means of multi-factor orthogonal machining. Surface roughness was increased as the feed rate or width of cut increased, and decreased as the cutting speed increased. A finite element analysis (FEA) was established by Sandstrom and Hodowany (1998) to predict the cutting temperature and effective plastic strain, and this work demonstrated great contribution to understand the machining process and improve the predictive capability. Furthermore, in the case of micro-cutting of *Al 7050-T6* alloy, Lu et al. (2007) mentioned that the maximum temperature located on the shear plane and the maximum Mises stress location was in the area ahead of tool-chip contact region. The cutting

energy increased as the uncut chip thickness decreases due to the ploughing effect associated with the size effect affected by the tool edge radius (Zhou et al., 2008), as predicted in the FEM model. In the predicted results, the plastic shear zone was found thinner when using the sharp tool, while it became wider and extended toward the rake and clearance sides of the tool.

In another study concerning machining of *Al 7050-T7451* alloy (Su and Liu, 2014), specific shear energy decreased as the cutting speed was raised due to the reduction of flow stress resulted by the thermal softening effect. It also declined as the uncut chip thickness increases. Sánchez et al. (2005) studied the tool-wear mechanisms of dry machining of *Al 7050-T7451* alloy. They found that build-up edge was formed by mechanical adhesion and then extended over the rake face of the tool after plastic deformation induced by machining as shown in Figure 2.28.

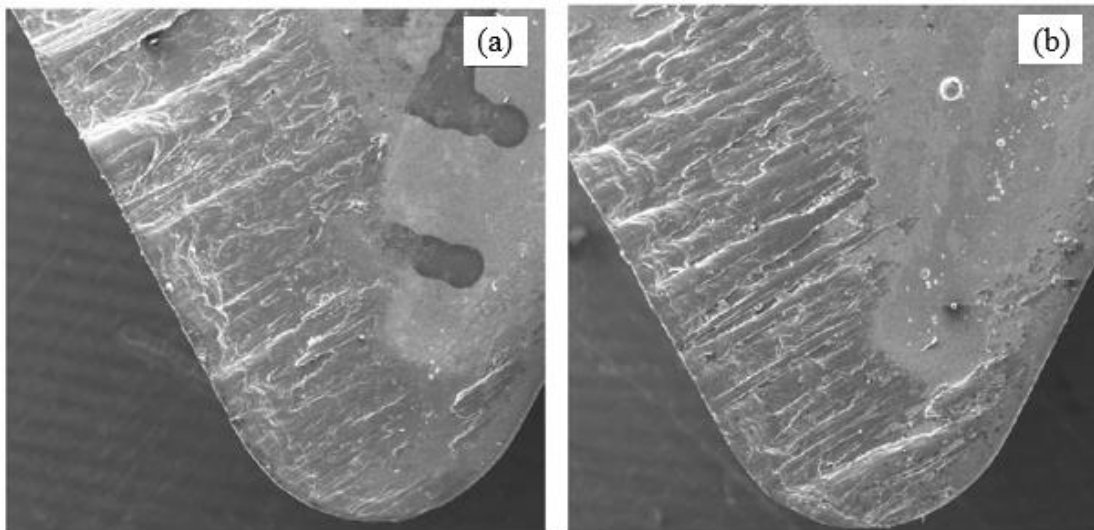


Figure 2.28: SEM images acquired on different *TiN* covered inserts after dry turning 175mm of *Al 7050* alloy bars at (a) $V = 43$ m/min; and (b) $V = 64$ m/min (Sánchez et al., 2005).

In conclusion, past researchers have been focusing on the machining performance of *Al 7050-T7451* alloys, in terms of cutting force, temperature, surface roughness, tool-wear, chip morphology, etc. However, from the work material point of view, surface integrity aspects including microstructure, microhardness, wear/corrosion resistance, fatigue life etc., are rarely investigated in the academic community. Therefore, the effects of machining on the surface integrity will be studied in the research presented in this dissertation.

2.5 Burnishing of Aluminum alloys

As one of the chipless post-machining processes, burnishing has been used to perform on the manufactured components in order to reduce surface roughness, increase surface/subsurface hardness and improve other surface integrity aspects by means of eliminating tool marks/scratches, pits or porosity existed on the surface of the work materials. In the burnishing process, the surface of the work material is compressed by a specifically designed tool made of hardened roller or ball with good polished and smooth surface as illustrated in Figure 2.29.

The generation of refined layers with ultra-fine grains or nano-grains can be observed in the burnished surfaces induced by burnishing processes, attributing to severe plastic deformation and the associated dynamic recrystallization. Compressive residual stresses distributed within these harder refined layers also provide the benefits to increase the fatigue life and improve the wear/corrosion resistance of the components.

Burnishing will be used as the post-machining process to induce SPD on the surface and subsurface of the machined *Al 7050-T7451* alloy with near-UFG structure in order to enhance the surface integrity. Literature review about burnishing of aluminum alloys is indispensable to have the basic understanding of the burnishing effects on the work materials and to provide guidance to determine the experimental setup for burnishing including the burnishing speed, depth of penetration, cooling condition etc. However, there is lack of direct literature regarding burnishing of *Al 7050-T7451* alloys, as the literature shows that the past work was largely focused on the burnishing of other aluminum alloys, while it also gives the guidance to understand the burnishing process to some extent.

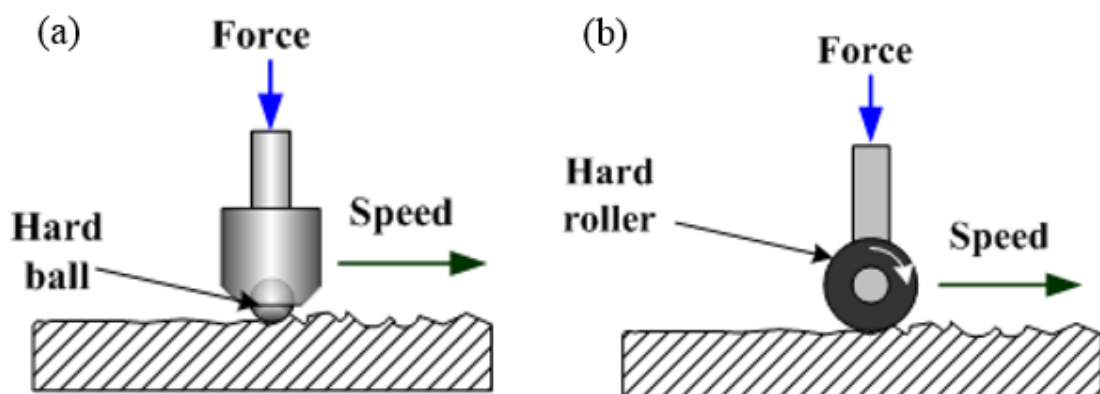


Figure 2.29: The schematics of burnishing process: (a) ball burnishing; and (b) roller burnishing (Substech, 2013).

Surface roughness and hardness are two parameters which have been extensively researched most by the academic community. Hassan (1997) reported that the surface hardness increased with the increase of burnishing forces and the number of passes performed by the burnishing tool while the surface roughness reached the optimum value when certain burning force was used on the commercial aluminum bars. The same

trend was also found by Némat and Lyons (2000) when they investigated the effects of burnishing of *Al 6463* alloy. In their research, the surface roughness was improved by up to 70%, and the employment of lower burnishing feed and speed was found to be beneficial to increase the surface hardness of the work material. Luo et al. (2006) demonstrated that the surface microhardness of aluminum alloy *LY12* was influenced by the burnishing speed, feed and depth, and among which, burnishing feed was the most affected factor. And, the burnishing force was influenced the most by the burnishing depth.

The microhardness of the burnished *Al 2014* alloy was also investigated by El-Axir et al. (2008), the depth of penetration in the range from 0.025 mm to 0.045 mm was chosen in order to obtain the best surface microhardness. In addition, compressive residual stresses induced by the burnishing process were also investigated. The maximum value of residual stresses introduced in the burnished surface of *Al 6061* alloy was decreased with the increase of burnishing speed (El-Khabeery et al., 2011). The increase of the depth of penetration and/or number of burnishing passes was attributed to the increase of the maximum compressive residual stress. Prevéy and Cammett (2004) showed that low plasticity burnishing (LPB) induced the burnishing-influenced layer with compressive residual stresses on the burnished surface of *Al 7075-T6* alloy, and that the introduction of compressive residual stress contributed to the improvement of fatigue life and strength. They observed that the endurance limit under the corrosion environment in 3.5% *NaCl* solution was increased to 310 MPa. It was worth noting that the work material possessed a lower endurance limit of 100 MPa under the same

corrosion condition compared with the original strength of 205 MPa. The details of the residual stress and fatigue strength are shown in Figures 2.30 and 2.31, respectively.

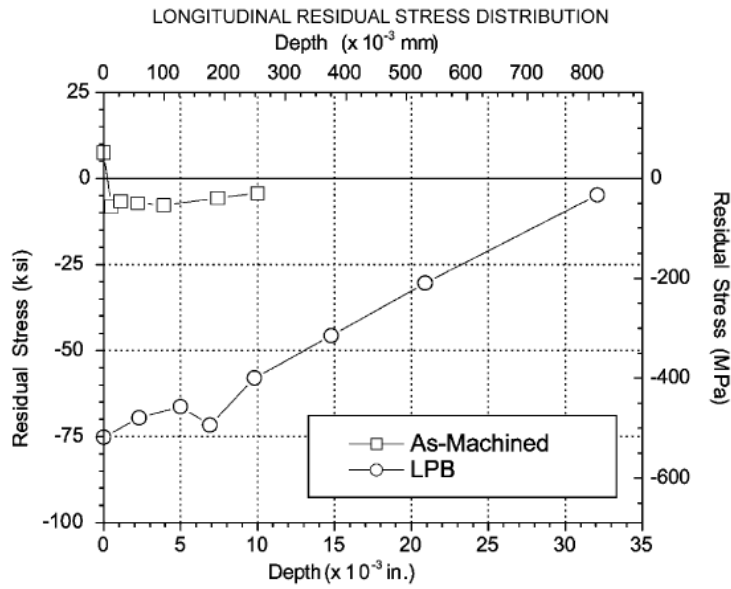


Figure 2.30: Residual stress distributions produced by end milling and LPB in *Al 7075-T6* alloy (Prevéy and Cammett, 2004).

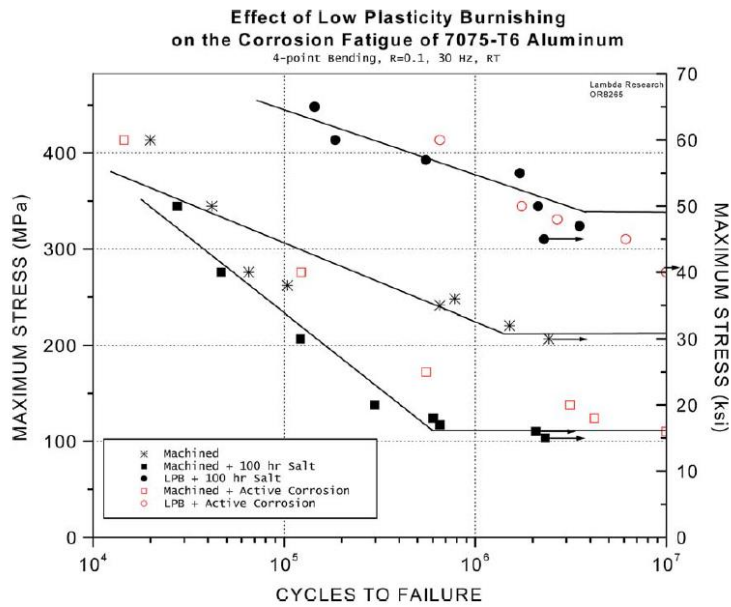


Figure 2.31: High cycle fatigue results for salt fog pitted and active corrosion fatigue of machined *Al 7075-T6* alloy with and without LPB processing prior to exposure to corrosion (Prevéy and Cammett, 2004).

The literature reviews of FSP, machining and burnishing of aluminum alloys are summarized in the previous sections. In the next two sections, the effects of cryogenic cooling will be discussed for the machining and burnishing processes, especially from the surface integrity point of view. Refined layers with UFG or nano grains are usually formed in the machined/burnished surface of the work materials as the grain growth is suppressed after DRX occurs due to rapid cooling effect of liquid nitrogen, these refined layers possess higher hardness and compressive residual stress induced by severe plastic deformation, thus improving the wear/corrosion resistance and fatigue life of the manufactured components.

2.6 Cryogenic processing

2.6.1 Cryogenic machining

Cryogenic machining, using liquid nitrogen as the coolant, has been investigated by the academic and industry communities for over the last two decades. According to Hong et al. (2001), by applying liquid nitrogen from the rake face of inserts, chip breakability can be improved due to the enhanced brittleness of the chips at a lower temperature resulting from the rapid cooling effect. A fluid cushion is formed between the chip-insert contact area, and it helps to reduce the material stickiness thus mitigating or eliminating the introduction of built-up edge. Moreover, the hardness of the tool insert material is also improved in the environment of lower temperature. Combining all the effects, the tool-life/tool-wear of inserts used in cryogenic machining can be enhanced. A schematic is shown in Figure 2.32 demonstrates the cryogenic applications in

general. Also, delivering liquid nitrogen from the clearance side of the insert will benefit the surface integrity of the manufactured components, and this will be discussed later.

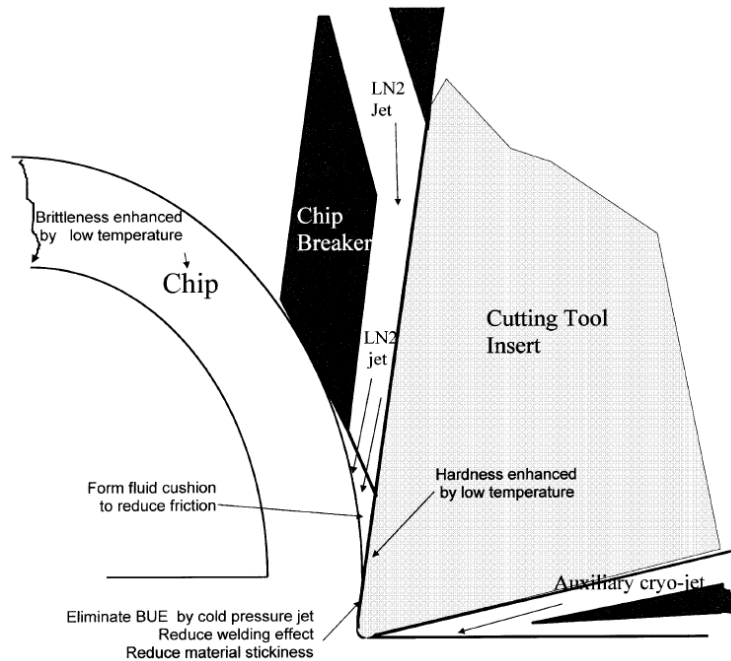


Figure 2.32: A schematic of the economical cryogenic machining approach (Hong et al., 2001).

The study conducted by Hong et al. (2001a) was to investigate the effects of cryogenic machining by a combination of two nozzles delivering liquid nitrogen. They found that optimizing the position of the nozzles could enhance the performance of the chip breaker. And, the tool-life was also increased up to 5 times compared with the ones used in dry machining.

Another systematic study was carried out by Hong et al. (2001b) to investigate the influence of cryogenic machining on the cutting temperature of *Ti-6Al-4V* alloy. The temperatures under various cooling methods were measured by thermo-couples, imbedded in the carbide tool insert and compared with the predicted results obtained

from a FEM-based predictive model. According to the experimental results and theoretical predictions, they concluded that the cutting temperature was in the increasing trend following this order: simultaneous cryogenic cooling on the rake and flank sides, cryogenic cooling on the rake side, cryogenic cooling on the flank side, pre-cooling the work material, flood-cooling and dry condition. Details of the temperature distributions under different cooling conditions are shown in Figure 2.33. From this study, the lowest temperature could be achieved when liquid nitrogen was delivered from the rake and flank sides simultaneously.

In another report (Dhar et al., 2002), the cutting temperatures of machining *AISI 1040* and *AISI 4320* steels were found to be lowered by cryogenic cooling, the cutting forces were also reduced due to the lower temperatures and it also helped to maintain the sharpness of the cutting edges of the tool inserts.

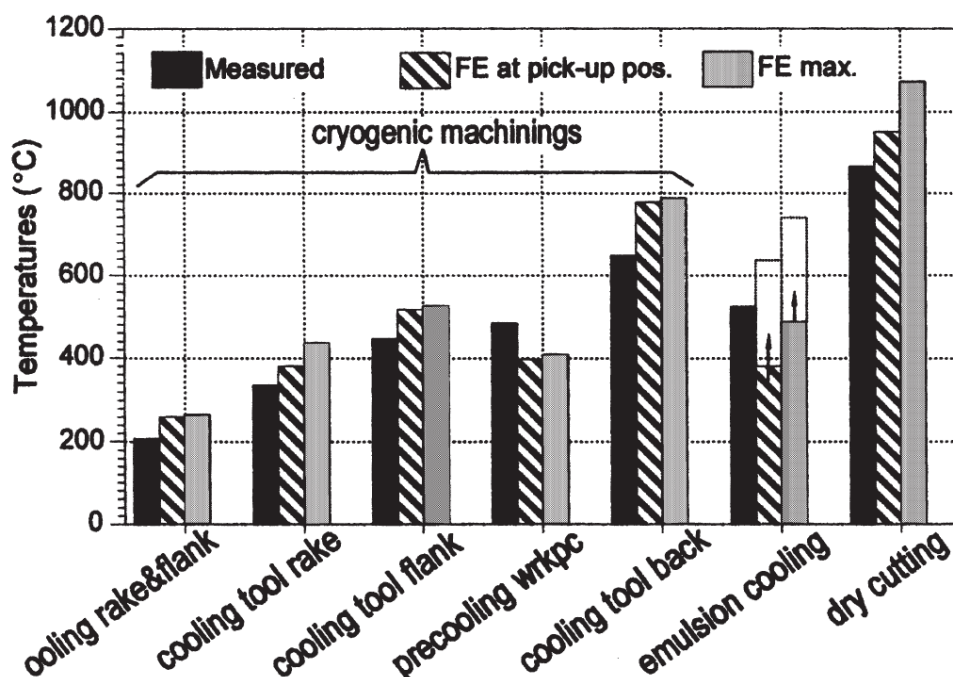


Figure 2.33: Measured and predicted tool temperature (Hong et al., 2001b).

The capability of reducing the tool-wear is one of the most remarkable contributors in the utilization of liquid nitrogen delivery during machining processes. Kaynak et al. (2013) demonstrated the improvement of tool-wear performance in cryogenic machining of *NiTi* shape memory whose machinability is generally very poor limiting its application in the aerospace industry. As shown in Figure 2.34, in contrast to dry and MQL machining, both the flank and notch wear were improved by controlling the progressive tool-wear and tool-wear rate in the case of cryogenic machining. For the aerospace-based material Inconel 718, cryogenic machining also provided the enhanced machining performance in terms of tool-wear, temperature, surface integrity (Kaynak, 2014). These findings also proved that the number of nozzles used to deliver liquid nitrogen played a significant role to control the cutting forces and power consumption.

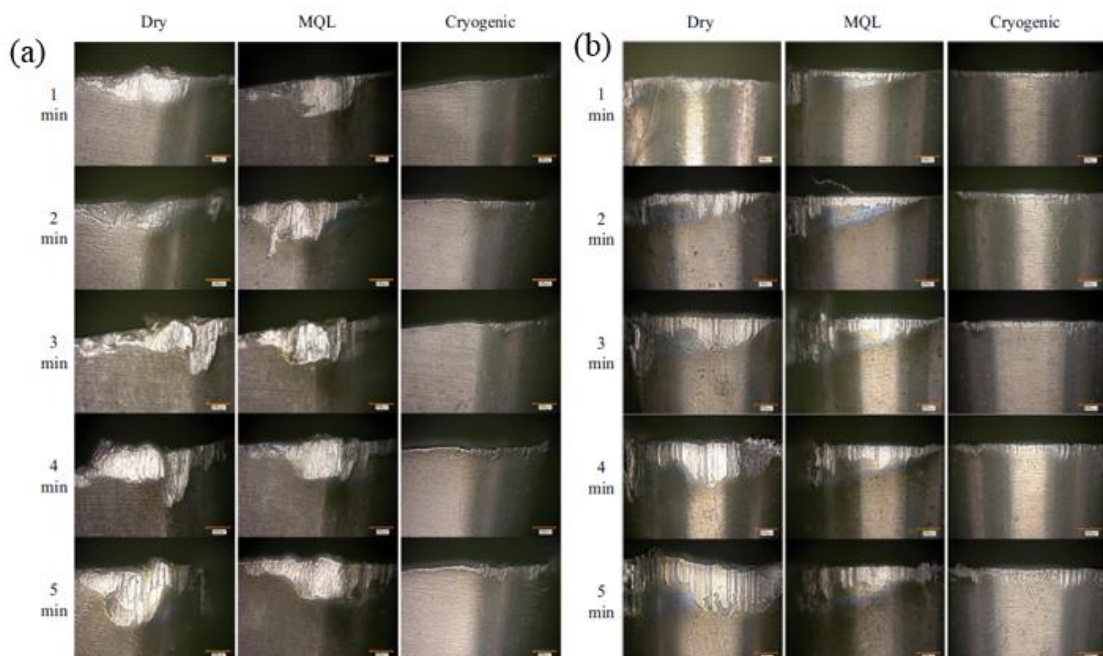


Figure 2.34: (a) Images of notch wear progression at the main cutting edge of the cutting tools; (b) Images of flank wear progression at the nose region of the cutting tool (Kaynak et al., 2013).

Furthermore, the contribution of cryogenic machining on the enhancement of residual stress distributed on the machined surface of the manufactured components was also studied by the researchers. Pu et al. (2012) conducted the cryogenic machining experiments on *AZ31B* alloy using liquid nitrogen as the coolant. The surface integrity of the work material was significantly improved in terms of the surface finish, remarkable grain refinement from 12 μm to 31 nm, with nano grains, and up to 10 times more compressive residual stress with the utilization of the larger cutting edge radius (70 μm). The detailed distributions of residual stresses measured from the samples with two different cutting edge radii under dry and cryogenic conditions, are shown in Figure 2.35.

As seen from the residual stresses from the circumstantial and axial directions, both dry and cryogenic machining induced more compressive residual stresses compared with the one measured from the as-received material. And, more compressive residual stresses were introduced by cryogenic machining using the large cutting edge radius in contrast to dry machining. Conversely, dry machining was found to provide better performance on the residual stress profiles, however, a thicker white layer detrimental for the components was formed on the machined surface in dry machining of *52100* steels (Umbrello et al., 2012). However, the thickness of the white layer could be limited and the surface roughness was also improved by cryogenic machining.

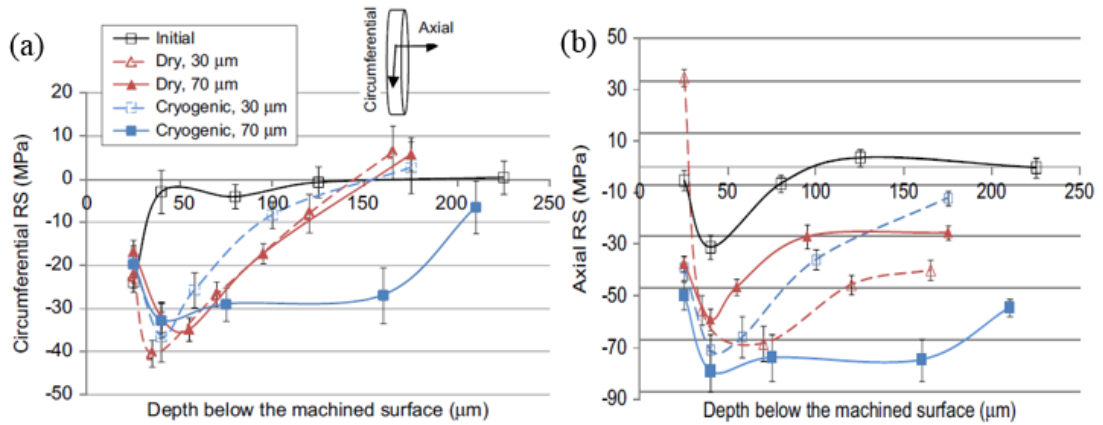


Figure 2.35: Residual stresses after machining using cutting tools with different edge radii and cooling conditions in circumferential and axial directions (Pu et al., 2012).

The recent review article by Kaynak et al. (2014) provides more details of the advantages induced by cryogenic machining on the surface integrity characteristics, such as surface roughness, grain refinement, machining-induced layer, microhardness, phase transformation, residual stresses, fatigue life, etc., and compared with the effects resulting from MQL and flood-cooled machining. Pusavec et al. (2011) also investigated the effects of cryogenic machining on the surface integrity of machined Inconel 718. The compressive residual stress zone was extended from 40 μm to 70 μm and the surface hardness was increased to 800 HV from the original hardness of 500 HV. And, the depth of SPD layer was 1-2 μm achieved by cryogenic machining while the depth of SPD layer was much thicker at 5-10 μm obtained in the cases of dry and MQL machining.

The influence of cryogenic machining on the surface integrity characteristics and machining performance was reviewed and analyzed based on the studies conducted by previous researchers. In the next section, the effects of cryogenic burnishing using

liquid nitrogen as the coolant will be discussed as burnishing is more frequently used as the final process to enhance the mechanical properties of the components.

2.6.2 Cryogenic burnishing

There are very few publications regarding cryogenic burnishing, and the limited findings by the researchers are reviewed and considered as the references for the study presented in this dissertation. Caudill et al. (2014) investigated the effects of cryogenic burnishing on *Ti-6Al-4V* alloy and found that more increased hardness was achieved on the surface and subsurface of the burnished sample, in comparison with the hardness measured from the samples burnished by dry and flood-cooled burnishing due to less thermal softening effect resulting from cryogenic cooling.

The research conducted by Yang et al. (2013) was to study the influence of cryogenic burnishing of *Co-Cr-Mo* alloy used in biomedical applications. They showed that the employment of liquid nitrogen during burnishing was helpful to suppress the grain growth after DRX has occurred, thus attributing to its rapid cooling effect. The depth of SPD layer was also found to be increased from 30 μm to 43 μm in dry burnishing when the depth of penetration was raised from 0.127 mm to 0.254 mm, while under the same condition, the depth of SPD layer could be improved to 138 μm from 42 μm , observed from cryogenic burnishing. The microstructures of the SPD layers formed by dry and cryogenic burnishing are shown in Figure 2.36. The grain size of 300-600 nm was found in the topmost surface of the SPD layers induced by cryogenic burnishing when the depth of penetration was 0.254 mm, whereas the grain size was approximately 1 μm in the dry case. In addition, up to 87% hardness increase was acquired in

cryogenic burnishing, in contrast to the hardness of the bulk hardness as shown in Figure 2.37.

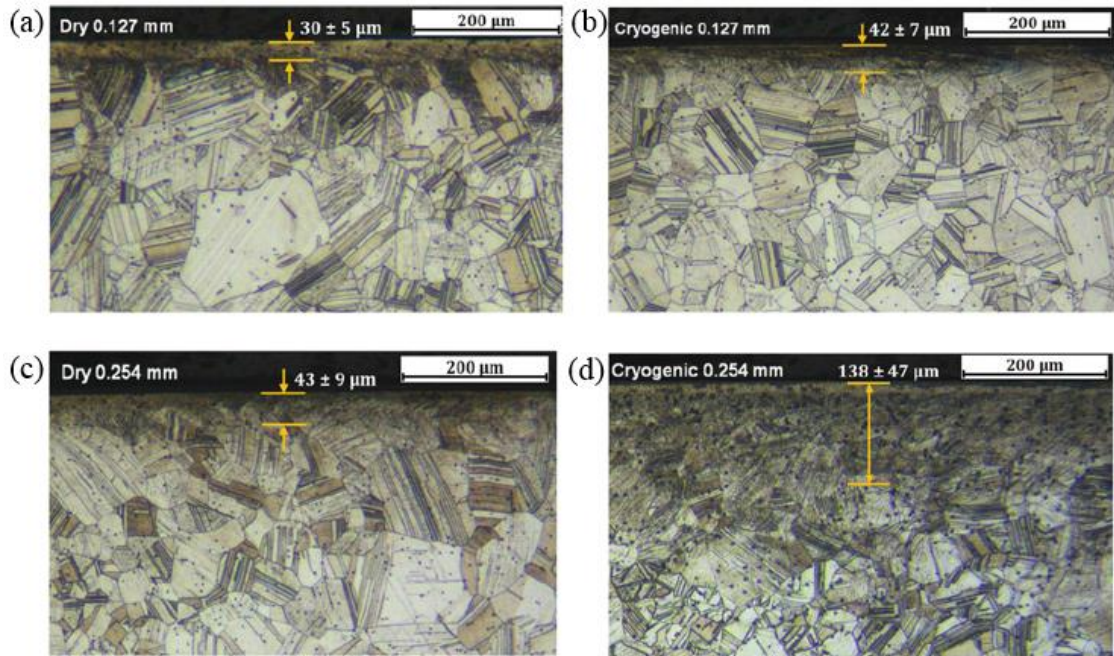


Figure 2.36: Microstructure of the surface after burnishing under different conditions: (a) dry burnishing, depth of penetration (DoP) = 0.127 mm; (b) cryogenic burnishing, DoP = 0.127 mm; (c) dry burnishing, DoP = 0.254 mm; and (d) cryogenic burnishing, DoP = 0.254 mm (Yang et al., 2013).

Moreover, a significant increase of the relative intensity of hexagonal close packing (hcp) peak was obtained in the cryogenic burnished surface, benefiting to improve the wear resistance of this biomedical material (Yang et al., 2015) as shown in Figure 2.38. From the topographic profiles of the tool-wear zone, cryogenic burnished samples exhibited better wear resistance especially when the depth of penetration was large.

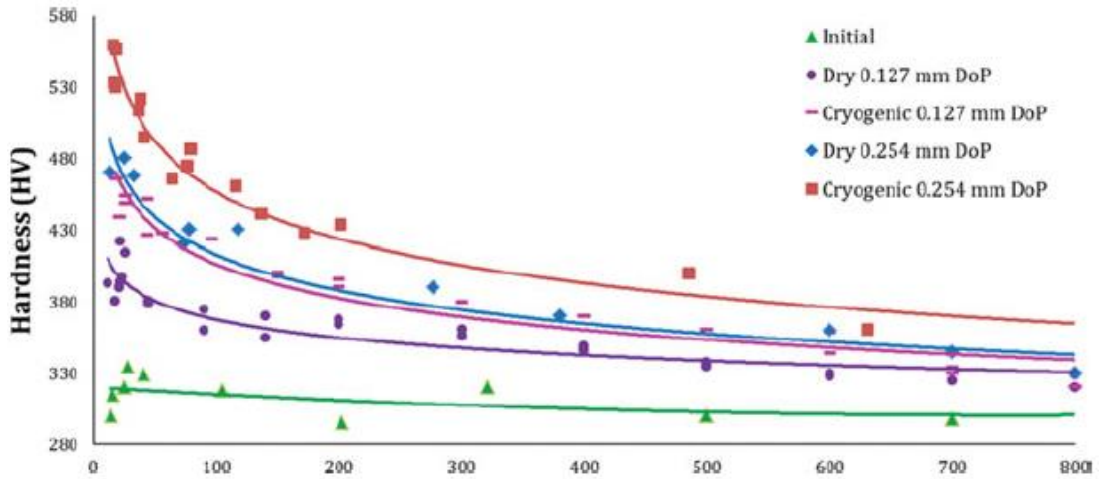


Figure 2.37: Hardness variation with depth below the burnished surface (Yang et al., 2013).

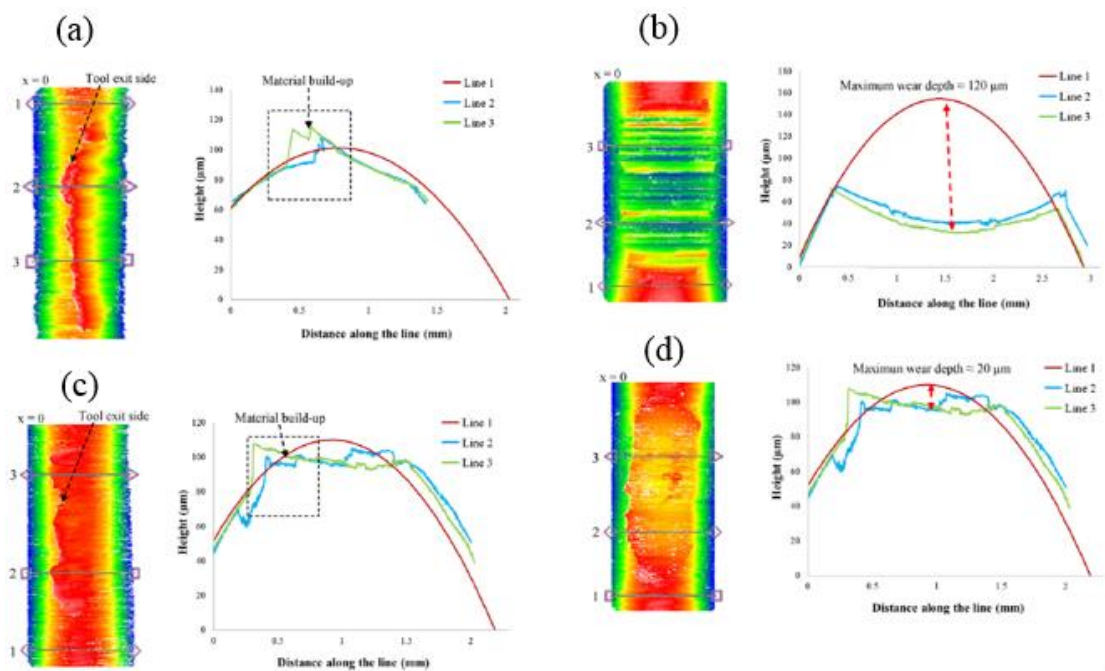


Figure 2.38: 3-D topographic profiles of the tool-wear zone: (a) dry, 0.15 mm DoP; (b) cryogenic, 0.15 mm DoP; (c) dry, 0.21 mm DoP and (d) cryogenic, 0.21 mm DoP. (14.3 mm tool diameter, 100 m/min burnishing speed) (Yang et al., 2015).

A refined layer was produced on the burnished surface of AZ31B alloy by cryogenic burnishing. The depth of SPD layer was measured to be approximately 3.4 mm, and the hardness was increased to 1.35 GPa from the original 0.86 GPa, whereas the initial

grain size of $12\ \mu\text{m}$ was refined to $263\ \text{nm}$. The detailed microstructures observed at certain depths from the surface are shown in Figure 2.39. The corrosion resistance was also improved remarkably, attributing to the combined effects of grain refinement and strong basal texture (Pu et al., 2011).

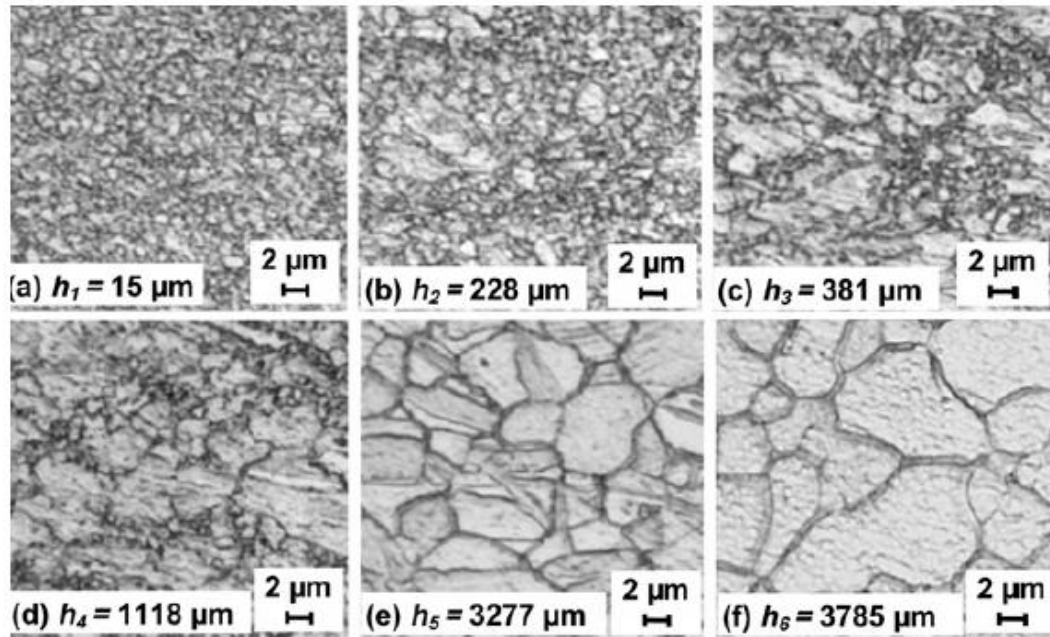


Figure 2.39: Typical microstructures at different depths from the surface, marked by $h1-h6$ (Pu et al., 2011).

CO_2 snow was also used as the coolant during the burnishing process. Ball burnishing tool with a larger diameter and high rolling pressure resulted in high hardness penetration depth and low surface roughness in cryogenic burnishing of $X210\text{Cr}12$ (AISI $D3$), reported by Meyer (2012). Similarly, high surface quality could be obtained by cryogenic burnishing of $41\text{Cr}4$ (AISI 5140) steel (Žak et al., 2014). The surface roughness R_a was measured and found to be about $0.2\ \mu\text{m}$ whereas R_z was less than $1\ \mu\text{m}$. They demonstrated that the hardness increase of the burnished surface was due to the phase transformation from austenite to martensite.

The beneficial effects of cryogenic burnishing are reviewed above in terms of surface integrity characteristics, including microstructure refinement, induced SPD layer, surface roughness, hardness, residual stresses, wear/corrosion resistance, etc. These parameters can be significantly enhanced by cryogenic burnishing when the input parameters are selected appropriately. In the next section, modeling efforts in burnishing will be discussed in order to understand the burnishing mechanism better, and to utilize the proper theoretical assumptions and principle to predict the output parameters, such as burnishing forces, temperature, grain size, depth of refined layer, residual stress and etc.

2.7 Burnishing model

Both the analytical and numerical models have been developed for the burnishing process by the researches in the recent decades. By employing the analytical models, burnishing force was one of the most frequently predictive parameters studied to understand the burnishing mechanisms. Considering the natural physical effects of the particular parameters of the burnishing tool and work material surface, including the pressure force, the radius of tool tip rounding and the height of the initial surface roughness, Korzynski (2009) constructed an analytical model to predict the deformation of roughness wedges formed by the axial force for the case of sliding burnishing with a ball burnishing tool on a low-hardness steel, as illustrated in Figure 2.40. The formula used in the model was to calculate the displacement of the burnished

surface roughness tips by taking into account of the effects of material factors, contact face geometry and the initial surface stereometry.

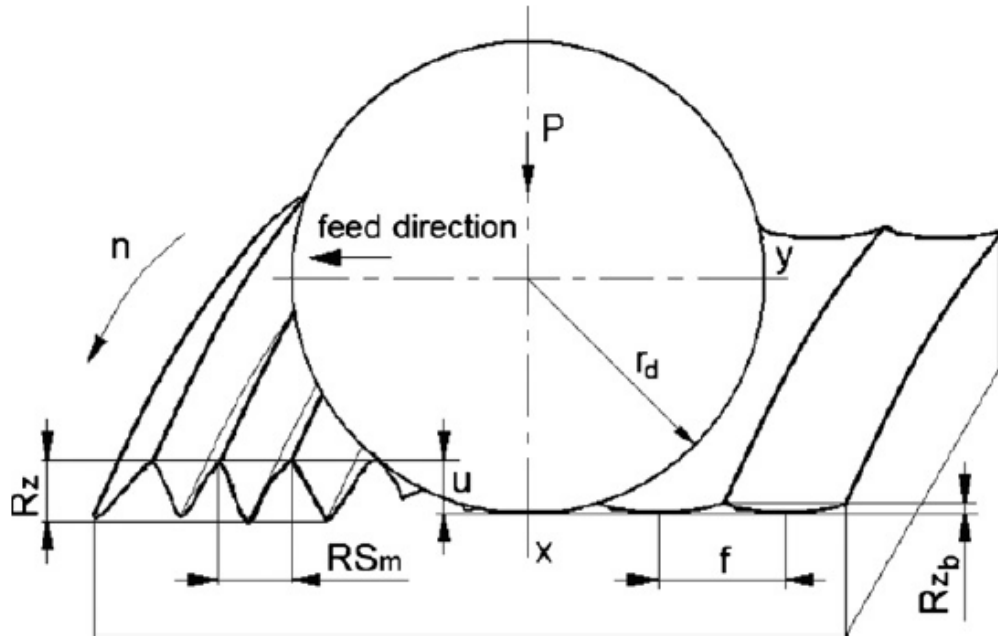


Figure 2.40: Model of smoothing slide burnishing with a ball-tipped tool: P is the burnishing force (burnishing pressure, tool pressure force), f is the feed, n is the rotational speed, R_z is the surface roughness before burnishing, R_{z_b} represents the surface roughness after burnishing, r_d is the radius of tool tip rounding, u is the tool indentation, RS_m is the mean spacing of profile irregularities before burnishing (Korzynski, 2009).

The surface profile produced by the burnishing process was also predicted by an analytical model based on the coverage of the cutting parameters, tool geometry, the materials of work material and burnishing tool, and the vibration phenomenon (Bougharriou et al., 2014). The predicted results were verified by experiments and good agreement was achieved. Li et al. (2012) mentioned in their study that the lowest surface roughness acquired by burnishing was proportional to the original surface roughness before burnishing and the surface roughness of the work material could be decreased by up to 75%-87.5%, depending on the semi-angle of asperity.

Three-dimensional burnishing forces were predicted by Luo et al. (2006) by means of an analytical model incorporating the contact and impact mechanics. This model included the mechanical and physical properties, burnishing parameters, macro-and micro-shape parameters. In most of the cases, the experimental and simulated results were in good agreement. There are many numerical models established to predict the residual stresses induced by burnishing as it is one of the most significant factors influencing the fatigue life of the burnished components.

The process of low plasticity burnishing was simulated by a 3D FEM-based model to predict the residual stress distribution along the depth of the work material and the associated plastic deformation (Mohammadi et al., 2014). They showed that large compressive residual stresses could be achieved by increasing the number of burnishing passes or reducing the diameter of the ball burnishing tool. Another 3D FEM-based model was employed to simulate the burnishing process with a roller burnishing tool by Balland et al. (2013) to predict the surface roughness and residual stresses introduced on the surface of the burnished materials. The ploughing effect shaping the burnished surface by pressing a ridge interacting with the initial profile, was investigated, and the mechanical effect of roller burnishing was studied as well. Klocke et al. (2011) also developed a FEA-based model to calculate the compressive residual stress distributions and strain hardening of burnished Inconel 718 alloy. The calculated residual stress was verified by the experimental results as shown in Figure 2.41.

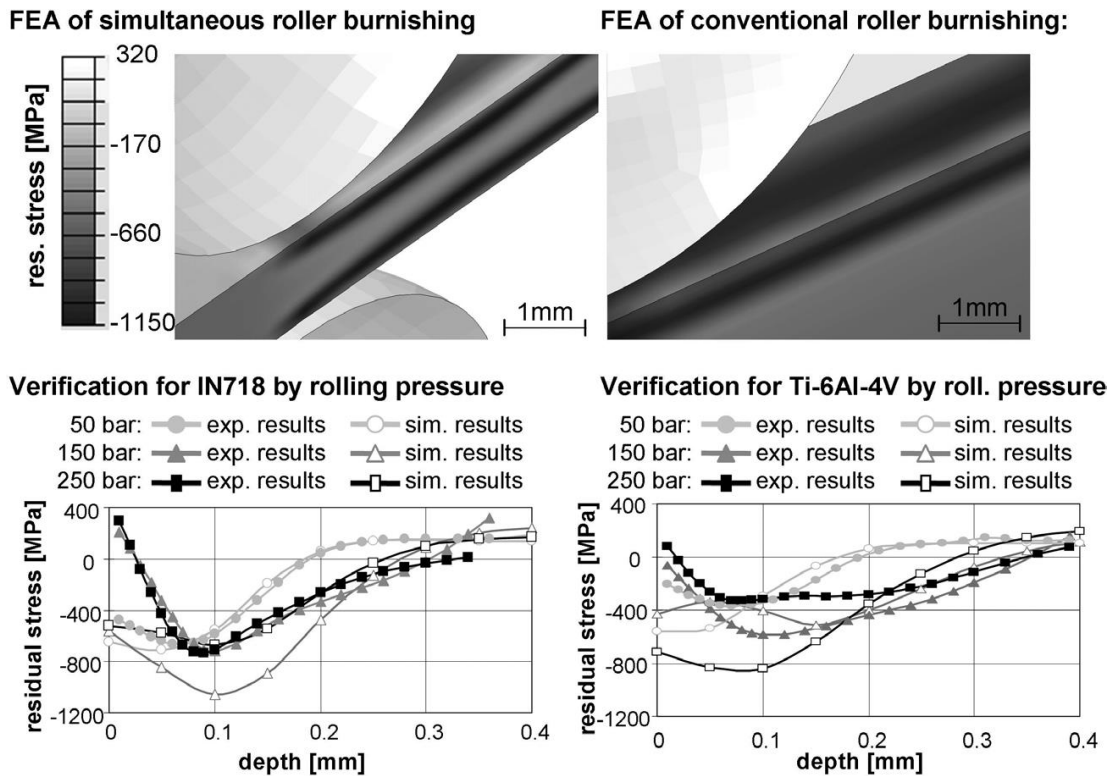


Figure 2.41: Verification of the roller burnishing FE model (Klocke et al., 2011).

Sayahi et al. (2013) indicated that better prediction accuracy could be obtained by 3D FEM-based model for burnishing of *Ti-6Al-7Nb* alloys compared with 2D FEM-based model when predicting the residual stress. They found that the maximum axial residual stress predicted by 2D FEM-based model had a 40% difference with the experimental results, while a much less difference of smaller than 7% was achieved by 3D FEM-based model. Salahshoor and Guo (2013) studied the burnishing of *MgCa0.8* alloys with the applications as biomaterials. The dent geometry, amount of elastic recovery, temperature, maximum axial tensile and radial compressive residual plastic strains and, residual stresses were predicted by the 2D axisymmetric FEM model to conduct the numerical evaluation of the burnishing process mechanism in ball burnishing, verified by the experimental results.

By reviewing the literatures of burnishing model development, the main focuses of the researchers have been to predict the residual stresses and burnishing-induced surface profile with the methods of analytical and numerical models. Apparently, very few investigations are conducted to simulate the burnishing forces, burnishing temperature, or other surface integrity characteristics, such as grain refinement, depth of SPD layer induced by burnishing, hardness, etc. In this dissertation, a theoretical model will be developed for burnishing processes to investigate the above surface integrity parameters associated with the experimental study of burnishing of *Al 7050-T7451* alloy.

CHAPTER 3

MICROSTRUCTURE REFINEMENT OF *Al 7050-T7451* ALLOYS ACHIEVED BY FRICTION STIR PROCESSING

3.1 Introduction

In recent years, the preparation of materials with UFG structure through SPD methodologies has gained a greater attention in the research communities and industry groups. Due to the excellent attributes in hardness, strength, ductility, superplasticity (Baro et al., 2001), wear and corrosion resistance (Balyanov et al., 2004), UFG materials have found greater and broader applications in medical industries, aerospace and transportation industries where components are manufactured from lightweight materials (Morehead et al., 2007), and in sports goods manufacturing industries (Lapovok et al., 2012).

Friction Stir Processing (FSP) has been proved to be an effective process to induce UFG structure. The working mechanism of FSP is relatively simple compared with other SPD methodologies such as equal channel angular extrusion, multi-axis restrain deformation, twist extrusion, cyclic extrusion compression, multi-directional forging, etc. The pin of the FSP tool is inserted into the hole created by pilot drilling until the tool shoulder contacts the workpiece surface. The friction heat generated between the rotation tool shoulder and the workpiece surface softens the material, meanwhile the tool feeds in certain direction. Dynamic recrystallization and grain refinement occur due to the stir action caused by the rotating pin. The UFG structure of the grains is

beneficial for metallic materials to improve their functional performance, such as the fatigue, wear and corrosion resistance.

The objective of the work presented in this section is to investigate the effects of FSP on *Al 7050-T7451* alloys in terms of microstructural changes, grain size distribution, hardness variation and texture change through XRD measurements. As discussed in the literature review presented in Section 2.1, *Al 7050-T7451* alloys are one of the highly anisotropic metallic materials, thus limiting their applications. In this particular material, the crack growth behavior along the short transverse direction is very different from the one measured along the long transverse direction. Also, the elongated grains are formed parallel to the rolling direction of *Al 7050-T7451* alloys, particularly in the sheet applications. Thus, a microstructure variation exists in the two orientations perpendicular and parallel to the rolling direction.

FSP has been employed to modify the microstructure of *Al 7050-T7451* alloy by means of DRX introduced by friction and stir actions. The grain size less than 2 μm could be achieved and more homogeneous microstructures are targeted especially in cryogenic FSP using liquid nitrogen as the coolant, compared with dry FSP. The hardness of the FSPed materials was measured when different rotational speeds and cooling conditions are used. XRD is also used to identify the texture change induced by FSP. Another important study is to process the whole sheet by FSP to ensure that homogeneous microstructure is acquired in a relatively large scale for the purpose of expanding the sheet applications of the work material in the corresponding industries, such as the aviation/aerospace, transportation, etc.

3.2 Experimental work

3.2.1 Work material

The material used in this study is an *Al 7050-T7451* alloy in sheet form, with the thickness of approximately 1/8 inches (3.2 mm). *T7451* is referred to the heat treatment conditions including solution heat-treated at 477°C for 30 minutes, and then water quenching followed by aging at 121°C and 163°C for 2 and 21 hours respectively, finally 2% stretching in the sequential order (Yan et al, 2009). The detailed chemical composition of *Al 7050-T7451* alloy used in this study is shown in Table 3.1. Each sample with the square form (115 mm × 115 mm) was cut from the whole sheet prepared for the FSP experiments.

Table 3.1: Chemical composition of *Al 7050-T7451* alloy (in wt. %) used in experimental work.

<i>Si</i>	<i>Fe</i>	<i>Cu</i>	<i>Mn</i>	<i>Mg</i>	<i>Cr</i>	<i>Zn</i>	<i>Ti</i>	<i>V</i>	<i>Zr</i>	<i>Al</i>
0.05	0.08	2.1	0.1	2.1	0.03	6.2	0.03	0.01	0.08	Bal.

3.2.2 FSP experiments

A Hass CNC machine tool, VF-2 was employed to perform the FSP experiments, a *H13* steel-based FSP tool developed for the experiments consisted of one tool shoulder with the diameter of 19.1 mm and one flat pin with the diameter and height of 6.4 and 2.5 mm, respectively. The pin height is slightly shorter than the thickness of plates as it is necessary to keep a safe distance between the bottom-end of the pin and the bottom-side of the plate after the pin is inserted into the work material and operated in the feed

direction. Holding clamps are used to fix the work materials in a staple state during FSP experiments. The Air Products and Chemicals ICEFLY[®] system is used to deliver liquid nitrogen at a fairly constant flow rate of about 10 g/s under the pressure of 1.5 MPa. Figure 3.1 illustrates the detailed setup of machine tool, cooling system, FSP tool and clamps used in the FSP experiments.

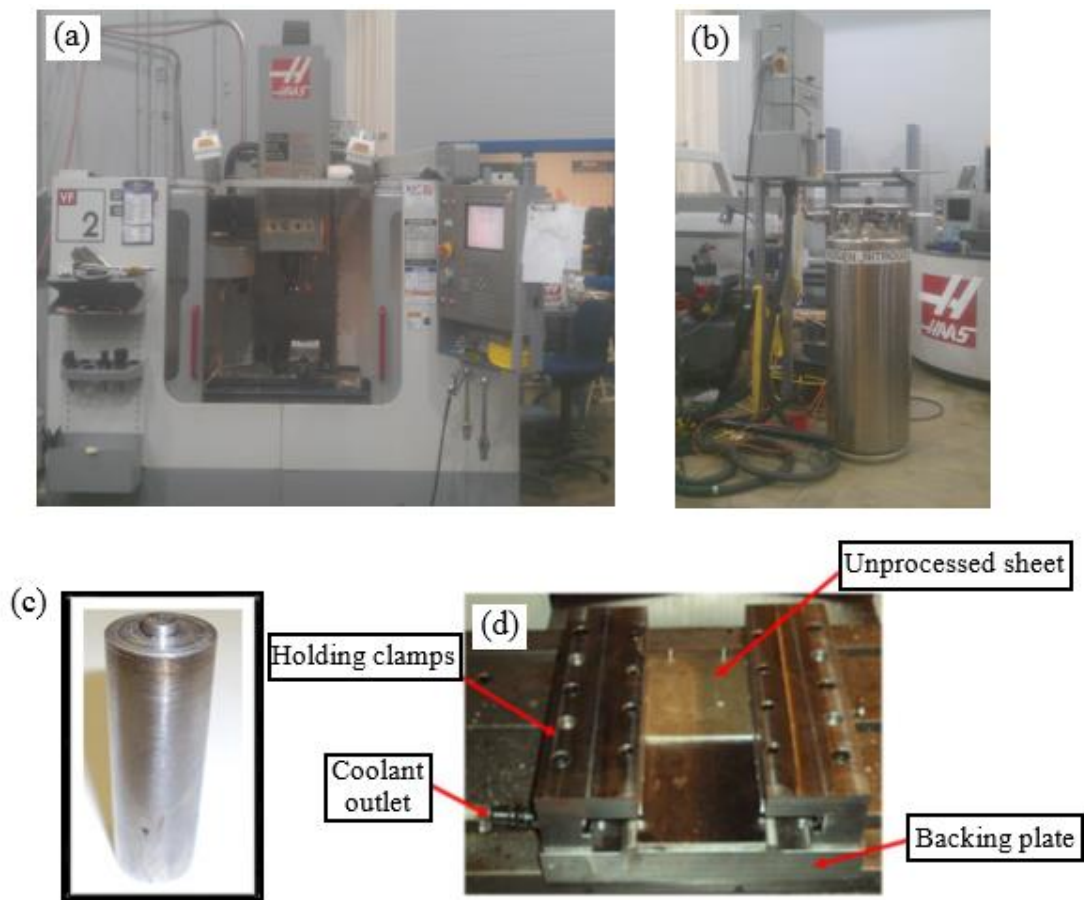


Figure 3.1: Equipment used in the FSP experiments: (a) Hass CNC machine tool VF-2; (b) ICEFLY[®] coolant delivery system; (c) FSP tool; and (d) Clamping system.

The inhomogeneity of grain size distributed through the thickness of plates existed (Mohammed, 2011) due to the fact that the friction heat generates between the tool shoulder and top surface of the plate and starts to transfer from the top-surface to the

bottom-side, and grain grows faster in the top-section of the plate in contrast to the ones in the center and bottom sections after DRX occurs during FSP.

For the purpose of solving the inhomogeneity problem, double-sided processing is adopted to homogenize the grain size distribution by first processing from the top-side of the plate, then flipping over the plate and processing the other side. 12 overlapping passes were used to process the entire plate for each side, as illustrated in Figure 3.2. The distance between two consecutive passes is the same as the diameter of the pin at 6.4 mm, it is used to solve the inhomogeneity issue among different passes as it is worth mentioning that for single pass (FSW), the grain size varied in different zones. The uniformity of large area processed by multi-pass FSP is the primary objective attempted to be achieved in this study. Additionally, liquid nitrogen is also applied during FSP to take away the extra heat residing in the FSPed region in order to suppress the grain growth after DRX. A more homogeneous microstructure with smaller grain size is expected compared with dry FSP, the detailed experimental setup of cryogenic FSP is shown in Figure 3.2.

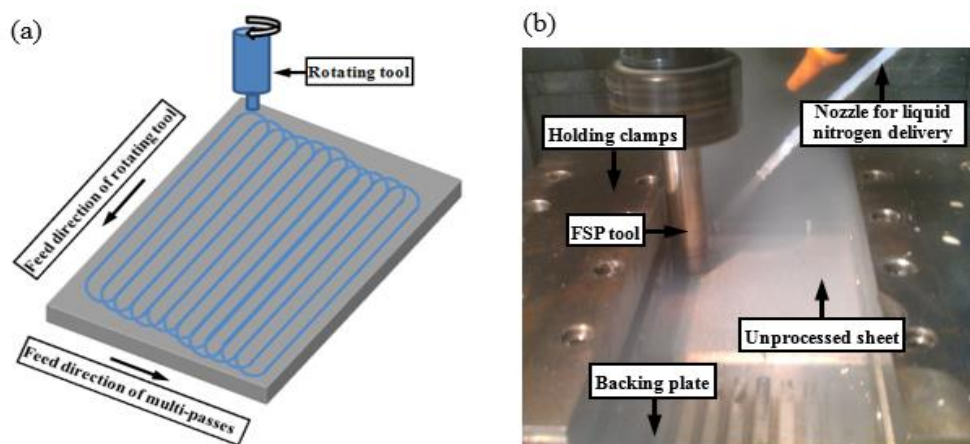


Figure 3.2: (a) Illustration of multi-pass FSP; and (b) Experimental setup of cryogenic FSP.

The matrix of FSP experiments was determined by reviewing the work of other researchers. The rotational speeds and feed rates commonly used are listed in Table 3.2 for more details, and the appropriate rotational speed and feed rate highlighted were selected from the list. Feed rate was a more straightforward parameter influencing the grain refinement. Less heat will stay in the processed material when a higher feed rate is used for FSP. Therefore, smaller grain size and higher hardness are expected to be obtained due to reduced thermal softening effect. In this study, the feed rate was 101.6 mm/min and was kept as the constant. The applied processing speeds were 19.2, 24, 28.8 and 48 m/min converted from the rotational speeds of 320, 400, 480 and 800 rpm, respectively. Two cooling methods used in the FSP experiments are: dry and cryogenic conditions. The detailed experimental matrix is shown in Table 3.3.

Table 3.2: (a) The rotation speeds and feed rates selected from the literature.

References	Rotation speed (rpm)	Feed rate (mm/min)
Brown et al., 2009	540	408
Fuller et al., 2010	200, 600	101.6, 109
Jata et al., 2000	396	102
John et al., 2003	240	142.2
Long et al., 2007	200, 400, 600, 800	76.2
Miles et al., 2006	350	127
Pao et al., 2001	400	100
Su et al., 2005	350	15
Tian et al., 2011	235	190

Table 3.2: (b) Statistical classification of rotation speeds and feed rates

Range of feed rate (mm/min)	Feed rate (mm/min)
0-50	15
50-100	76.2
100-150	100, 101.6 , 102, 109,
150-200	190
>200	408

Range of rotational speed (rpm)	Rotational speed (rpm)
0-100	
100-200	
200-300	200, 235, 240
300-400	350, 396, 400
>400	540, 600, 800

Table 3.3: FSP experimental matrix.

Cooling method	Rotational speed (m/min)	Feed rate (mm/min)
Dry	19.2	101.6
Dry	24	101.6
Dry	28.8	101.6
Dry	48	101.6
Cryogenic	19.2	101.6
Cryogenic	24	101.6
Cryogenic	28.8	101.6
Cryogenic	48	101.6

3.2.3 Measurements of surface integrity characteristics

To investigate the microstructures, the metallurgical samples were cut from the cross sections through the thickness orientation of the processed plates. In the sequential order, mounting, grinding, polishing and etching were performed to reveal the microstructure of the samples processed by dry and cryogenic FSP, and Keller's reagent was used to etch the samples. Nikon EPIPHOT 300 with Leica DFC425 optical microscope was used to observe the microstructure.

To statistically analyze the homogeneity of the work materials processed by dry and cryogenic FSP, 45 microstructure images were examined and the average grain size of each corresponding microstructure was calculated using average grain intercept (AGI) method. The cross sections perpendicular to the feed direction of FSP were cut, the length of the cross sections studied was approximately 60 mm, and 9 evenly distributed positions were focused along the length direction. When it comes to the thickness direction, 5 evenly distributed positions were located. For the positions approaching the top- and bottom-side of the processed plates, the grain size was measured in the positions that 100 μm below and above the top and bottom side respectively, due to the rough surface finish of FSP. Figure 3.3 shows the example of measurement rectangulars in which the grain size is measured for the processed materials in each individual condition. For each microstructure image observed, 200 μm \times 150 μm were the rectangular dimensions and the average grain size was measured therein.

Hardness was measured by using one Vickers indenter on the CSM Micro-Combi Tester in which 25 gf load was applied for 15 seconds for the indentation. And, for

analyzing the phase transformation of FSPed samples, a X-ray diffraction (XRD) equipment-Bruker AXS D8 Discover, with a quarter Ellurian cradle sample holder was used. The X-ray diffraction patterns were measured using $CuK\alpha$ radiation ($\lambda = 1.54184\text{\AA}$, $K\alpha1/K\alpha2 = 0.5$) from a source operated at 40 kV, and 40 mA. The 2θ scans were carried out between 35 and 80° . The scan speed was 1.5 deg / min .

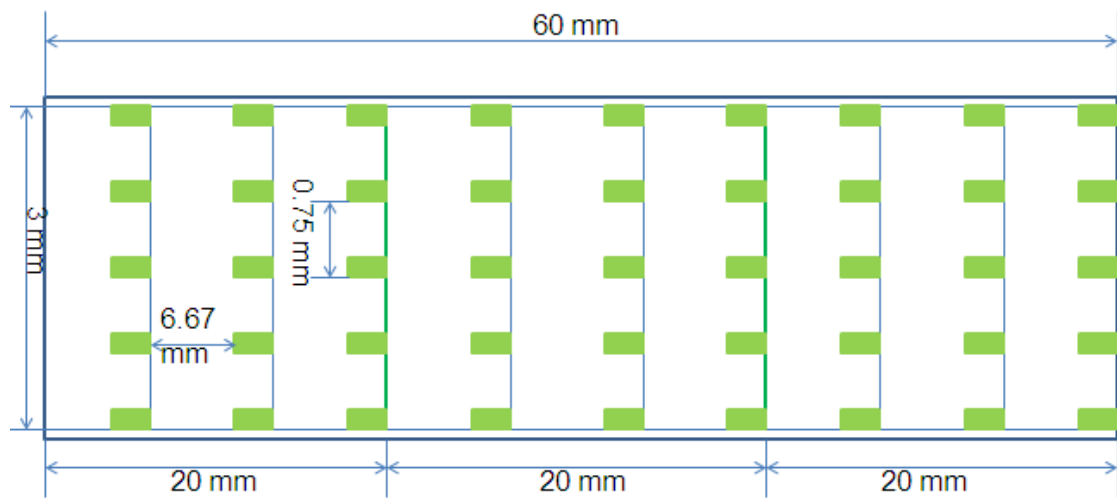


Figure 3.3: Measurement locations highlighted by Green rectangulars used for measuring the grain size for each processed material sample.

3.3 Experimental results and discussion

3.3.1 Microstructure

Five microstructure images are obtained for each individual processed sheet material under four rotational speeds and two cooling methods: dry and cryogenic FSP. For instance, one column in the illustration of Figure 3.3 corresponds to the five microstructure images. From top to bottom side along the thickness orientation of the cross section, the homogeneous extent is reflected by the five images. Limited by the size of the dissertation, not all the 45 microstructure images are shown for every

condition, only the five representatives from one column are presented. All microstructure images are shown in Figures 3.4 - 3.11 to illustrate the comparisons between dry and cryogenic FSP and the effects of rotational speeds.

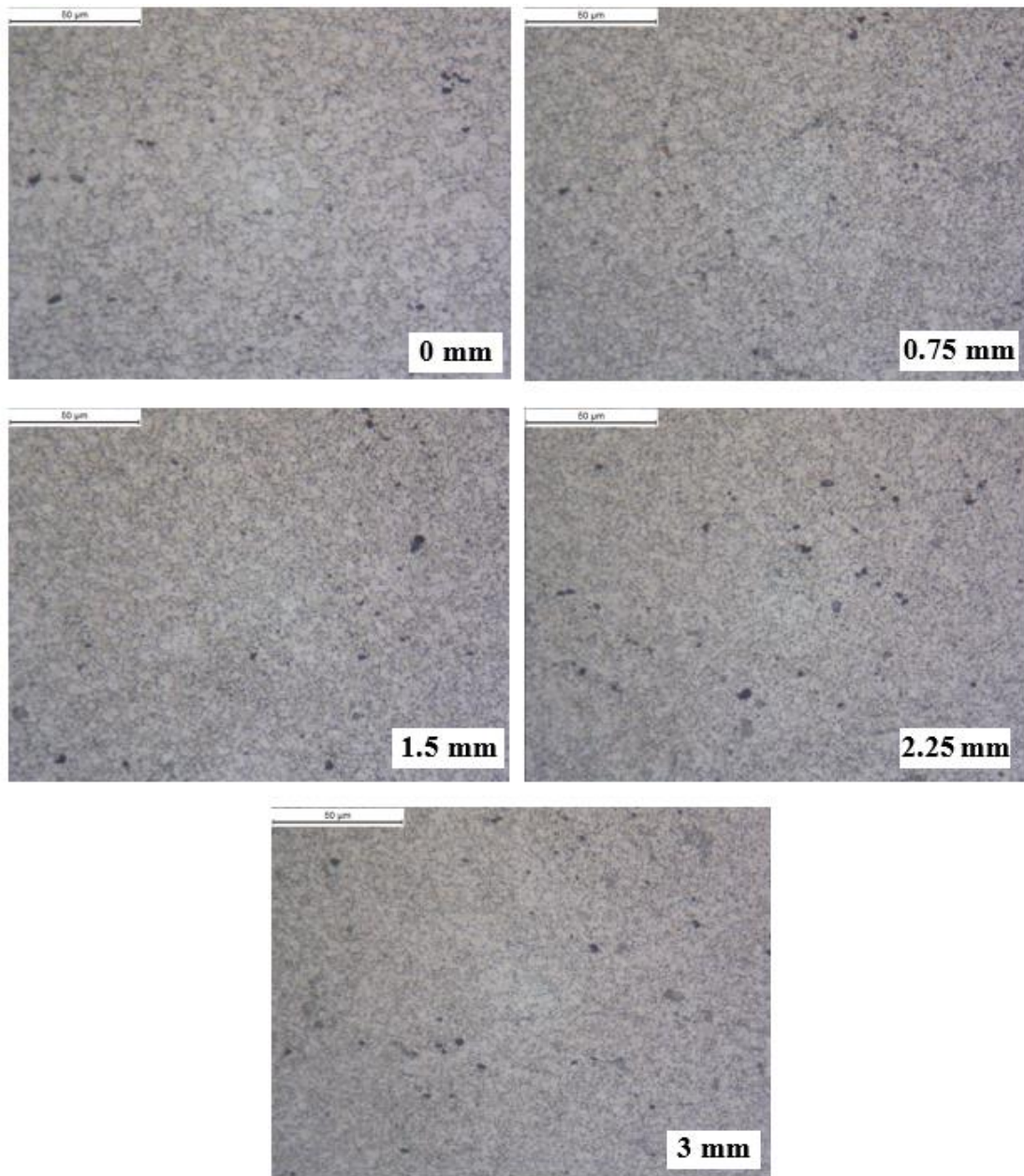


Figure: 3.4: Microstructure images of the work material processed by dry FSP under the rotational speed of 19.2 m/min and feed rate of 101.6 mm/min at the positions of approximately 0 mm, 0.75 mm, 1.5 mm, 2.25 mm and 3 mm along the orientation of the plate thickness.

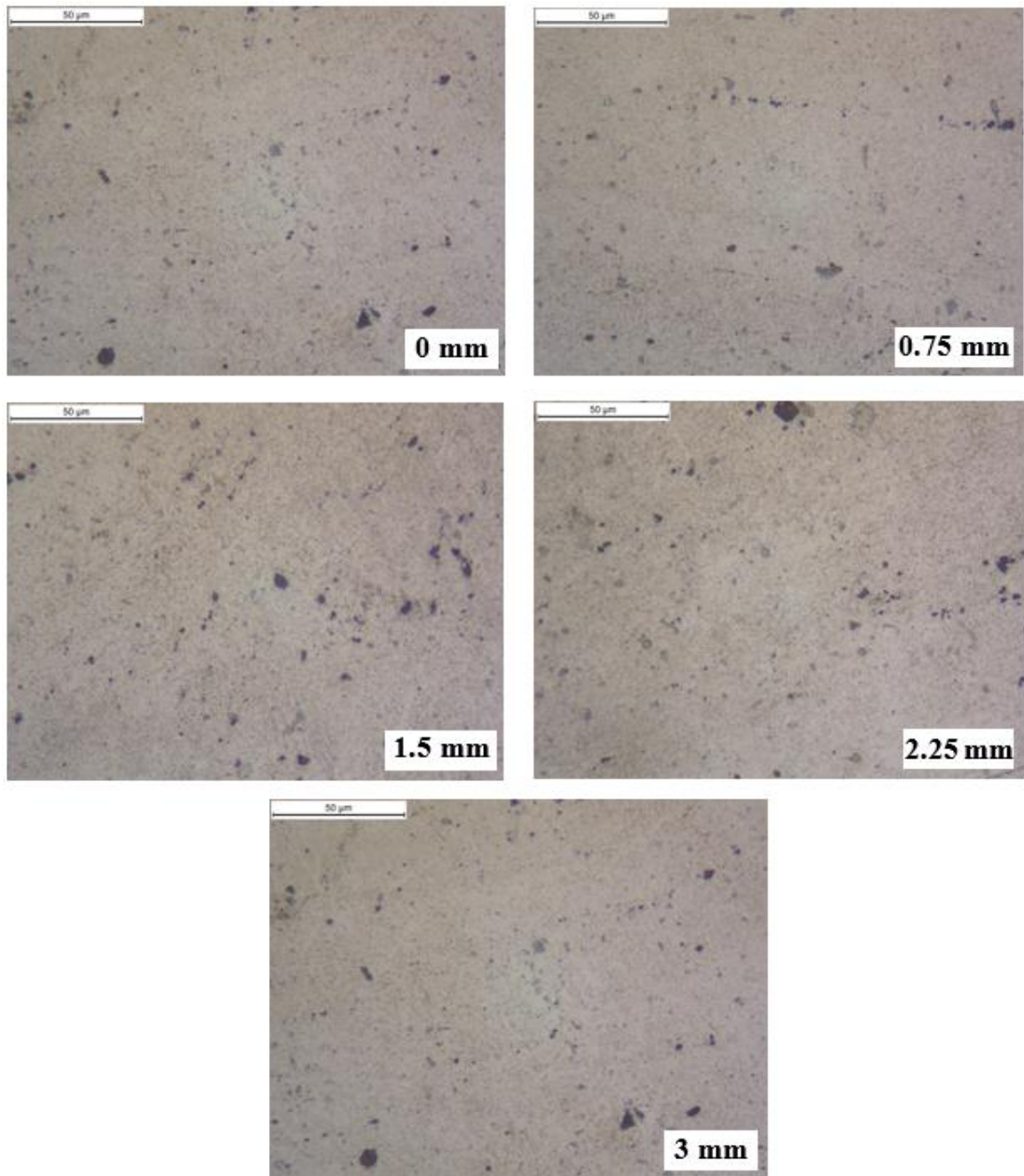


Figure: 3.5: Microstructure images of the work material processed by cryogenic FSP under the rotational speed of 19.2 m/min and feed rate of 101.6 mm/min at the positions of approximately 0 mm, 0.75 mm, 1.5 mm, 2.25 mm and 3 mm along the orientation of the plate thickness.

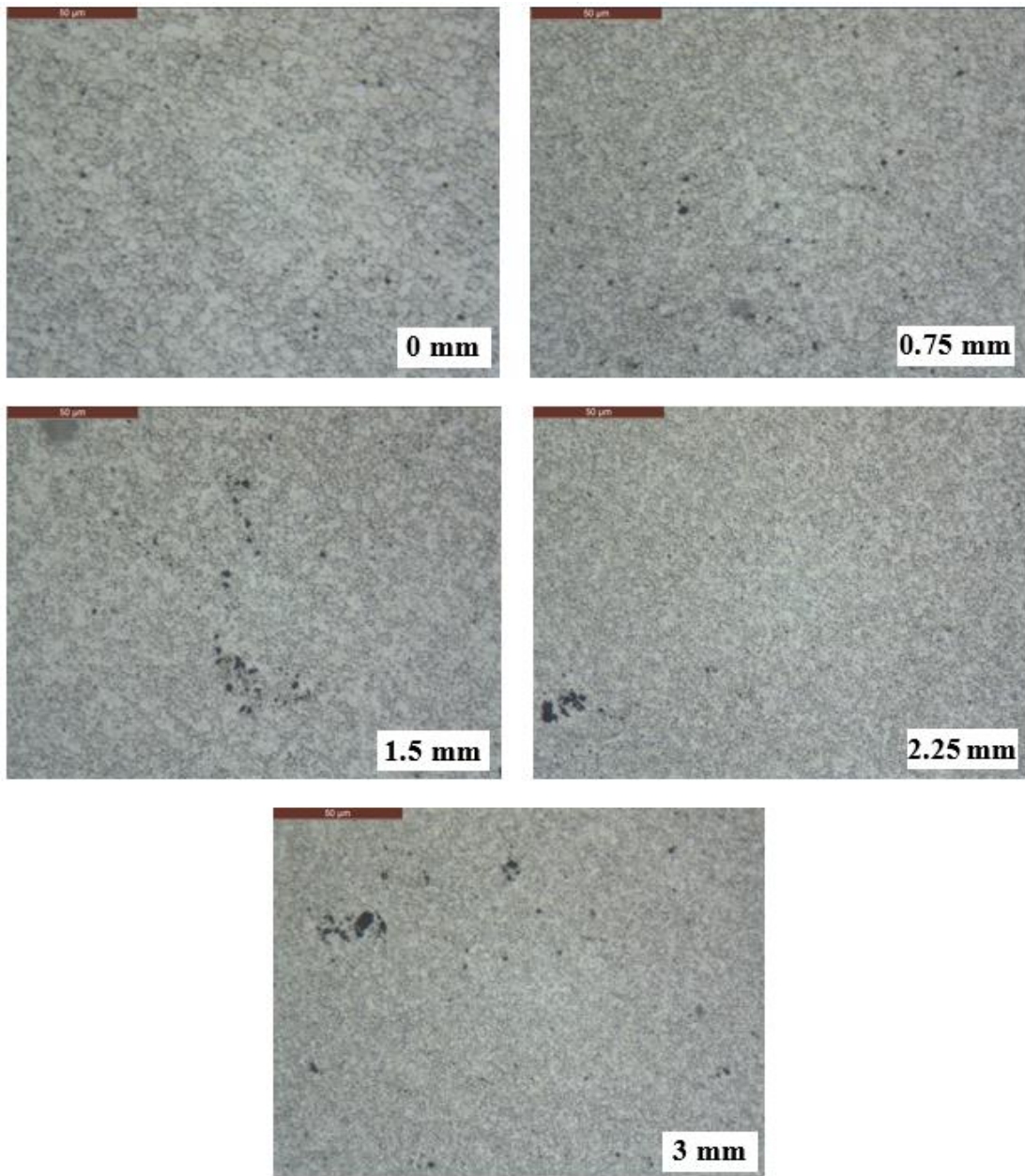


Figure: 3.6: Microstructure images of the work material processed by dry FSP under the rotational speed of 24 m/min and feed rate of 101.6 mm/min at the positions of 0 mm, 0.75 mm, 1.5 mm, 2.25 mm and 3 mm along the orientation of the plate thickness.

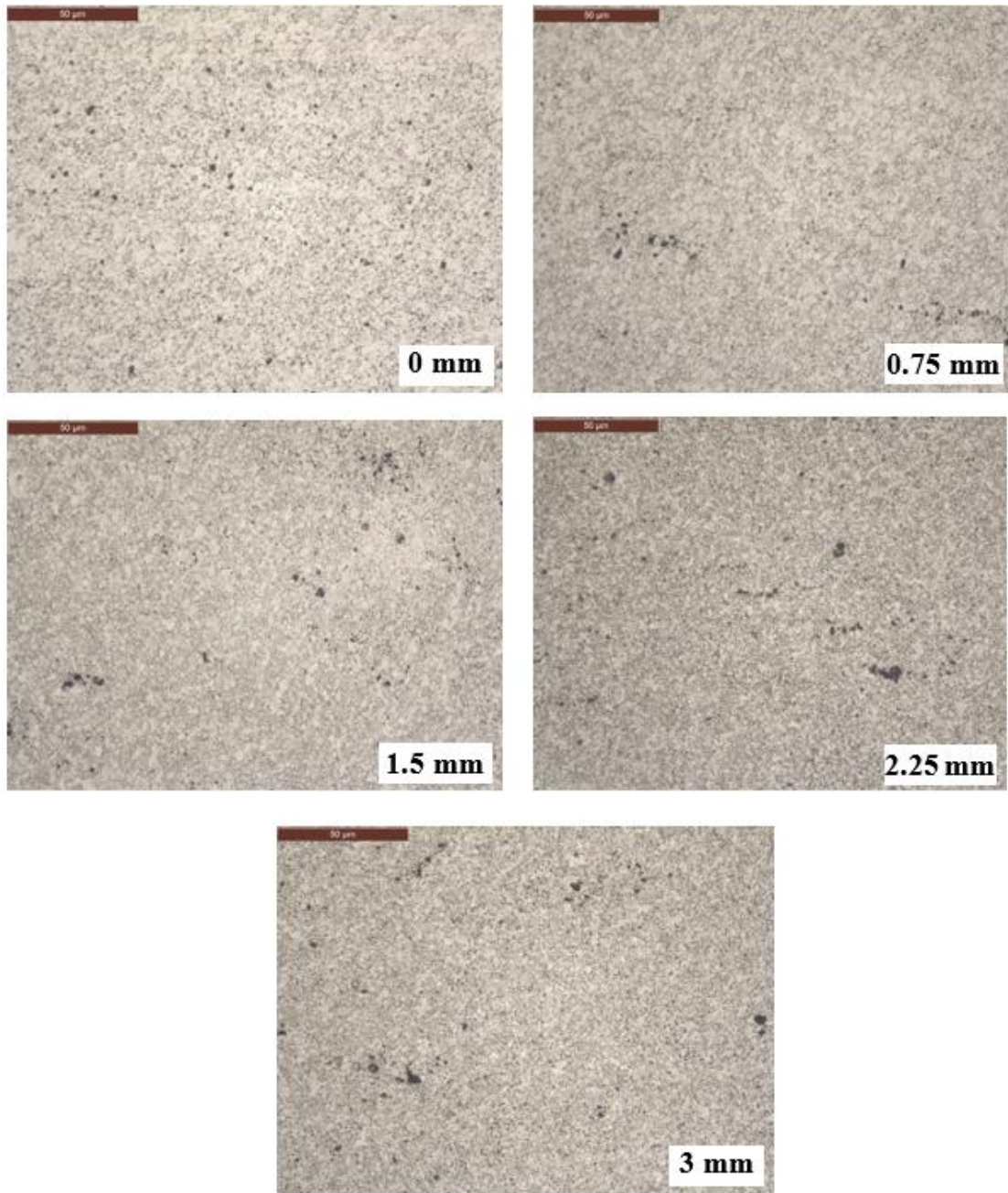


Figure: 3.7: Microstructure images of the work material processed by cryogenic FSP under the rotational speed of 24 m/min and feed rate of 101.6 mm/min at the positions of approximately 0 mm, 0.75 mm, 1.5 mm, 2.25 mm and 3 mm along the orientation of the plate thickness.

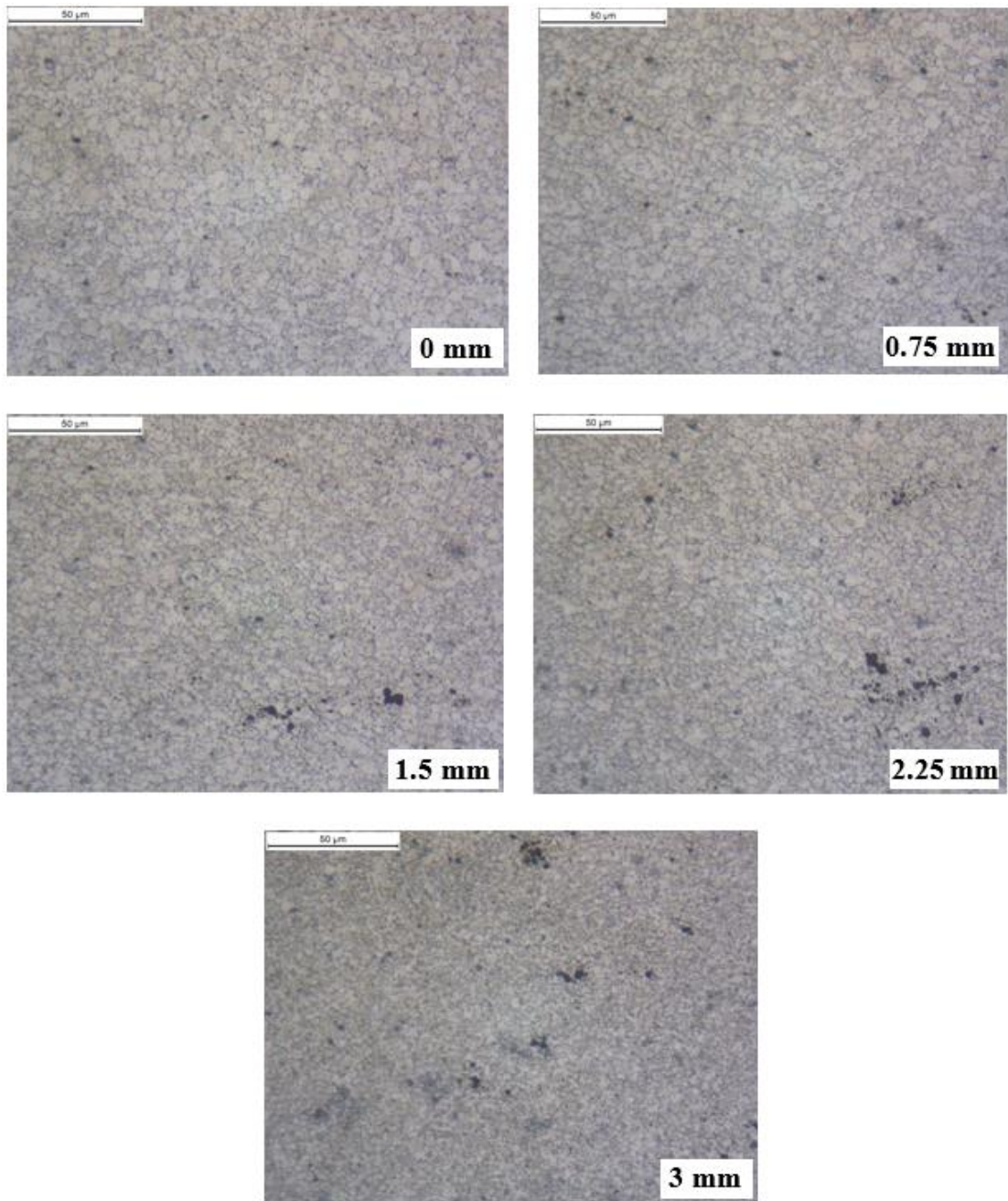


Figure: 3.8: Microstructure images of the work material processed by dry FSP under the rotational speed of 28.8 m/min and feed rate of 101.6 mm/min at the positions of 0 mm, 0.75 mm, 1.5 mm, 2.25 mm and 3 mm along the orientation of the plate thickness.

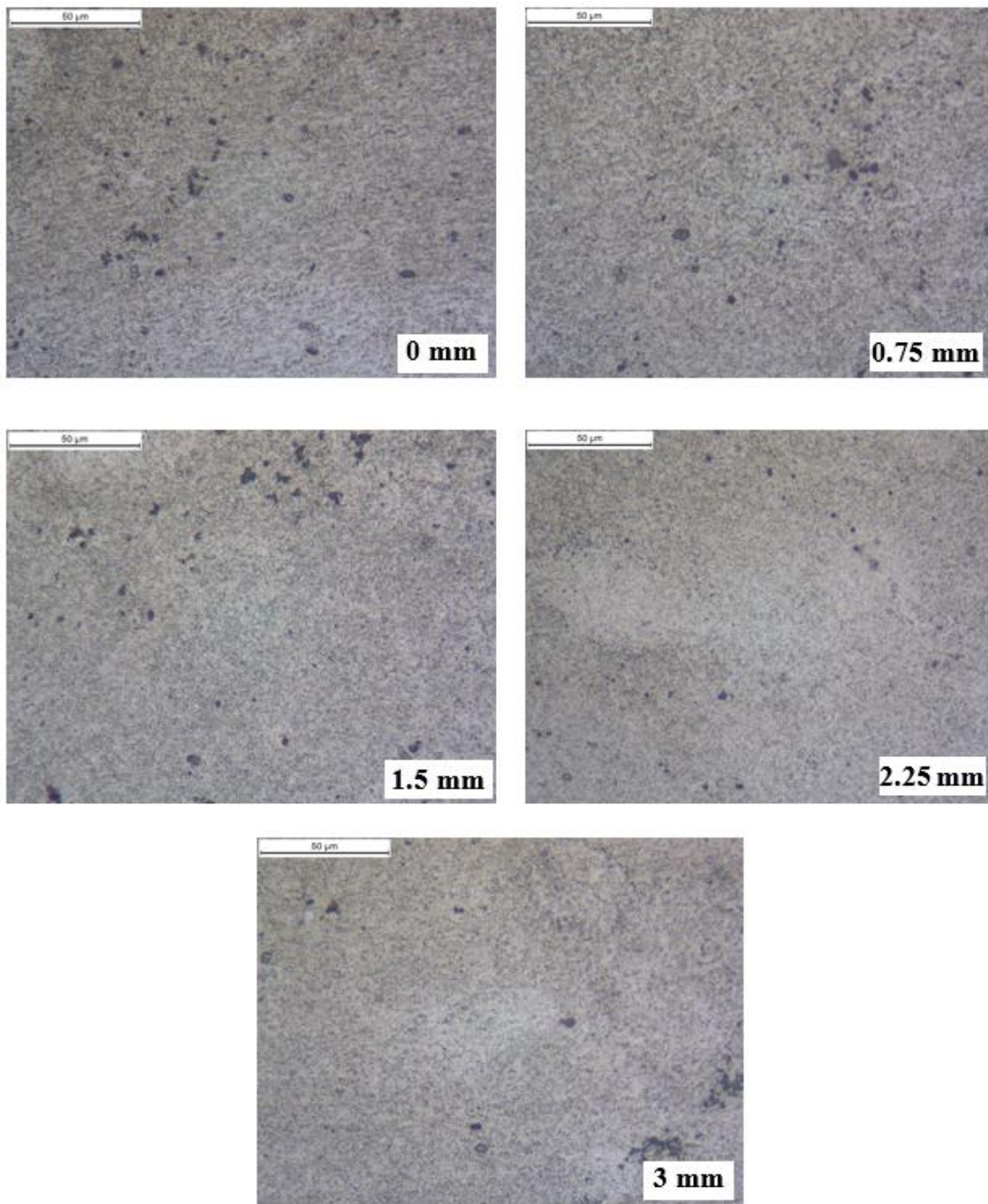


Figure: 3.9: Microstructure images of the work material processed by cryogenic FSP under the rotational speed of 28.8 m/min and feed rate of 101.6 mm/min at the positions of 0 mm, 0.75 mm, 1.5 mm, 2.25 mm and 3 mm along the orientation of the plate thickness.

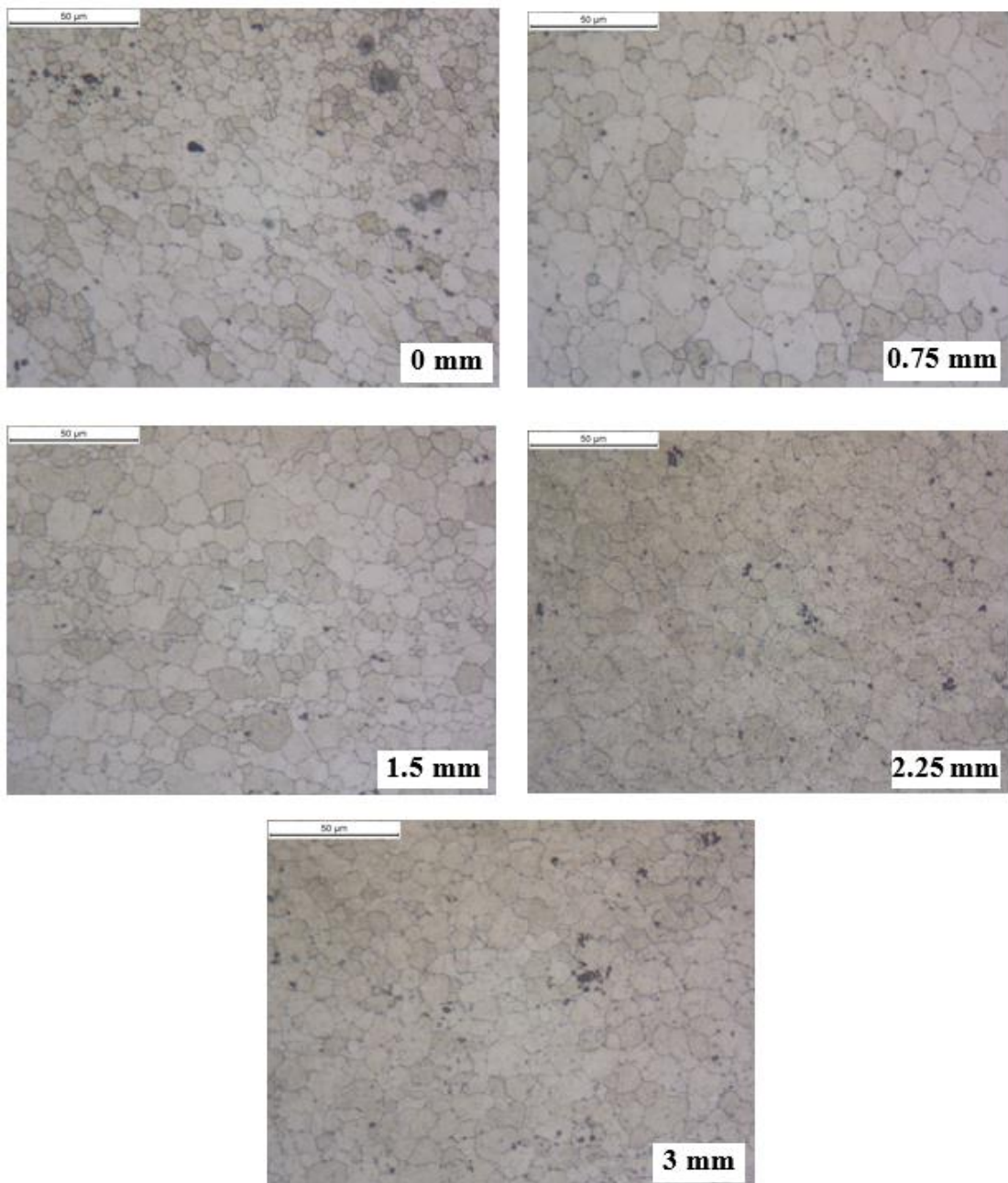


Figure: 3.10: Microstructure images of the work material processed by dry FSP under the rotational speed of 48 m/min and feed rate of 101.6 mm/min at the positions of 0 mm, 0.75 mm, 1.5 mm, 2.25 mm and 3 mm along the orientation of the plate thickness.

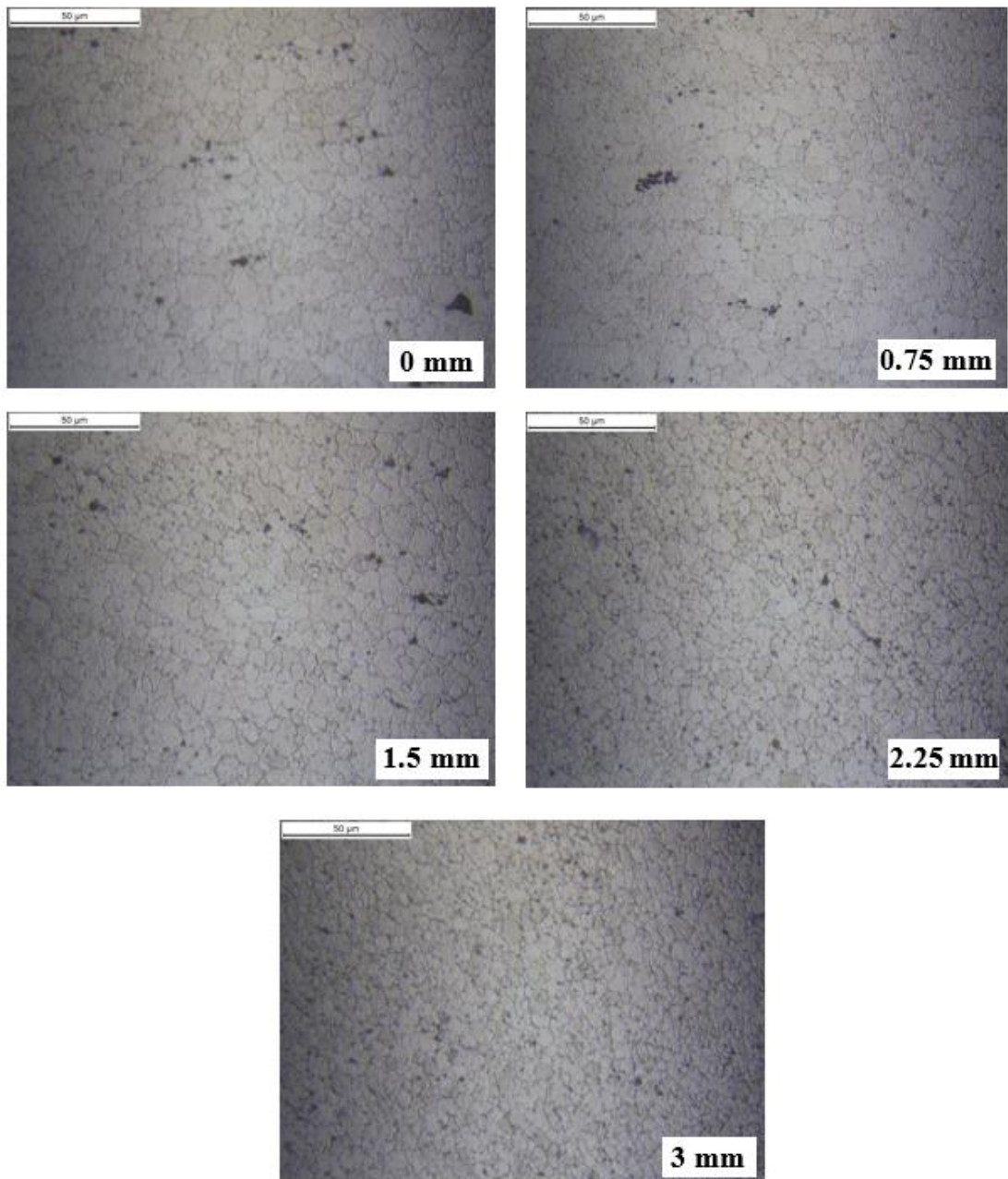


Figure: 3.11: Microstructure images of the work material processed by cryogenic FSP under the rotational speed of 48 m/min and feed rate of 101.6 mm/min at the positions of 0 mm, 0.75 mm, 1.5 mm, 2.25 mm and 3 mm along the orientation of the plate thickness.

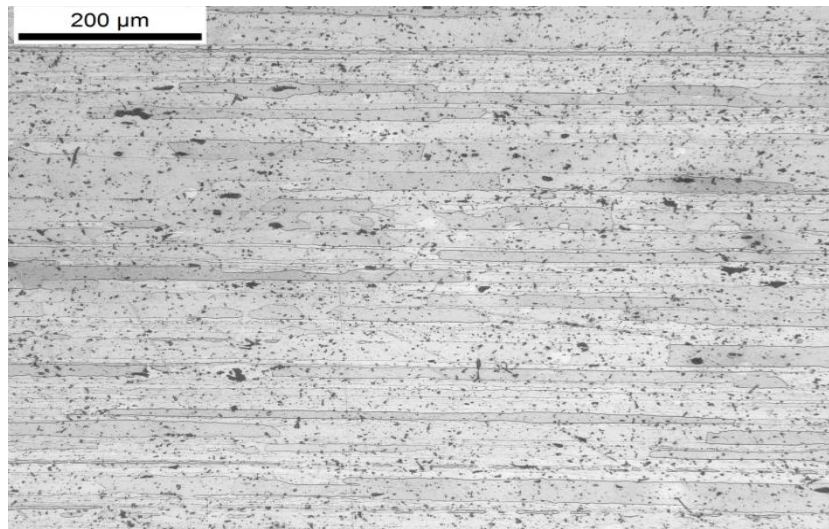


Figure 3.12: The microstructure image of the as-received material.

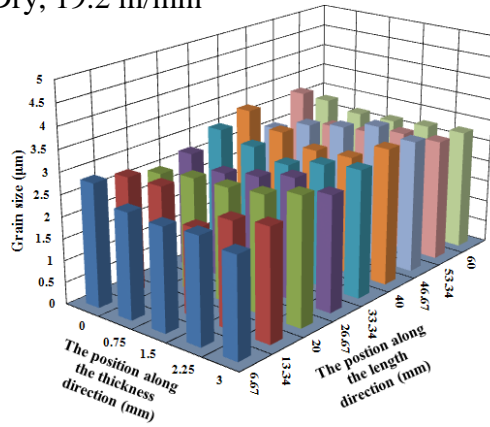
With the comparisons among microstructure images of dry and cryogenic FSP using four different rotational speeds as shown in Figure 3.4-3.11, the grain size and homogeneity could be identified. Grain refinement was very apparent by reducing elongated coarse grains of as-received materials as shown in Figure 3.12 to near UFG level. It was observed that the average grain size became larger with increasing rotational speed, because more friction heat was generated when using a higher rotational speed. After DRX occurred during FSP, the recrystallized grains absorbed more heat to grow and became larger compared with the grains generated at a lower rotational speed. This had been confirmed by Rhodes et al. (Rhodes et al., 2003) in their study. Similar observations were made when using double-sided FSP to process *Al 7050-T7451* plates in this investigation too.

For cryogenic FSP, more heat was taken away by liquid nitrogen delivered from the nozzle located behind the operating FSP tool. Therefore, recrystallized small grains

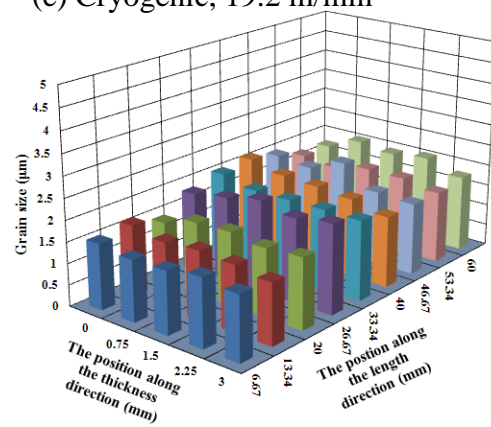
would absorb less heat to grow and finally reach a smaller level in contrast to the dry condition. From the 3D plots as shown in Figure 3.13, the homogeneity of grain size located at different positions was clearly seen. It is understandable that the less heat generated and transferred through the plate, the more homogeneous microstructure processed by FSP would be. Thus, it can be concluded that cryogenic FSP could provide more homogeneous microstructure from the grain size point of view when a lower rotational speed was used during FSP. More detailed homogeneity analysis is illustrated in Figure 3.14, with the error bars represented in the range of 95% confidence level. The error bars indicate the approximately upper and lower limits of the average grain sizes achieved, and cryogenic FSP provided a better opportunity to obtain more homogeneous materials with near UFG microstructure.

By taking the average value of grain size from each individual condition of dry and cryogenic FSP as shown in Figure 3.15, an increasing linear trend of grain size was observed for both dry and cryogenic FSP when increasing the speed. An approximately 30% reduction was achieved from cryogenic FSP compared with the dry FSP, and more homogeneous microstructure could be obtained in the cryogenic condition as discussed above.

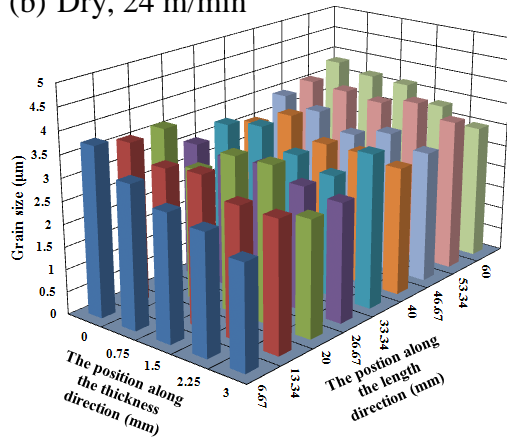
(a) Dry, 19.2 m/min



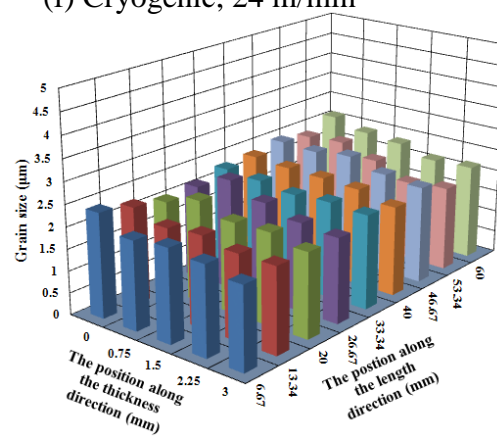
(e) Cryogenic, 19.2 m/min



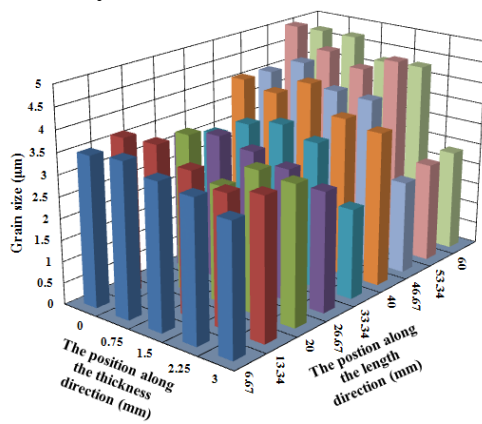
(b) Dry, 24 m/min



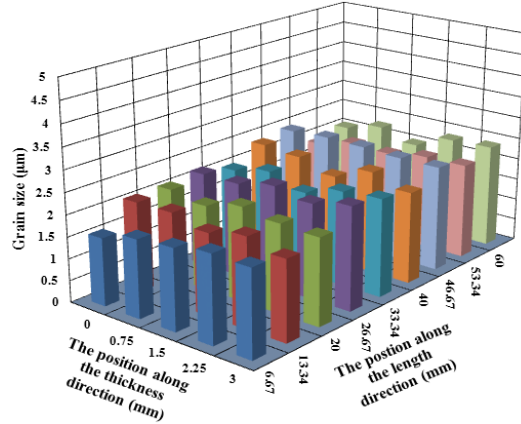
(f) Cryogenic, 24 m/min



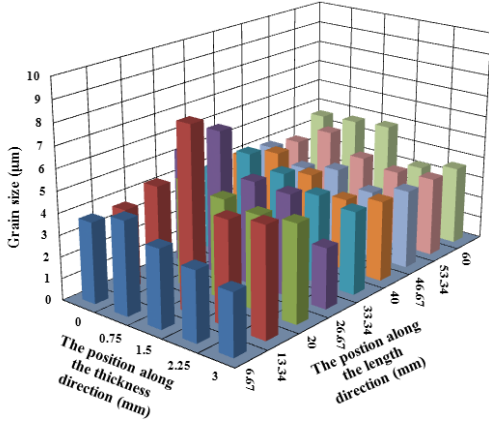
(c) Dry, 28.8 m/min



(g) Cryogenic, 28.8 m/min



(d) Dry, 48 m/min



(h) Cryogenic, 48 m/min

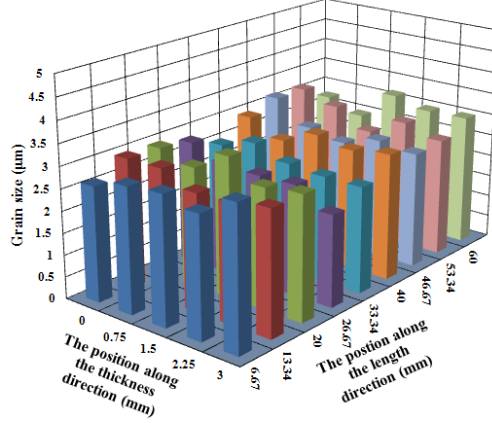
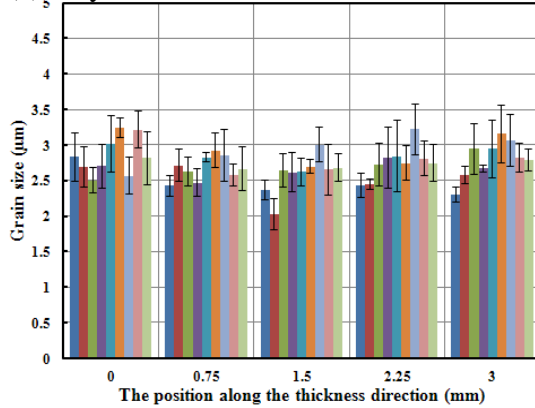
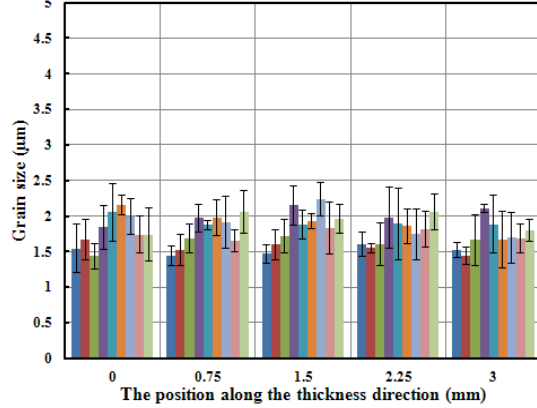


Figure 3.13: Grain size distributions among the samples processed by dry and cryogenic FSP at four different rotational speeds of 19.2, 24, 28.8, and 48 m/min: (a) dry, 19.2 m/min; (b) dry, 24 m/min; (c) dry, 28.8 m/min; (d) dry, 48 m/min; (e) cryogenic, 19.2 m/min; (f) cryogenic, 24 m/min; (g) cryogenic, 28.8 m/min; and (h) cryogenic, 48 m/min.

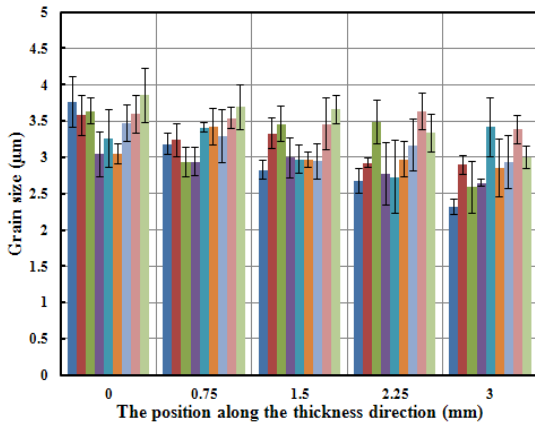
(a) Dry, 19.2 m/min



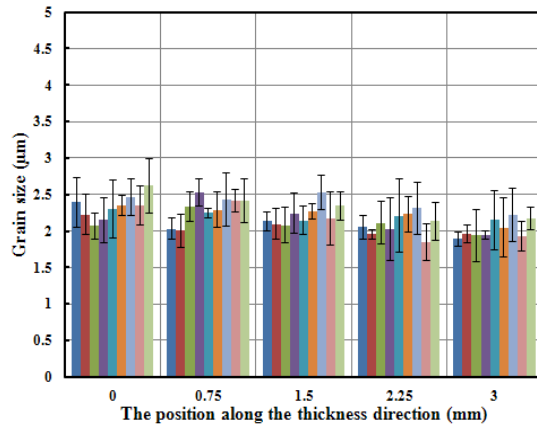
(e) Cryogenic, 19.2 m/min



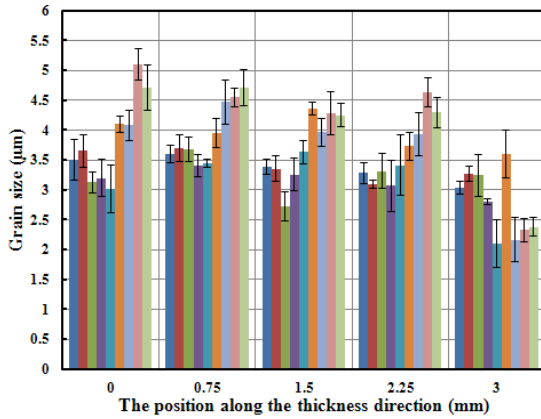
(b) Dry, 24 m/min



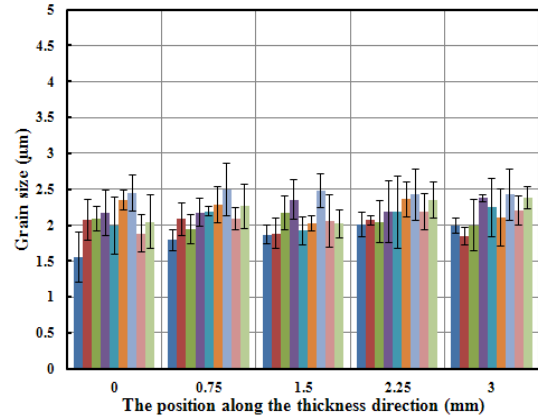
(f) Cryogenic, 24 m/min



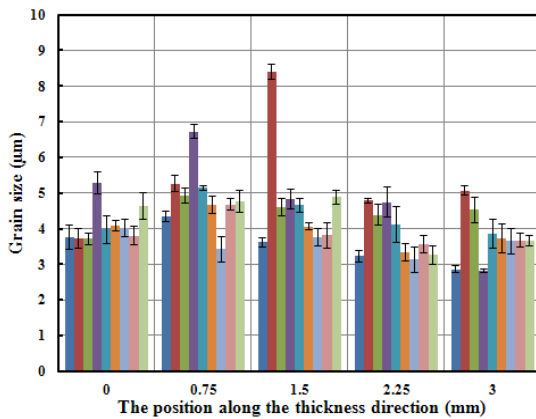
(c) Dry, 28.8 m/min



(g) Cryogenic, 28.8 m/min



(d) Dry, 48 m/min



(h) Cryogenic, 48 m/min

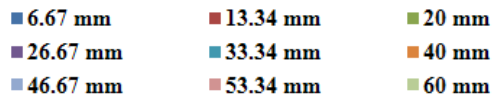
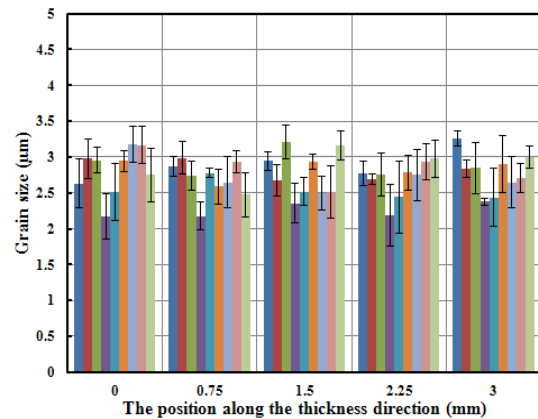


Figure 3.14: Grain size distributions among the samples processed by dry and cryogenic FSP at four different rotational speeds of 19.2, 24, 28.8, and 48 m/min: (a) dry, 19.2 m/min; (b) dry, 24 m/min; (c) dry, 28.8 m/min; (d) dry, 48 m/min; (e) cryogenic, 19.2 m/min; (f) cryogenic, 24 m/min; (g) cryogenic, 28.8 m/min; and (h) cryogenic, 48 m/min.

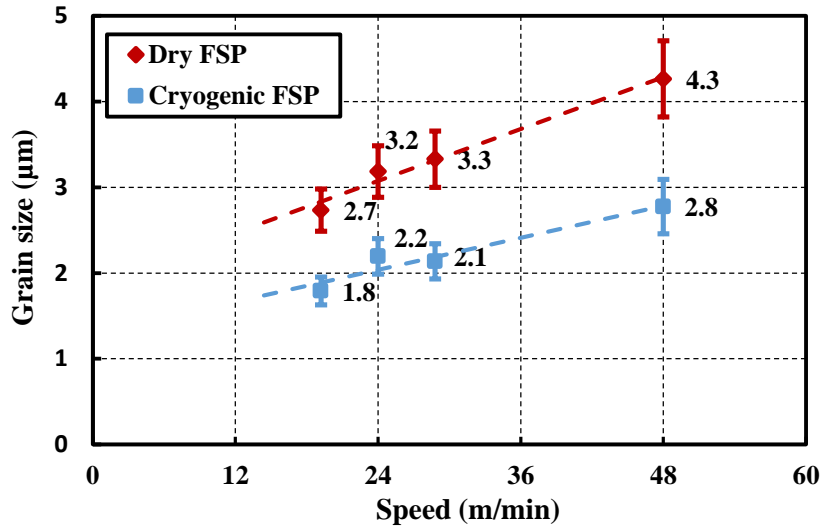


Figure 3.15: Grain size variation in dry and cryogenic FSP at four different speeds: 19.2, 24, 28.8, 48 m/min.

3.3.2 Hardness

Hardness measurement was performed in the same way as for the microstructure. 45 positions in each processed samples were tested and measured by the Vickers indenter. For each position, five indentations were made to provide the average value of hardness, and the upper and lower limits could be determined with the largest and smallest values measured among the five hardness data. All the hardness values are presented in Figure 3.16 for all processing conditions of dry and cryogenic FSP. Observed from these plots, the decreasing hardness was found for all FSP conditions compared with the hardness of the as-received material at approximately 136 HV. Similarly, decreasing hardness results were also found in work by other researchers previously in their experimental work with FSW experiments (Yan et al., 2009; Brown et al., 2009; Reynolds et al., 2005).

It is known that the hardness of *Al-Zn-Mg-Cu* alloys highly depends on the fine precipitates located in the inner parts of grains and grain boundaries. The materials become harder if the density of the precipitates is higher while the precipitates are finer. The precipitation sequence of such aluminum alloys is shown below as the aging temperature increases.

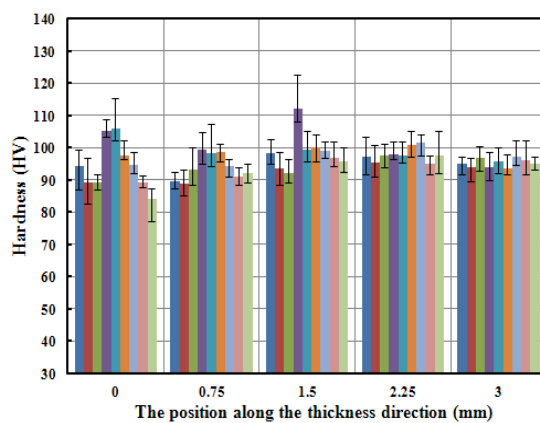
Solid solution \rightarrow GP zones $\rightarrow \eta'$ (Mg(Zn, Cu, Al)₂) $\rightarrow \eta$ (MgZn₂ and Mg₃Zn₃Al₂)

It was reported that the dissolution temperature of η' precipitates is between 180°C and 260°C (Mahoney et al., 1998). The temperature was found to be 400°C-500°C during FSW of *Al 7050-T7451* alloy (Upadhyay et al., 2010; Kamp et al., 2009; Long et al., 2007). It is higher than the dissolution temperatures of both η' and η precipitates. The dissolution and coarsening of the two precipitates occurred based upon the research by Su et al. (2003). In their work, the solution and re-precipitated precipitates were observed in the dynamically recrystallized zone when *Al 7050* alloy was friction stir welded. The same phenomenon may occur in multi-pass dry and cryogenic FSP as well. Therefore, the hardness of FSPed samples of *Al 7050-T7451* alloy plates decreased due to the dissolution and coarsening of precipitates in η' and η phases.

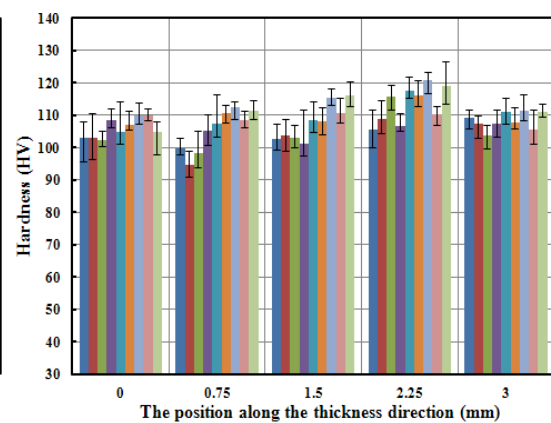
It is seen in Figure 3.16 that higher hardness was obtained in cryogenic FSP experiments than dry condition as liquid nitrogen lowered the temperature to constrain the dissolution and coarsening of the precipitates to some extent. The samples of dry and cryogenic FSP possessed better homogeneous performance in contrast to the ones acquired by the FSW experiments (Yan et al., 2009; Brown et al., 2009; Reynolds et

al., 2005; Fuller et al., 2010) in which the hardness varied at different zones. Both the hardness values of dry and cryogenic FSPed samples were very consistent at all positions covered by the hardness measurements, and the hardness achieved by cryogenic FSP was slightly more homogeneous than dry FSP at each processing condition. The overview of the hardness distribution is presented using 3D plots for all the eight conditions as shown in Figure 3.17 to demonstrate more comprehensive hardness distributions.

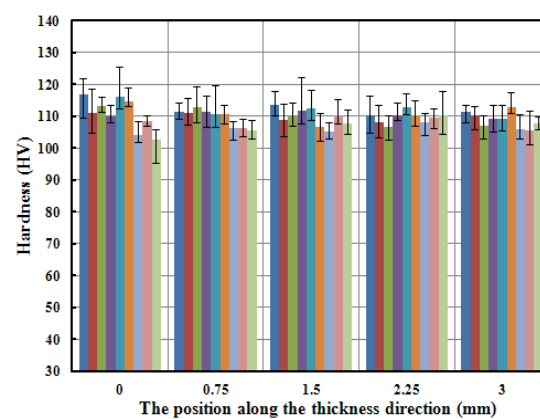
(a) Dry, 19.2 m/min



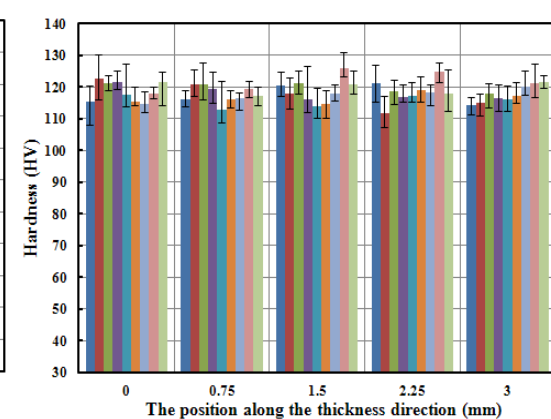
(e) Cryogenic, 19.2 m/min



(b) Dry, 24 m/min

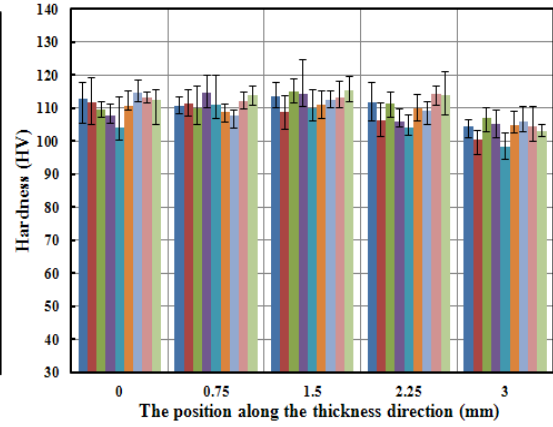
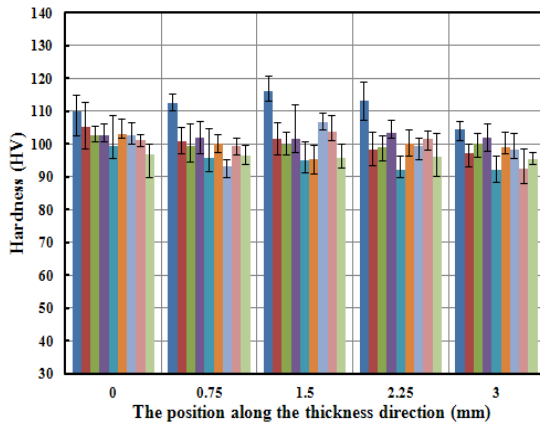


(f) Cryogenic, 24 m/min



(c) Dry, 28.8 m/min

(g) Cryogenic, 28.8 m/min



(d) Dry, 48 m/min

(h) Cryogenic, 48 m/min

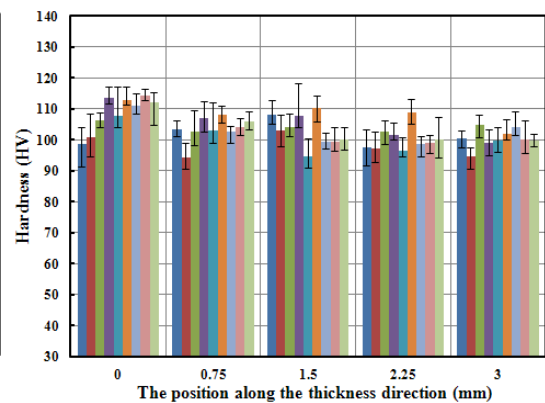
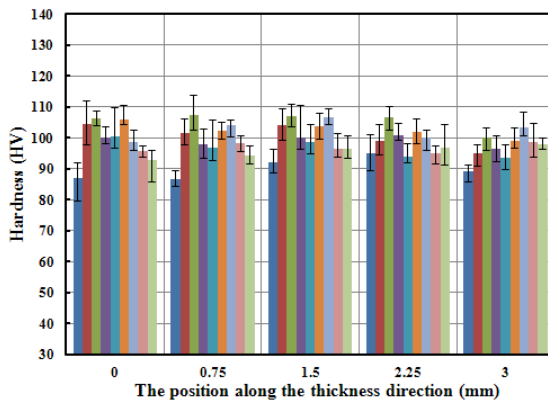
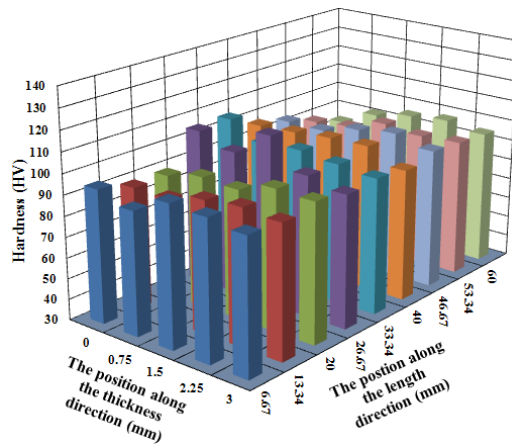
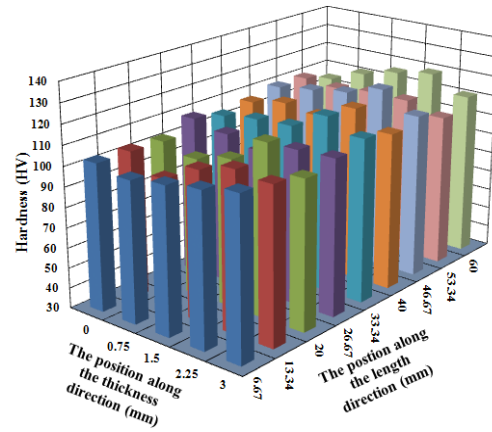


Figure 3.16: Detailed hardness distributions among the samples processed by dry and cryogenic FSP at four different rotational speeds of 19.2, 24, 28.8, and 48 m/min: (a) dry, 19.2 m/min; (b) dry, 24 m/min; (c) dry, 28.8 m/min; (d) dry, 48 m/min; (e) cryogenic, 19.2 m/min; (f) cryogenic, 24 m/min; (g) cryogenic, 28.8 m/min; and (h) cryogenic, 48 m/min.

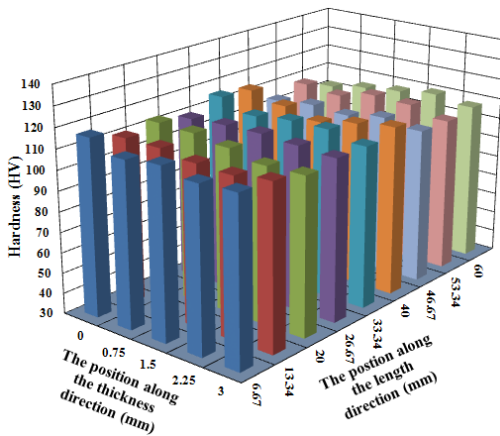
(a) Dry, 19.2 m/min



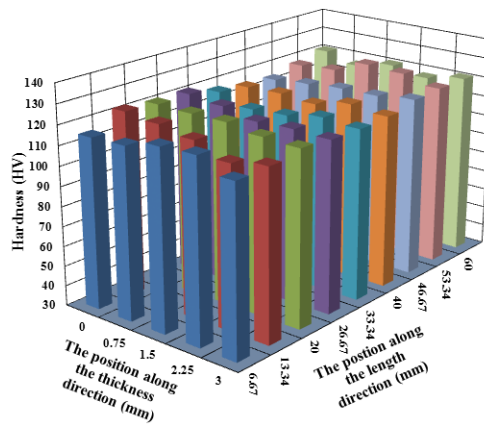
(e) Cryogenic, 19.2 m/min



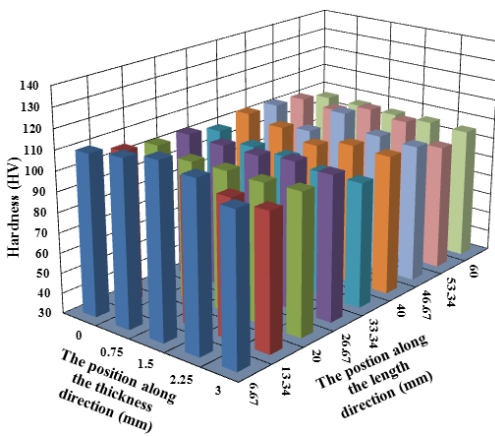
(b) Dry, 24 m/min



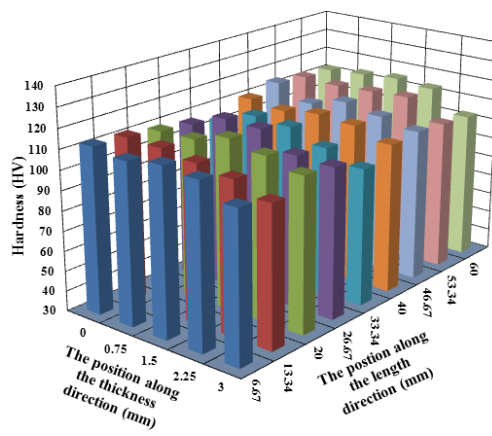
(f) Cryogenic, 24 m/min



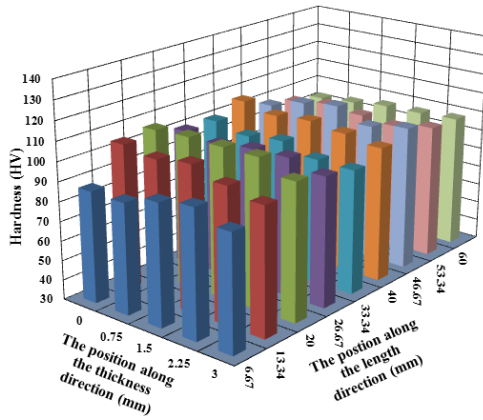
(c) Dry, 28.8 m/min



(g) Cryogenic, 28.8 m/min



(d) Dry, 48 m/min



(h) Cryogenic, 48 m/min

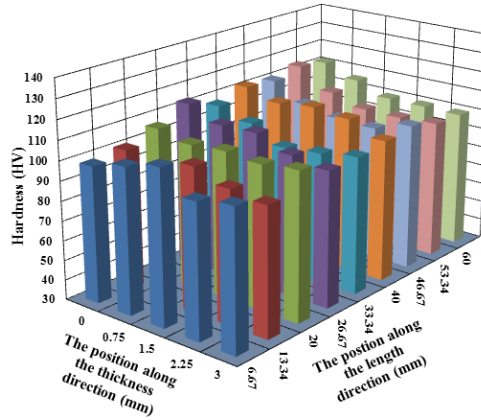


Figure 3.17: Hardness distributions among the samples processed by dry and cryogenic FSP at four different rotational speeds of 19.2, 24, 28.8, and 48 m/min: (a) dry, 19.2 m/min; (b) dry, 24 m/min; (c) dry, 28.8 m/min; (d) dry, 48 m/min; (e) cryogenic, 19.2 m/min; (f) cryogenic, 24 m/min; (g) cryogenic, 28.8 m/min; and (h) cryogenic, 48 m/min.

By means of hardness measurement to analyze the homogenization, the material processed by dry and cryogenic FSP using double-sided processing, turned to be much more consistent from the perspective of hardness when compared with the as-received *Al 7050-T7451* alloy with coarse grains and relatively inconsistent hardness. Figure 3.18 shows the average values of microhardness at four different speeds for dry and cryogenic FSP.

The highest hardness value could be achieved when the rotational speed was 24 m/min for both dry and cryogenic FSP, compared with other FSP conditions, because relatively optimal results could be achieved where the highest volume fraction of re-precipitated precipitates might be existing, corresponding to the specific temperature achieved by FSP with the selection of the rotational speed of 24 m/min.

In the case where a lower speed was chosen, the precipitates were dissolved and coarsened, and very few re-precipitates could be generated due to the lower temperature. Whereas in the circumstance when a higher speed was selected, the higher temperature would dissolve the newly formed re-precipitated precipitates and the former precipitates. Thus, the optimum volume fraction of re-precipitated precipitates was achieved when a medium speed was chosen. It explains the reason why a hardness peak exists among certain FSP conditions.

In details, the temperature reached during FSP increased when the rotational speed was faster, thus one part of η' precipitates dissolves, and the other part transforms into coarser η precipitates during the short time of each pass of FSP within around 15 seconds. The hardness increased when the speed was changed from 19.2 to 24 m/min as more η precipitates transformed from η' precipitates, because the temperature was not high enough to dissolve both precipitates. The temperature reached during FSP started to dissolve η precipitates, as well as when the speed was selected at about 24 m/min. After this point, the hardness decreased due to the dissolution of both η' and η precipitates. It is worth noting that cryogenic FSP could improve the hardness by approximately 10%, compared with dry condition since a lower temperature was reached and less precipitates are dissolved.

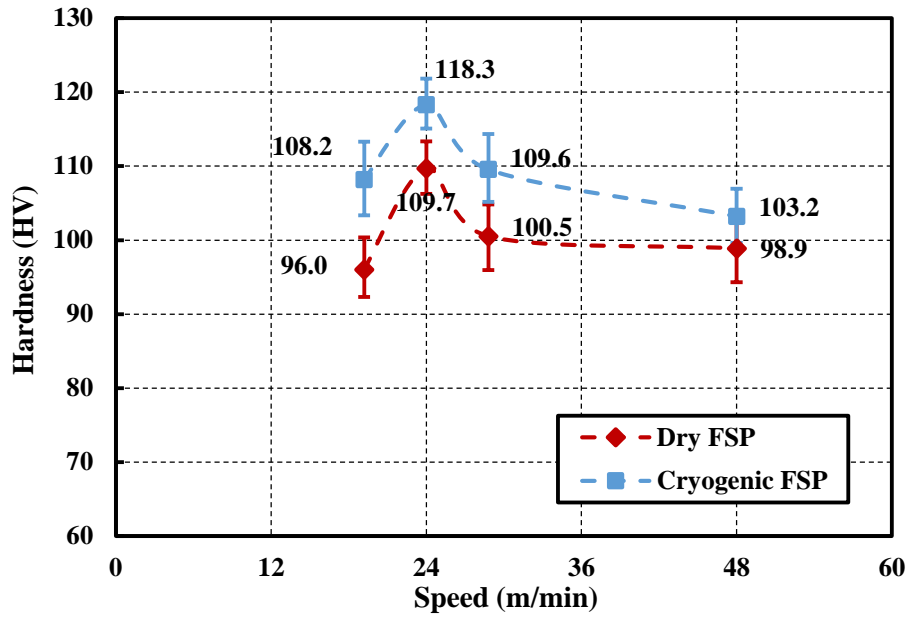


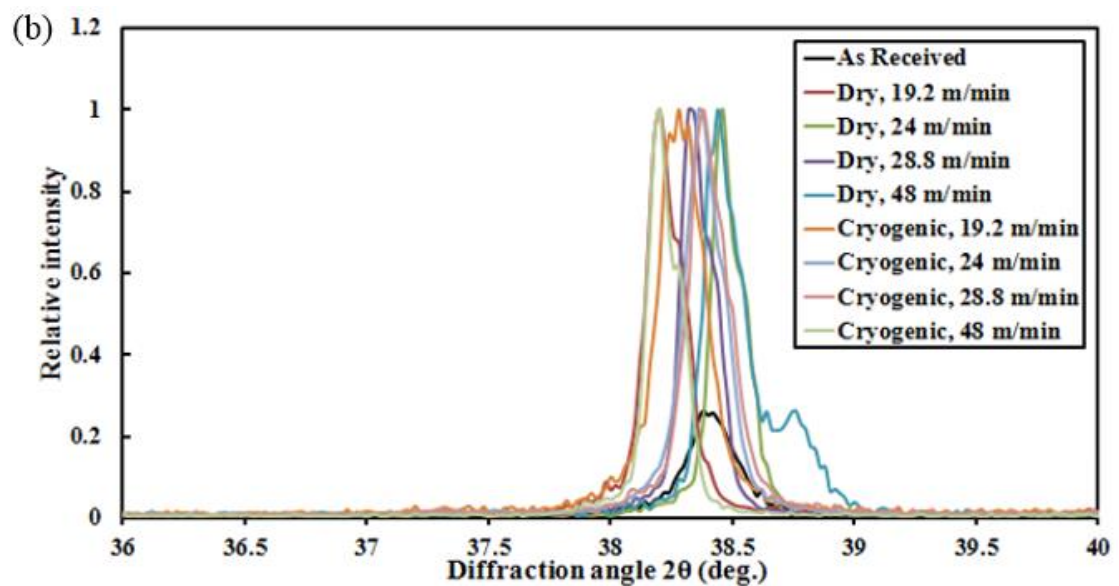
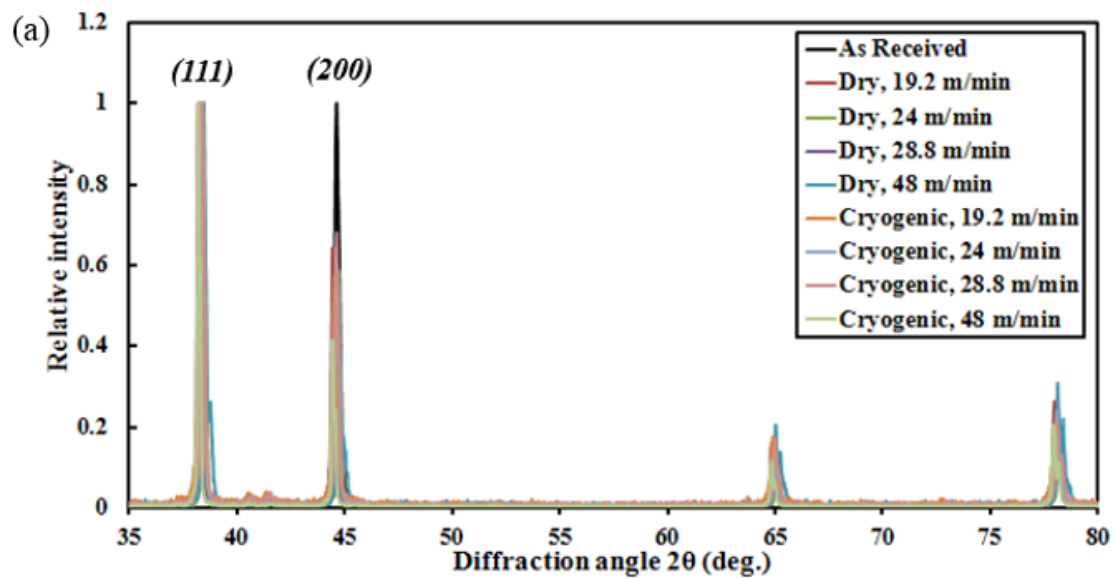
Figure 3.18: Hardness variation in dry and cryogenic FSP at four different speeds.

3.3.3 XRD measurements

XRD measurements have been made for all the eight conditions of dry and cryogenic FSP. It is known that *Al 7050-T7451* alloy is one of the high-strength *Al-Zn-Mg-Cu* alloys, and face centered cubic (FCC) structure is the primary crystal structure of the element aluminum. In the XRD patterns, the relative intensity of atomic plane *Al (111)* could be seen through the peak between 38° to 40° , whereas the atomic plane *Al (200)* could be observed between 41° to 43° (Zhao et al., 2005).

Observed from Figure 3.19, the relative intensities of *Al (111)* were found to become larger while the counterparts of *Al (200)* became smaller in all eight FSP conditions. Therefore, the texture change from *Al (200)* to *Al (111)* was very obviously found from all eight FSP conditions in contrast to the bulk material. *Al (111)* has been considered to be the most densely packed plane in the FCC-based aluminum alloys, and it exhibited

the lowest surface energy, which made it more preferable in the applications using interfaces between metals and ceramics, such as heterogeneous catalysis, microelectronics, thermal barriers and corrosion protection (Siegel et al., 2002). Thus, FSP could play an important role to broaden the applications of *Al 7050-T7451* alloy by means of texture change.



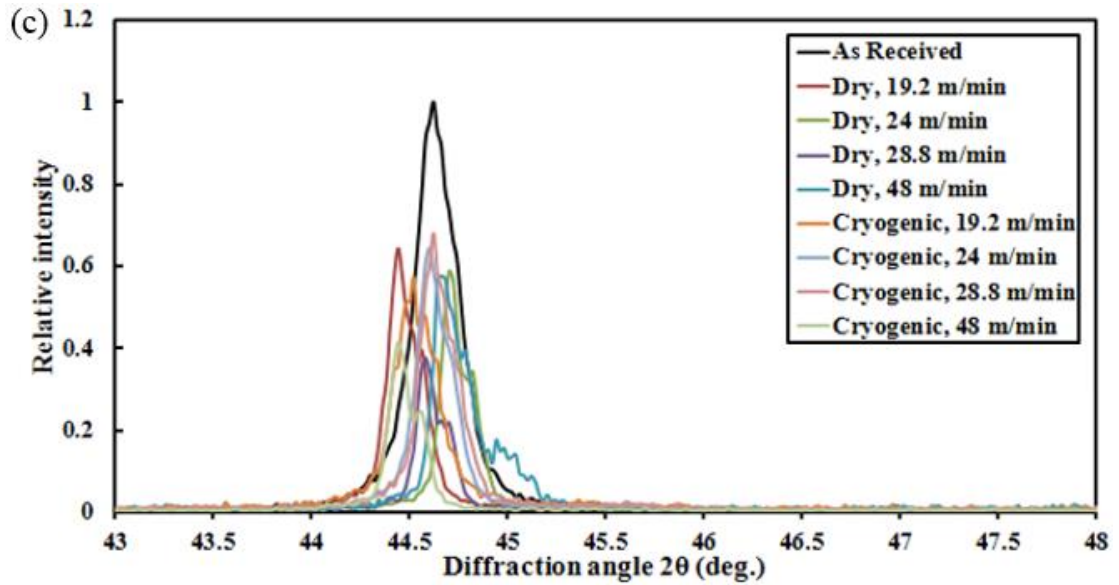


Figure 3.19: (a) XRD plot ranging from 35° to 80° ; (b) XRD distribution of $Al(111)$; and (c) XRD distribution of $Al(200)$.

3.4 Chapter conclusion

Dry and cryogenic FSP were performed to refine the microstructures of as-received $Al\ 7050-T7451$ alloys with coarse grains. Surface integrity characteristics were analyzed in order to investigate the effects of FSP in terms of rotational speed and cooling condition. The major findings observed from the FSP experiments are as follows:

- Equiaxed smaller grains with the grain size of $2-3\ \mu\text{m}$ were obtained in most of the processing conditions by dry and cryogenic FSP when four different rotational speeds were used.
- Homogeneous microstructures were produced by both dry and cryogenic FSP, whereas cryogenic FSP resulted in more uniform microstructure compared with dry FSP due to the efficient cooling effect suppressing the grain growth after DRX.
- Attributing to the thermal softening effect induced by FSP, a decreasing trend of

hardness was found in both dry and cryogenic FSP, compared with the bulk hardness of the as-received materials.

- Approximately 10% increase in hardness was measured from cryogenic FSPed samples, in comparison with dry FSP.
- The texture change from *Al (200)* to *Al (111)* demonstrates that FSP was a potential methodology to broaden the application of *Al 7050-T7451* alloys, due to better properties of *Al (111)* with the most densely packed plane of FCC-based aluminum alloys exhibiting lower surface energy.

In conclusion, the aforementioned observations from the experiments prove that FSP can remarkably modify the microstructures with uniform grain size and hardness, especially through cryogenic FSP. Near UFG-structure materials are obtained in this study, and it provides the foundation for the following investigations of cryogenic machining and burnishing as FSP cannot be used as the final process of the manufactured components. Further machining and burnishing effects will be studied in order to achieve more accurate dimensions and better surface integrity properties. Near UFG-structure materials are achieved, and samples were prepared for the subsequent investigations of machining and burnishing processes.

CHAPTER 4

IMPROVED SURFACE INTEGRITY FROM CRYOGENIC MACHINING OF *Al 7050-T7451* ALLOY WITH NEAR-UFG STRUCTURE

4.1 Introduction

Surface integrity induced by machining describes the mechanical, metallurgical and chemical states of the surface and sub-surface properties of the machined components. Therefore, it plays a significant role and has critical influence on their functional performance, concerning surface finish, microstructure, grain size, microhardness, residual stress, etc., in the machined surface and sub-surface (Jawahir et al., 2011). And, it also affects fatigue life, wear and corrosion resistance of manufactured components (M'Saoubi et al., 2008). Processes resulting in severe plastic deformation, such as low plasticity burnishing (LPB), surface mechanical attrition treatment (SMAT), are beneficial to improve the surface integrity of the components.

As a SPD process, machining inducing large plastic strain and strain-rate was considered to be an effective methodology to cause grain refinement on the machined surface (Guo et al., 2011). Cryogenic machining was reported to generate machined surface layer which enhanced corrosion resistance and increased microhardness in magnesium alloy *AZ31*. And, the residual stresses on the machined surface layer became more compressive using liquid nitrogen as the coolant compared with dry machining condition (Pu et al., 2012). Thermal and mechanical aspects such as temperature, machined surface, hardness modification, microstructure of *AISI 52100* were shown to be significantly influenced by cryogenic machining. White layer

thickness was limited on the machined surface as a result of the lower temperature achieved by cryogenic cooling that restricted or prevented martensitic phase change (Umbrello et al., 2012). Therefore, surface integrity improvement can be achieved from machining, especially under cryogenic conditions.

Friction stir processing as one of the SPD processes was applied to produce UFG materials by which both the mechanical and material properties could be improved. Using the method of FSP, hardness and wear resistance of the produced surface composite layer was found to be much better than the ones of as-received *Al* material (Shafiei-Zarghani et al., 2011). It was demonstrated that the phase transformation of *AISI 1080* steel from pearlite to martensite state was achieved by FSP and the microhardness of the 5 mm surface layer was increased to 7 GPa from the previous 3 GPa of as-received material, while significant reduction in wear rate was observed from FSPed samples under oil lubrication (Aldajah et al., 2009). Moreover, greater corrosion resistance was exhibited when FSPed *NiAl* bronze materials were immersed in the 3.5% *NaCl* solution in static immersion corrosion test compared with the cast counterpart with coarse grains and defects (Ni et al., 2010). Researchers also investigated the effect of FSP on the corrosion resistance of *Al 2219* alloy, and they found that FSPed samples had superior corrosion resistance, compared to the base metal (Surekha et al., 2008).

However, FSP as one of the SPD processes will not be the final process for the products as the requirements of dimensional accuracy and free form configurations for certain products need to be satisfied due to their specific working functions. Further machining is the critical process to form and shape bulk UFG materials for the commercial

applications in order to produce dimensionally-precise and free form geometric parts (Brandão et al., 2008; Coelho et al., 2010). Nonetheless, through literature review, it is apparent that there is no systematic study showing the effect of machining process on the final surface integrity characteristics of components processed by FSP.

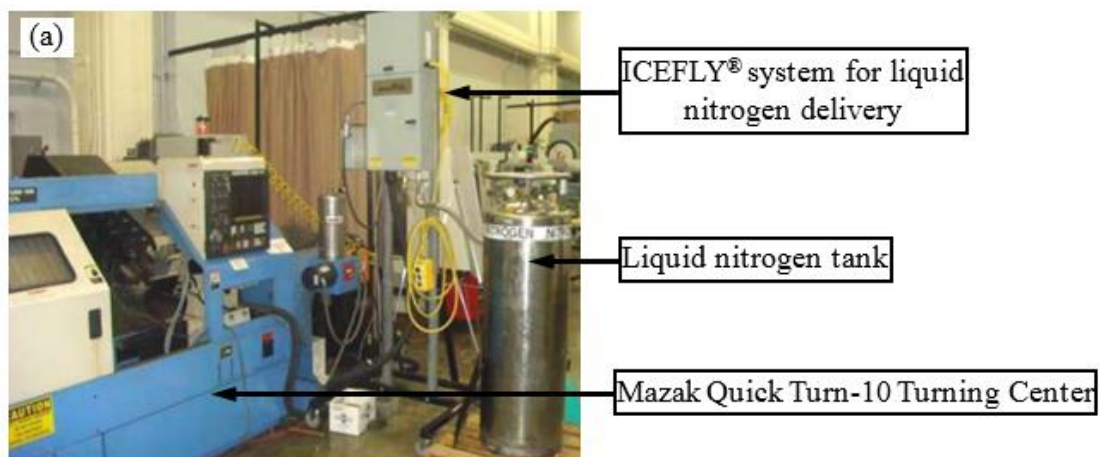
The research presented in this chapter is to focus on cryogenic machining of *Al 7050-T7451* alloys with near UFG structure obtained by FSP. Double-sided FSP has been performed to produce UFG materials with homogeneous microstructure and hardness. Surface integrity characteristics, resulting from dry and cryogenic machining, such as microstructure, grain size, and hardness of machined samples, were investigated in the study. In addition, the analysis of cutting forces, cutting temperature, and chip morphology was also done in this experimental study.

4.2 Experimental work

The work materials used in the experiments were *Al 7050-T7451* alloy with near UFG structure produced by FSP. Flat plates/sheets with 3.2 mm-thickness were processed by double-sided FSP (rotational speed of the FSP tool was 19.2 m/min and the feed rate was 101.6 mm/min under dry condition), and then cut into discs with about 65 mm-diameter by vertical milling. The average grain size of the processed disc was approximately 1.82 μm , and the hardness after FSP was 92.6 HV in Vickers before the machining process. Each disc was fixed on a specially-designed work-holding mandrel using three bolts, and orthogonal machining was performed on a Mazak Quick Turn-10 Turning Center. Figure 4.1 illustrates the experimental setup for cryogenic

machining of *Al 7050-T7451* discs with near-UFG structure. The tool insert used in the study was an uncoated carbide insert, TPG 432 with the grade K313 provided by Kennametal, whose cutting edge radius was approximately 16 μm . Tool holder CTCPN 644 manufactured by Kennametal was attached with Kistler 9121 three-component dynamometer used to measure the cutting forces. The effective rake and clearance angles of the cutting tool were 3° and 11° , respectively. As shown in Table 4.1 of the experimental matrix, cutting speeds used in the experiments were 50, 100, 200 and 300 m/min, and the feed rate was 0.1 mm/rev, and was kept constant.

The surface integrity measurements involved the same equipment and methodologies mentioned in the section of experimental work of Chapter 3, for obtaining the output parameters, including microstructure, hardness, grain size etc. In addition, a FLIR thermal imaging system/camera was used to measure the cutting temperatures of *Al 7050-T7451* discs with near-UFG structure in dry and cryogenic machining.



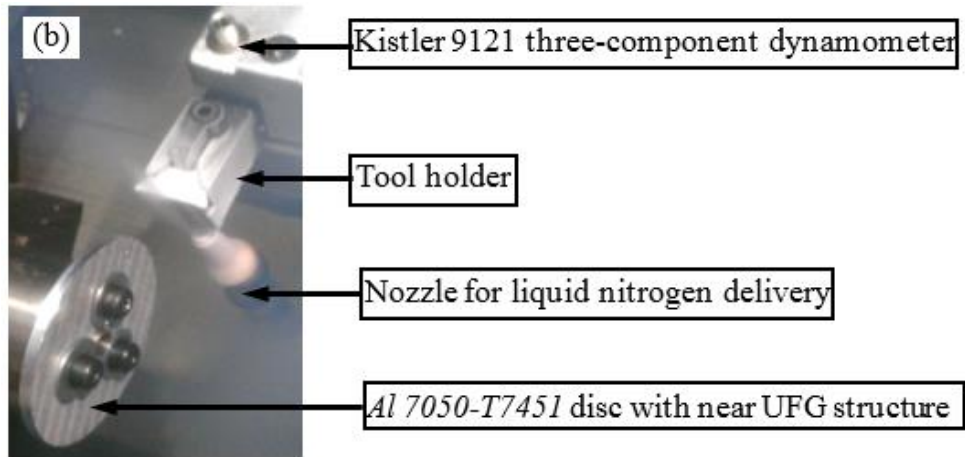


Figure 4.1: Experimental setup: (a) Mazak Quick Turn-10 Turning Center and cryogenic coolant delivery system; and (b) detailed illustration of cryogenic machining of *Al 7050-T7451* disc with near-UFG structure.

Table 4.1: Experimental matrix regarding machining of *Al 7050-T7451* alloys with near-UFG structure.

Cooling method	Cutting speed (m/min)	Feed rate (mm/rev)
Dry	50	0.1
Dry	100	0.1
Dry	200	0.1
Dry	300	0.1
Cryogenic	50	0.1
Cryogenic	100	0.1
Cryogenic	200	0.1
Cryogenic	300	0.1

4.3 Experimental results and discussion

4.3.1 Cutting force components

As shown in Figure 4.2, the cutting and thrust force components were very consistent under all the machining conditions for dry and cryogenic machining. The average

cutting force was about 250 N, and similar results were found in the papers for machining of *Al 7050* alloys (Fu et al., 2010a; Tang et al., 2009). From the perspective of cutting forces, there is no big difference between machining materials with coarse grains and materials with near-UFG structure (Morehead et al., 2007). The cutting /thrust force ratio was observed to be smaller than the common cases, usually thrust force would be smaller than cutting forces for orthogonal machining of aluminum alloys (Fang and Wu, 2005).

Due to grain refinement caused by FSP, the equiaxed grains distributed in *Al 7050-T7451* with near-UFG structure, as will be seen in later section, whereas the elongated and coarse grains spread along the rolling direction for the initial as-received materials. Hence, cutting and thrust force components had very close values because of the more homogeneous structure that existed in the FSPed *Al 7050-T7451* materials.

Liquid nitrogen delivered from the clearance side of the tool insert did not impact the forces in cryogenic machining, and it depended more on the material properties modified by FSP. As the cutting speed increases from 100 m/min to 300 m/min, the force components slightly reduced, and this was due to the increasing temperature discussed in the following section and the increased thermal softening effect correspondingly.

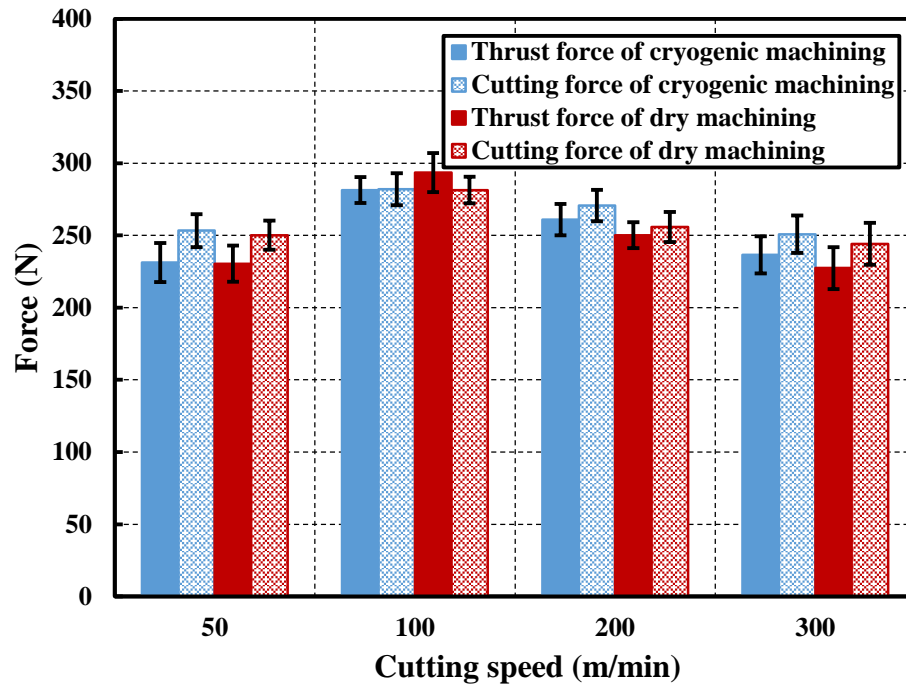


Figure 4.2: The cutting and thrust force components measured from the experiments of dry and cryogenic machining of *Al 7050-T7451* alloys with near-UFG structure.

4.3.2 Cutting temperature

In order to acquire more accurate temperature measurements, the emissivity was determined by the literature review of previous work performed in machining of aluminum alloys, and through careful reading of the manual of the infrared camera, as it is one of the most important factors influencing the accuracy of infrared camera. The emissivity of both materials, *Al 7050* and *Al 7075* alloys, were considered to be the options for the setup of infrared camera as they were both 7xxx series aluminum alloys and had similar material properties.

The range within 0.05 to 0.2 was found to be reasonable for these two aluminum alloys (Fang et al., 2009; Wen et al., 2004; Strasik et al., 2010), and through calibration and comparison with the similar temperature measurements with respect to machining of

Al 7050 alloy (Fu et al., 2010a; Tang et al., 2009; Sandstrom and Hodowany, 1998; Zhou et al., 2010b), the value of 0.09 was selected as the emissivity in this study, and this was also the recommendation from the manual of FLIR infrared camera. As shown in Figure 4.3, the area where the highest temperature was located on the disc was near the work material-tool contact area denoted by the white rectangular box, and the software associated with the infrared camera provided the temperature distribution with the exact value of the highest temperature.

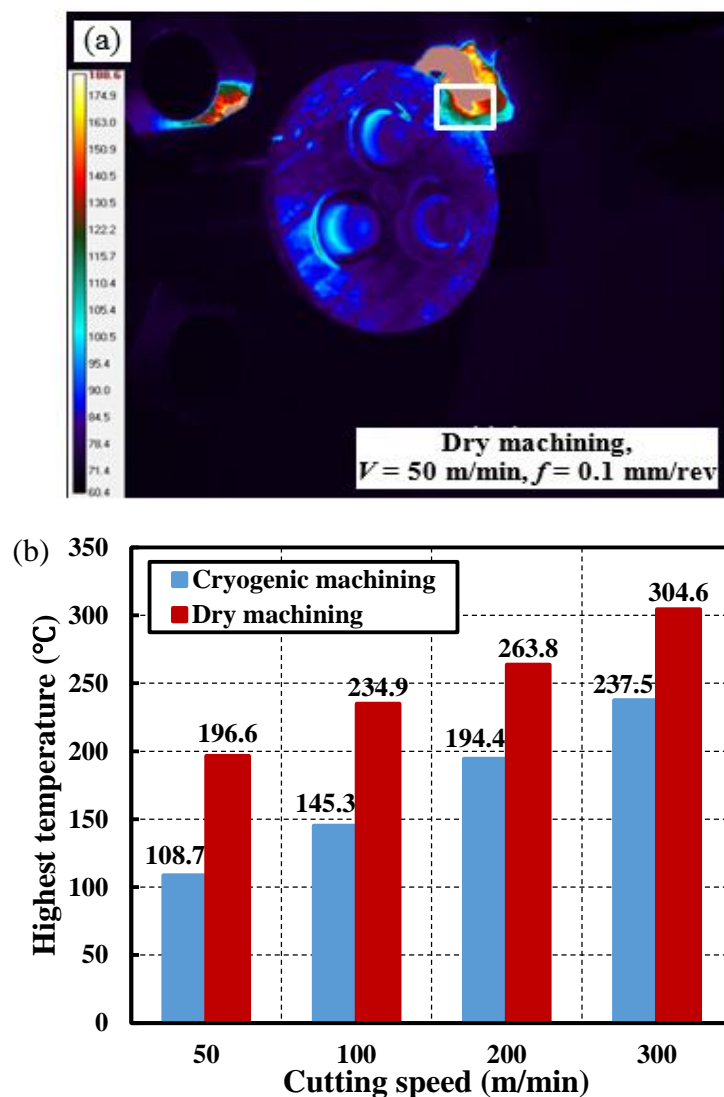


Figure 4.3: (a) Image example of temperature distribution obtained by infrared camera; and (b) Highest temperature achieved in dry and cryogenic machining in the work material-tool contact area.

An increasing trend of high cutting temperature is seen when increasing the cutting speed, for both dry and cryogenic machining. Compared with dry machining, the highest temperature was decreased by 44.7%, 38.1%, 26.3% and 22.0%, respectively for cryogenic machining. As the flow rate was kept constant, the cooling effect became progressively less effective at higher cutting speeds during the machining experiments because more heat was generated in these situations. Similar results were previously reported with the highest temperature being reduced by approximately 60% when using liquid nitrogen as coolant while machining magnesium alloys (Pu, 2012). When turning *Ti-6Al-4V* alloy with liquid nitrogen as the coolant, the temperature of the machined surface was also shown to be reduced to 440 °C from 880 °C in dry machining, with an effective 50% reduction (Hong et al., 2001b).

4.3.3 Microstructure

The microstructures of the machined surface and subsurface are shown in Figure 4.4, comparing the differences between dry and cryogenic machining effects at four cutting speeds. As seen from the figure, grain refinement occurred in the machined surface for the cryogenic machining, especially at the cutting speeds 50 and 100 m/min, while in dry machining, only a slight grain refinement is seen, and however, it was not obvious for the conditions with the higher cutting speed at 300 m/min. Detailed distributions of grain size in the machined surface and subsurface are presented in Figure 4.5, where the total depth considered in the study was 100 µm from the machined surface and it was evenly divided into four zones where the average grain size was measured and calculated by using average grain intercept method.

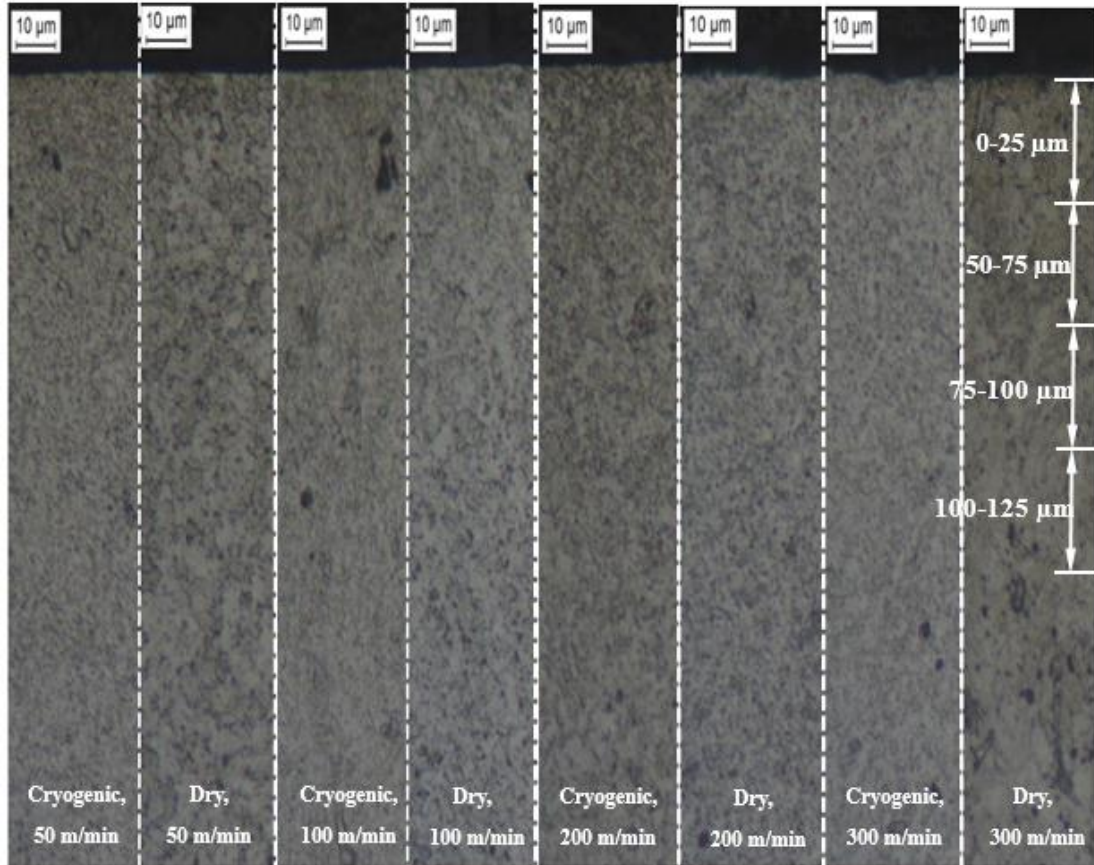


Figure 4.4: Microstructures of the machined surface layers produced by dry and cryogenic machining of *Al 7050-7451* alloys with near-UFG structure at four different cutting speeds: 50, 100, 200 and 300 m/min.

Dynamic recrystallization took place in the machined surface, while strain-rate and temperature met the requirement to explain the phenomenon of grain refinement. Zener-Hollomon parameter $Z = \dot{\epsilon} \exp(Q/RT)$ was introduced for the deformation behavior of *Al 7050* alloy (Deng et al., 2011; Lu et al., 2008), where $\dot{\epsilon}$, Q , R and T represent strain-rate, activation energy of lattice diffusion of the material, gas constant and the local temperature, respectively. Combined with the equation $d = d_0 \cdot \alpha \cdot Z^m$ (Yang, 2012), the grain size achieved from DRX could be calculated, in which d_0 , α and m represent the initial grain size of the bulk materials and two material constants separately. After DRX, recrystallized grains began to grow due to the heat generated

during the machining process. Liquid nitrogen applied in the cryogenic machining experiments could slow down or suppress the grain growth (Yang et al., 2012; Pu et al., 2012; Yang, 2012), thus it explains the reason why smaller grain size could be achieved by cryogenic machining in the machined surface compared with dry machining.

Higher temperature caused by higher cutting speed is shown in Figure 4.3, and this means that more heat would be absorbed by the recrystallized grains in such circumstances. Therefore, the grain size was larger when a higher cutting speed was used in dry machining. However, the grain size from cryogenic machining was very consistent due to the cryogenic cooling effect. Smaller grain size could be obtained in the machined surface layer at the depth within 0-25 μm and 25-50 μm for cryogenic machining when cutting speeds of 50 and 100 m/min were chosen, respectively. Because of the previous grain refinement induced by FSP, the initial grain size of *Al 7050-T7451* plate was reduced to 1.82 μm from the very coarse grains in the elongated direction of the as-received sheet. The following machining process did not introduce obvious grain refinement in the machined surface in contrast to FSP, particularly for the case of dry machining. DRX occurred in the machined surface from cryogenic machining. The grain growth brought the grains back to their previous size after absorbing the heat generated by dry machining.

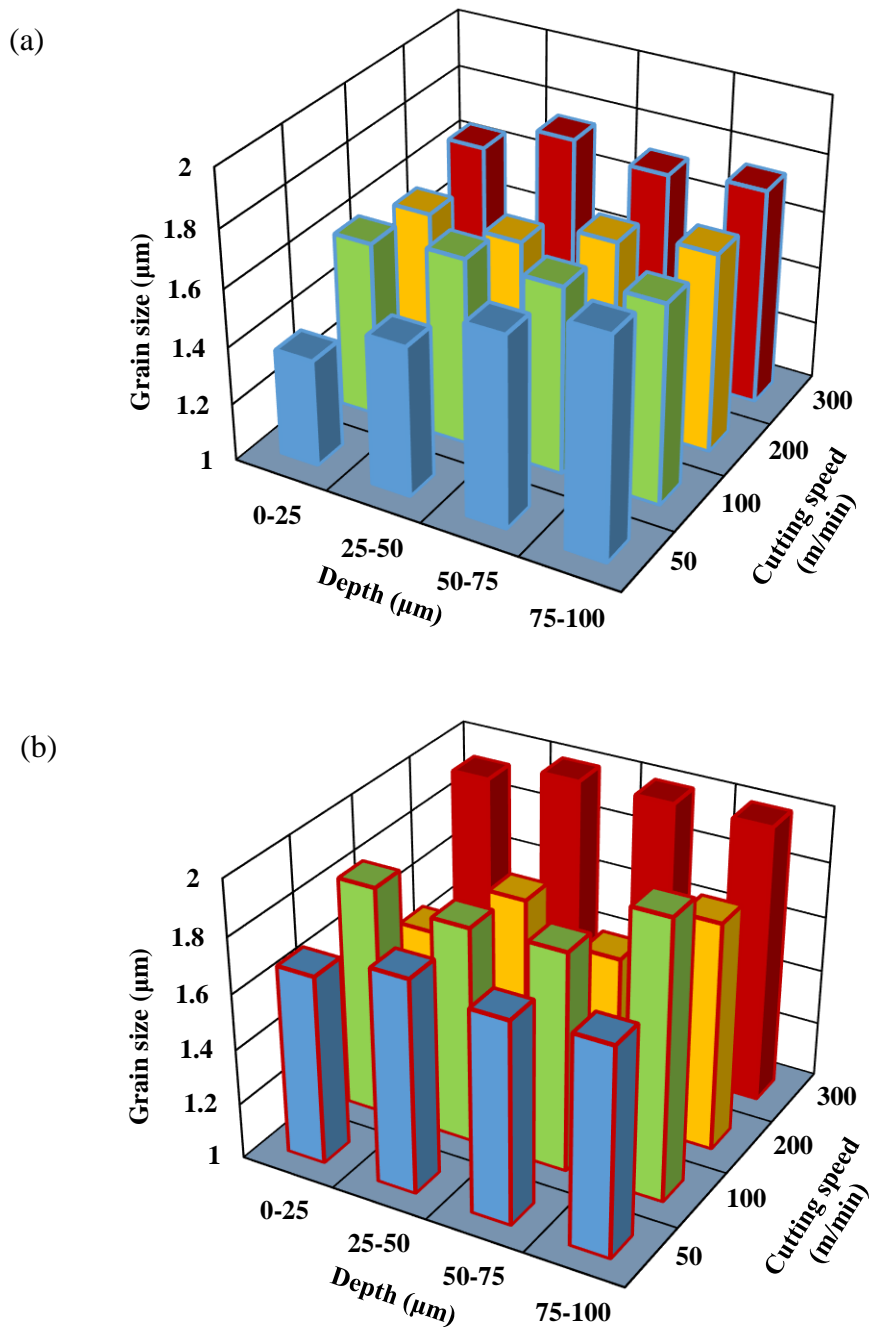
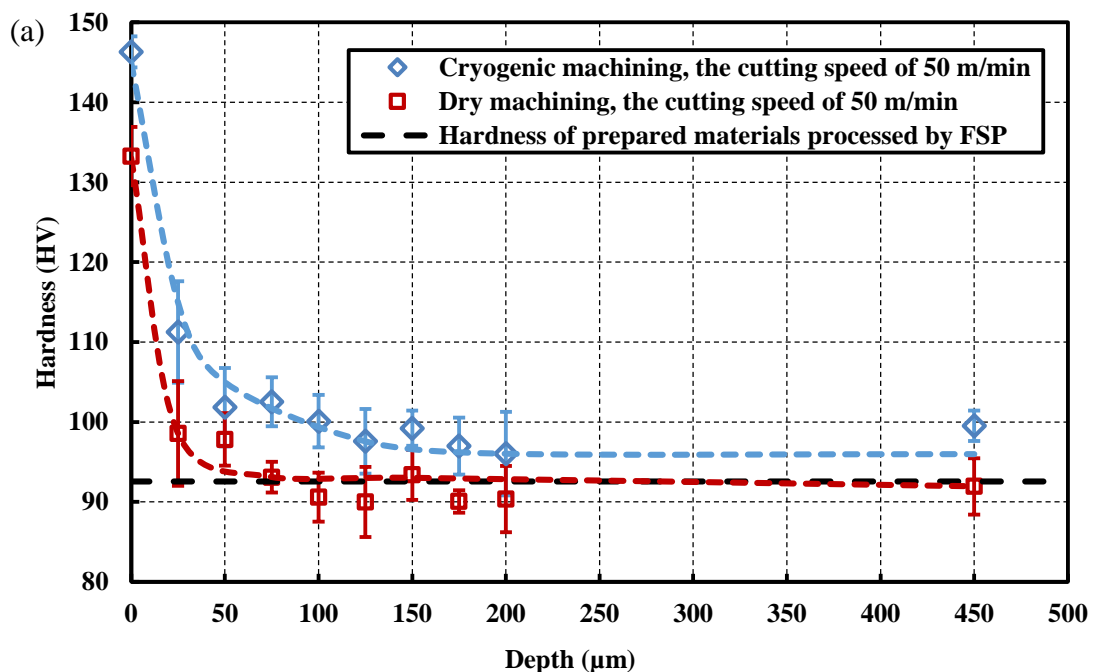


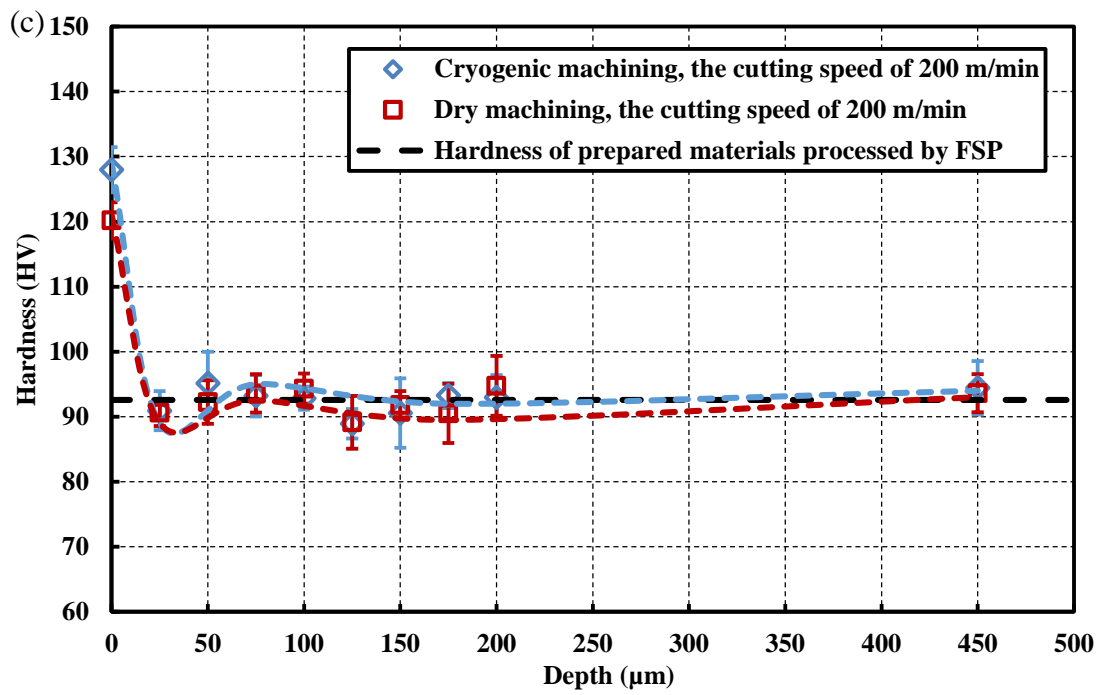
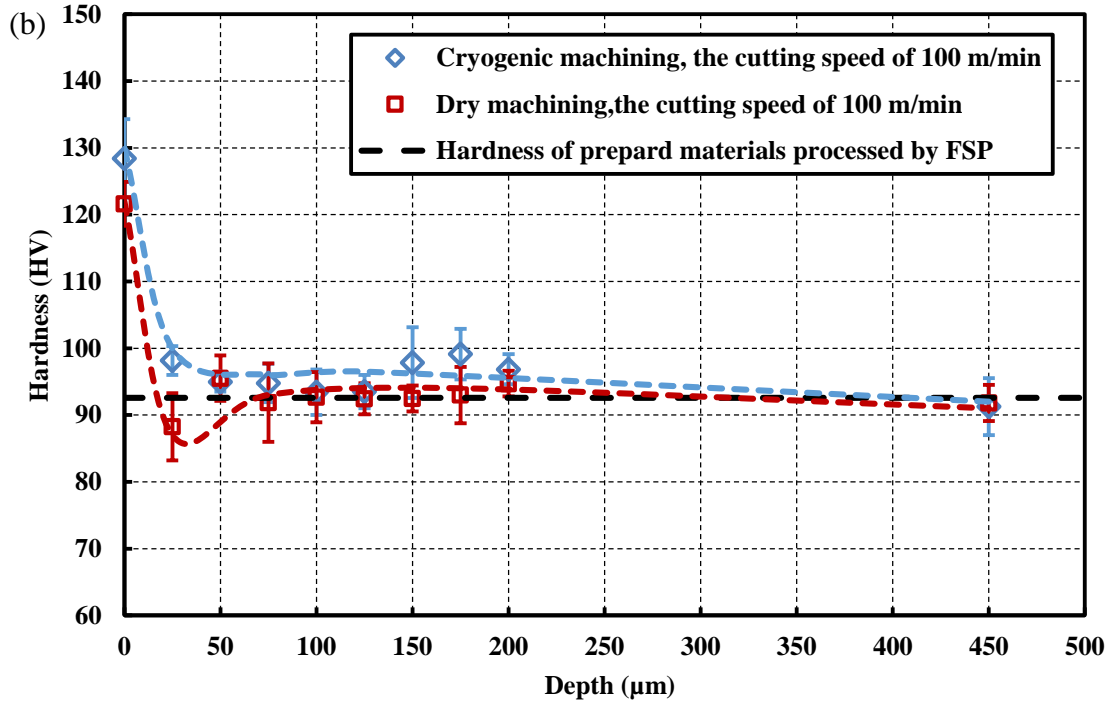
Figure 4.5: Grain size distributions in the machined surface layers from (a) cryogenic, and (b) dry machining of *Al 7050-T7451* alloys with near-UFG structure at four different cutting speeds.

4.3.4 Hardness

The hardness of the machined surface and subsurface layers was measured to see their distributions through the depth within 450 µm range as presented in Figure 4.6. Each

hardness data point presented in this figure, was calculated by averaging five measurements taken, and is within the acceptable upper and lower limits (95% confidence level). The highest hardness found in all eight hardness curves corresponding to the eight different conditions in which four cutting speeds were used in dry and cryogenic machining, was located on the machined surface. For cryogenic machining of *Al 7050-T7451* alloy with near-UFG structure, higher hardness was observed in the machined surface layers compared with dry condition, particularly at 50 and 100 m/min cutting speeds. When approaching the machined surface, hardness enhancement was more pronounced, whereas the hardness was only slightly influenced by the machining effect when the measurement was taken close to the bulk where the depth was over 200 μm .





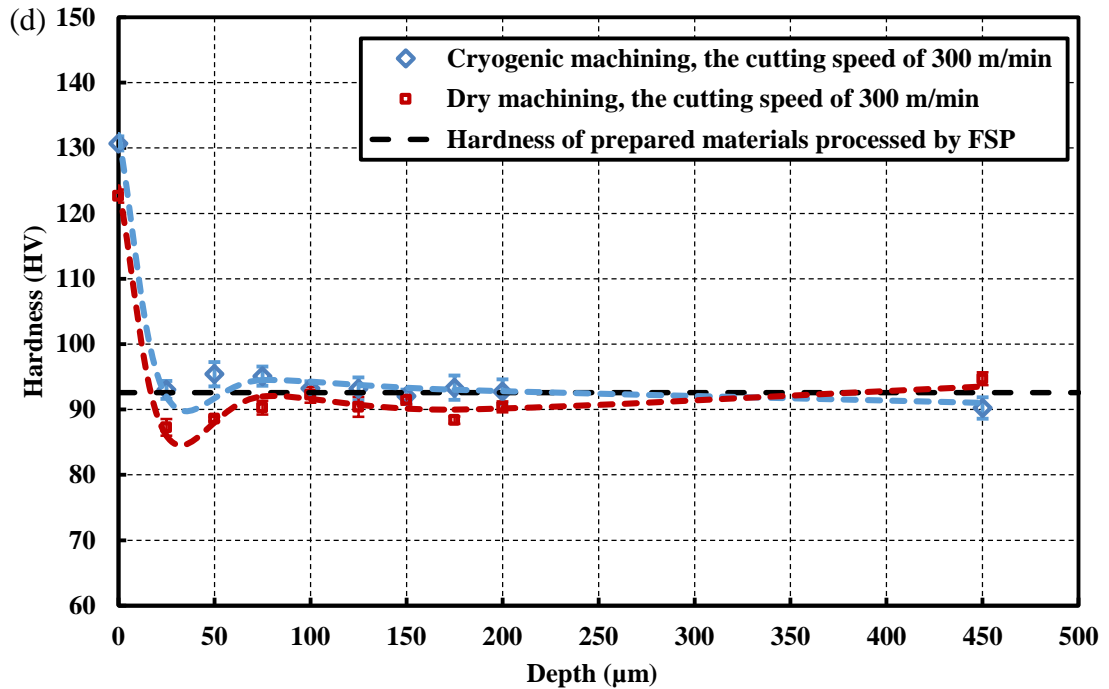


Figure 4.6: Hardness distribution in the machined surface layers with the comparison of dry and cryogenic machining of *Al 7050-T7451* alloy with near-UFG structure: (a) $V = 50$ m/min; (b) $V = 100$ m/min; (c) $V = 200$ m/min; and (d) $V = 300$ m/min.

The hardness obtained when the cutting speeds were 200 and 300 m/min, was not significantly increased, except at the machined surface for both dry and cryogenic machining. The factors influencing hardness variation in this study in dry and cryogenic machining are considered to be grain size, thermal softening and work hardening. The grain size was reduced to $1.82 \mu\text{m}$ by the prior FSP performed in order to achieve near-UFG structure. However, the grain size did not vary too much in different machining conditions, thus it would not be the strong point to explain the hardness variation. Thermal softening effect has been studied, and it was related to coarsening and dissolution of finer precipitates contributing to hardening of the aluminum alloys. It was reported that the dissolution temperature of η' precipitates is between 180°C and 260°C (Mahoney et al., 1998). The dissolution and coarsening of η' precipitates

occurred due to the thermal effect (Su et al., 2003). Based on the temperature measured in the machining experiments as shown in Figure 4.3, higher temperature was reached beyond 180°C for all the four conditions of dry machining on the machined surface. In the case of cryogenic machining, the temperature was also higher than 180°C at higher cutting speeds of 200 and 300 m/min. It is likely that hardness decreased specially in the machined surface layers within the depth of 25 μm due to the thermal softening effect resulting from the dissolution and coarsening of η' precipitates.

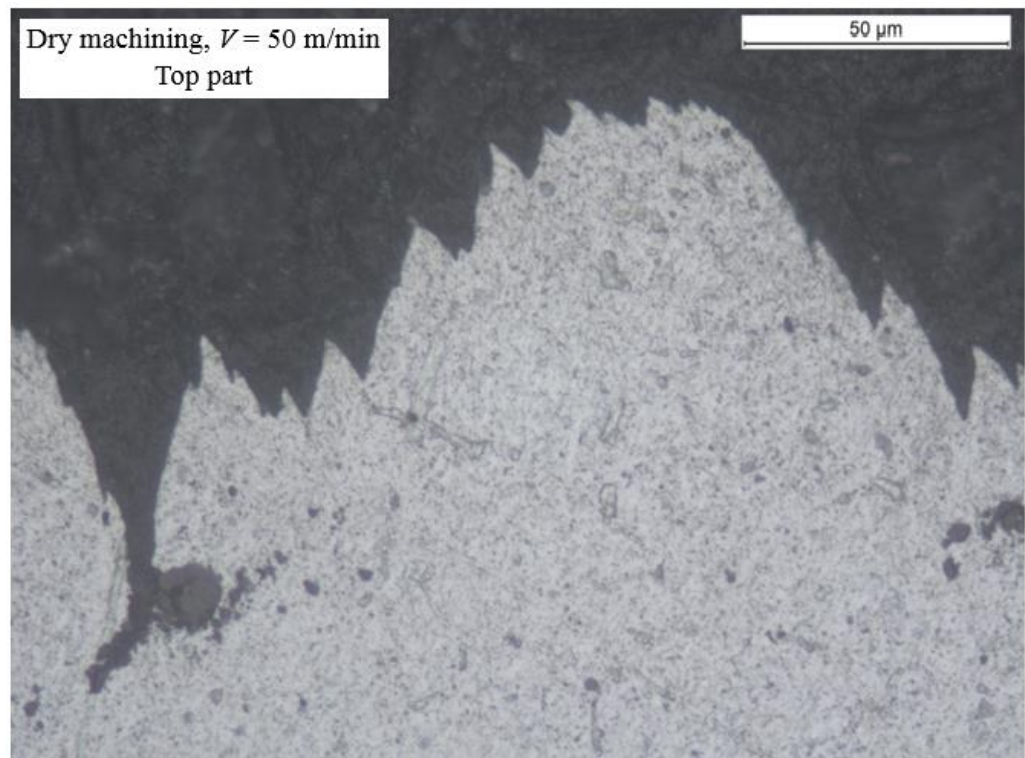
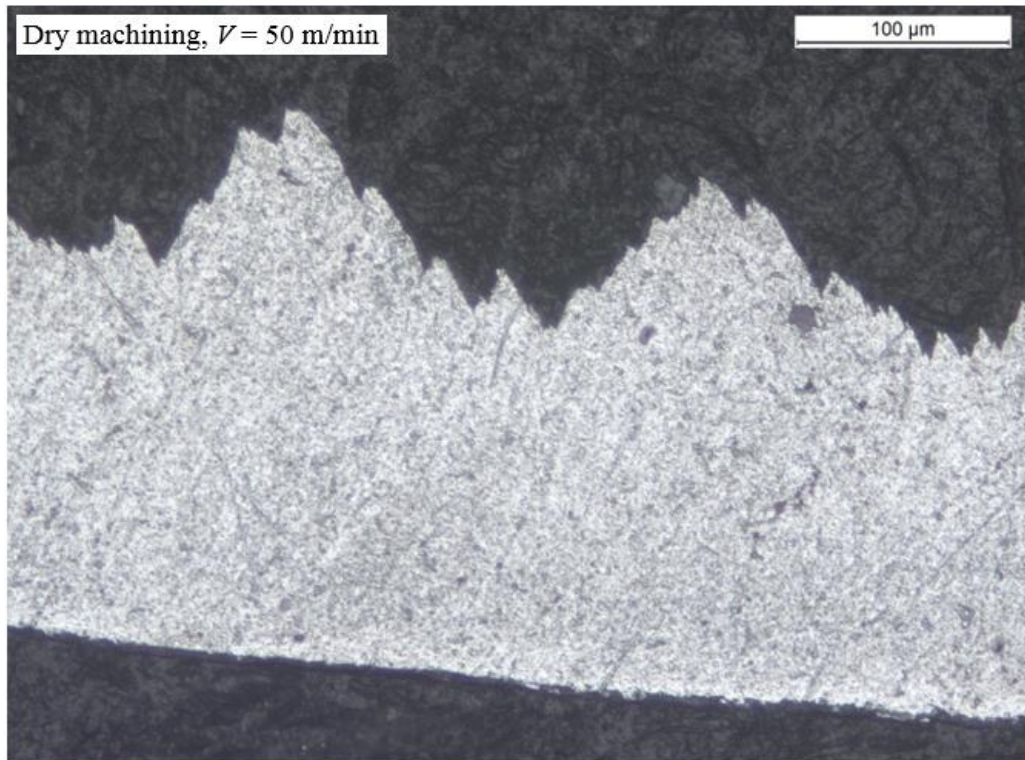
The work hardening effect has to be taken into account to explain the hardness variation. Machining is an effective process to induce high strain ranging from 2 to 10 and high strain-rate up to 10^6 s^{-1} on the machined surface (Guo et al., 2011). Hardness on the machined surface was found to improve because of work hardening effect during machining of magnesium *AZ31* alloy and *Al 7075* alloy (Pu et al., 2012; Rotella et al., 2011). Combining the effects of thermal softening and work hardening need to be understood for a specific material being machined, as the properties vary from one material to another. In the study, close to the machined surface, thermal softening was more dominant in most cases, except for two cases, where 50 and 100 m/min cutting speeds were used in the cryogenic machining. In these two cases, the temperature was lower than 180°C to reduce the thermal softening effect, whereas work hardening was more dominant to make the material harder. For the machined surface layers closer to the bulk material between 100 and 450 μm , thermal softening and work hardening balanced with each other, therefore the hardness was approximately the same as the bulk material. It is worth noting that liquid nitrogen delivered during cryogenic

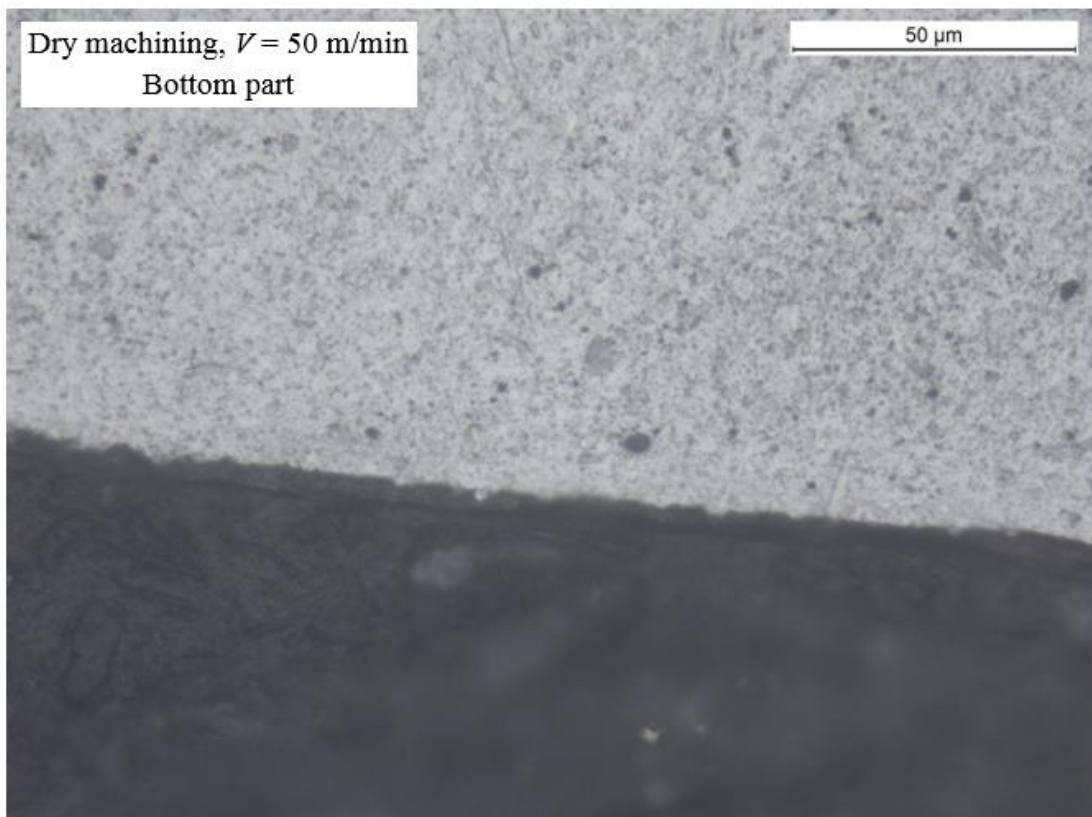
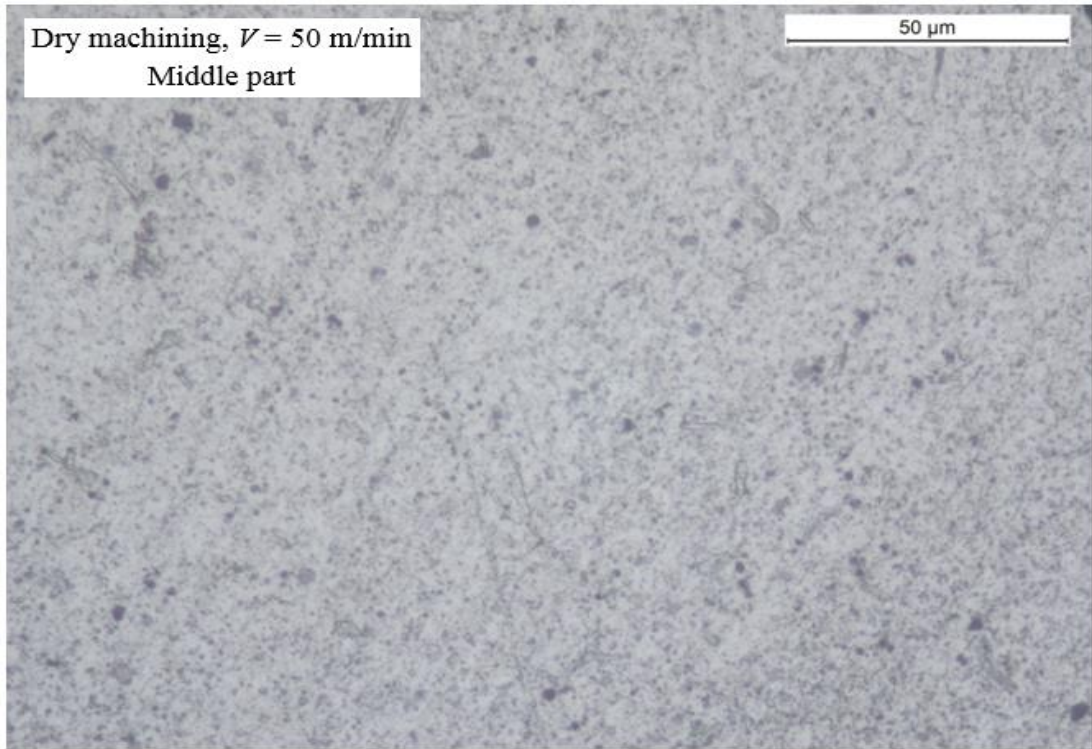
machining effectively lowered the temperature in the machined surface to reduce the effect of thermal softening, and because of this phenomenon, the work hardening effect could improve the hardness in the machined surface at lower cutting speeds in cryogenic machining.

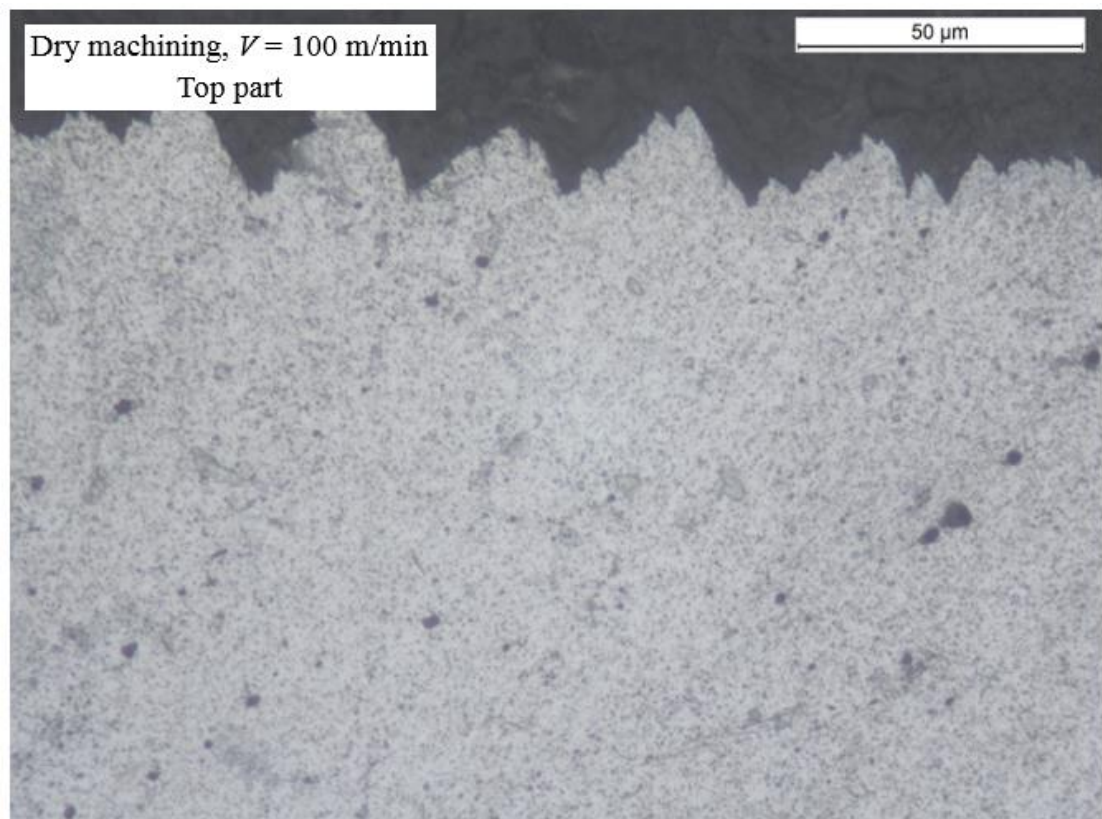
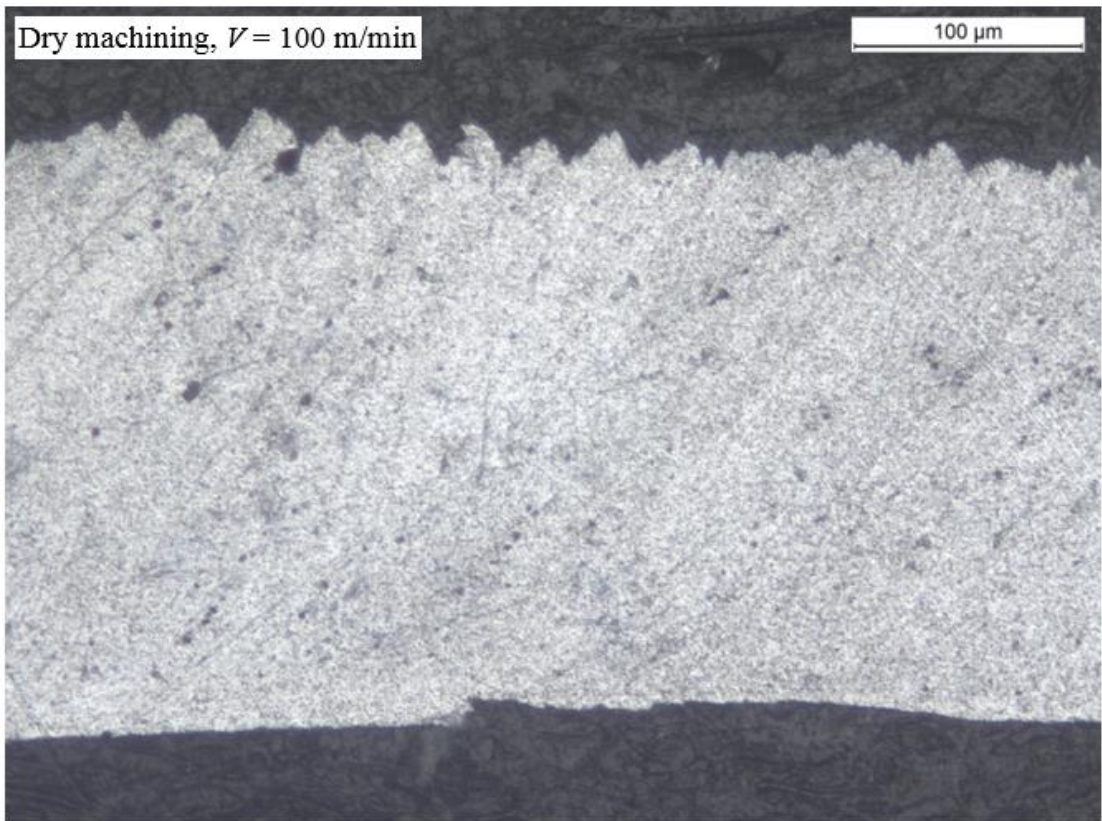
4.3.5 Chip microstructure

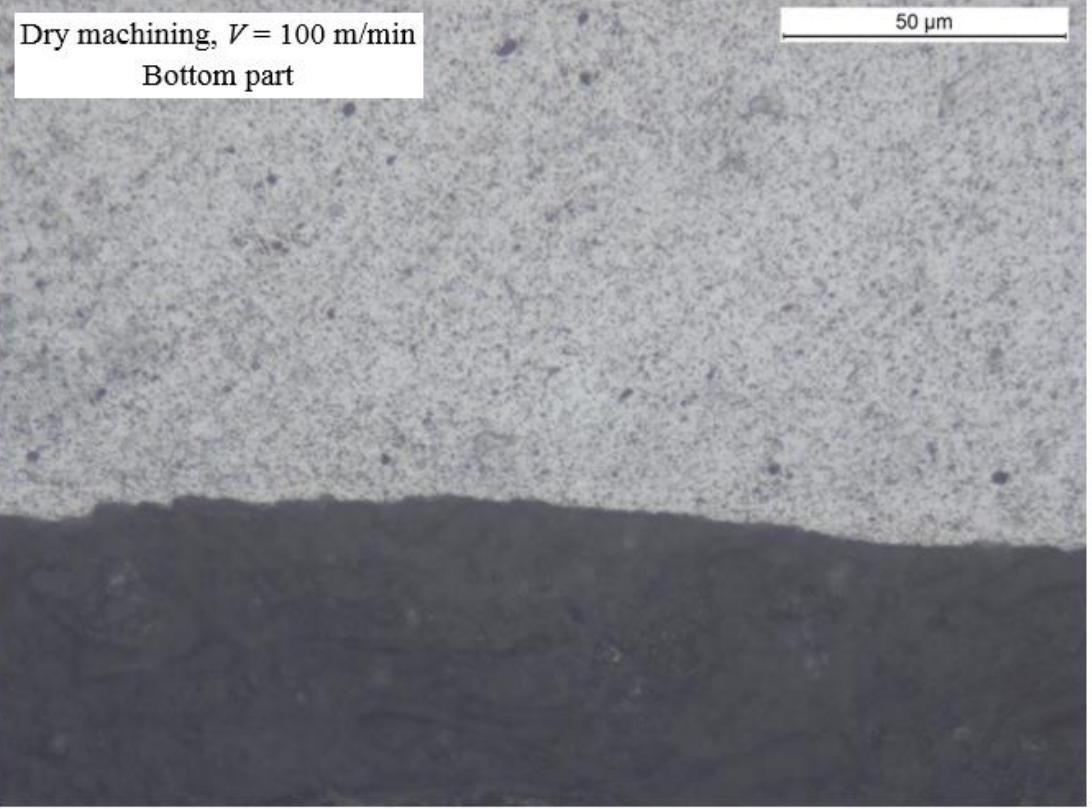
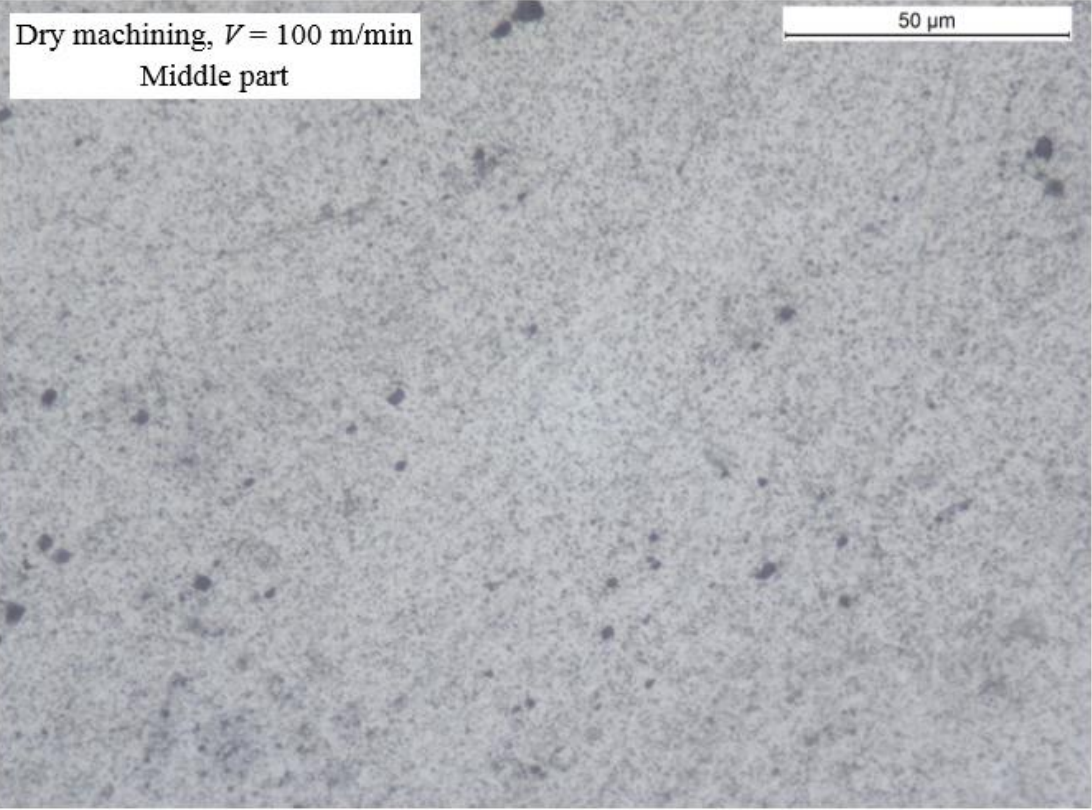
Continuous chips were observed in most cases of machining of *Al 7050-T7451* alloy with near-UFG structure, while it was found that serrated chips were generated at the cutting speed of 50 m/min. Details of obtained chip morphology is shown in Figure 4.7. It has been reported that the transition between continuous and serrated chip occurred in machining of *Al 7075* alloy due to the variation of cutting speeds (Davies and Burns, 2011). Similar continuous chips were also obtained when machining of *Al 7050-T7451* alloy (Zhou et al., 2010a).

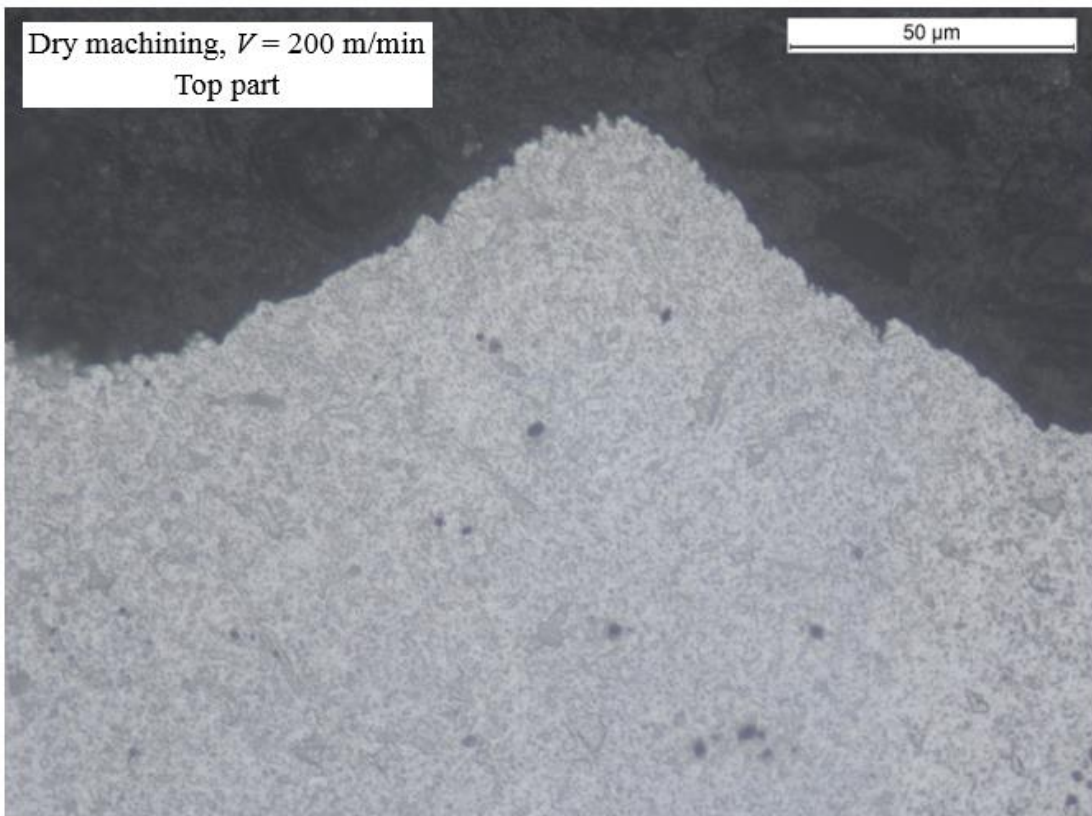
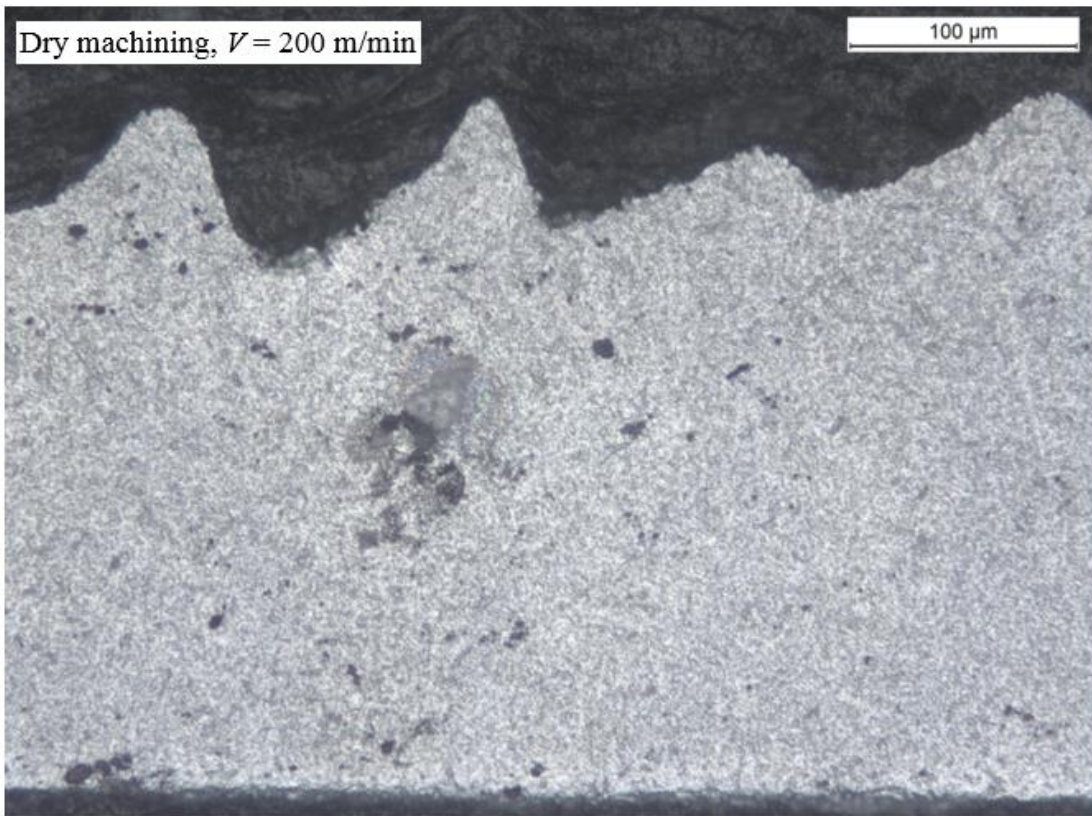
To obtain continuous chips, relatively constant strain, temperature and stress levels must be retained during machining. On the other hand, oscillatory strain, stress and temperature also produced serrated chips (Campbell et al., 2006). Nano- and UFG-grains were observed in the chips when machining of *Al 6061* alloy (Shankar et al., 2005) and magnesium alloy *AZ31B* (Pu et al., 2012). To study the microstructure and grain size of the chips produced during machining of *Al 7050-T7451* alloy with UFG structure, three zones were divided in the chips including the top, middle and bottom parts, as shown in Figure 4.7.

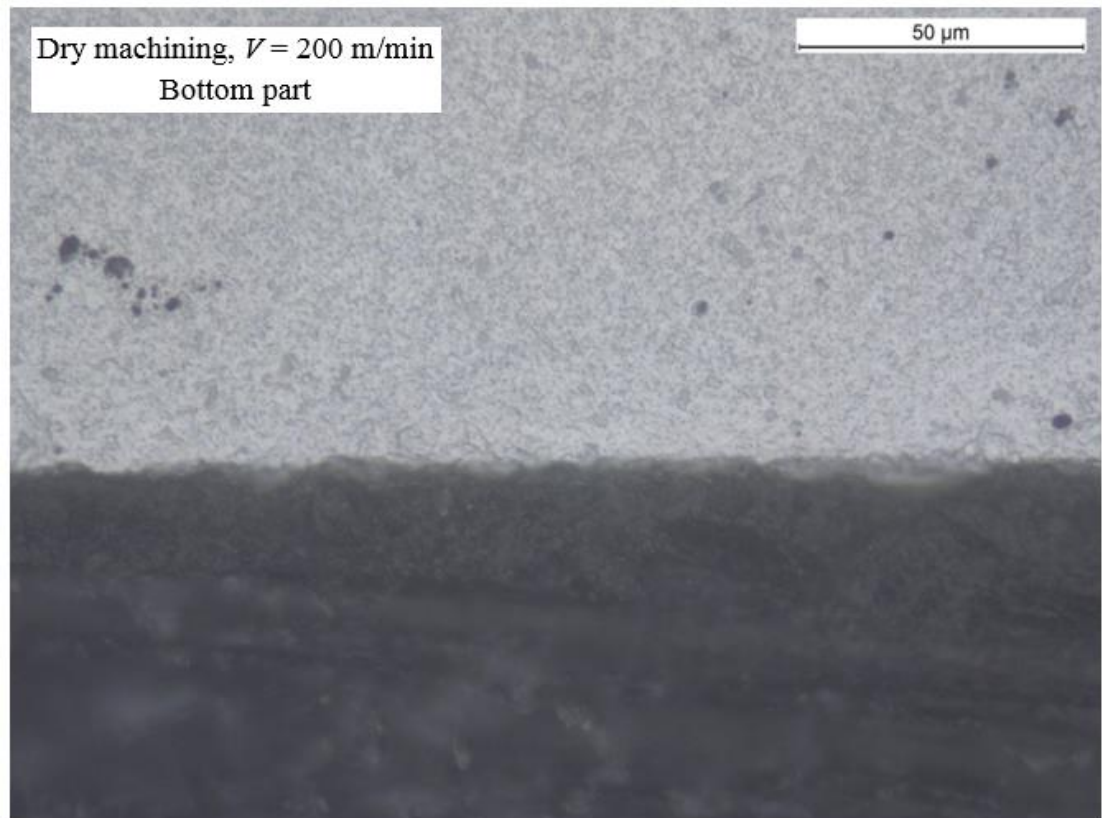
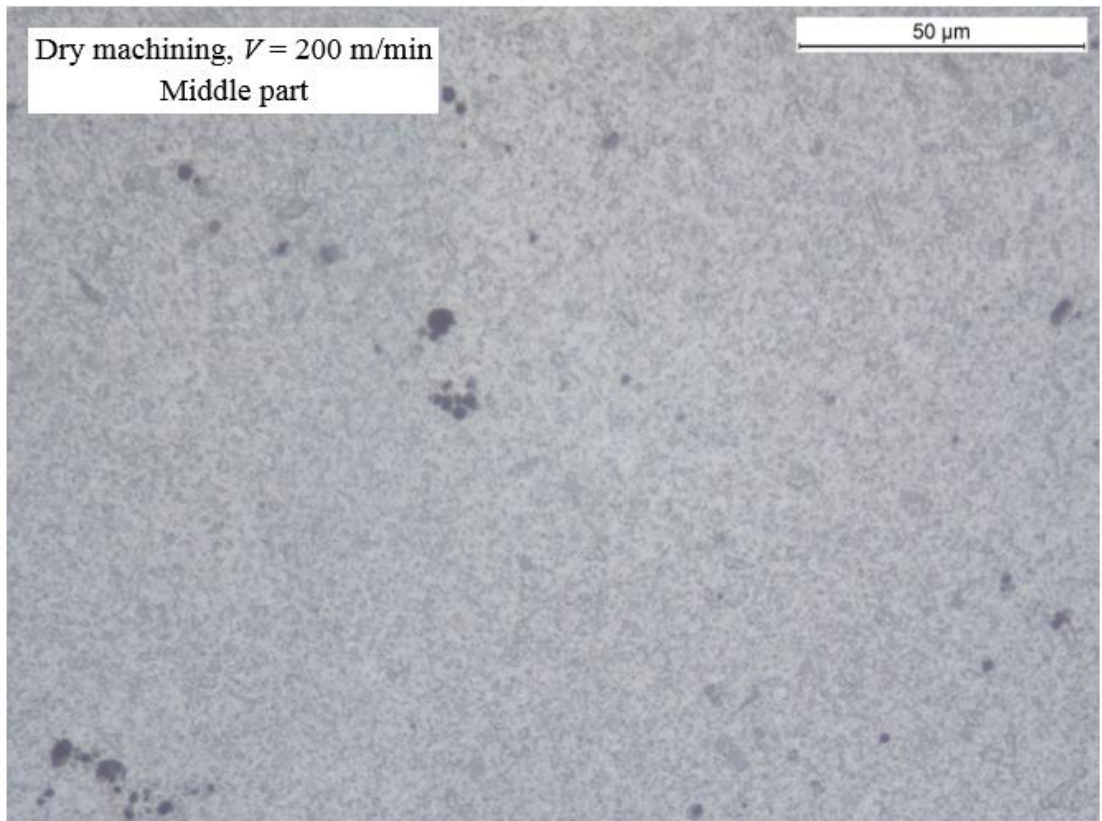


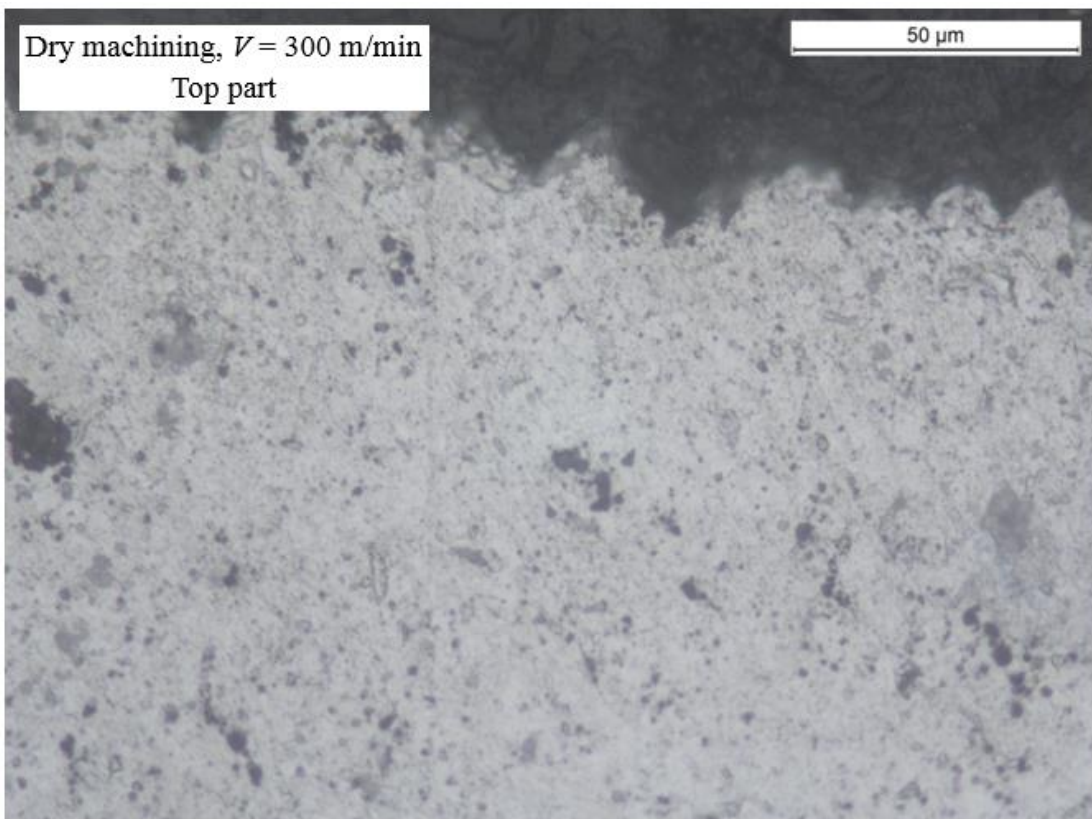
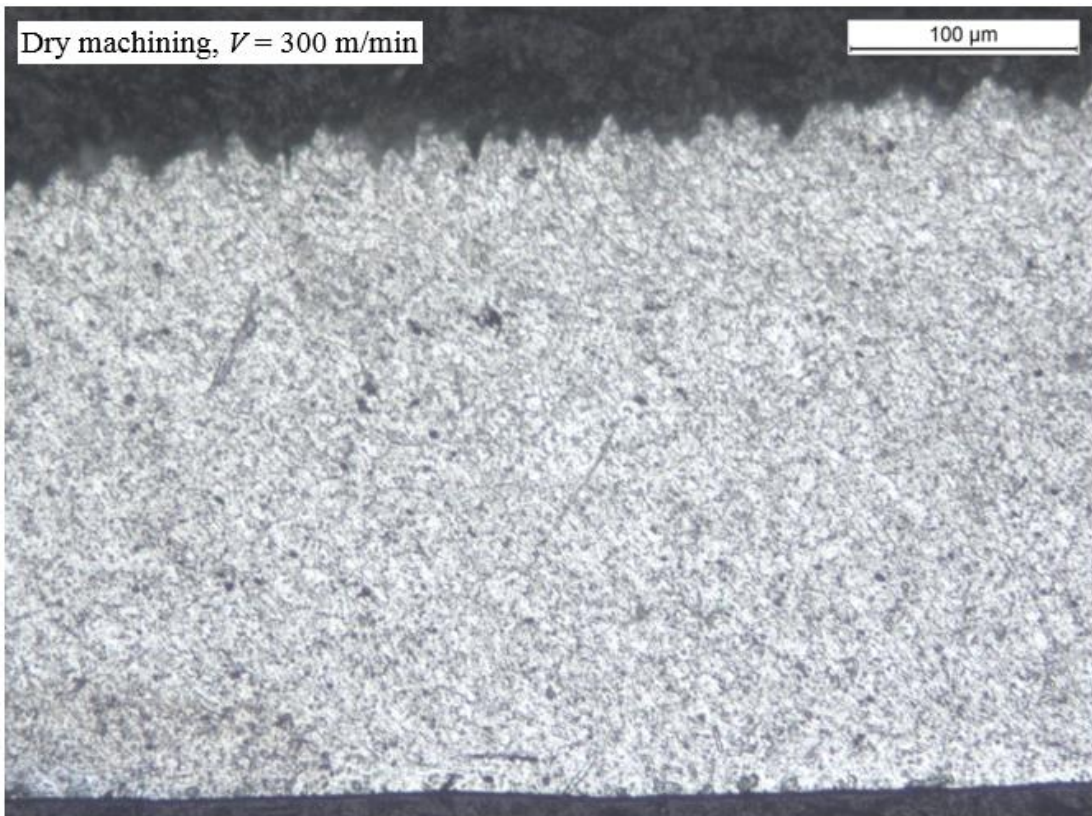


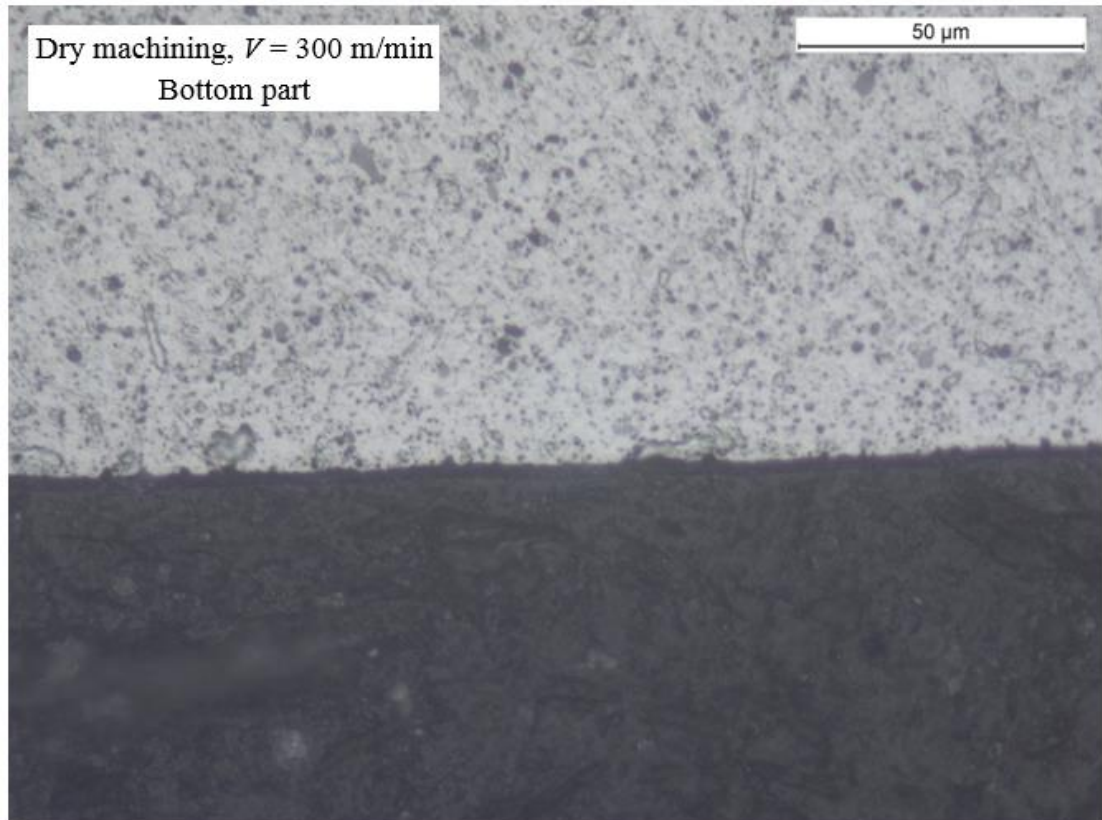
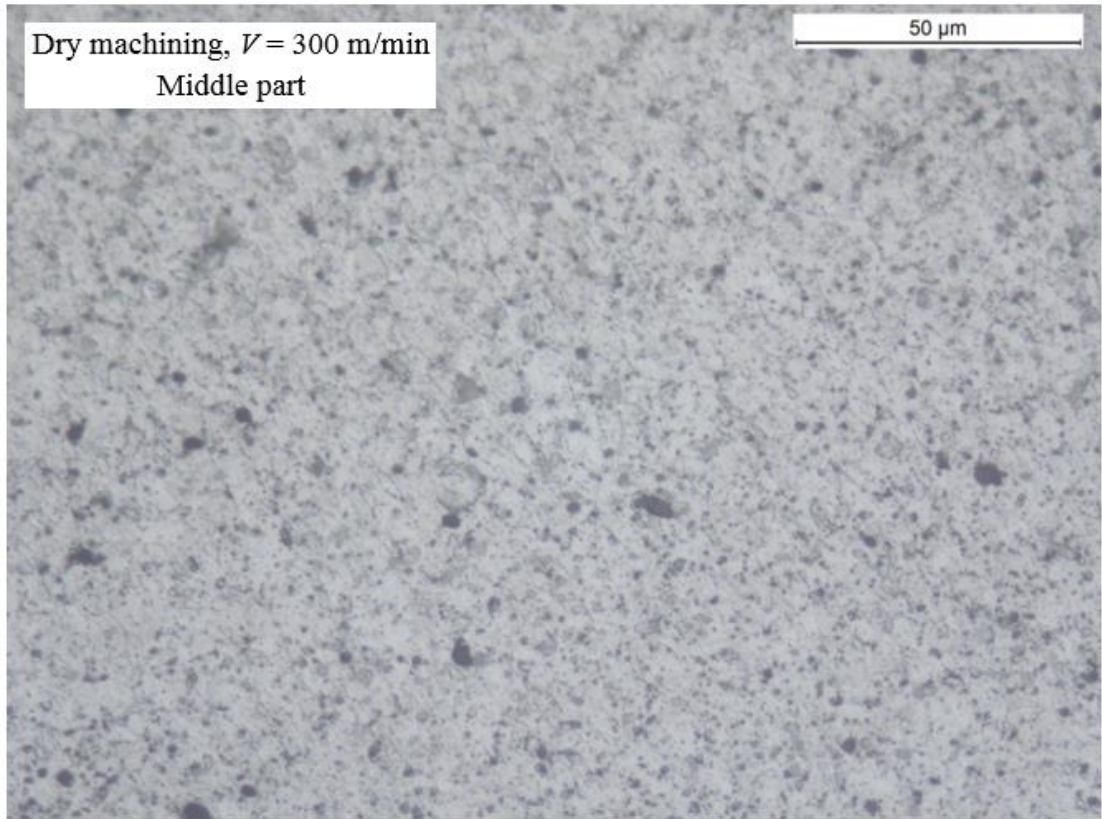


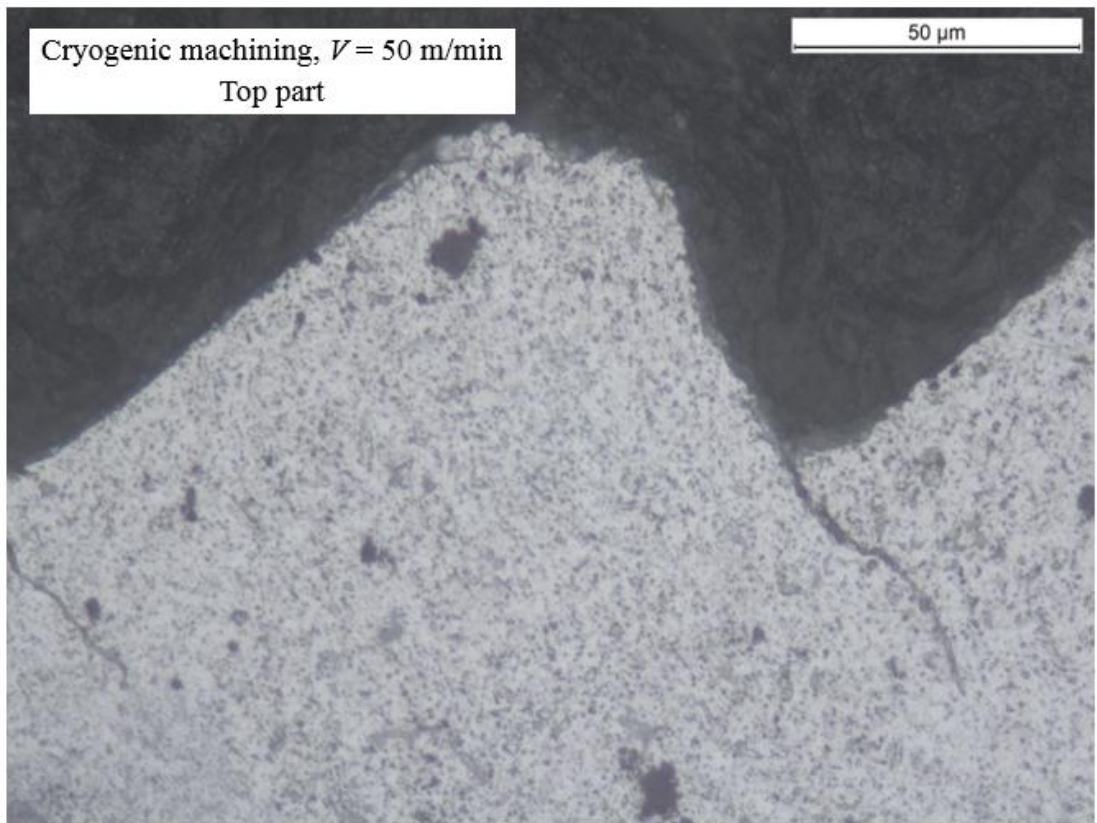
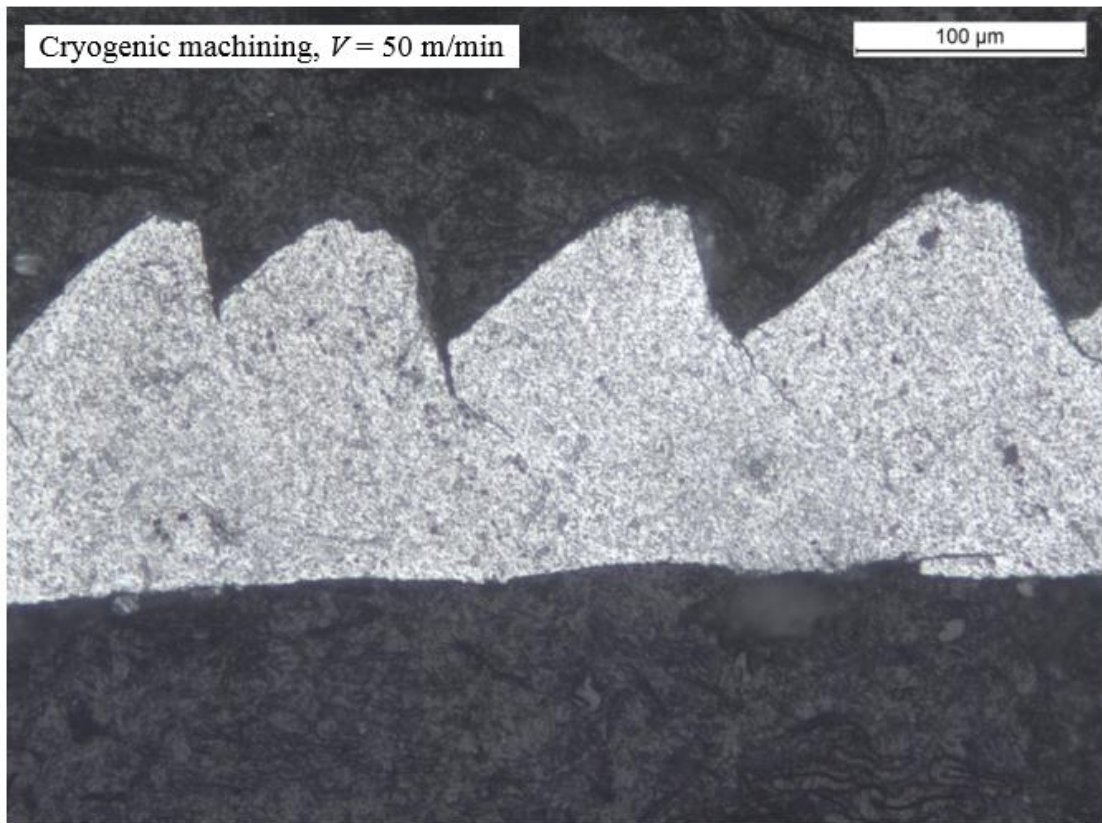


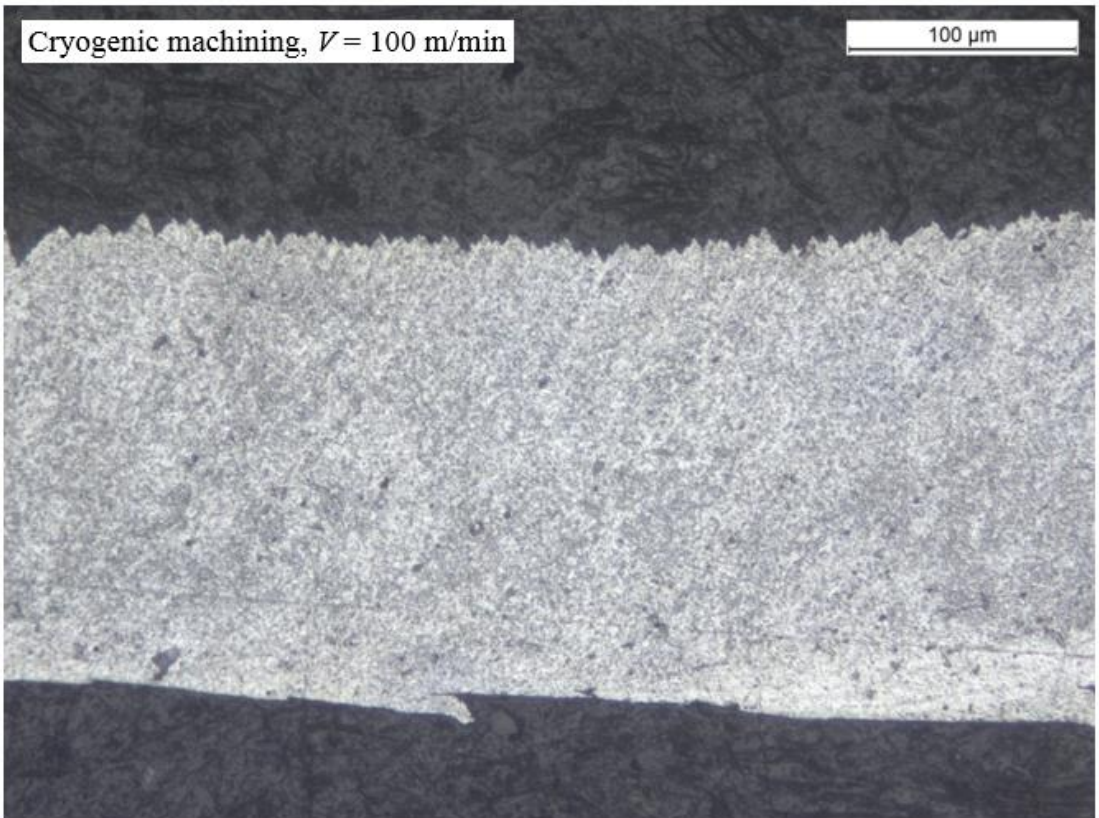
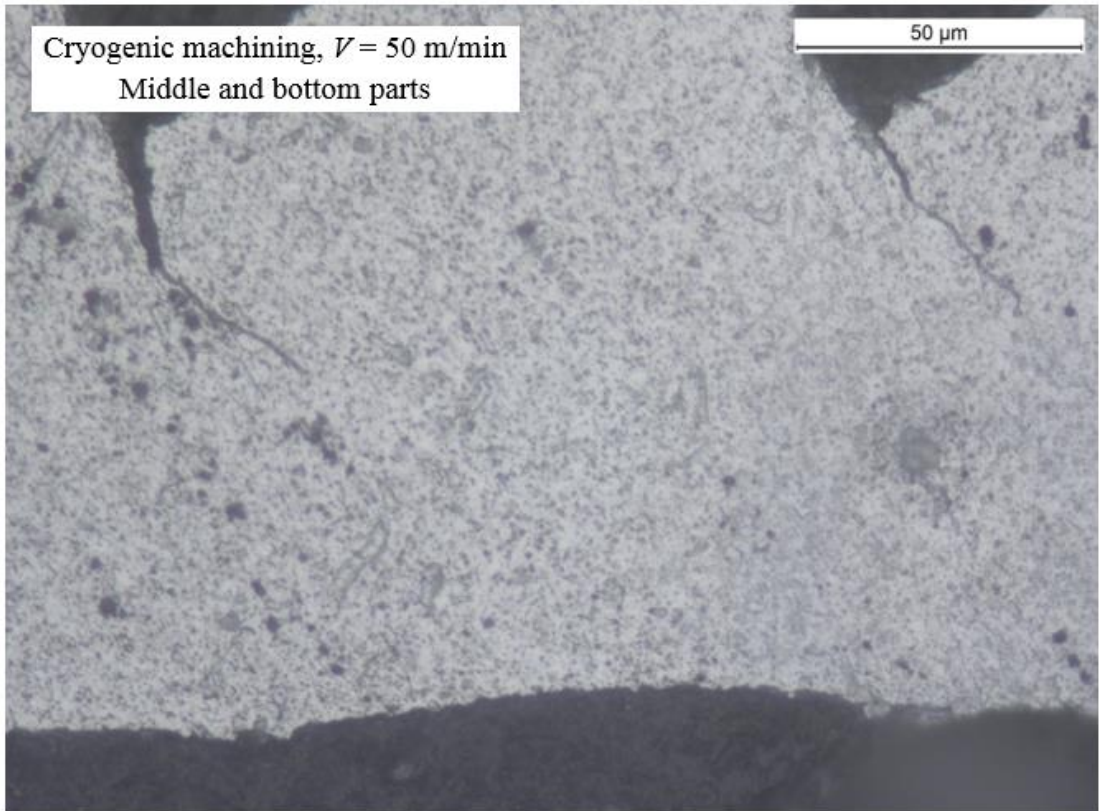


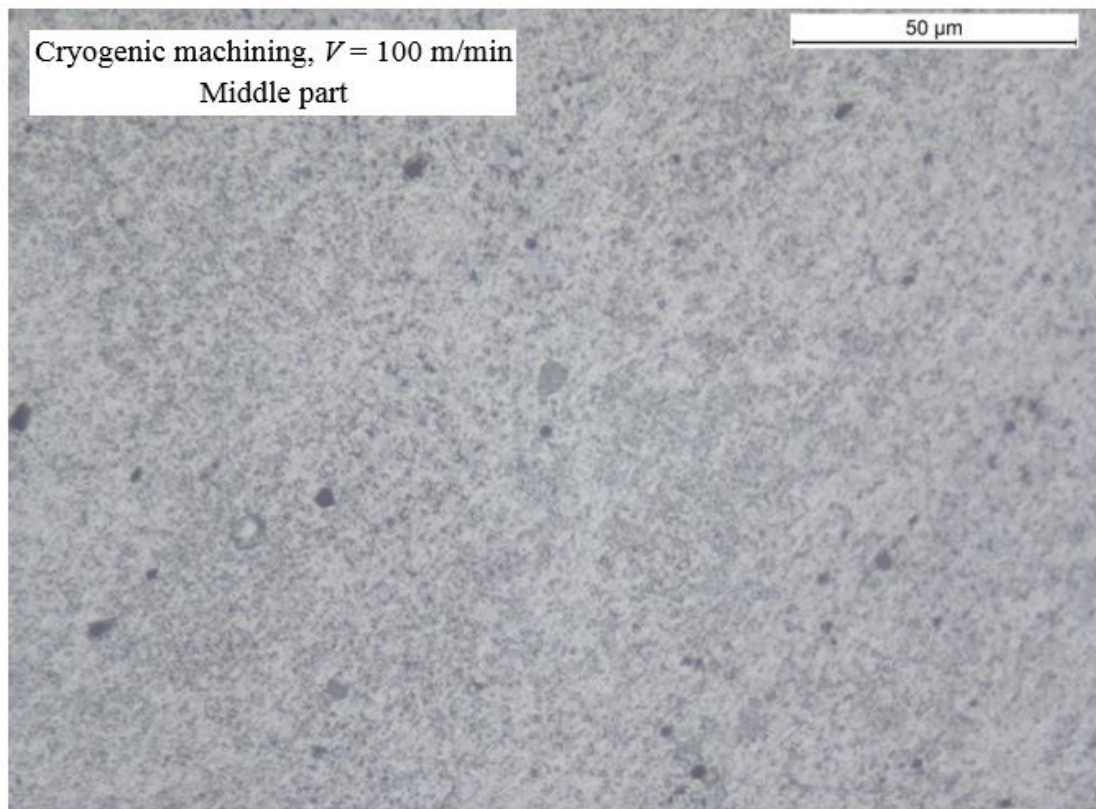
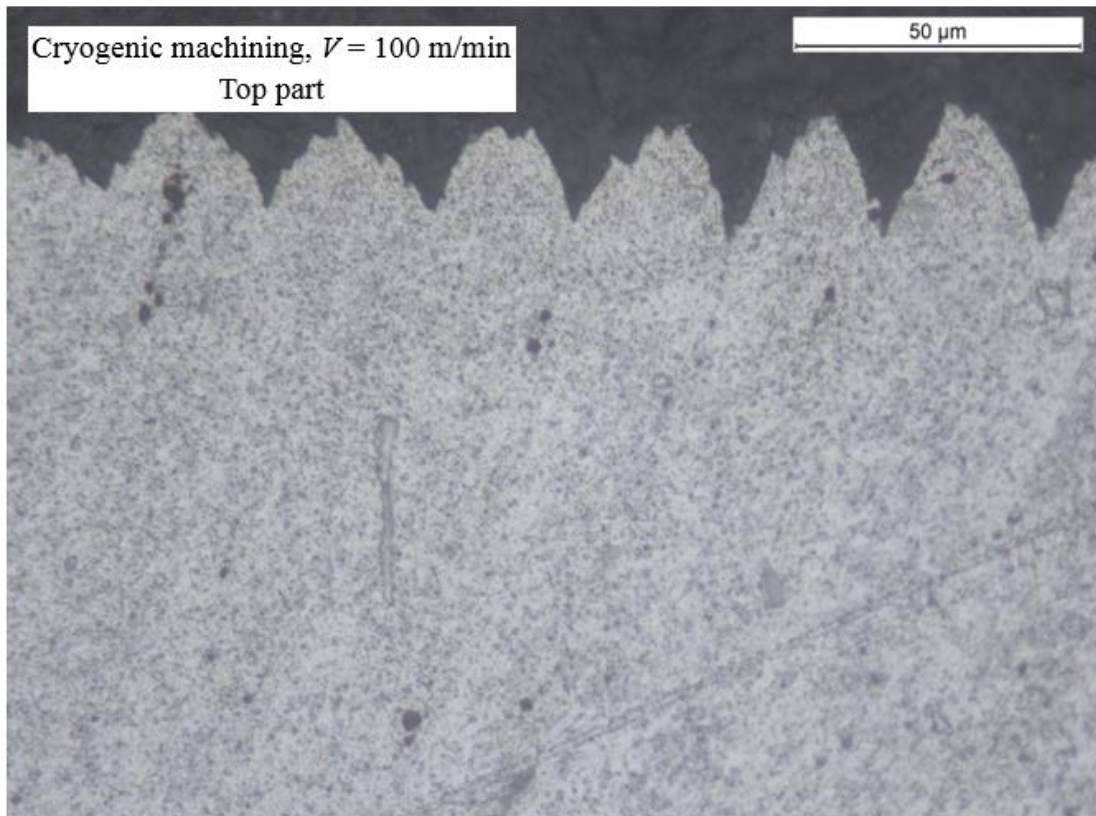


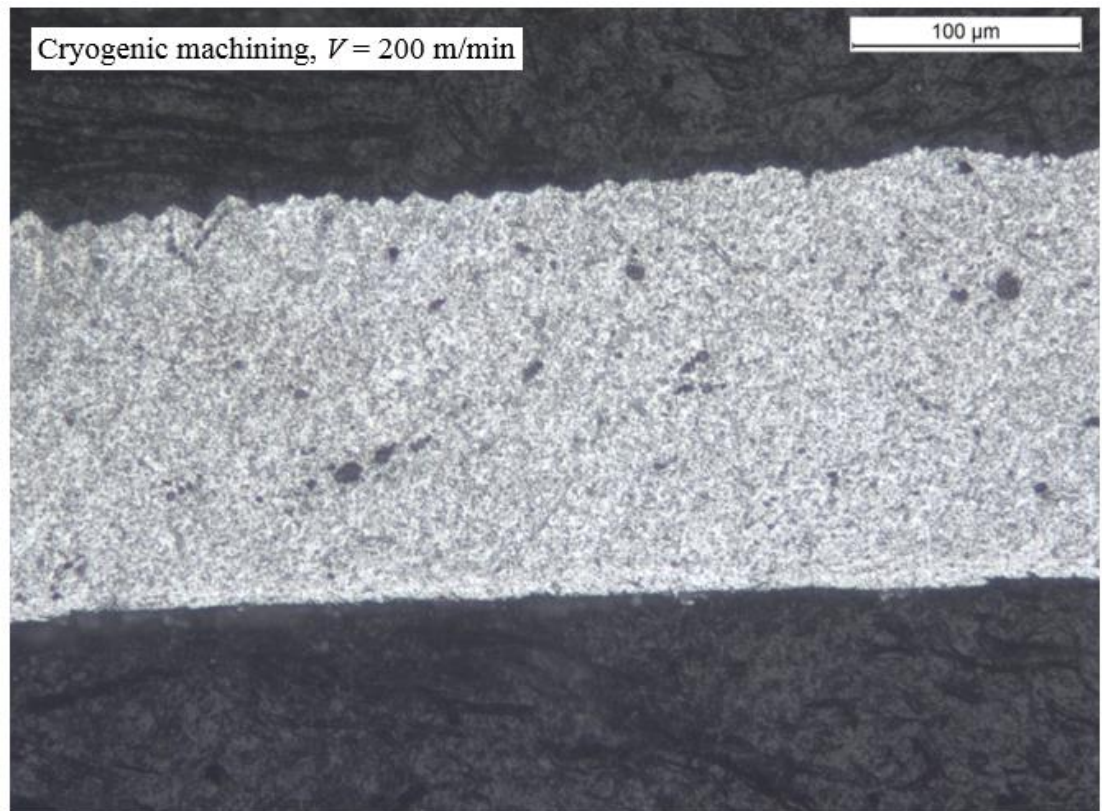
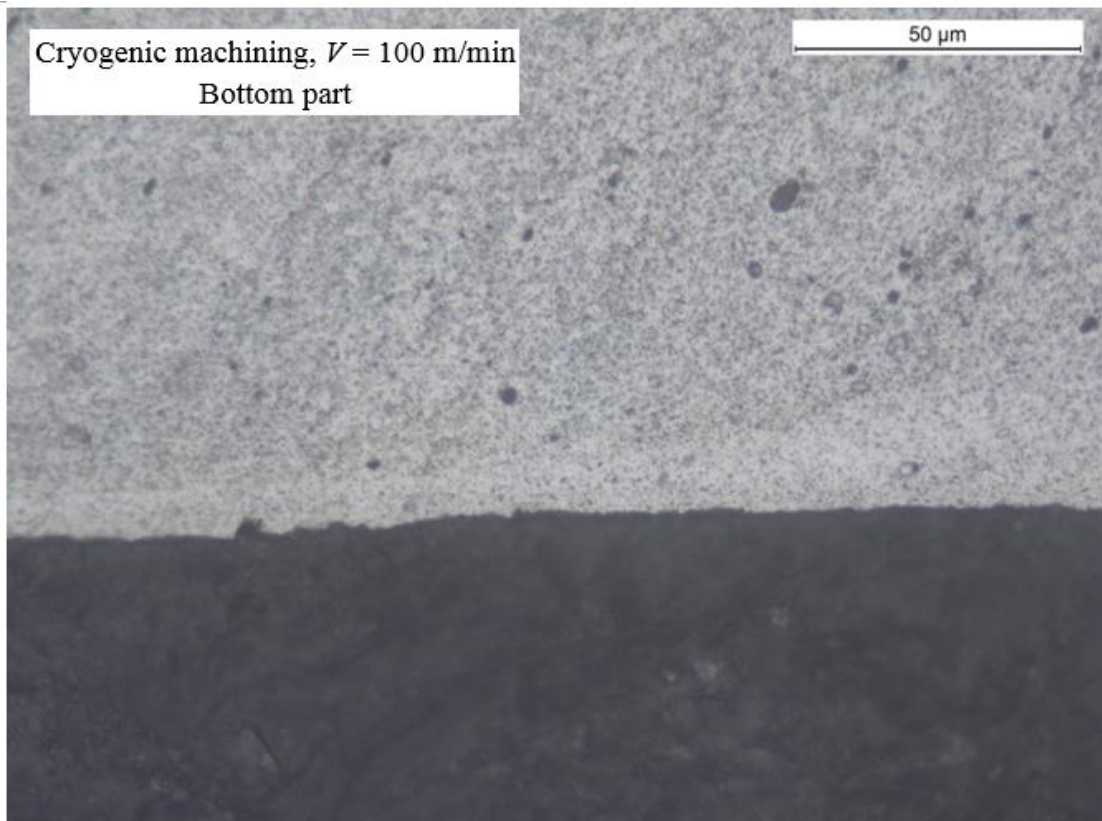


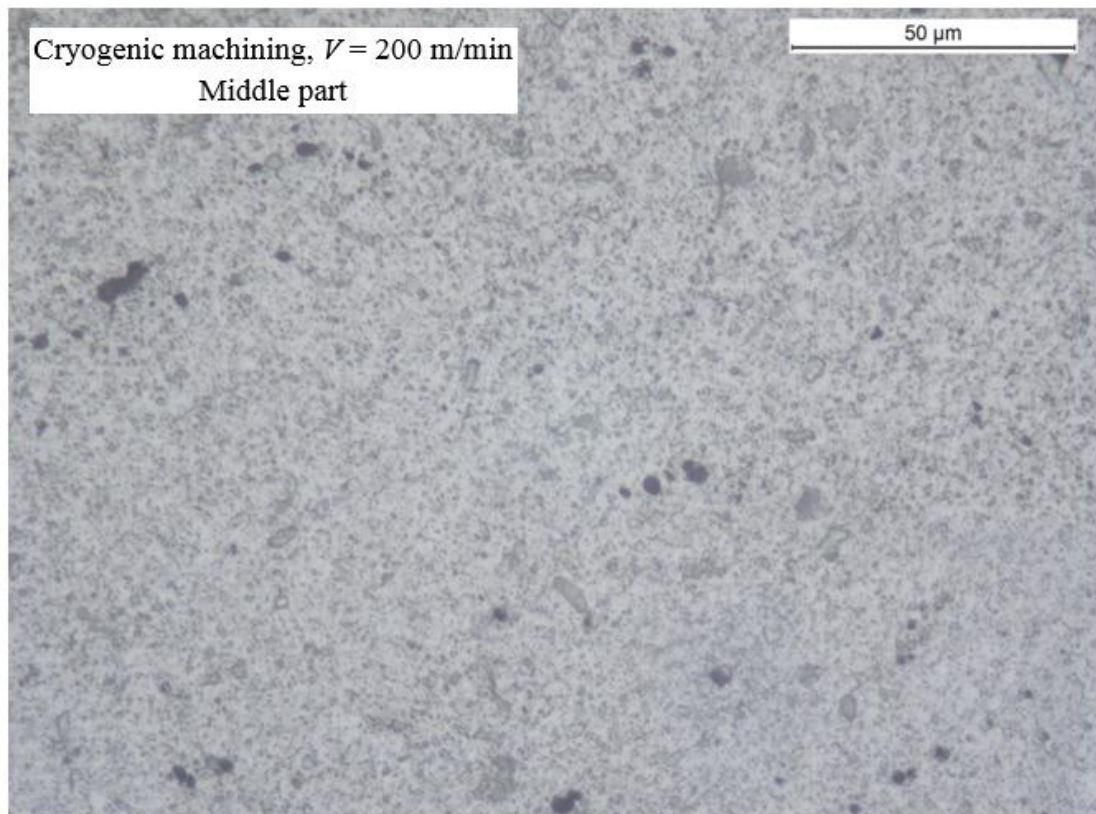
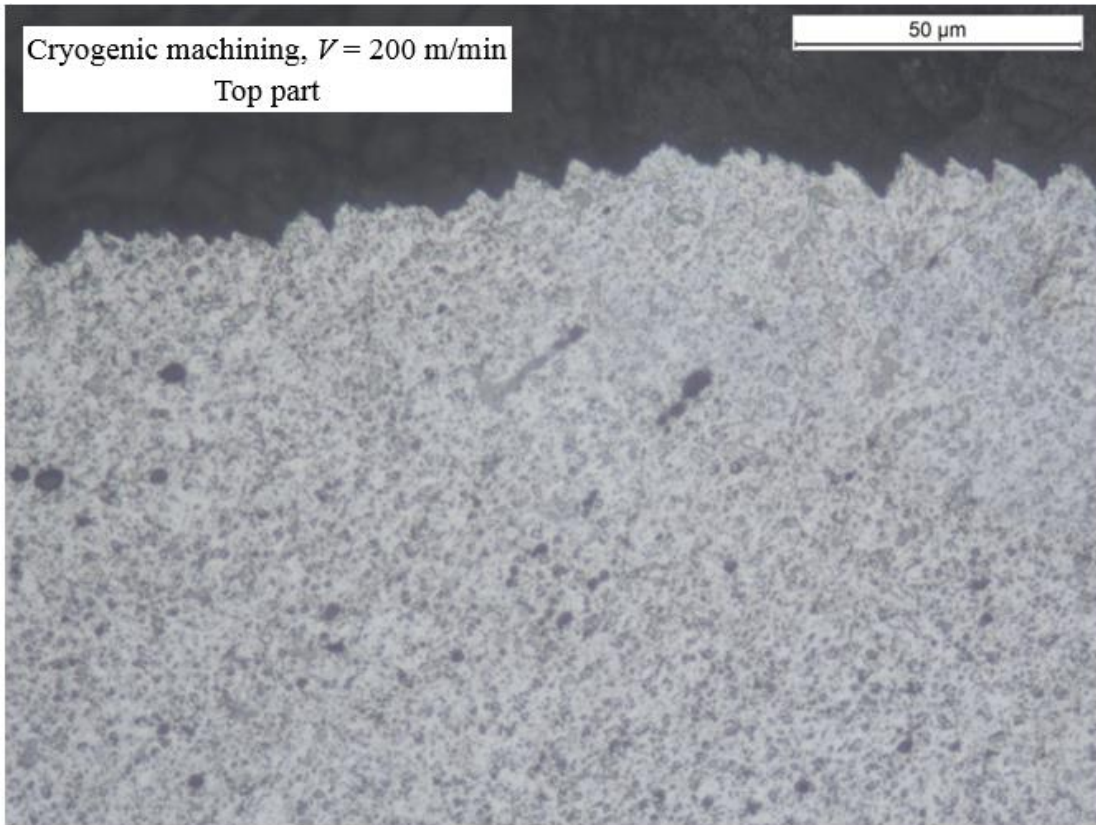


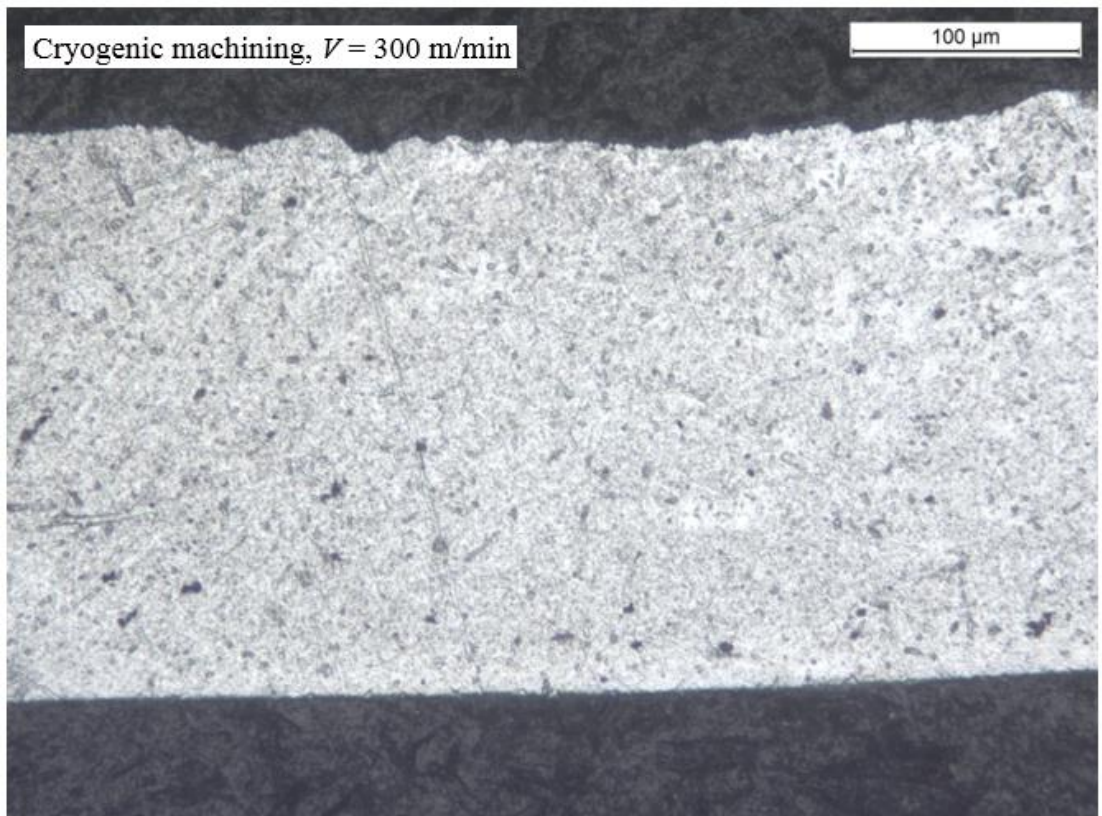
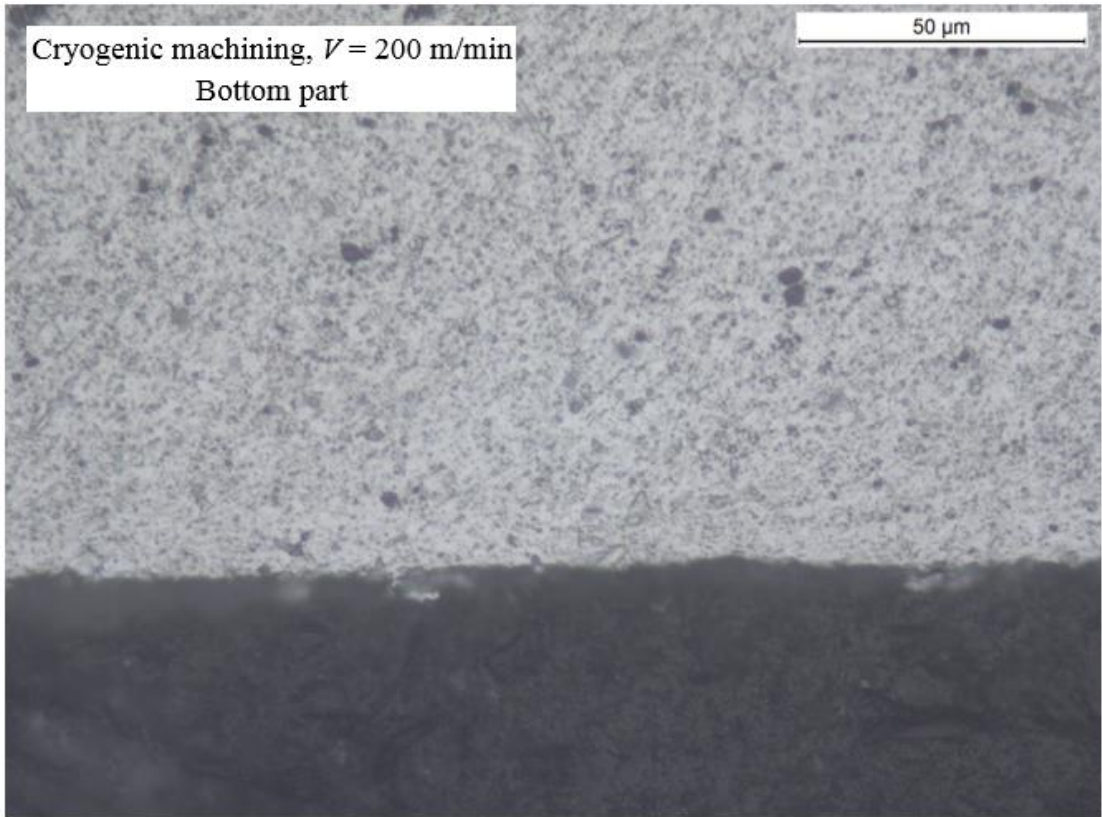


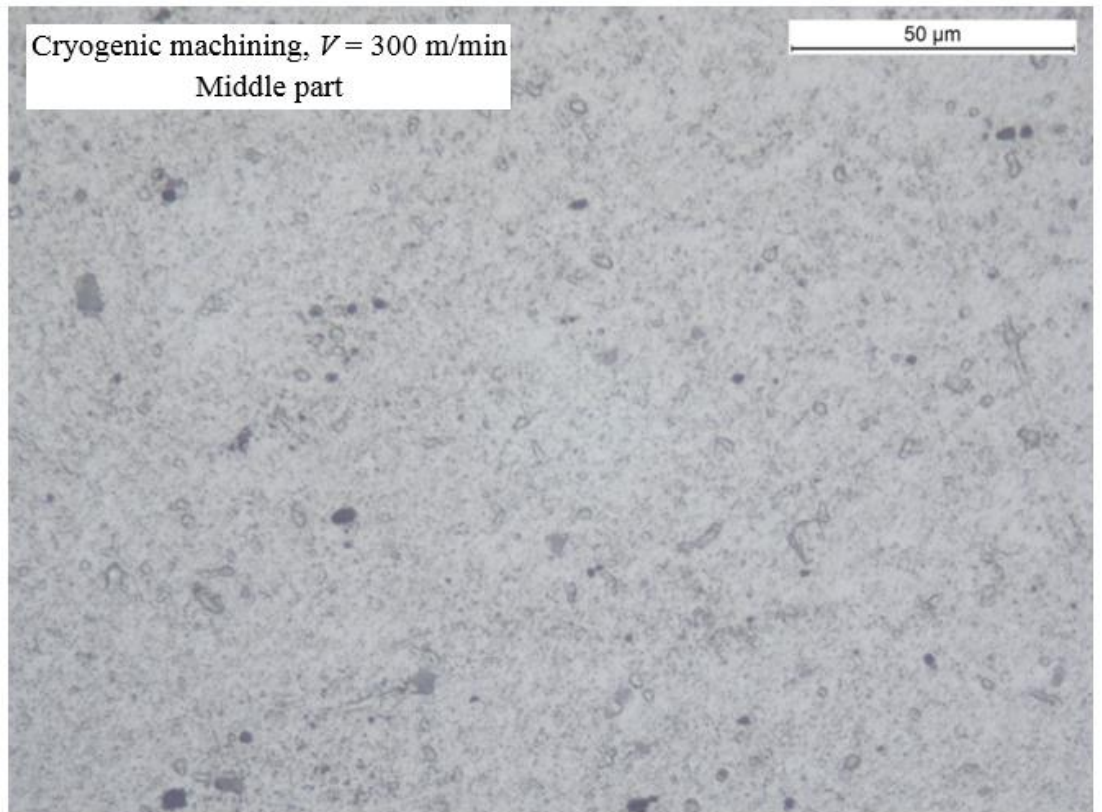
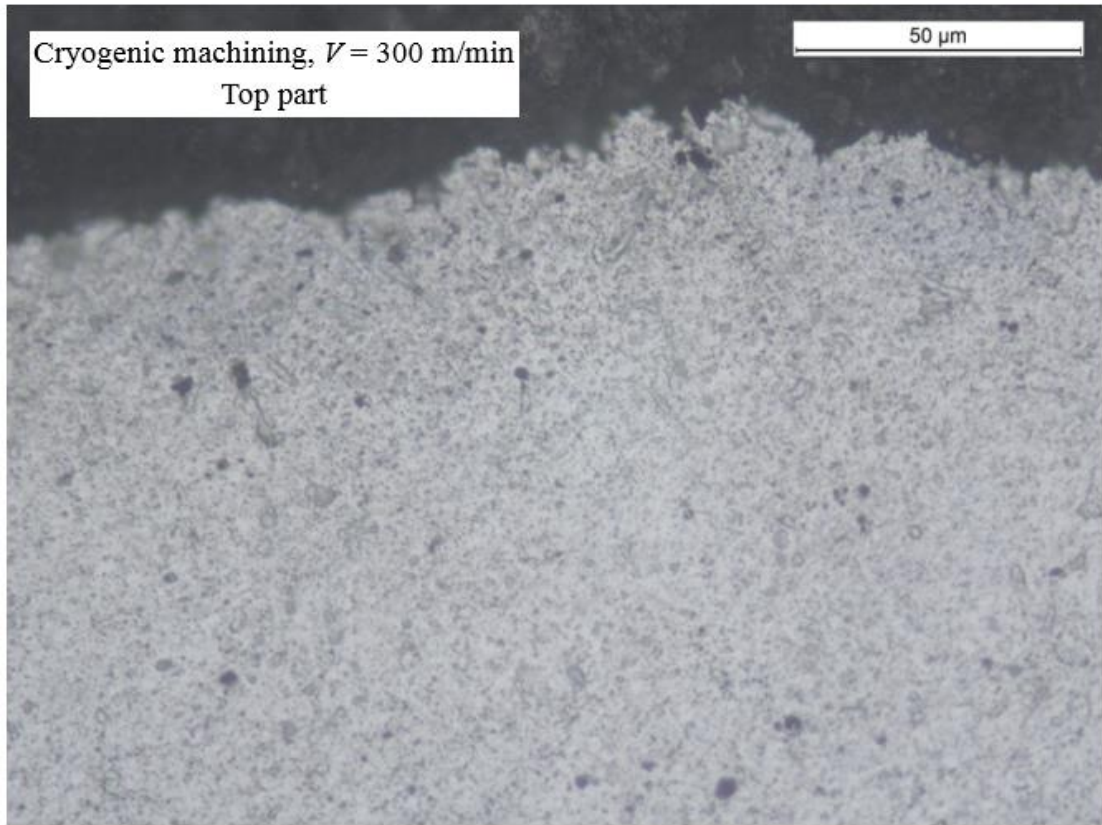












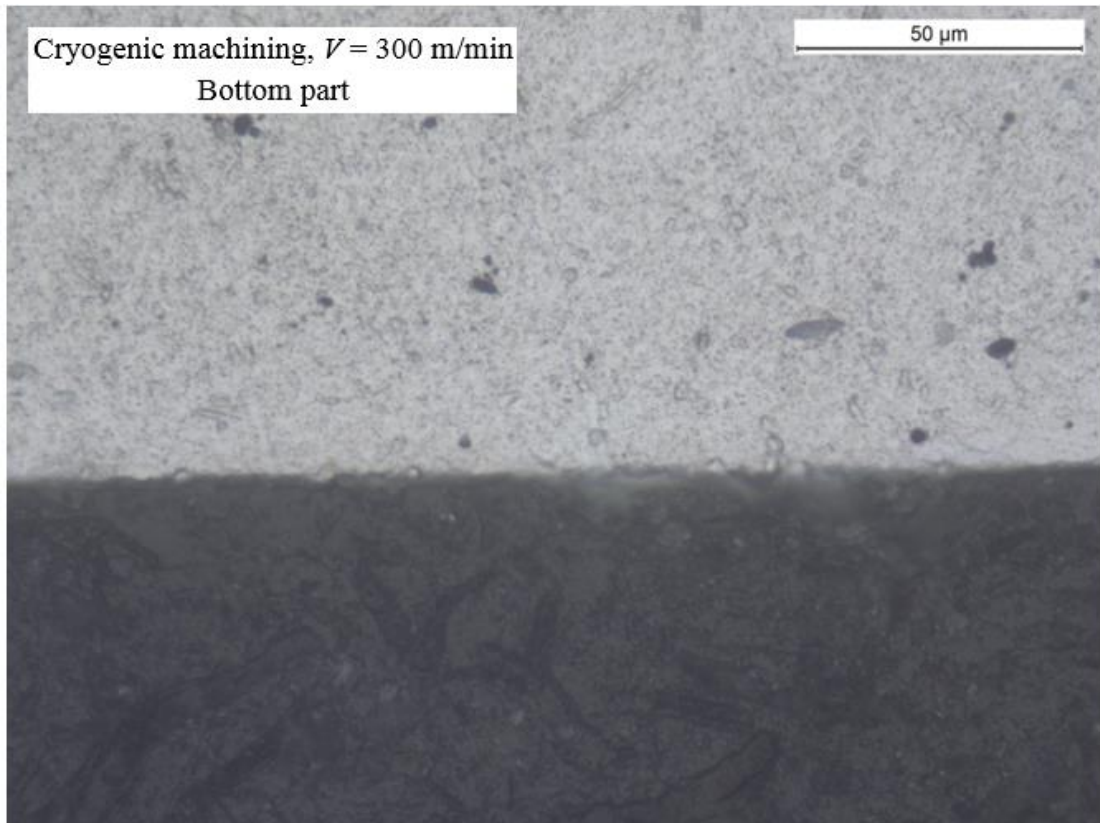


Figure 4.7: Chip morphology and microstructure in dry and cryogenic machining of *Al 7050-T7451* alloy with near-UFG structure at four cutting speeds.

The top part represents the area where small peaks were generated in serration due to the shear localization. While the bottom part represents the secondary shear zone where chip-tool rake face contact occurs during machining, and the middle zone is located between these two zones. Grain size was measured in the chip in these three parts for all eight conditions at four different cutting speeds in dry and cryogenic machining.

DRX occurred in the chips for both dry and cryogenic machining, similar to the machined surfaces. As seen in Figure 4.8, average grain size of approximately $1.2 \mu\text{m}$ was achieved in the chips. There was no big difference in the three parts from the grain size point of view. Large strain and strain-rate were induced during dry and cryogenic machining associated with changes in stresses and temperatures, and all of these

conditions were favorable for DRX to occur. However, in general, smaller grain size was obtained in the chips compared with the ones in the machined surfaces which was expected because the chip was subjected to much more severe plastic deformation, thus leading to smaller grains being generated. Grains have grown slower in the chips because the heat generated during machining was easier to be taken away and transferred to the air from the chips in both dry or cryogenic conditions and the temperature was decreased much faster to room temperature, particularly in the form of thin chips.

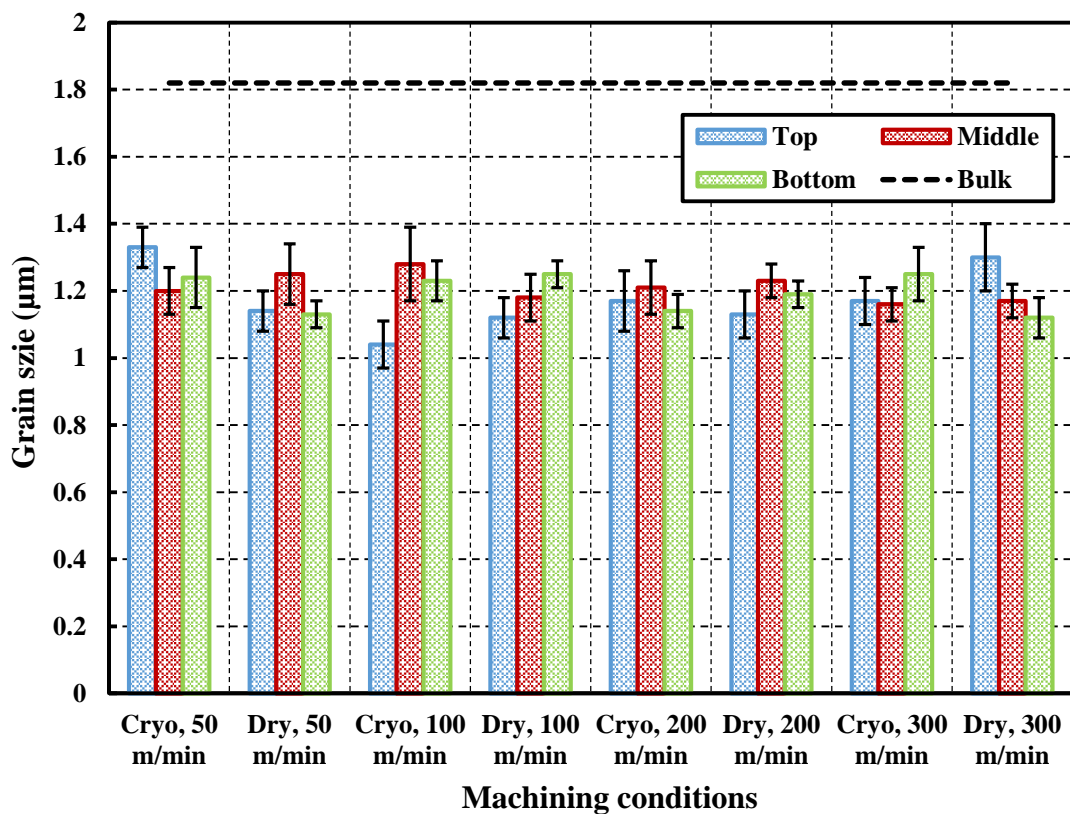


Figure 4.8: Grain size distributions in the three zones of chips produced by dry and cryogenic machining of *Al 7050-T7451* alloy with near-UFG structure.

4.3.6 Chip hardness

Chips produced by dry and cryogenic machining at four different cutting speeds were taken into account, and the hardness was measured in the three parts of each chip. Figure 4.9 shows all the results of measured hardness. The hardness measurements of the chips used the same method when measuring the hardness of machined surface layers. The average hardness of the chips was around 131.3 in Vickers, and was enhanced by nearly 41.8 %, compared to the work material hardness of *Al 7050-T7451* alloy with near-UFG structure processed by FSP. A similar observation has been made previously in machining of *Al 6061* alloy for the increased hardness (Shankar et al., 2005). In their study, chips were obtained from the over-aged bulk *Al 6061* alloy. Introduced by machining in which large strains between 3 and 4 were achieved, the chip hardness was improved to 135 in Vickers from 95, which was the initial hardness of bulk material. A similar finding was also observed from the chips produced by machining of *Al 7050-T7451* alloys in this study.

The obtained chip hardness of dry and cryogenic machining was very consistent as shown in Figure 4.9. The measured hardness values in both dry and cryogenically-machined chips were higher at a low cutting speed. Reduced tendency was observed in measured hardness values of chips as the cutting speed increased. At a lower cutting speed, work hardening effect was dominant, with increasing cutting speed, the thermal softening effect becomes much more dominant, and consequently, the generated chips become softer. Increased temperature during the deformation leads to recovery of the plastic deformation by reducing dislocation density (Kaynak et al., 2014b), and

consequently softening the chips. In addition, dissolution of fine precipitates in the chips also took place when the deformation temperature reaches high values. Nevertheless, further grain refinement associated with the introduction of large strain by machining also contributed to the hardness enhancement in the chips acquired by dry and cryogenic machining.

Due to the analogous grain size and induced strain, the hardness in these cases was very similar. Precipitate breaking was discovered in the other SPD processes for *Al 5083* (Dupuy and Blandin, 2002), *Al 7050* (Nam et al., 2003) and *Al-Cu* alloys (Murayama et al., 2001), and it was considered to contribute to fine microstructure and strengthening. In chips obtained from machining of *Al 6061* alloy, the phenomenon of precipitate breaking was also observed (Shankar et al., 2005). Similarly, for *Al 7050-T7451* alloy with near-UFG structure, the chips might undergo the same grain boundary dislocation and microstructure refinement within which precipitate breaking occurs due to large strain induced by machining.

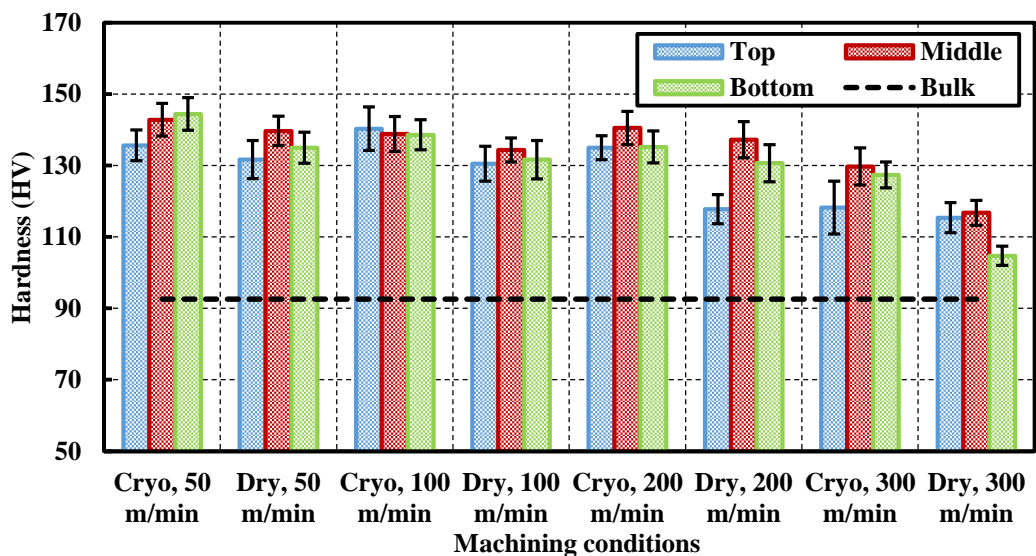


Figure 4.9: Chip hardness measurement in dry and cryogenic machining.

4.4 Chapter conclusion

In this chapter, dry and cryogenic machining experiments were conducted to study the surface integrity characteristics of *Al 7050-T7451* alloys with near-UFG structure induced by the machining process. Cutting force components and temperatures were also recorded and analyzed in order to understand the machining effects on surface integrity. Moreover, the measurements of chip microstructures and hardness supplemented the understanding of dry and cryogenic machining. A summary of findings from this study is given below:

- The average values of force components consisting of cutting and thrust forces, were about 250 N recorded at four different cutting speeds: 50, 100, 200 and 300 m/min, in dry and cryogenic machining, in which cutting forces were slightly greater than thrust forces in all eight conditions.
- Up to 44.7% reduction of cutting temperature was found when measured using the infrared camera by applying liquid nitrogen as the coolant in cryogenic machining compared to dry machining.
- From the microstructure point of view, marginal grain refinements indicate that DRX occurred in both dry and cryogenic machining. However, smaller grain size of approximately 1.6 μm was measured in the machined surface layers within the depth of 200 μm produced by cryogenic machining when the cutting speeds were 50 and 100 m/min.
- The hardness measurements in the machined surfaces demonstrate that cryogenic machining could benefit the hardness improvement, allowing the work hardening

effect to become more dominant by taking away the heat in a relatively short time, especially at low cutting speeds of 50 and 100 m/min, whereas in dry machining, the hardness of the machined surface was not enhanced due to more dominant thermal softening effect.

- Observed from the microstructure images of chips produced by dry and cryogenic machining, the average grain size of about 1.2 μm was seen from the microstructures measured from the samples processed by dry and cryogenic machining, proved that DRX took place in the machined surfaces and smaller grains maintained owing to quick heat transfer in the form of thin chips in contrast to much thicker work materials.
- Attributing to higher strain and strain-rate induced by more severe plastic deformation in the primary deformation zone, the hardness values of chips produced by dry and cryogenic machining were approximately 41.8% higher than the initial hardness of work materials prepared by FSP.

The machining effects on *Al 7050-T7451* alloys with near-UFG structure were investigated in terms of surface integrity characteristics, cutting forces, temperatures and chip morphology. The mechanical and material properties of the UFG materials can be improved according to the research findings discussed above. However, in order to further improve the properties of UFG materials, burnishing is an effective post-machining process to induce more severe plastic deformation and grain refinement for improved wear/corrosion resistance, fatigue life of the manufactured components. In the next chapter, the burnishing effects on *Al 7050-T7451* alloys with UFG structure

will be studied from the perspectives of surface integrity characteristics, including burnishing forces and temperatures, particularly for cryogenic burnishing with liquid nitrogen as the coolant.

CHAPTER 5

SURFACE AND SUB-SURFACE MODIFICATION BY CRYOGENIC BURNISHING OF *Al 7050-T7451* ALLOY WITH NEAR-UFG STRUCTURE

5.1 Introduction

As one of the chipless machining processes, burnishing operations are generally performed on manufactured components to reduce surface roughness, increase surface/subsurface hardness and improve other surface integrity characteristics. The generation of refined layers with ultra-fine grains or nano-grains can be observed in the burnished surface layers induced by burnishing processes, attributing to severe plastic deformation and the associated dynamic recrystallization. Compressive residual stresses, distributed within these harder refined layers, also provides the benefits with increased fatigue life and improve the wear/corrosion resistance of the components.

The effects of cryogenic burnishing on the surface integrity of *Al 7050-T7451* alloys have been studied and presented in this chapter. A specifically-designed roller burnishing tool was used to perform the cryogenic burnishing experiments by using liquid nitrogen as the coolant. Burnishing temperatures and forces were measured to compare the differences between dry and cryogenic burnishing in which lower temperatures and higher tangential burnishing forces could be observed from cryogenic burnishing due to the introduction of the work hardening and rapid cooling effects. Refined layers with nano-grains whose grain size was approximately 40 nm, were formed in the cryogenically burnished surfaces, in which an average hardness increase between 20% - 30% within the layer depth of 200 μm was obtained, compared with dry

burnished surfaces in which an average hardness increase between 5% to 10% was achieved, at the burnishing speeds of 25, 50 and 100 m/min. The depth of the refined layers was measured to be approximately 19, 26 and 50 μm when the above three burnishing speeds were used, respectively, in cryogenic burnishing.

Processes with the mechanism of severe plastic deformation have been considered to be the most effective methods to induce exceptional grain refinement in the metallic materials without changing their overall dimensions and shapes significantly, by imposing an extremely large strain on the bulk materials (Valiev et al., 2006). Various SPD processes were developed in the past by the research communities, such as equal channel angular pressing, high-pressure torsion, accumulative roll-bonding, torsion extrusion, cyclic closed-die forging, etc. (Azushima et al., 2008). Due to these processes, the desired material properties can be obtained by controlling the grain size, which is one of the critical factors influencing the mechanical behaviors of the metallic materials and their chemical response to the surrounding environments (Estrin and Vinogradov, 2013).

Burnishing is one of the SPD processes in which high strains and strain-rates are introduced to improve the surface integrity of the manufactured components (Skalski et al., 1995; Black et al., 1997). A better surface finish could be achieved by roller-burnishing, El-Khabeery and El-Axir (2001) reported that the surface roughness less than 0.25 μm was measured from the burnished surface of *Al 6061-T6* alloys. Similar improvements in surface roughness was also reported in ball burnishing of *41Cr4* low-alloy steel by Grzesik and Žak (2012). Two roller burnishing tools were used by Klocke

et al. (2011) to symmetrically process the turbine blades made of Inconel 718 and Ti-6Al-4V alloys. They found that the plastic component deflection could be prevented and the fatigue life of the processed components was improved because of the strain hardening effect and the induced compressive residual stress. Hamadache et al. (2006) showed that the hardness of the burnished surface was increased by 10% when Rb40 steel was processed by the ball and roller burnishing tools. The corrosion fatigue strength of Al 7075-T6 alloy processed by low plasticity burnishing (LPB) was increased to 310 MPa, which was three times compared to the unburnished samples according to early research of Prev y and Cammett (2004).

By using liquid nitrogen as the coolant during the burnishing process, cryogenic burnishing can generate refined surface layers with nano or ultra-fined grains as the heat generated during burnishing is taken away very quickly and the grain growth of the recrystallized grains within the surface and subsurface layers is constrained after dynamic recrystallization (DRX) which occurs due to the burnishing effect. The physical and mechanical properties of cryogenically-burnished components, such as corrosion/wear resistance and fatigue life, would be enhanced due to the formations of refined layers with higher hardness and more compressive residual stress. Yang et al. (2013) investigated the burnishing effects on Co-Cr-Mo biomedical alloy, in which the refinement of microstructure was achieved and grains with the grain size of 300-600 nm were generated in the burnished surface by cryogenic burnishing. Also, an 87% hardness increase was obtained in the refined layer compared to the bulk material. The performance of wear resistance was improved, attributing to the formation of the hard

surface layers with ultra-fine grains developed by Yang (2012). A similar phenomenon of grain refinement was also found in cryogenic burnishing of *AZ31B Mg* alloy, where the surface hardness was increased from 0.86 to 1.35 GPa and the corrosion resistance was significantly improved because of the grain refinement associated with the strong basal texture induced by the effect of cryogenic burnishing (Pu et al., 2011). *Ti-6Al-4V* alloys with the application of turbine blades in the aerospace industry, were cryogenically-burnished by Caudill et al. (2014), they found that the surface hardness was increased to 56 HRC in contrast to the bulk hardness of approximately 35 HRC at the preload of 2500 N. A maximum reduction of 56.7% was achieved in the surface roughness measured from the cryogenically burnished surface, as presented in their study.

Al 7050-T7451 alloys with near-UFG structure processed by FSP, are used as the work materials in the experiments of cryogenic burnishing. The burnishing effects on surface integrity characteristics, burnishing forces and temperatures are among the factors investigated in the work presented in this chapter.

5.2 Experimental work

The work materials prepared for the experiments were *Al 7050-T7451* alloys with near-UFG structure processed by FSP. The as-received materials in the sheet form with the thickness of 3.2 mm were processed by FSP, double-sided (processing the sheet from one side and then flipping it over and processing the other side), to make sure the materials were homogeneous enough. The specific processing parameters of FSP were

selected appropriately in order to achieve the grain size of approximately 1.82 μm for the work materials. The two important parameters influencing the grain size are the rotational speeds and feed rates of FSP tools. In this study, the rotational speed and feed rate used were 19.2 m/min and 101.6 mm/min, respectively. The sheet was cut into discs specimens, with the diameter of 65 mm by vertical milling for the orthogonal burnishing experimental work. Each disc was fixed on a work-holding mandrel specifically designed with three bolts, and a Hass TL-2 CNC lathe was used to perform the burnishing experiments in dry and cryogenic conditions.

A roller-burnishing tool made of uncoated carbide with the diameter of 14.3 mm was used in the burnishing experiments, and the roller head was not fixed and could rotate along with the disc during burnishing. A systematic experimental matrix, as shown in Table 5.1, was developed to comprehensively study the burnishing effects on *Al 7050-T7451* alloys with near-UFG structure. A range of depths of penetration was chosen as 0.05, 0.1, 0.15 and 0.2 mm, and the burnishing speeds used in dry and cryogenic burnishing were 25, 50 and 100 m/min. The dwell time during which the burnishing tool kept contacting with the disc was set to be 10 seconds after the depth of penetration was achieved. The detailed setup of the burnishing experiments is shown in Figure 5.1.

The radial and tangential force components were measured by a Kistler 9121 three-component tool dynamometer during dry and cryogenic burnishing. From the clearance side of the burnishing tool, liquid nitrogen was delivered by ICEFLY[®] system, the flow rate was approximately 10 g/s mass under 1.5 MPa pressure. The temperatures of *Al 7050-T7451* discs were measured by a FLIR infrared imaging system/camera. In order

to study the surface integrity characteristics, the metallurgical samples were cut from the burnished discs. In the sequential order, a range of metallurgical operations such as mounting, grinding, polishing and etching were performed to study the microstructure of the samples. Keller's reagent was used to etch the samples of *Al 7050-T7451* alloy. To observe the microstructure, Nikon EPIPHOT 300 with Leica DFC425 optical microscope was used in the experiments. Atomic force microscopy (AFM) images were taken by Agilent Technologies 5500 Scanning Probe Microscope to observe the nano-grains generated in the refined surface layers in cryogenic burnishing. Hardness was measured by using one Vickers indenter of the CSM Micro-Combi Tester in which 25 gf load and 15 seconds duration were selected to make the indentation.

Table 5.1: Burnishing experimental matrix of *Al 7050-T7451* alloys with near-UFG structure.

Cooling method	Burnishing speed (m/min)	Depth of penetration (mm/rev)
Dry	25	0.05
Dry	25	0.1
Dry	25	0.15
Dry	25	0.2
Dry	50	0.05
Dry	50	0.1
Dry	50	0.15
Dry	50	0.2
Dry	100	0.05
Dry	100	0.1
Dry	100	0.15
Dry	100	0.2
Cryogenic	25	0.05
Cryogenic	25	0.1
Cryogenic	25	0.15
Cryogenic	25	0.2
Cryogenic	50	0.05
Cryogenic	50	0.1
Cryogenic	50	0.15
Cryogenic	50	0.2
Cryogenic	100	0.05
Cryogenic	100	0.1
Cryogenic	100	0.15
Cryogenic	100	0.2

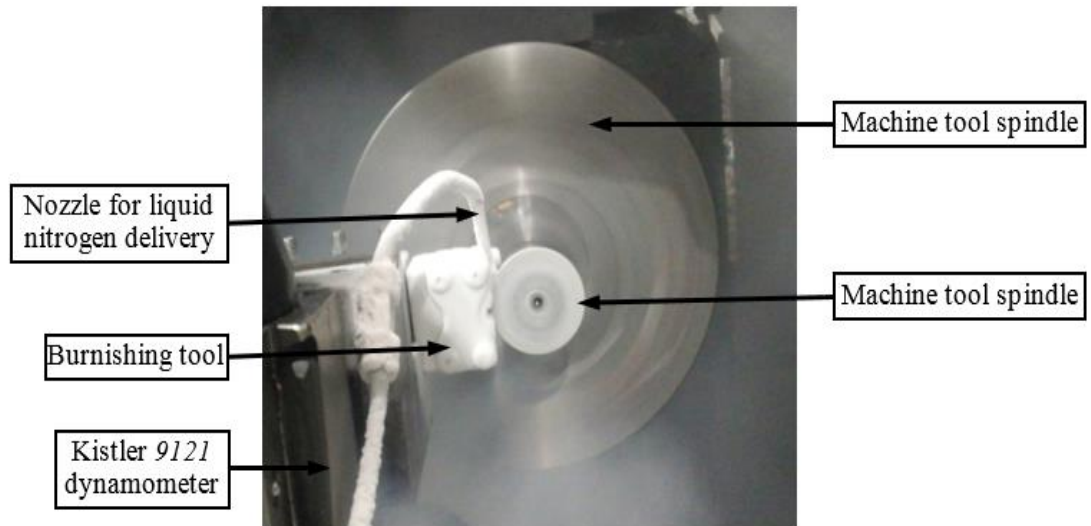


Figure 5.1: Experimental setup for orthogonal cryogenic burnishing.

5.3 Experimental results and discussion

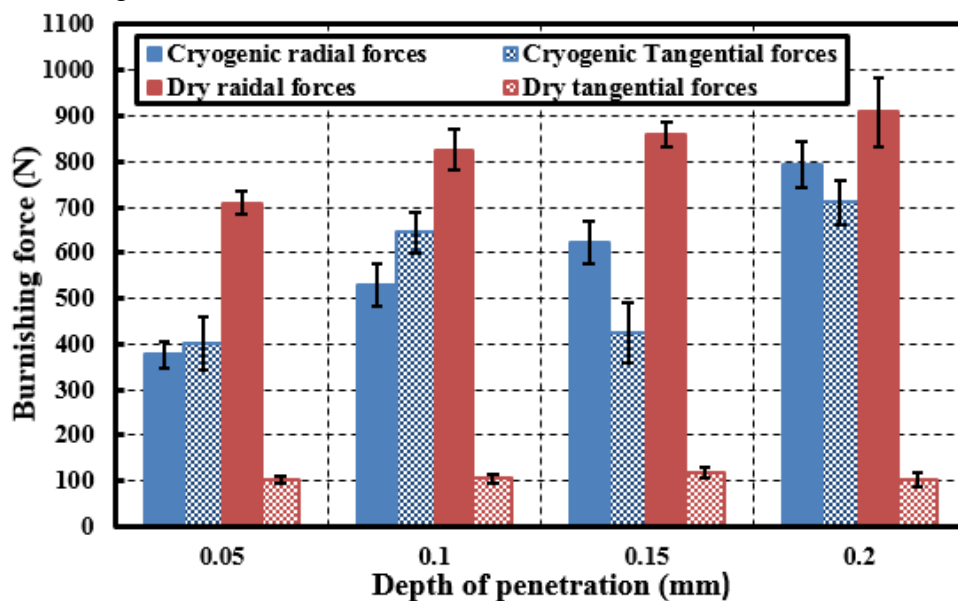
5.3.1 Burnishing forces

Two components of the burnishing force, representing the radial and tangential forces, were measured during the burnishing experiments under dry and cryogenic conditions. As shown in Figure 5.2, for the radial forces, as the depth of penetration increases, the radial forces of both dry and cryogenic burnishing increase. However, the radial forces measured from cryogenic burnishing are not affected by the various burnishing speeds of 25, 50, 100 m/min, and their values are very close to each other when the same depth of penetration is applied. While in the dry condition, the radial forces decrease as the burnishing speeds increase when the same depth of penetration is used. The thermal softening effect becomes more dominated which leads to reduced yield stress of *Al 7050-T7451* alloy when the temperature of dry burnishing raises with increasing burnishing speed. It explains the decreasing of the radial forces under the condition of

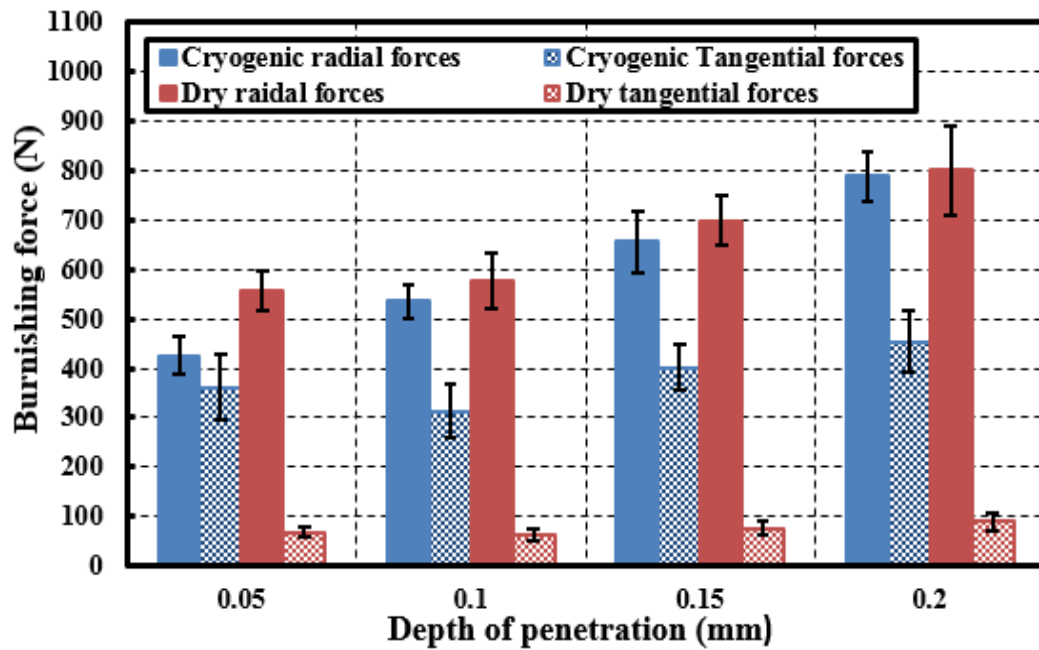
dry burnishing. The details of temperatures achieved in dry burnishing will be discussed in the next section.

Due to the rapid cooling effect of liquid nitrogen, the heat generated during burnishing can be taken away by liquid nitrogen in a relatively short time. Thus, the work hardening effect plays a more important role, while the effect of thermal softening is very marginal. The radial forces increased when increasing the depth of penetration due to more heavier severe plastic deformation. On the other hand, both the tangential forces in dry and cryogenic burnishing increase as the depth of penetration was increased. The tangential forces reduced as the burnishing speed increases at the same depth of penetration due to the thermal softening effect. Compared with dry burnishing, the tangential forces are much higher, as the material becomes harder and stronger due to the cryogenic cooling effect and the resulting higher yield stress (Zhao and Hong, 1992) making the material more difficult to be burnished. Similar experimental findings were also reported by Yang et al. (2011).

(a) Burnishing forces ($V = 25$ m/min)



(b) Burnishing forces ($V = 50$ m/min)



(c) Burnishing forces ($V = 100$ m/min)

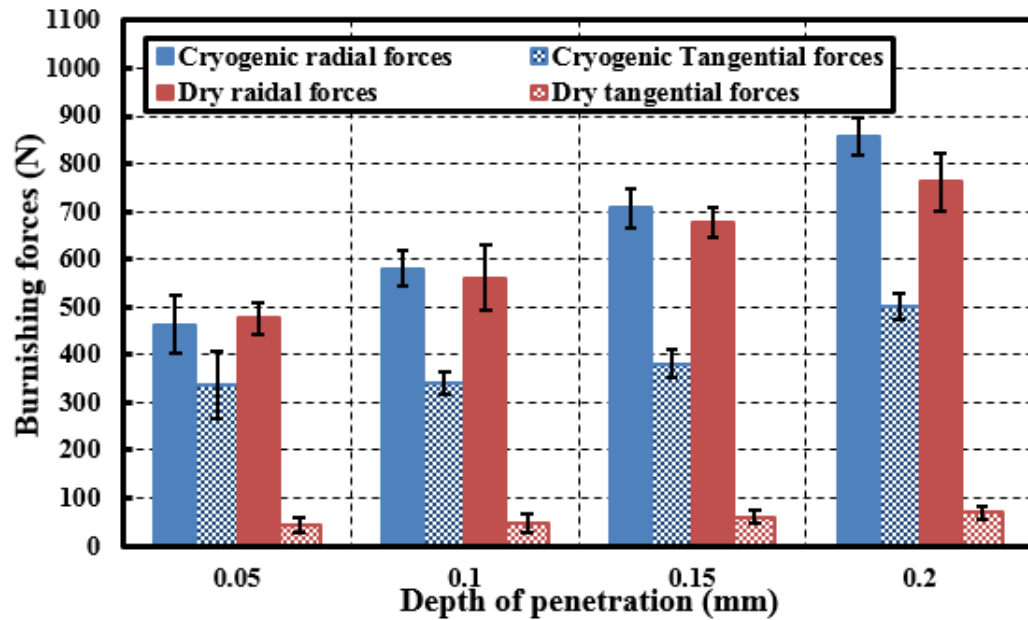


Figure 5.2: Radial and tangential burnishing forces under four different depths of penetration: (a) at the burnishing speed of 25 m/min; (b) at the burnishing speed of 50 m/min; and (c) at the burnishing speed of 100 m/min.

5.3.2 Burnishing temperatures

The highest temperatures were measured by a FLIR infrared camera associated with the corresponding software in the experiments of dry burnishing. As the emissivity is one of the important factors influencing the accuracy of the temperature measurement, it is determined by reviewing the previous work on processing *Al 7050-T7451* alloys. As discussed in the previous chapter in Section 4.3.2 of cryogenic machining, the value of 0.09 was used as the emissivity of *Al 7050-T7451* alloys in the burnishing experiments.

As shown in Figure 5.3 (a), the white rectangular box represents the area, where the highest temperature is measured in the contact zone between the burnishing tool and the work material during dry burnishing. Whereas in cryogenic burnishing, the temperature cannot be measured as the heat generated during burnishing is taken away by liquid nitrogen in a very short time, which is beyond the capability of the infrared camera to record the temperature below zero degree in Celsius. Observed from Figure 5.3 (b), the highest temperature measured in the contact zone increased when increasing the depth of penetration within the range from 0.05 to 0.2 mm at the same burnishing speed. Higher processing temperature is introduced from more severe plastic deformation due to the increment of depth of penetration (Yang, 2012). A similar increasing trend is also found when increasing the burnishing speed within the range from 25 to 100 m/min at the same depth of penetration. Since more heat would build up in the tool-workpiece contact area during the same dwelling time of about 10

seconds after the depth of penetration was reached, the temperature is higher at higher speeds. This phenomenon was also demonstrated in the work of Yang (2012).

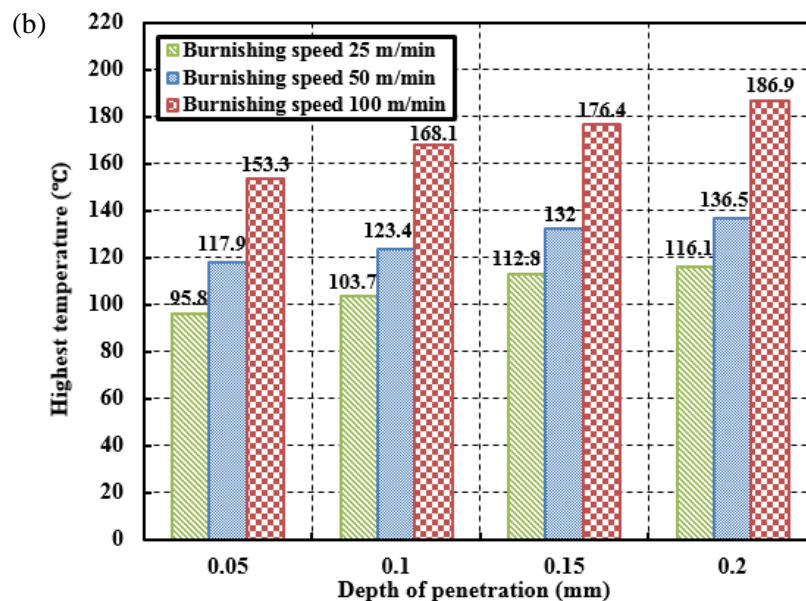
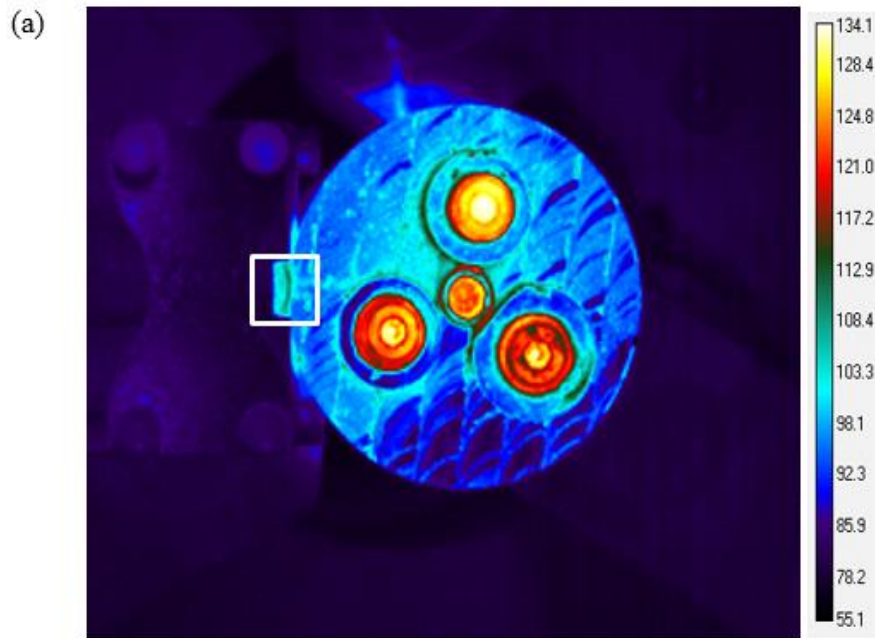


Figure 5.3: (a) The infrared image of temperature measurement (dry burnishing under the depth of penetration of 0.2 mm and burnishing speed of 25 m/min); and (b) The highest temperatures measured in dry burnishing at three different burnishing speeds of 25, 50 and 100 m/min and four different depths of penetration of 0.05, 0.1, 0.15 and 0.2 mm.

5.3.3 Microstructure

An apparent microstructure change was observed from cryogenic burnishing, where a refined layer was generated in the burnished surface. The formations of the refined layer with a featureless characteristics and the subsequent burnishing-influenced layer with a pattern of sweeping grains are very obvious in the burnished surface and sub-surface under the cryogenic condition, as shown in Figure 5.4. Also, nano-grains with the grain size of 38.9 ± 3.3 nm (95% confidence level), seen in Figure 5.4 (a), were measured by using AFM to show the characteristics of the refined layer obtained in cryogenic burnishing, when the depth of penetration was 0.2 mm and the burnishing speed was 25 m/min. However, there is no microstructure change observed in the surface and subsurface of the burnished sample in dry burnishing. DRX occurs during dry burnishing, but the heat generated in dry burnishing could not be taken away quickly enough, and the newly-formed recrystallized grains would become larger and close to the bulk materials with near-UFG structure. This point is also proved by the experimental findings presented in the previous chapter when dry machining is used to turn the disc of *Al 7050-T7451* alloy with near-UFG structure.

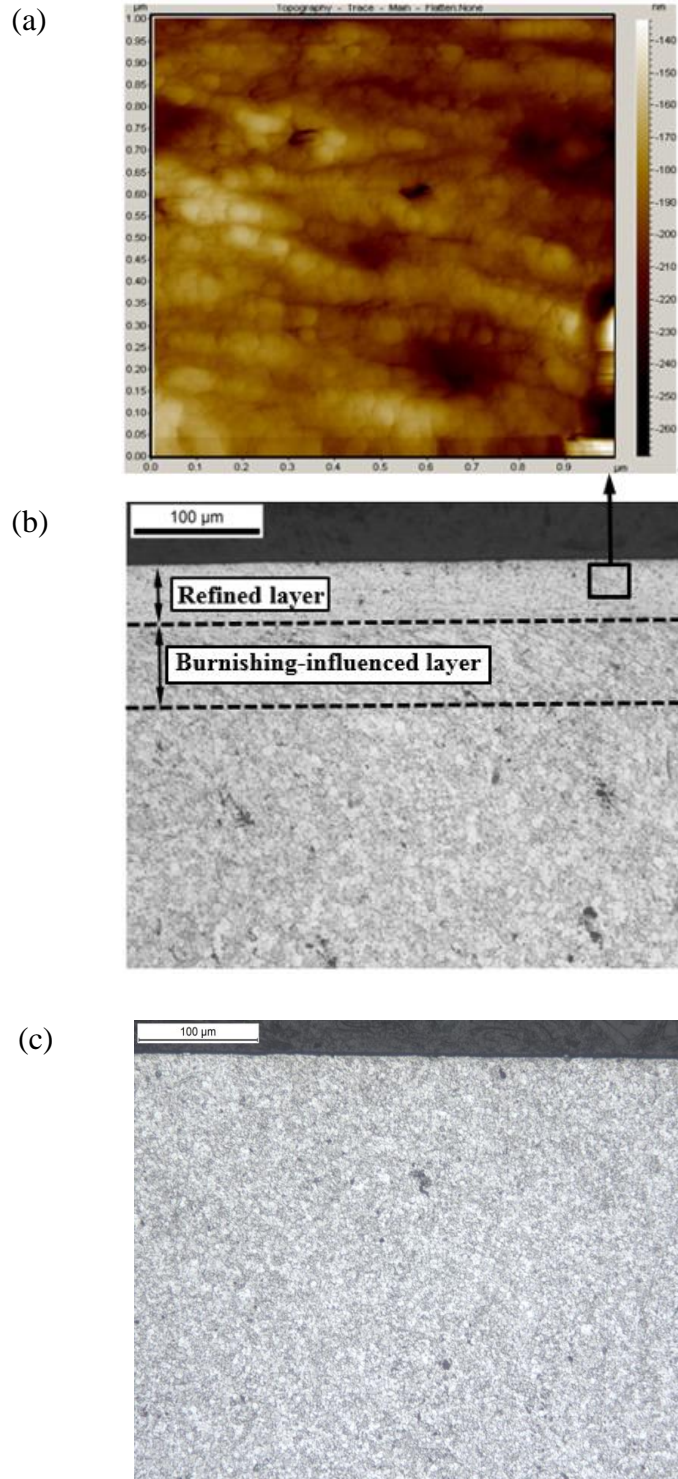
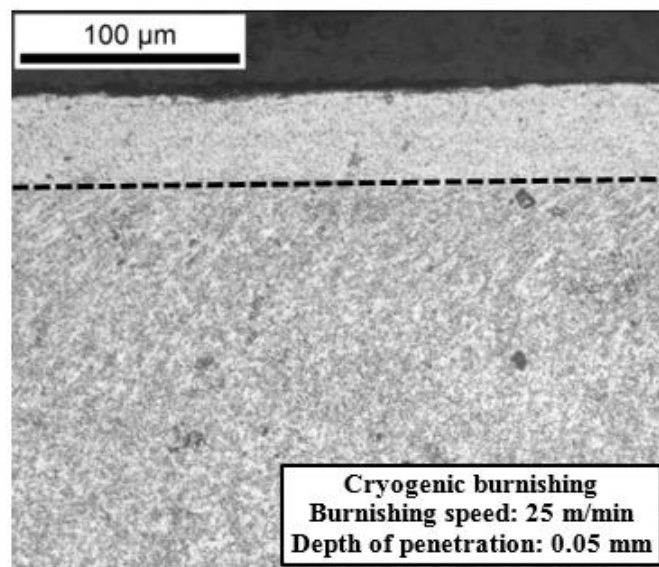


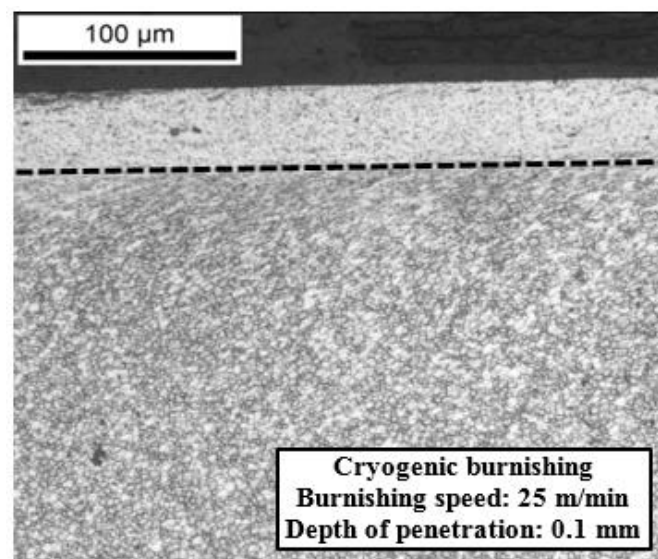
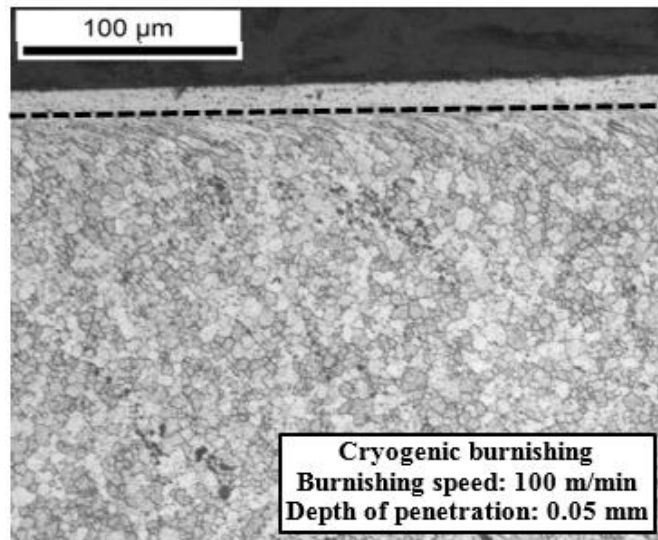
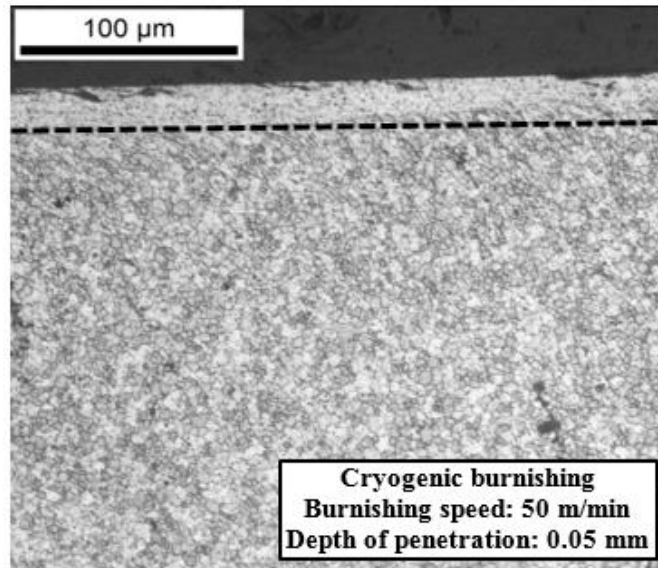
Figure 5.4: The microstructure of *Al 7050-T7451* alloy with near-UFG structure processed by cryogenic burnishing at the depth of penetration of 0.2 mm and burnishing speed of 25 m/min: (a) AFM image (measured from the refined layer denoted by the black rectangular box); (b) the microstructure of the burnished surface and sub-surface generated by cryogenic burnishing; and (c) the microstructure of the burnished surface and sub-surface generated by dry burnishing.

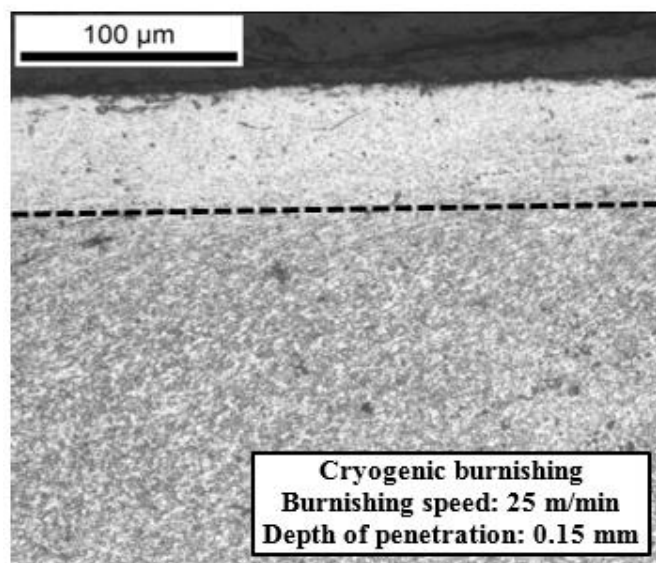
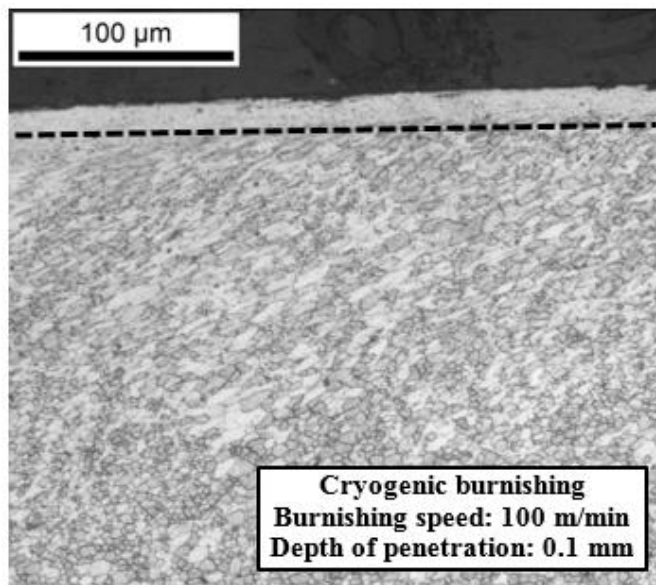
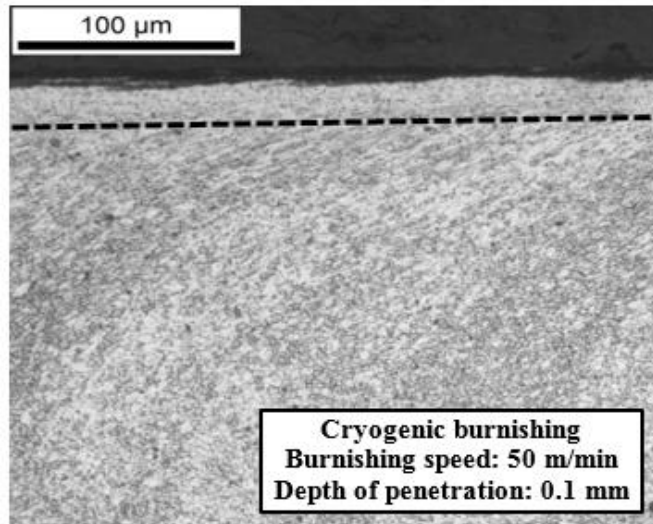
All details of the microstructure changes are shown in Figure 5.5 to demonstrate the microstructure images in the surface and sub-surface of the burnished samples under three burnishing speeds: 25, 50, 100 m/min, and four depth of penetrations: 0.05, 0.1, 0.15, 0.2 mm, in order to comprehensively understand the effects of cryogenic burnishing on the surface integrity of *Al 7050-T7451* alloy with near-UFG structure. The average values of refined layer depth were measured from the microstructure images, as shown in Figure 5.6. Concluded from the observations of Figures 5.5 and 5.6, the burnishing speed plays a more significant role in the microstructure change reflected by the depth of refined layers. Obtained at the burnishing speed of 25 m/min at four different depths of penetration, the average depth of refined layers is approximately 50 μm , and at the burnishing speeds of 50 and 100 m/min, the depths of refine layers are 26 and 19 μm , respectively.

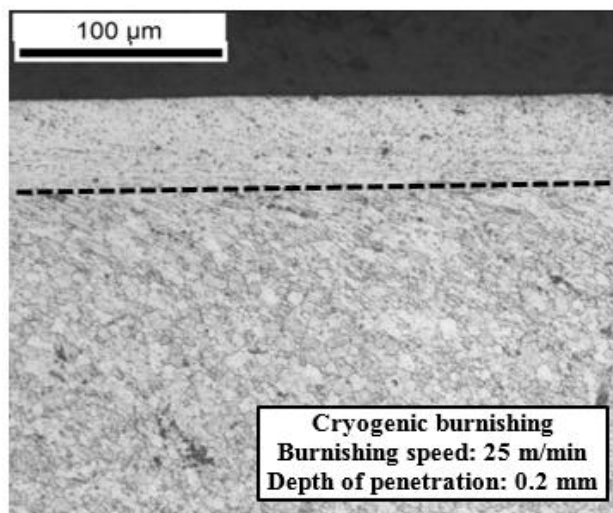
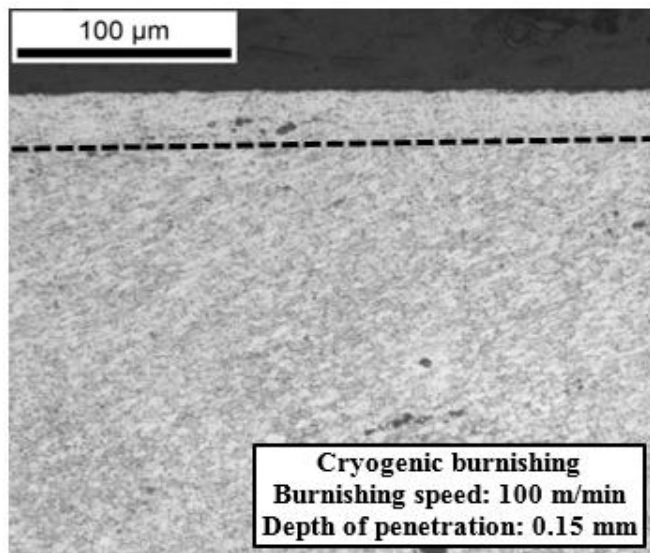
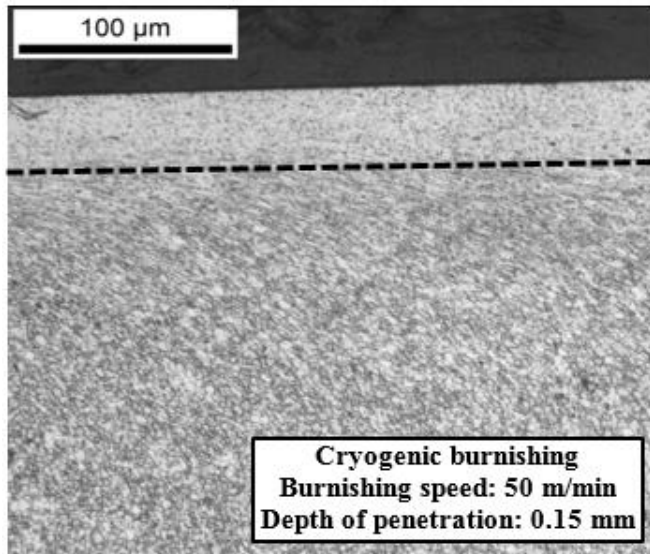
More heat is generated during burnishing when a higher burnishing speed is used. Even for cryogenic burnishing, it takes some time for the liquid nitrogen to take away the heat completely. During this short period of time, the recrystallized grains are growing as the heat stays on the burnished surface after DRX occurs. This phenomenon is clearly observed from the microstructure images when the burnishing speeds are 50 and 100 m/min. The depth of refined layers could reach 50 μm when the burnishing speed of 25 m/min is used as the heat generated during burnishing is taken away by liquid nitrogen quickly enough, it suppresses the grain growth of the recrystallized grains and their grain size can be maintained at a nanometer level.

On the other hand, the effect of depth of penetration is minor on the microstructure change for this material in burnishing. There is a slightly increasing trend for the depth of refined layer when the depth of penetration increases. It is due to the stronger thermal softening effect when the depth of penetration increases as the temperature would reach a higher level before the heat is taken away by liquid nitrogen, as reflected by the temperature measurements of dry burnishing discussed before. However, the work hardening effect introduced by cryogenic burnishing balances the increasing thermal softening effect, which leads to no significant change in the depth of refined layers. Yang (2012) demonstrated this point in cryogenic burnishing of *Co-Cr-Mo* biomedical alloys.









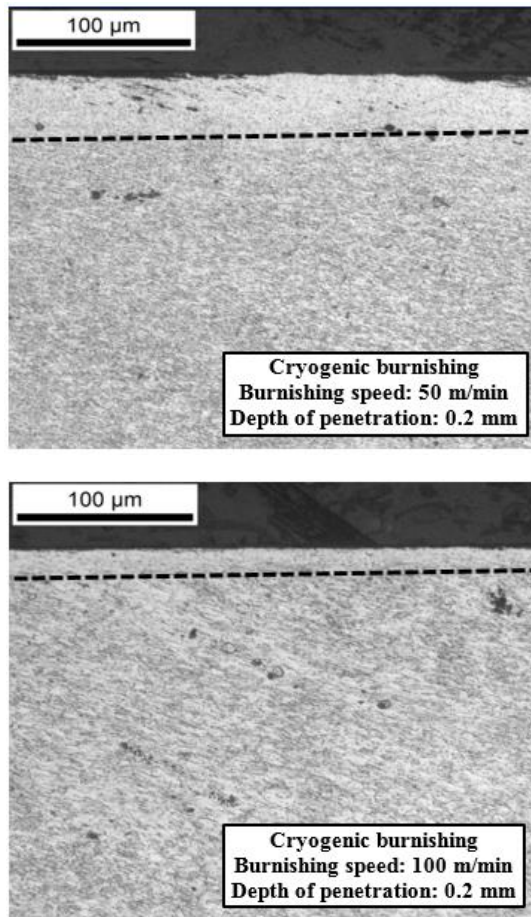


Figure 5.5: The microstructures of *Al 7050-T7451* alloys with near-UFG structure processed by cryogenic burnishing under the depths of penetration of 0.05, 0.1, 0.15, 0.2 mm and burnishing speeds of 25, 50, 100 m/min.

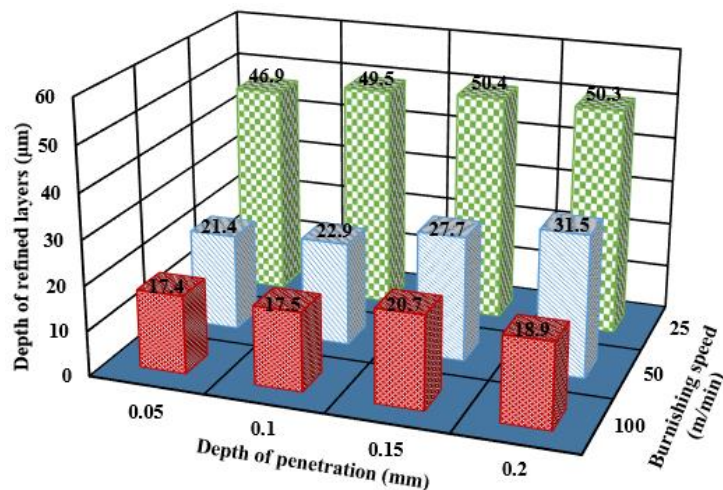


Figure 5.6: The depths of refined layers of *Al 7050-T7451* alloys with near-UFG structure processed by cryogenic burnishing under the depths of penetration of 0.05, 0.1, 0.15, 0.2 mm and burnishing speeds of 25, 50, 100 m/min.

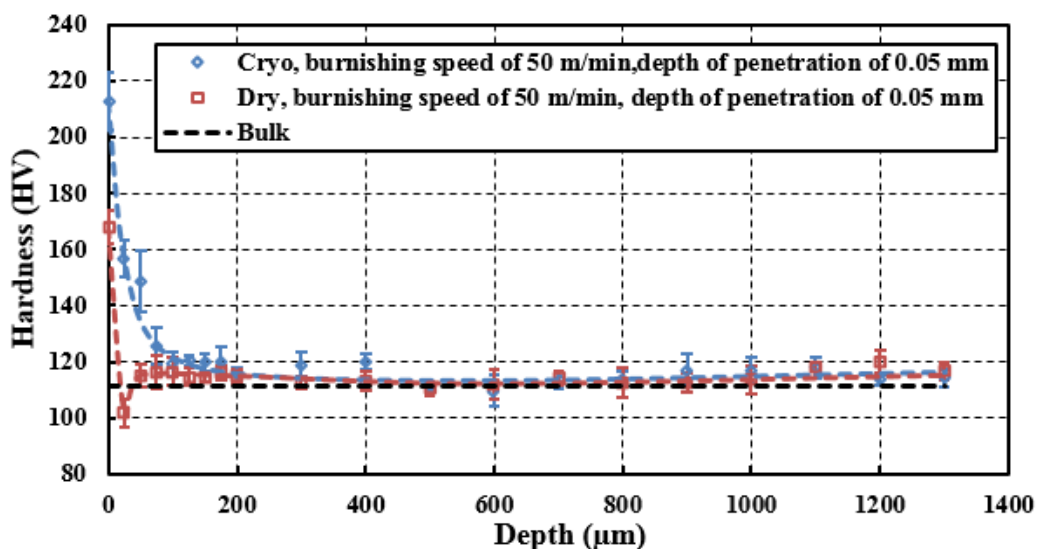
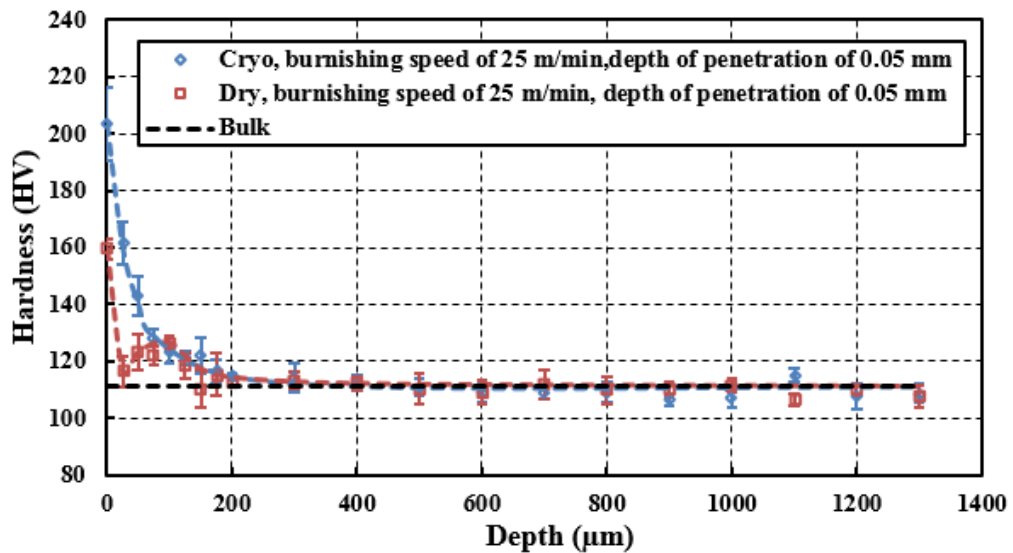
5.3.4 Hardness

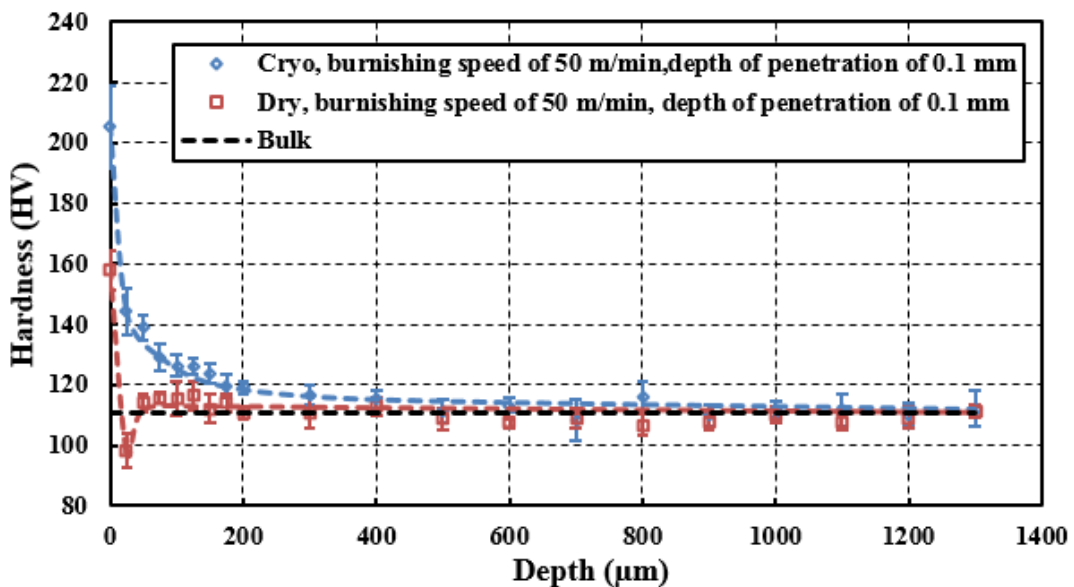
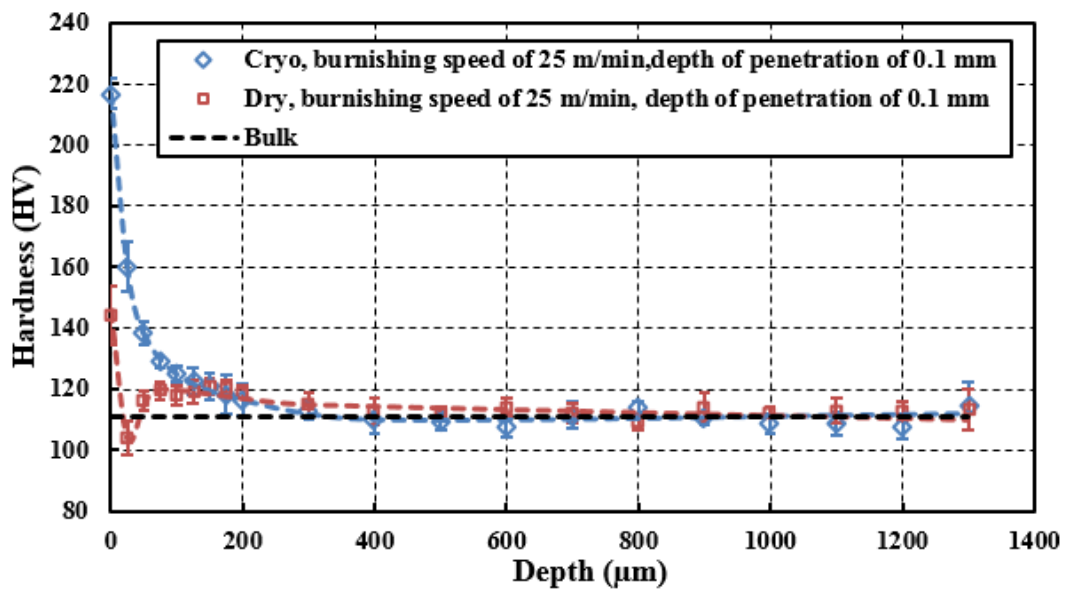
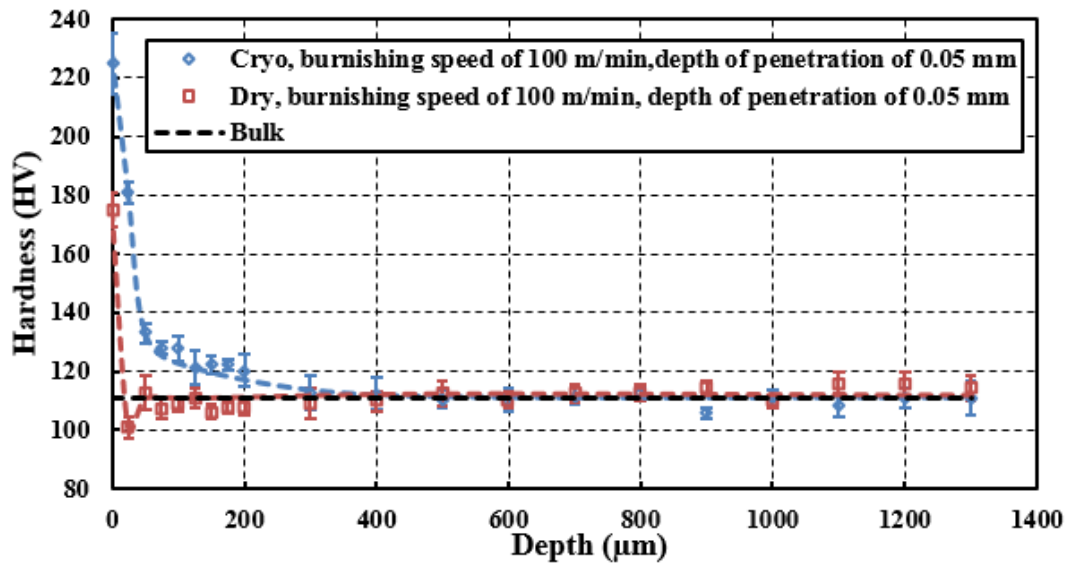
The hardness of the surface and sub-surface in the burnished samples was measured for each experimental condition under three burnishing speeds and four depths of penetration. As shown in Figure 5.7, the average surface hardness measured in the burnished surface is approximately 200 HV, which almost double the hardness of the bulk material. For dry burnishing, the surface hardness ranges from 140 to 160 HV that is also superior to the hardness of bulk materials. However, due to the formation of refined layers and burnishing-influenced layers induced by cryogenic burnishing, the hardness of surface and sub-surface layers is higher than the one measured from dry burnishing, especially within the depth of 200 μm . It is reflected by the hardness distribution along the depth plotted in Figure 5.7.

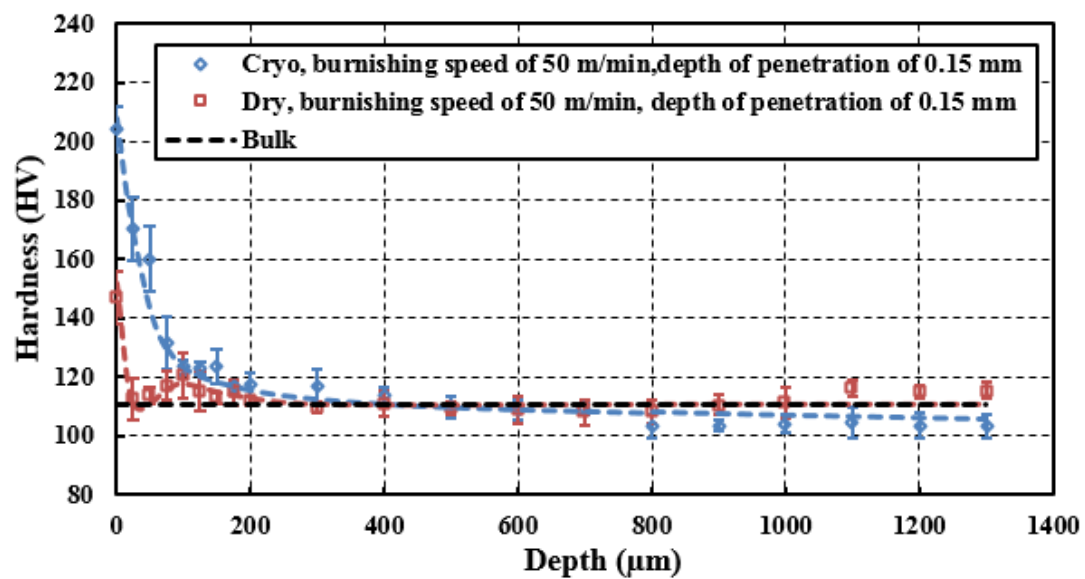
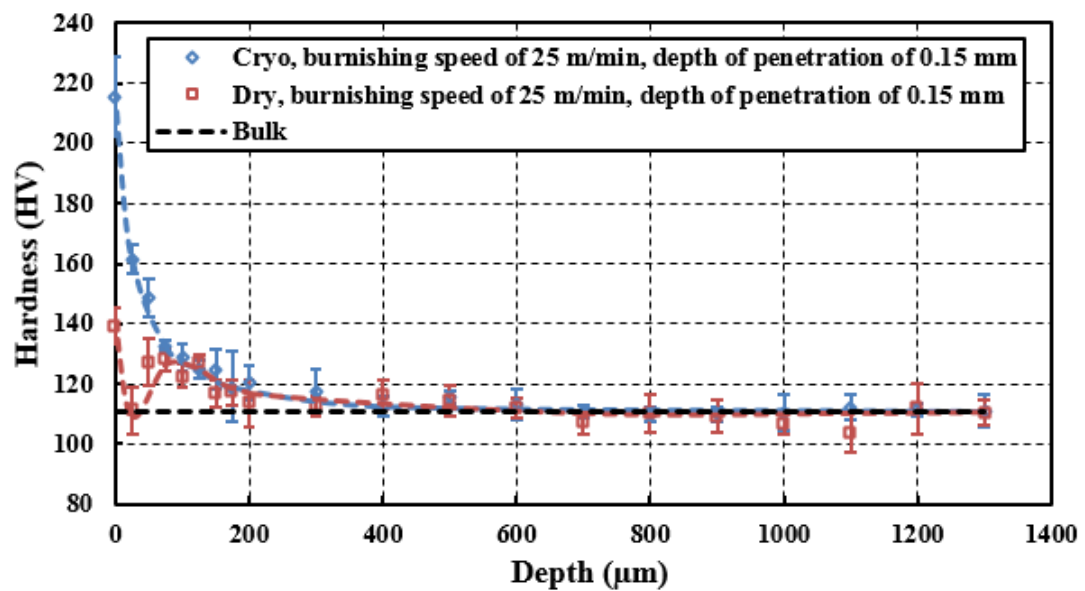
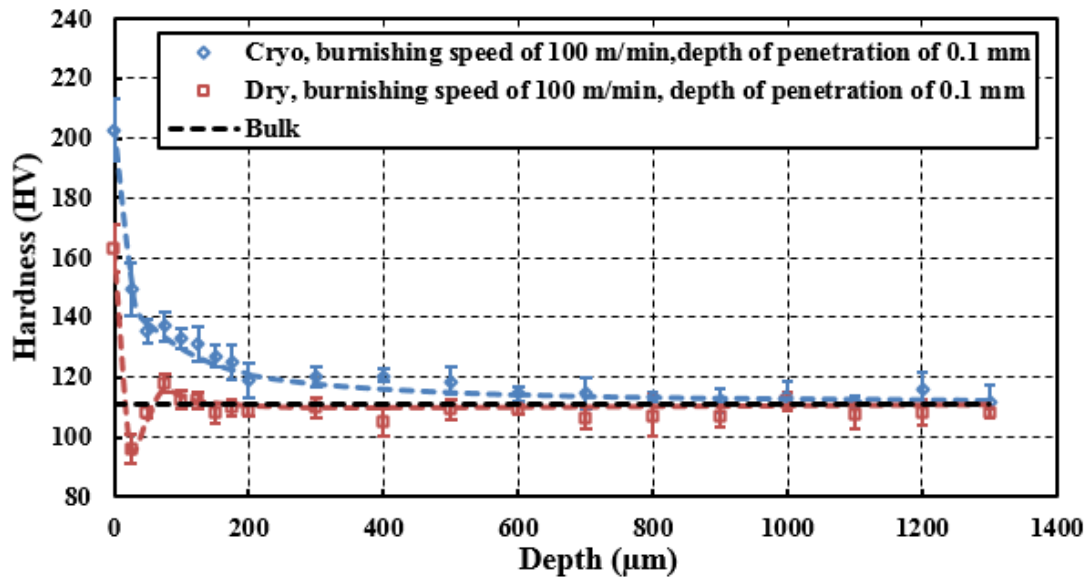
In order to study the hardness increase caused by burnishing more precisely, the average hardness within the depth of 200 μm is calculated by averaging the hardness values measured at the depth of every 25 μm , starting from the surface until the depth of 200 μm , for all conditions in dry and cryogenic burnishing. As seen from Figure 5.8, the hardness increase induced by cryogenic burnishing is relatively consistent because the work hardening effect plays a more critical role compared with the thermal softening effect as the heat generated during burnishing is taken away very quickly by the delivery of liquid nitrogen.

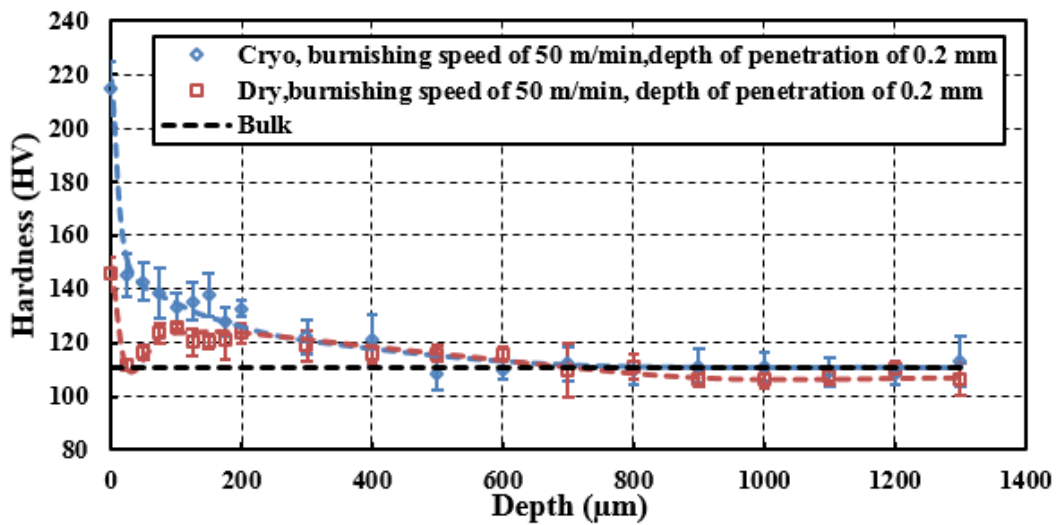
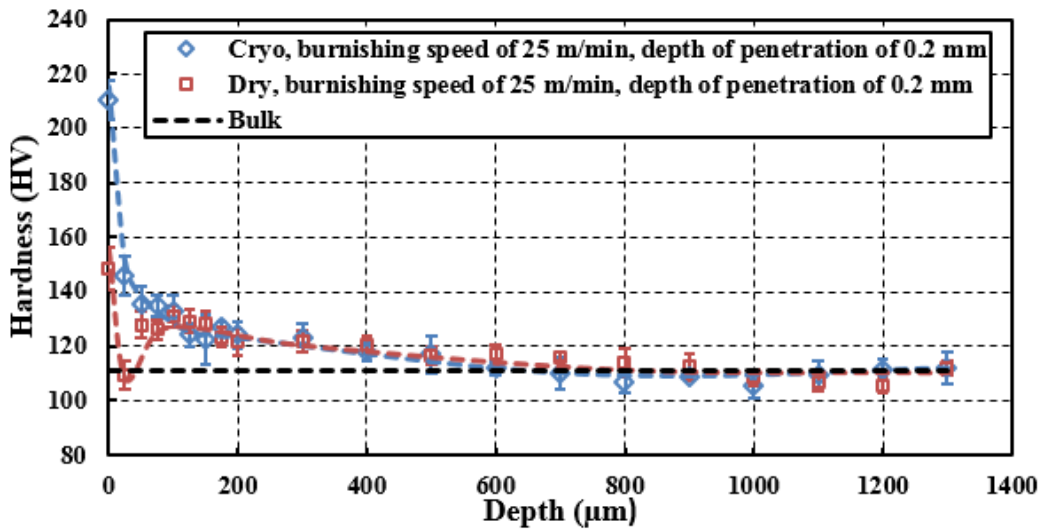
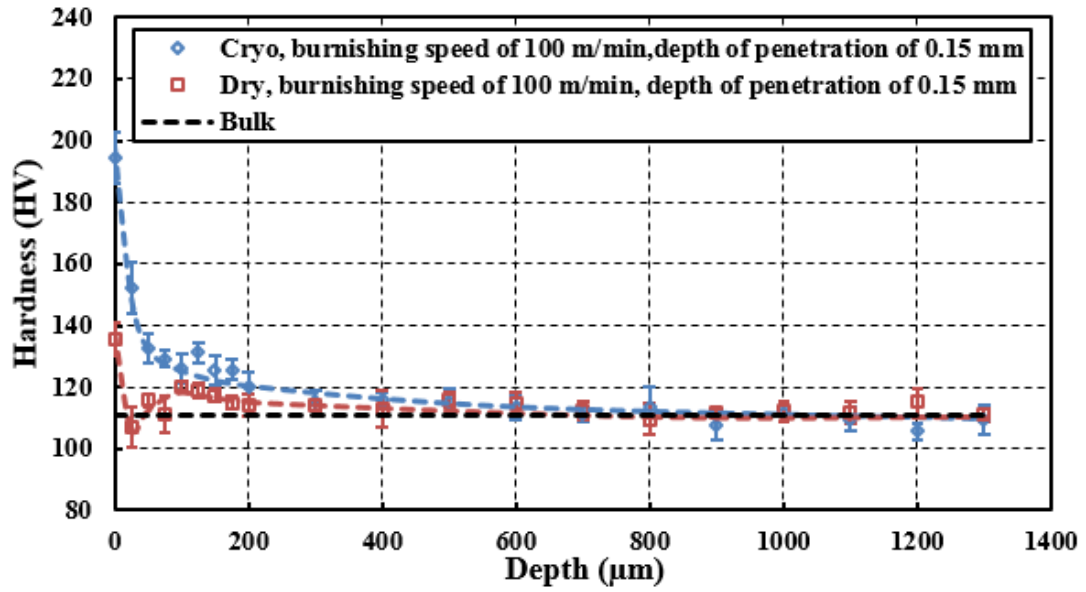
The average hardness increase with the range from 20% to 30% within the 200 μm depth, is obtained by cryogenic burnishing. In dry burnishing, a hardness increase of 14.7% is achieved when using the depth of penetration of 0.2 mm and the burnishing

speed of 25 m/min. Thermal softening effect is a more dominating factor in dry burnishing due to lack of rapid cooling. The hardness increase becomes marginal when the burnishing speed is higher as there is more thermal softening effect, owing to more heat generated during burnishing. However, when the burnishing speed is maintained as constant, the hardness increase is also influenced by the work hardening effect. More work hardening effect is induced as the depth of penetration increases compared with thermal softening effect in dry burnishing. Therefore, the hardness increase becomes greater when increasing the depth of penetration at a given burnishing speed.









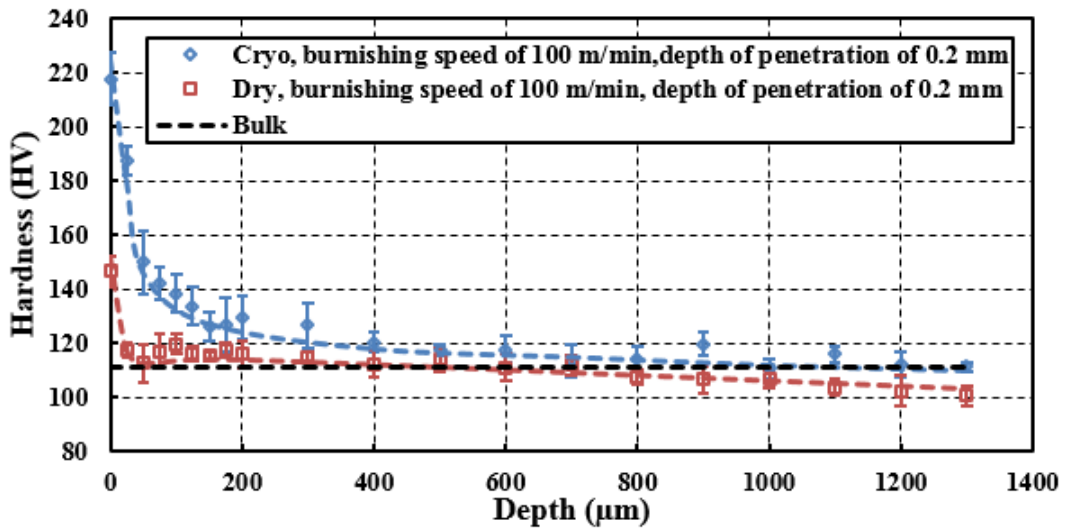
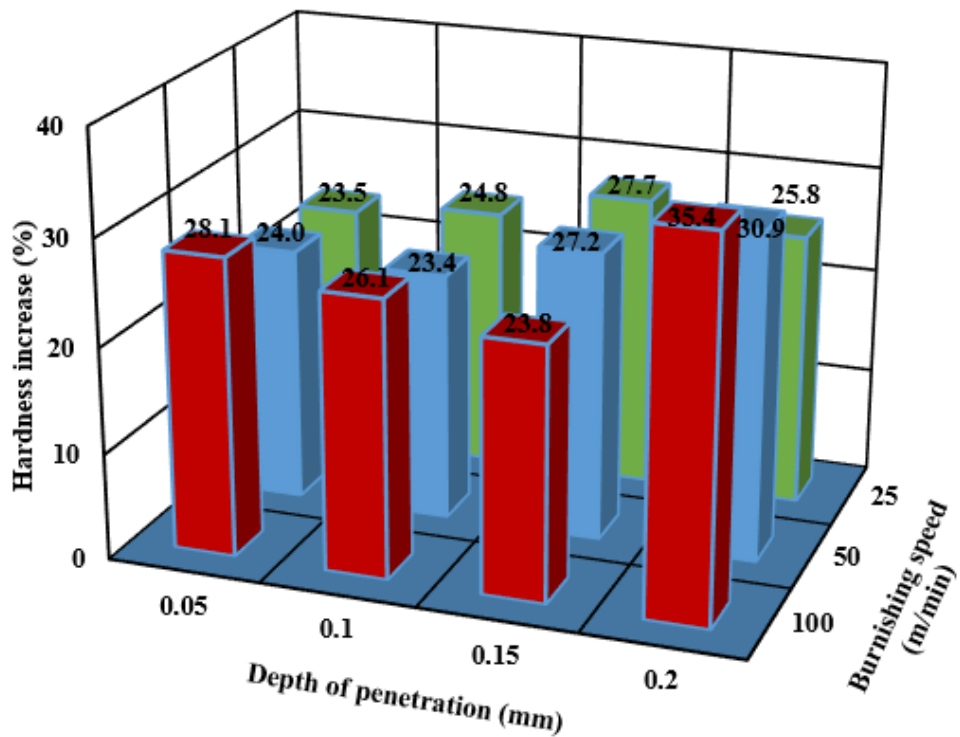


Figure 5.7: The hardness distributions of *Al 7050-T7451* alloys with near UFG structure processed by dry and cryogenic burnishing at the depths of penetration of 0.05, 0.1, 0.15, 0.2 mm and burnishing speeds of 25, 50, 100 m/min.

(a)



(b)

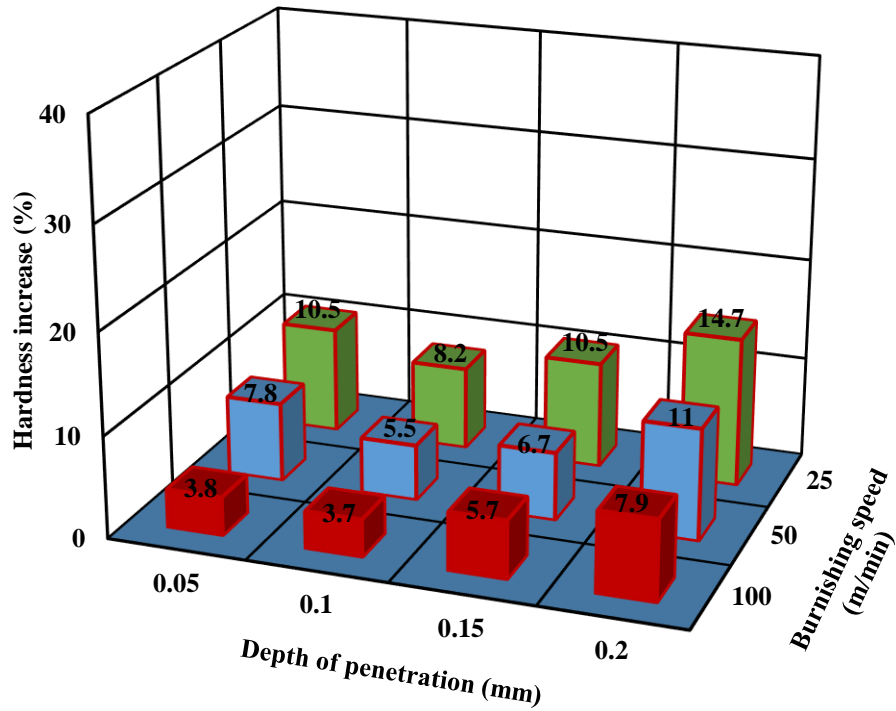


Figure 5.8: Hardness increase of *Al 7050-T7451* alloys with near-UFG structure processed by dry and cryogenic burnishing at the depths of penetration of 0.05, 0.1, 0.15, 0.2 mm and burnishing speeds of 25, 50, 100 m/min: (a) cryogenic burnishing; and (b) dry burnishing.

5.4 Chapter conclusion

Dry and cryogenic burnishing experiments were performed in the study presented in this chapter. Burnishing effects with the mechanism of SPD, associated with the cooling effect of liquid nitrogen, contributed to significant improvements of surface integrity characteristics, particularly from the viewpoints of microstructure and hardness. The measurement of burnishing forces and temperatures provided the evidence for better understanding dry and cryogenic burnishing of *Al 7050-T7451* alloys with near-UFG structure. The major findings observed from the burnishing experiments are summarized as follows:

- In dry burnishing, the burnishing forces showed an increasing trend when the depth of penetration increased due to more work hardening effect with high strain and strain-rate induced by burnishing. However, when the burnishing speed was increased, because of more thermal softening effect reflected by the measurements of burnishing temperatures, less burnishing forces were observed.
- In cryogenic burnishing, the same increasing trend was also found from the measurements of burnishing forces, especially the radial components, when the depth of penetration was selected to be higher. Compared with dry burnishing, the radial burnishing forces were higher because the work materials became harder due to the cryogenic cooling effect.
- Burnishing temperatures increased with the increased depth of penetration and burnishing speed, and this phenomenon was shown by the measurements of highest burnishing temperatures in dry burnishing.
- The microstructure images demonstrate the formation of refined layers and burnishing-influenced layers in the burnished surface and sub-surface induced by cryogenic burnishing. Average depths of refined layers were approximately 50, 26, 19 μm measured from the microstructure images acquired in cryogenic burnishing under the burnishing speeds of 25, 50 and 100 m/min, respectively.
- Up to 35.4% hardness increase was achieved within the layer depth of 200 μm in the burnished surface introduced by cryogenic burnishing, while dry burnishing only resulted in up to 14.7% hardness increase.

In addition to this experimental study, findings of the theoretical work will be presented in the next chapter to enable good and meaningful knowledge about burnishing process. The prediction of variables in the burnishing process will be performed numerically by using a FEM-based software DEFORM, and the simulation results will be compared with the experimental results for the purpose of verification and modification of the burnishing model developed, based on a modified Johnson-Cook material model associated with the specific setting of cryogenic cooling window.

CHAPTER 6

FINITE ELEMENT MODELING OF SURFACE LAYER MODIFICATION INDUCED BY CRYOGENIC BURNISHING

6.1 Introduction

In Chapter 2, under the literature review, modeling work conducted by other previous researchers was summarized. Modeling of burnishing processes was somewhat limited, but some of the previous research focused on the theoretical studies for predicting the surface profile/roughness and, residual stresses induced by the burnishing process, through the analytical or numerical modeling. However, the simulations of surface integrity characteristics are rarely investigated by the research community, especially for burnishing operations.

It is important to conduct theoretical work for accurately predicting major surface integrity characteristics, such as grain size, hardness, depth of surface layer, residual stresses, etc., as these parameters directly influence the wear/corrosion resistance and fatigue life of the burnished components. Accurate modeling and simulation could minimize the numbers of practical experiments to verify the burnishing effects induced in the burnished components and help to reduce the trial and error based experimental work and improve product design activities.

A FEM-based model is developed to predict burnishing forces and temperatures, and in comparison with the experimental results, the model is verified and modified for better accuracy in prediction. A Johnson-Cook material equation is also implemented in the program, and modified and used to accurately describe the flow stress of *Al 7050-*

T7451 alloys in the burnishing model performed by using the commercial FEM-based software DEFORM. Moreover, the depth of SPD layer is predicted and compared with the measured values from the microstructure images.

6.2 Modeling setup

6.2.1 Numerical setup of work material and burnishing tool

The burnishing model was developed to simulate the burnishing effects of dry and cryogenic burnishing on forces, temperatures and the depth of SPD layer. Previous modeling work by Yen et al. (2005) and Yang (2012), provided some guidance to understand the modeling setup and development. The utilization of the commercial FEM code DEFORM-2D facilitated the modeling work, and user-routines describing detailed FORTRAN programs allow the users to modify the flow stress, grain size calculation, etc. Robust remeshing also allows a simulation to continue when the self-contact boundary condition undergoes a lap or fold formation.

The work material with a rectangular dimension of 22 mm × 3.8 mm was used in the model, and it consists of 8500 isoparametric quadrilateral elements. In order to obtain more accurate simulation results, a mesh density window was used to apply a higher mesh density by adjusting the user-defined distribution weighting. For the mesh window used for the work material, a rectangular window of 20 mm × 1 mm was applied on the surface of the work material in which the smallest element size was approximately 50 μm. On the other hand, the number of quadrilateral elements used for the burnishing tool was 2800. The assumptions were made for the materials of

workpiece and burnishing tool in this burnishing model, and the work material was considered to be plastic, while the burnished tool was assumed to be rigid. However, due to the limitations of corresponding burnishing research and lack of tests for material properties, some of the input parameters have to be determined by evaluating and calibrating the experimental data presented in the previous chapter.

6.2.2 Material properties of work material and burnishing tool

Uncoated carbide was used as the material for the burnishing tool, and it was the same material that previous researcher Yang (2012) selected in her burnishing experiments. The thermal and mechanical properties of this material were taken from her work as listed in Table 6.1. Similarly, the thermal and mechanical properties of *Al 7050-T7451* alloys were determined by reviewing the related work. Young's modulus of this material was found to be within the range between 70 GPa to 72 GPa (Dixit et al., 2008; Liu et al., 2007). Research regarding Poisson's ratio of *Al 7050-T7451* alloys gave a reasonable range from 0.33 to 0.358 (Liu et al., 2007; Zhang et al., 2010; Lalpoor et al., 2009; Slempt et al., 2011).

In addition, the thermal conductivity of the work materials varied when the processing temperature was increased (Zhang et al., 2010; Xu et al., 2011; Hamilton et al., 2009). To take their work into consideration, detailed thermal conductivities corresponding to different temperatures are shown in Table 6.2 (Hamilton et al., 2009). The specific heat capacity is also determined in a similar way through the literature review (Xu et al., 2011; Li et al., 2013; Li et al., 2004; Hamilton et al., 2008; Hamilton et al., 2009), as

listed in Table 6.3. Also, the important properties such as Young’s modulus, Poisson’s ratio and density of *Al 7050-T7451* alloys are summarized in Table 6.4.

Table 6.1: Thermal and mechanical properties of uncoated carbide (Yang, 2012).

Young’s Modulus	N/A
Poisson’s Ratio	0.23
Thermal Conductivity	82.24 W/(m·K)
Specific Heat Capacity	5.79 J/(kg·K)

Table 6.2: Thermal conductivity of *Al 7050-T7451* alloy at various temperatures (Hamilton et al., 2009).

Temperature (°C)	Thermal Conductivity (W/(m·K))
19	155
42	156
77	159
177	171
277	180
377	176
400	174
532	163
640	81
720	85
800	87.5

Table 6.3: Specific heat capacity of *Al 7050-T7451* alloy at various temperatures (Hamilton et al., 2009).

Temperature (°C)	Specific heat capacity (J/(kg·K))
27	2.54
77	2.62
127	2.68
177	2.74
227	2.8
277	2.87
327	2.94
377	3.01
402	3.02
427	3.06
477	3.37

Table 6.4: Thermal and mechanical properties of *Al 7050-T7451* alloy (Hamilton et al., 2009).

Young's Modulus	72 GPa
Poisson's Ratio	0.33
Density	2.83 g/cm ³
Specific Heat Capacity	2.54 J/(kg·K)

6.2.3 Boundary conditions

The work material was considered to be fixed in all directions, and for the first step, the burnishing tool was set to move in the vertical orientation until the desired depth of penetration was achieved for the penetration purpose. In the second step, the burnishing tool could be moved horizontally at a certain burnishing speed. The left and right side of the work material was set to be free, and the temperatures on the left and bottom sides of the work material were considered to be 20°C which was the room temperature. Whereas the right- and top-sides of the work material were available to exchange heat with the environment where the heat convection coefficient was 0.02 kW/(m²K) for free air convection. To do the boundary condition setup of the burnishing tool, the top part was set to be 20°C and the bottom part was also considered to exchange heat with the environment with the same convection coefficient.

In order to simulate the cooling effect of liquid nitrogen, a rectangular window with the size of 3 mm × 1 mm was moving behind the tool in a relatively fixed position, and it could be considered to be attached with the burnishing tool and they moved at the same speed. In the cryogenic window, the local temperature was set to be -184°C, and the convection coefficient of the local heat exchange was assumed to be 10000 kW/(m²K) (Yang, 2012). All details of the boundary conditions are shown in Figure 6.1.

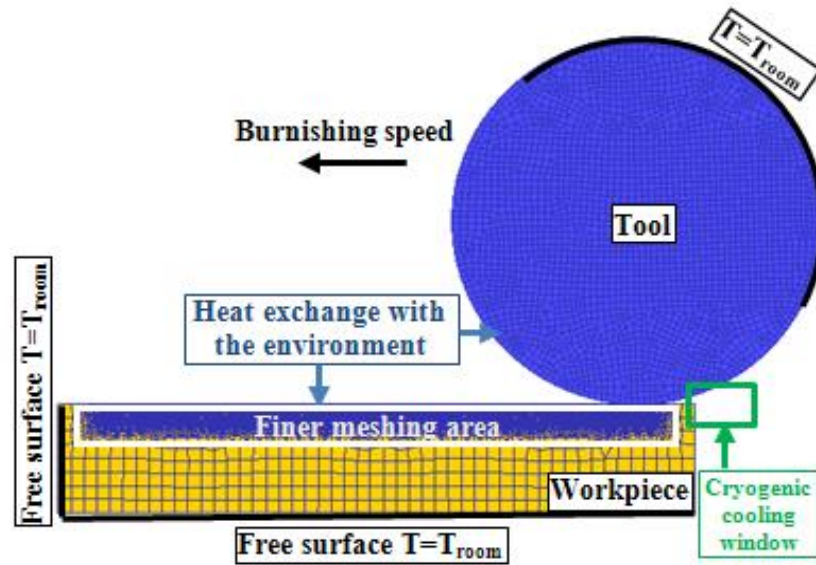


Figure 6.1: The boundary conditions of FEM-based numerical model.

6.2.4 Model of material flow stress

An accurate material flow stress model describing the work material's constitutive behavior, is very necessary for the numerical model in order to obtain better simulation results. As shown in Figure 6.2, the flow stress increases as the strain is increased due to the work hardening effect. In the case of dynamic recovery, the generation and accumulation of dislocation are compromised by the dislocation rearrangement and annihilation (Yang, 2012). A saturated flow stress (σ_{sat}) will be achieved due to the balance between work hardening and softening when a slow processing method is used. Sometimes, DRX will occur if the phenomenon of grain refinement exists. The initiation of DRX starts when the prerequisites are met when the critical strain (ϵ_{cr}) is reached during the process, depending on the material properties. After reaching the point of the critical strain, a peak value of flow stress (σ_p) after which the stress decreased, will be reached when the strain is increased to the peak strain (ϵ_p). A sudden

drop will follow after the peak strain is reached until the flow stress in the steady state (σ_{ss}) is achieved because the grain refinement occurs. In machining, the drop of flow stress due to DRX, was observed when a very high strain-rate induced by machining was used (Umbrello, 2004). Observed from the microstructure images, grain refinement definitely occurred in cryogenic burnishing of *Al 7050-T7451* alloys with near-UFG structure. Therefore, it is necessary to use a proper flow stress model governing before DRX occurs, associated with a constitutive material flow stress model describing the material behavior after DRX occurs.

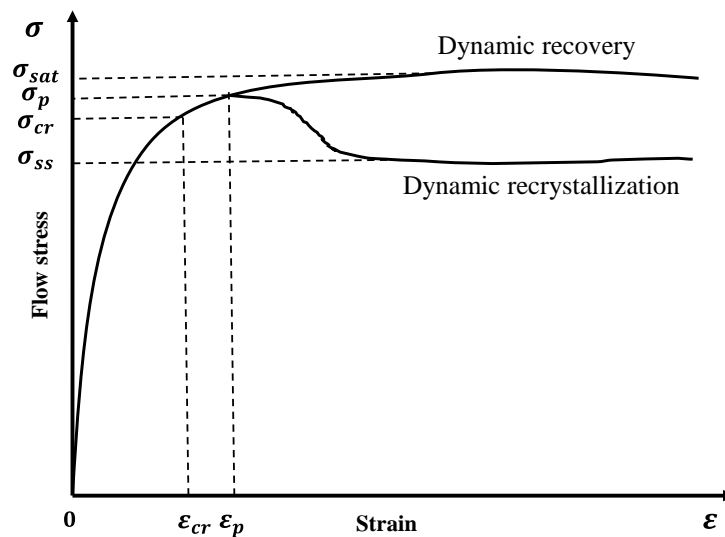


Figure 6.2: The flow stress curve in the case of dynamic recovery and dynamic recrystallization (Sarkar et al., 2011).

Dynamic recrystallization was taken into consideration in order to achieve more accurate simulation results. Before DRX occurs when the critical strain is not reached, the governing flow stress equation used in the theoretical study is Johnson-Cook material model (Johnson and Cook, 1985). After the critical strain is reached, the constitutive equations, characterizing the flow stress behavior after DRX, are borrowed

from a previous study to reflect the effects of microstructure change on the flow stress, based on their experimental results and kinetic analysis (Wu et al., 2012).

A FORTRAN-based user-subroutine has been programmed to apply the flow stress model used in this study by combining Johnson-Cook model governing before DRX and the constitutive equations describing the material behavior after DRX. Figure 6.2 illustrates the dynamic recovery curve relating to the flow stress without considering DRX while the dynamic recrystallization curve corresponds to the flow stress considering DRX (Sarkar et al., 2011). Eqn. (1) is Johnson-Cook flow stress equation and Eqns. (2) to (10) show the constitutive equations describing the flow stress after DRX occurs (Wu et al., 2012).

$$\sigma_{DRV} = (A + B \varepsilon^n)(1 + C \ln \dot{\varepsilon}) \left[1 - \left(\frac{t-t_r}{t_m-t_r} \right)^m \right] (\varepsilon < \varepsilon_{cr}) \quad (1)$$

$$\sigma_{DRX} = \sigma_{DRV} - (\sigma_{sat} - \sigma_{ss}) \left\{ 1 - \exp \left(-K \left(\frac{\varepsilon - \varepsilon_{cr}}{\varepsilon_p} \right)^{1.39} \right) \right\} (\varepsilon \geq \varepsilon_{cr}) \quad (2)$$

$$\sigma_{sat} = 66.4 \sinh^{-1} \left[\left(\frac{Z}{6.23 \times 10^7} \right)^{0.2} \right] \quad (3)$$

$$\sigma_{ss} = 66.4 \sinh^{-1} \left\{ \left[\frac{\dot{\varepsilon} \exp(136836/(R(T+\Delta T)))}{2.07 \times 10^9} \right]^{0.21} \right\} \quad (4)$$

$$Z = \dot{\varepsilon} \exp \left(\frac{122132}{RT} \right) \quad (5)$$

$$\Delta T = 1.30 Z^{0.14} \eta \quad (6)$$

$$\eta = \begin{cases} 1 & (\dot{\varepsilon} \geq 1.0) \\ \frac{1}{3} (3 + \ln(\dot{\varepsilon})) & (10^{-3} < \dot{\varepsilon} < 1.0) \\ 0 & (\dot{\varepsilon} \leq 10^{-3}) \end{cases} \quad (7)$$

$$K = 5.02 \times 10^{-3} Z^{0.13} \quad (8)$$

$$\varepsilon_p = 1.07 \times 10^{-3} Z^{0.19} \quad (9)$$

$$\varepsilon_{cr} = 8.54 \times 10^{-4} Z^{0.19} \quad (10)$$

In Eqns. (1) and (2), σ_{DRV} is the equivalent flow stress of dynamic recovery; The constants A and B represent the initial yield strength and hardness modulus of the material, respectively; C is the strain-rate sensitivity coefficient; ε is the equivalent strain and $\dot{\varepsilon}$ is the effective strain-rate; n and m represent the hardening coefficient and the thermal softening exponent; t , t_m and t_r are the temperatures of the work material, the material melting temperature and the reference room temperature; σ_{DRV} and σ_{DRX} refer to the equivalent flow stresses before and after DRX occurs; σ_{sat} and σ_{ss} are the saturation flow stress without considering DRX and the steady flow stress after DRX occurs; K is the material constant based on the deformation condition; ε_{cr} is the critical strain determining when DRX occurs and ε_p are the peak strain; Z represents Zener-Hollomon parameter where R is the universal gas constant; ΔT and η are the temperature rise and the heat conversion factor.

From the literature review, the material constants were found to be varying, depending on the studies of different researchers due to lack of proper material tests. To determine the material constants of *Al 7050-T7451* alloys, calibrations have been made with the curve fitting between the calculated flow stress and the flow stress data previously established (Wu et al., 2012). Through calibration, constants A and B has been determined and validated between the predicted and experimental results to allow the smallest difference, as discussed in the next section. Learning from the previous work (Wang et al., 2010; Wang et al., 2012; Fu et al., 2010a), the values of C , n , m , t_m and t_r are 0.005, 0.32, 0.99, 635 and 20, respectively, while the material constants of Eqns. (2) to (10) were borrowed from the work of Wu et al. (2012).

6.3 Calibration and validation of burnishing model by comparing the predicted radial burnishing forces and temperatures with the experimental results

The calibration of the numerical 2D model with FEM-based method, was carried out by comparing the predicted and experimental burnishing forces and temperatures. The thermal/mechanical properties, shear friction coefficient and the material constants, A and B used in the modified Johnson-Cook model of *Al 7050-T7451* alloys employed in this model, could be calibrated and modified continuously until the smallest differences between the predicted and experimental results were achieved. The flow chart shown in Figure 6.3 illustrates the working mechanism of the model calibration.

Figures 6.4 and 6.5 give the examples on the calibration procedure, where the radial forces and highest burnishing temperatures were used when using the depth of penetration of 0.2 mm and burnishing speed of 50 m/min in dry burnishing. Through the calibration and validation between the simulated and experimental results, the material constants A and B were determined to be 420 MPa and 30 MPa and the shear friction coefficient was 0.38, which were used in the flow stress and friction models, respectively.

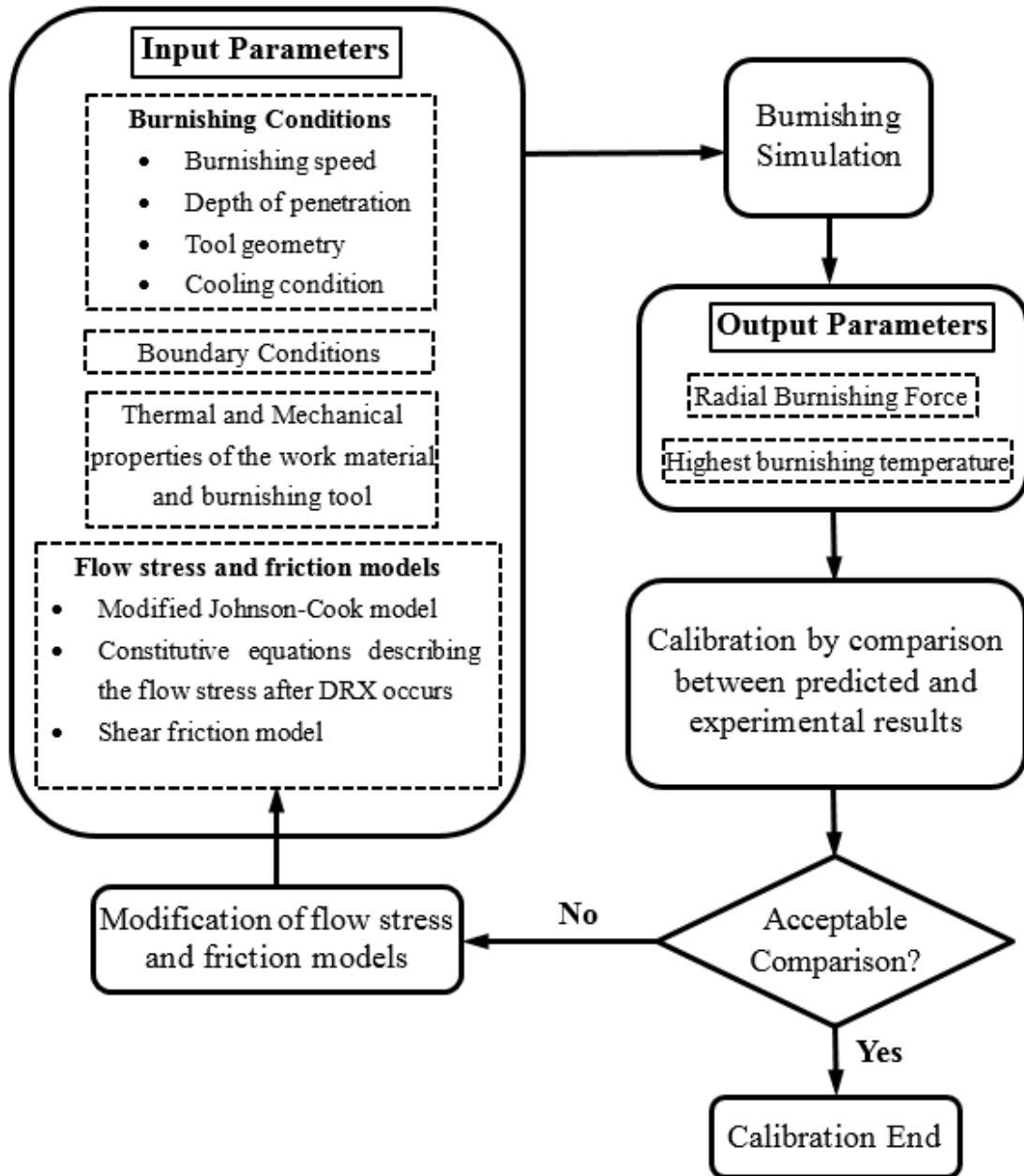


Figure 6.3: Calibration of the numerical burnishing model.

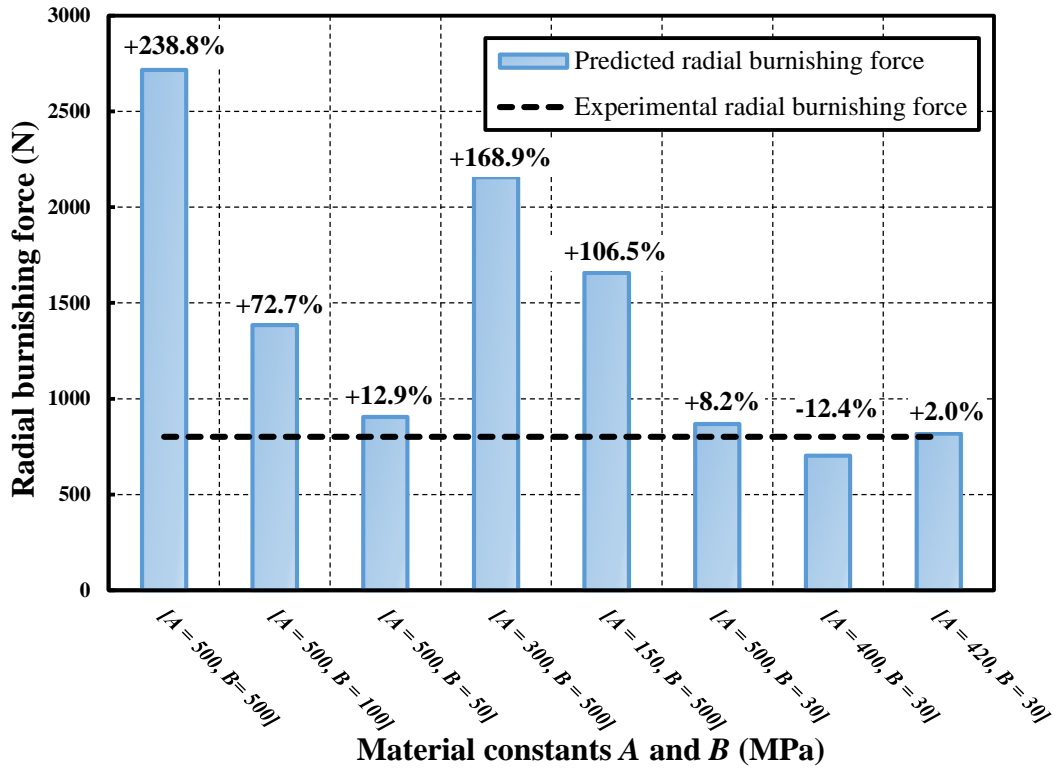


Figure 6.4: The calibration between predicted and experimental results to determine the material constants A and B used in the modified Johnson-Cook material model (dry burnishing, under the burnishing speed of 50 m/min and the depth of penetration of 0.2 mm).

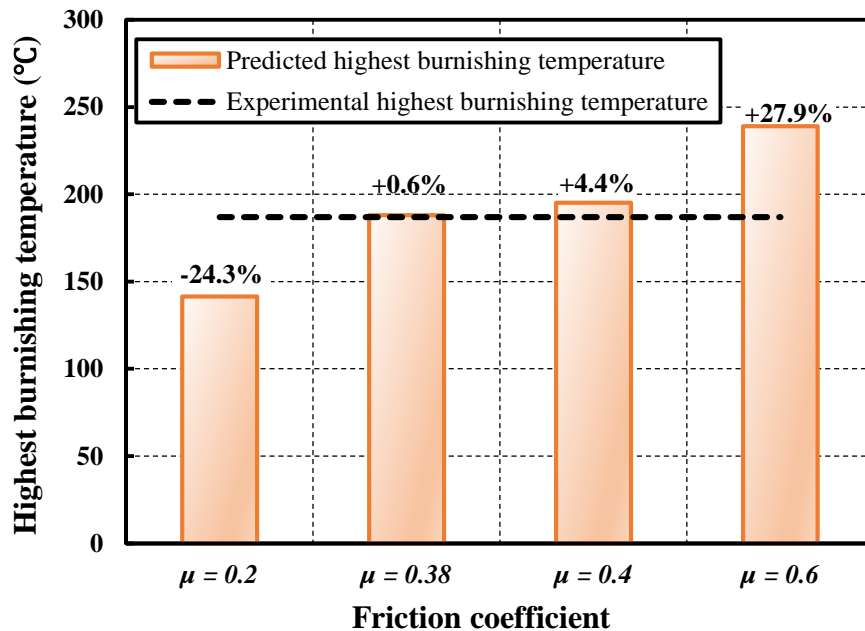
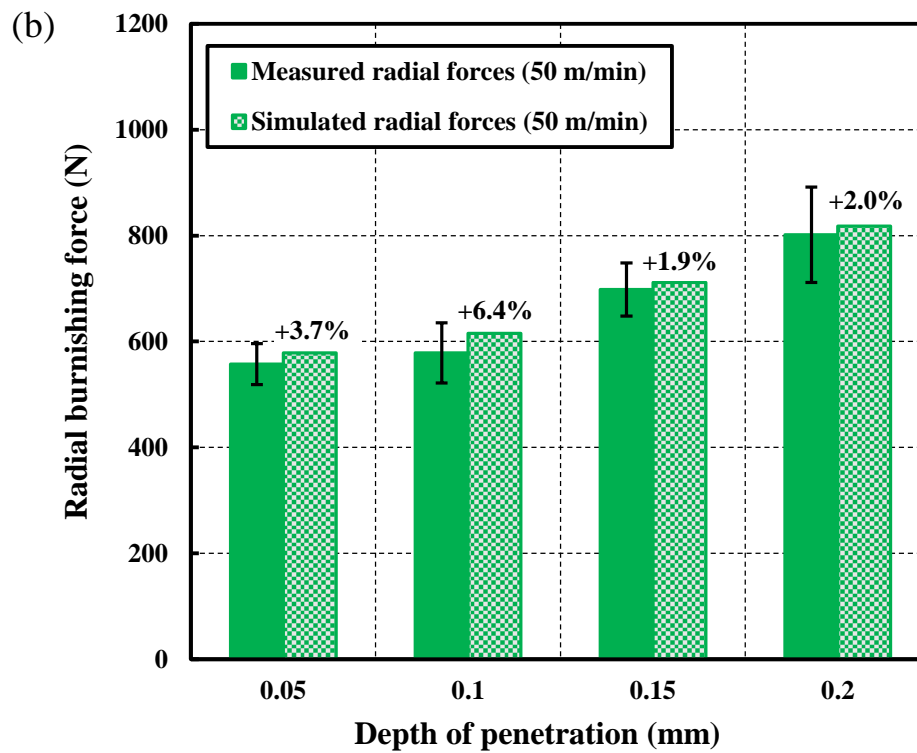
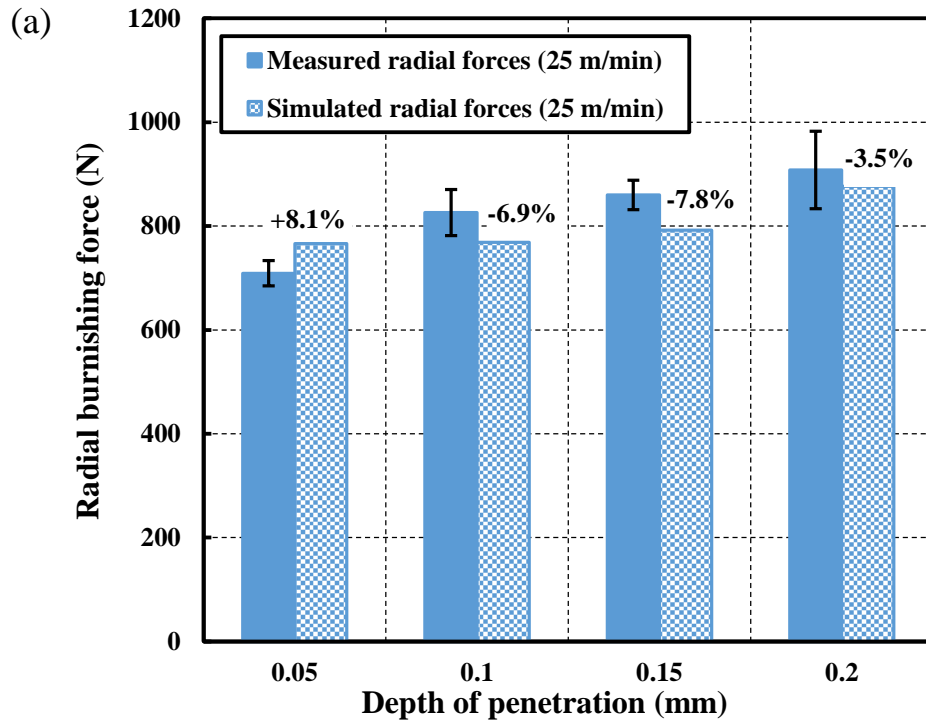


Figure 6.5: The calibration between predicted and experimental results to determine the friction coefficient used in the shear friction model (dry burnishing, under the burnishing speed of 50 m/min and the depth of penetration of 0.2 mm).

All radial burnishing force components were predicted by applying the numerical model based on 2D-FEM simulation. The details of the simulation results are shown in Figures 6.6 and 6.7 associated with the corresponding experimental results for all the dry and cryogenic burnishing conditions under four different depths of penetration and three burnishing speeds. Observed from Figure 6.6 for dry burnishing, almost all the differences between the predicted and experimental radial force components, were within the range from -10% to +10%. Good agreements were achieved in the prediction of dry burnishing forces.

However, Figure 6.7 shows that the predicted cryogenic burnishing radial force components have more than 10% variations, in contrast to the experimental results. There were also some acceptable simulation results that show that the numerical burnishing model was accurate enough to predict the radial force in cryogenic burnishing, particularly when a higher burnishing speed of 100 m/min was used, where less than 1% difference was obtained under the depths of penetration of 0.15 mm and 0.2 mm.

The comparisons between predicted and experimental tangential forces are also shown in Figure 6.8 and 6.9, respectively, where a variation between 10% to 20% was found in the case of dry burnishing, while the numerical model exhibited less accurate prediction of tangential forces in cryogenic burnishing, in which a difference of 20% to 30% were observed. Further modification will be performed to improve the accuracy of the numerical model by adjusting the setup of the simulated cryogenic window and the friction model in the future.



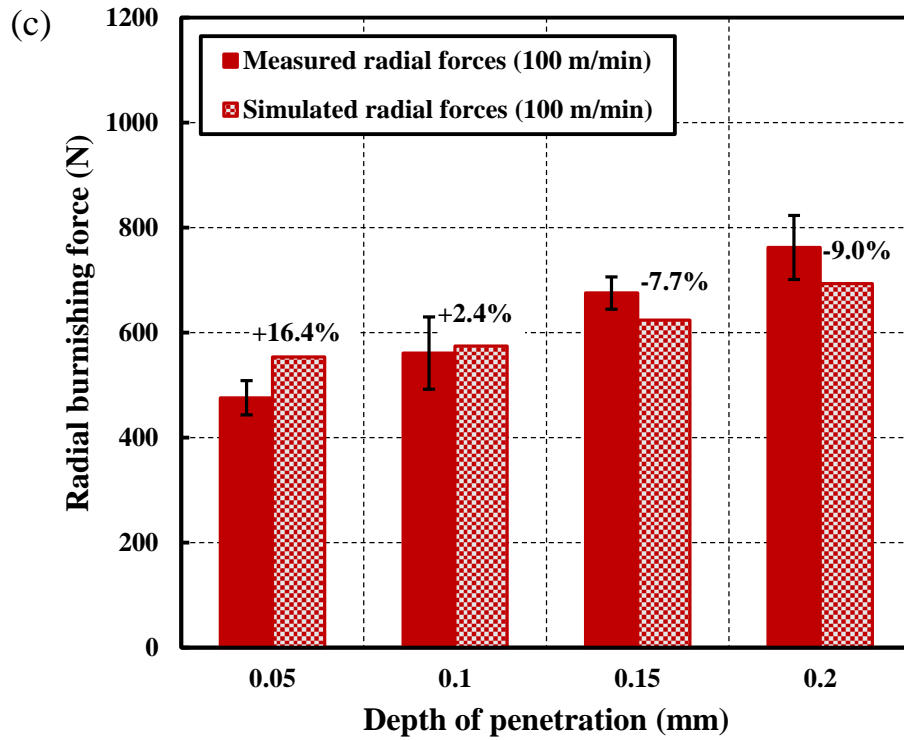
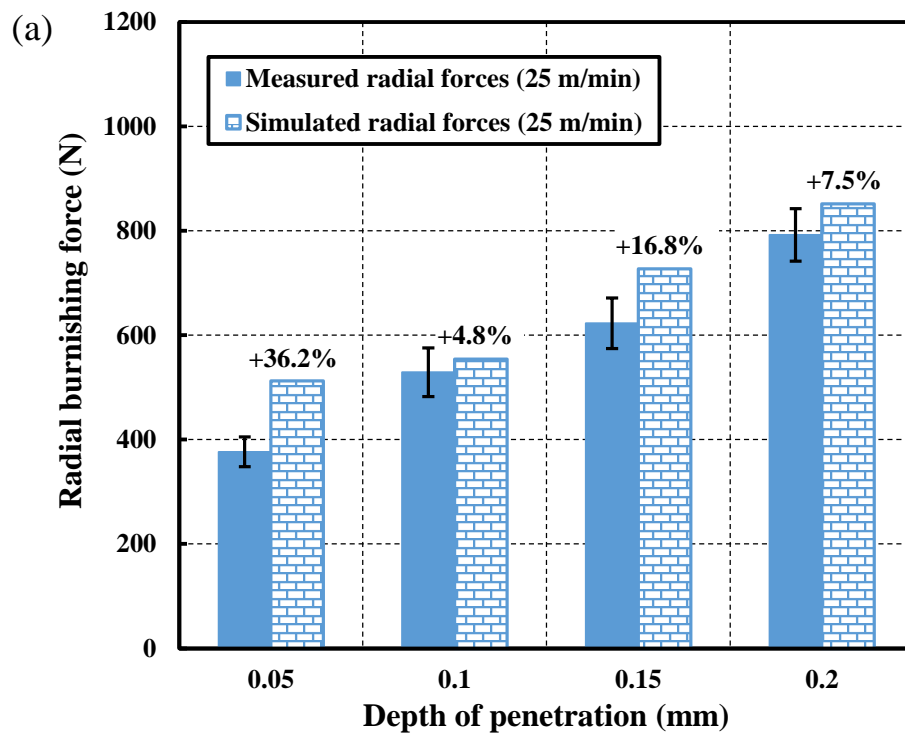


Figure 6.6: Comparison between predicted and experimental radial forces in dry burnishing: (a) burnishing speed of 25 m/min; (b) burnishing speed of 50 m/min; and (c) burnishing speed of 100 m/min.



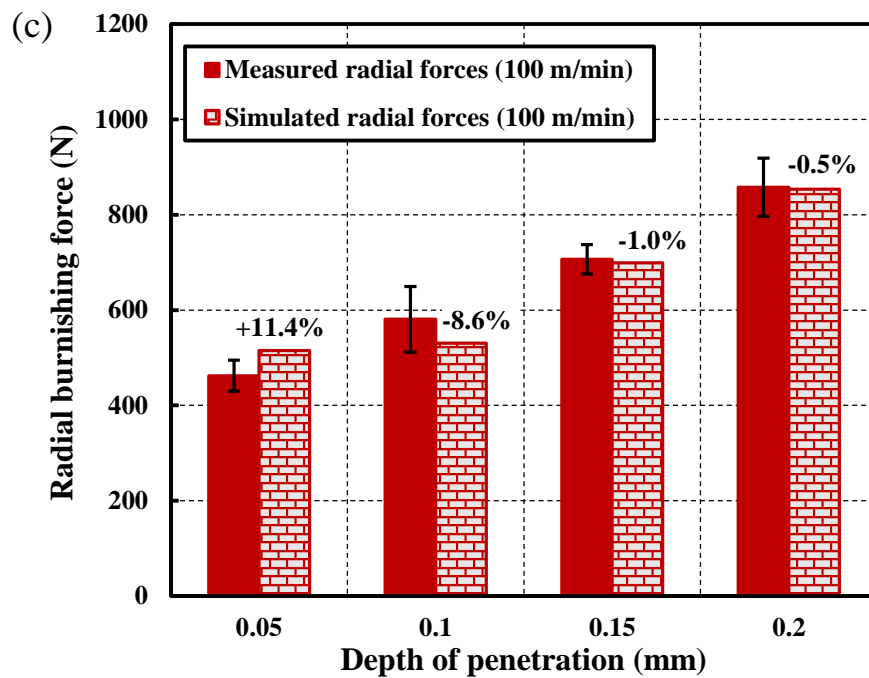
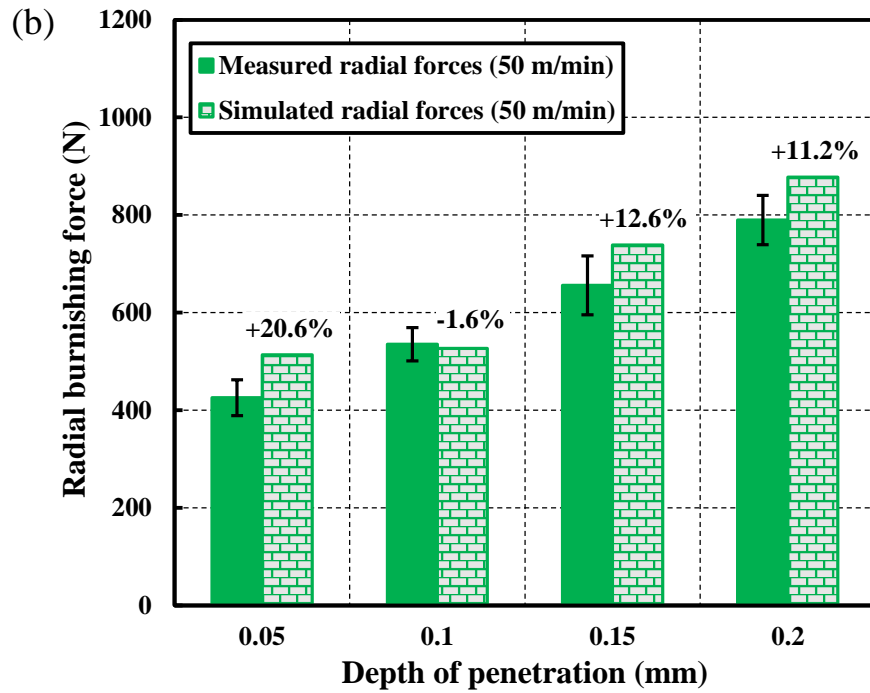
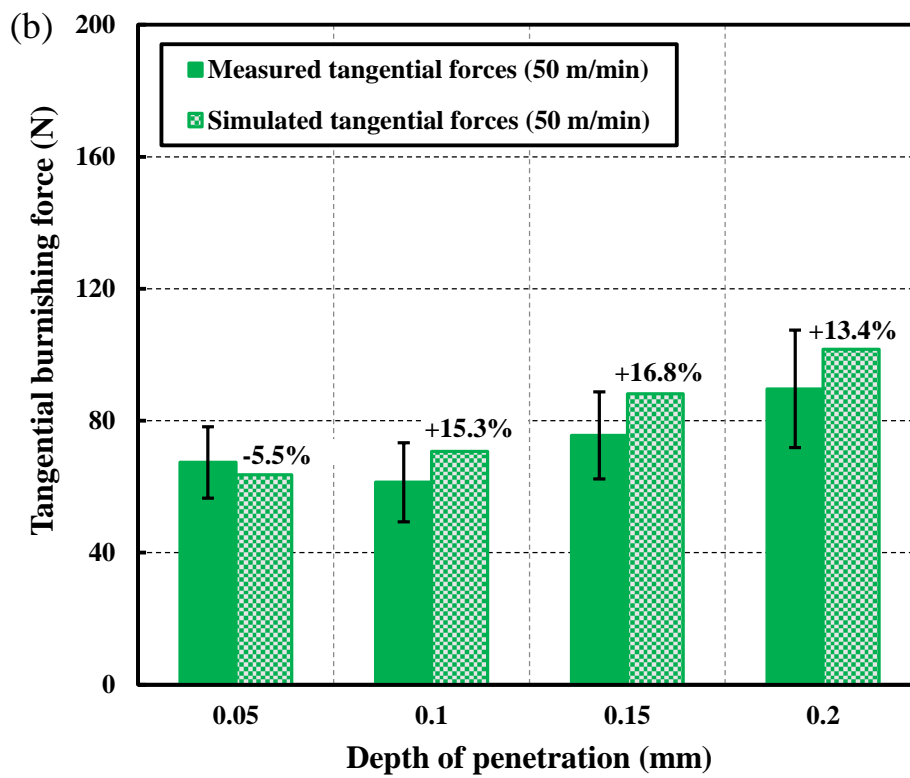
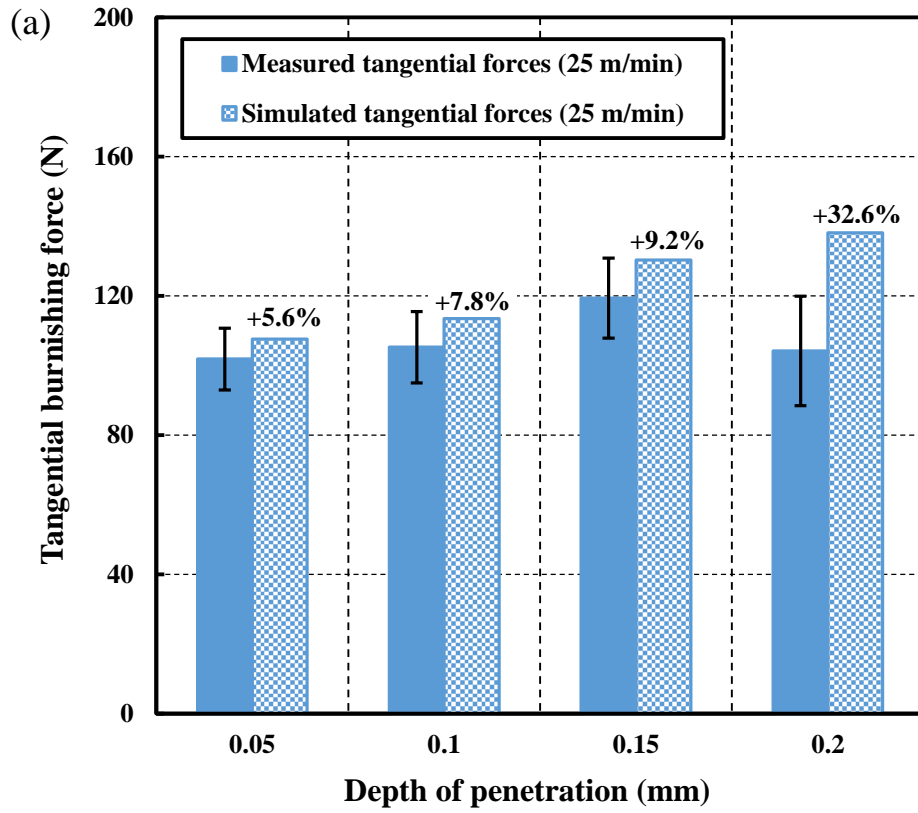


Figure 6.7: Comparison between predicted and experimental radial forces in cryogenic burnishing: (a) burnishing speed of 25 m/min; (b) burnishing speed of 50 m/min; and (c) burnishing speed of 100 m/min.



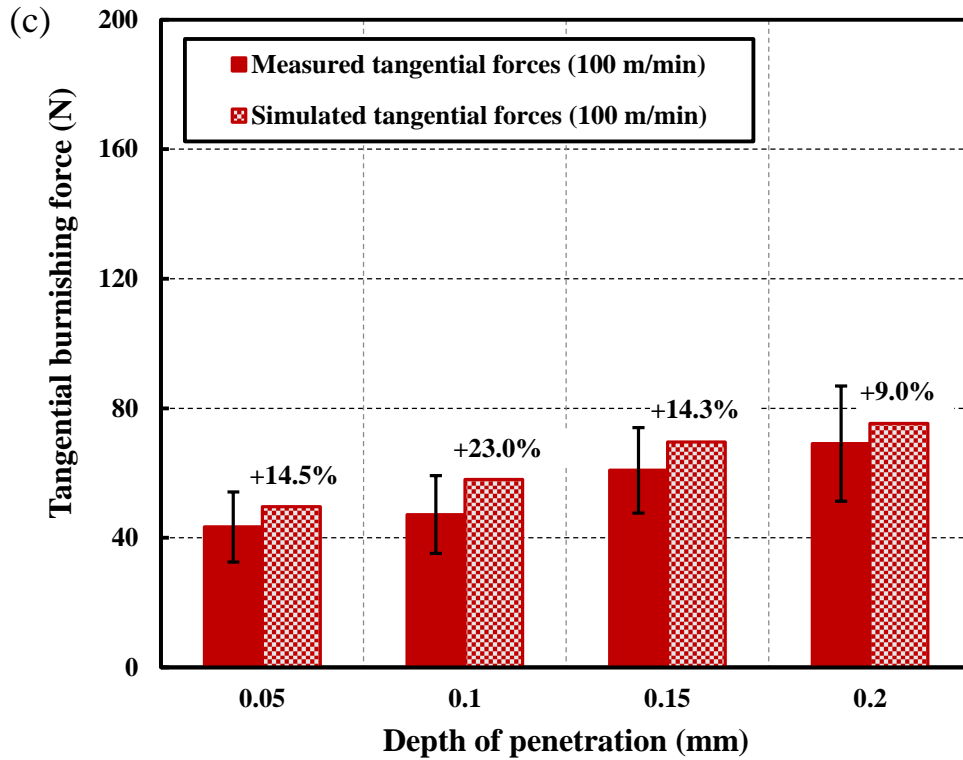
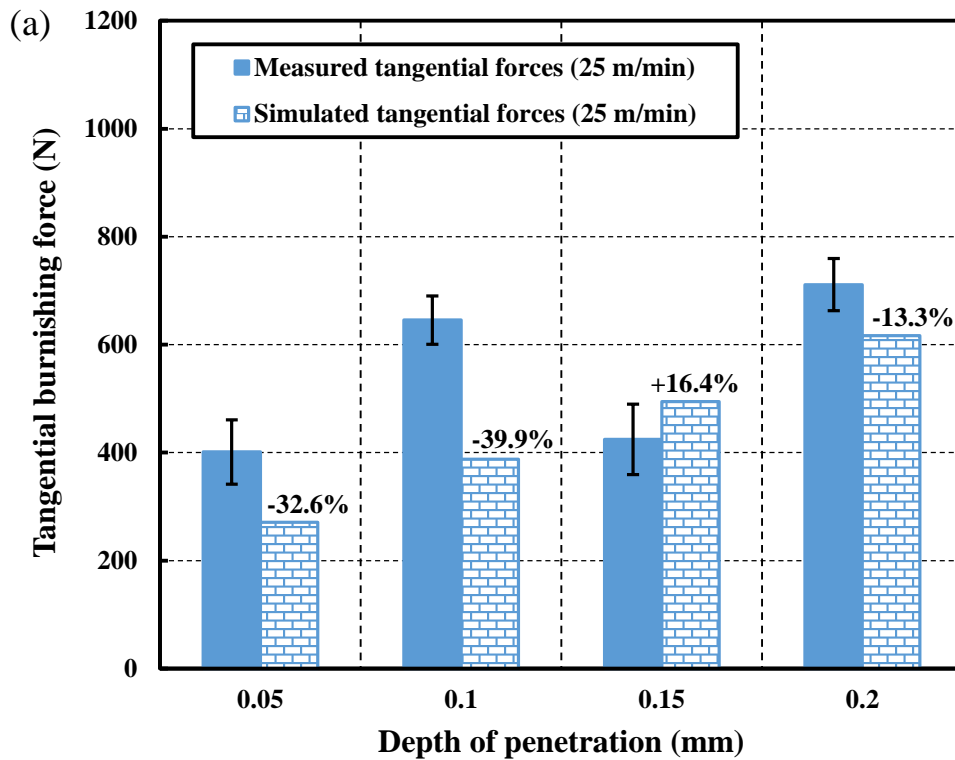


Figure 6.8: Comparison between predicted and experimental tangential forces in dry burnishing: (a) burnishing speed of 25 m/min; (b) burnishing speed of 50 m/min; and (c) burnishing speed of 100 m/min.



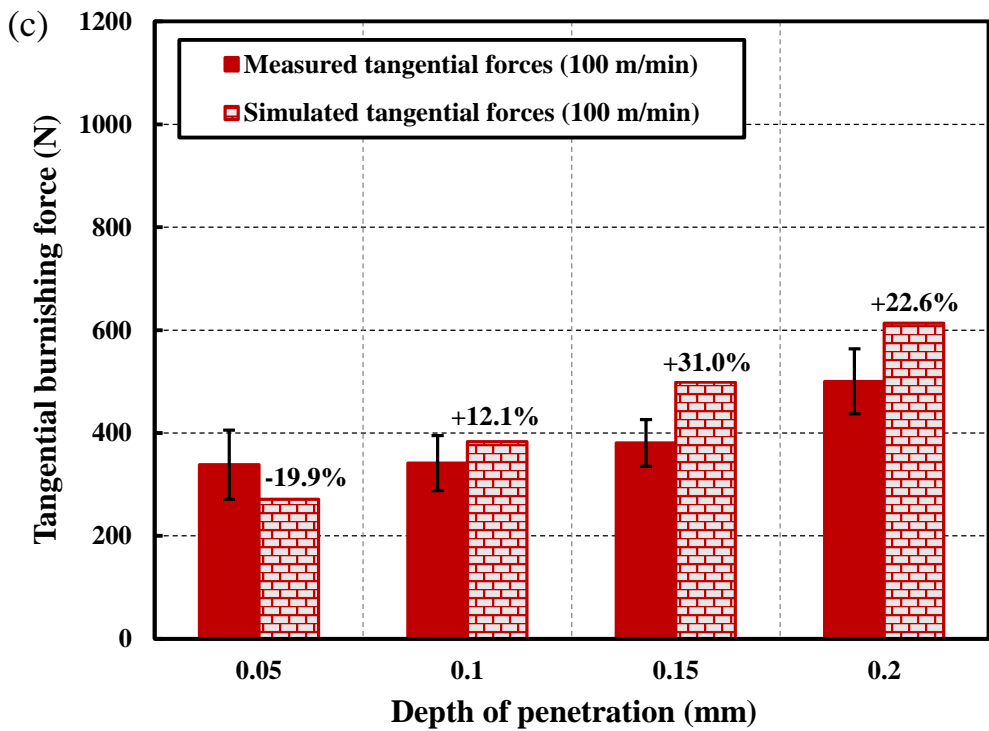
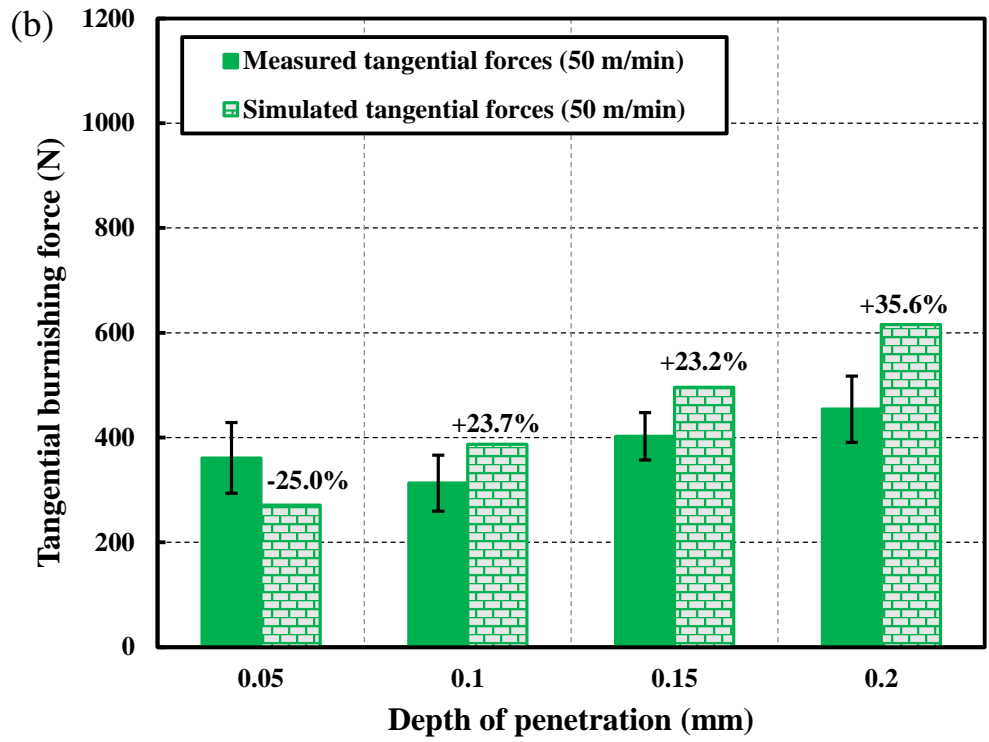
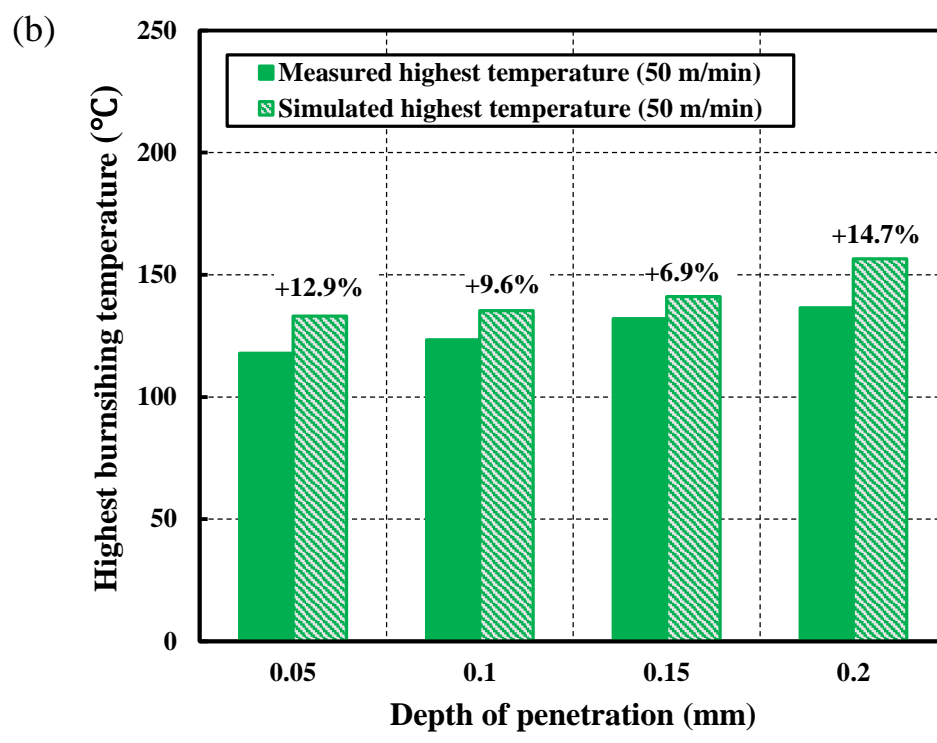
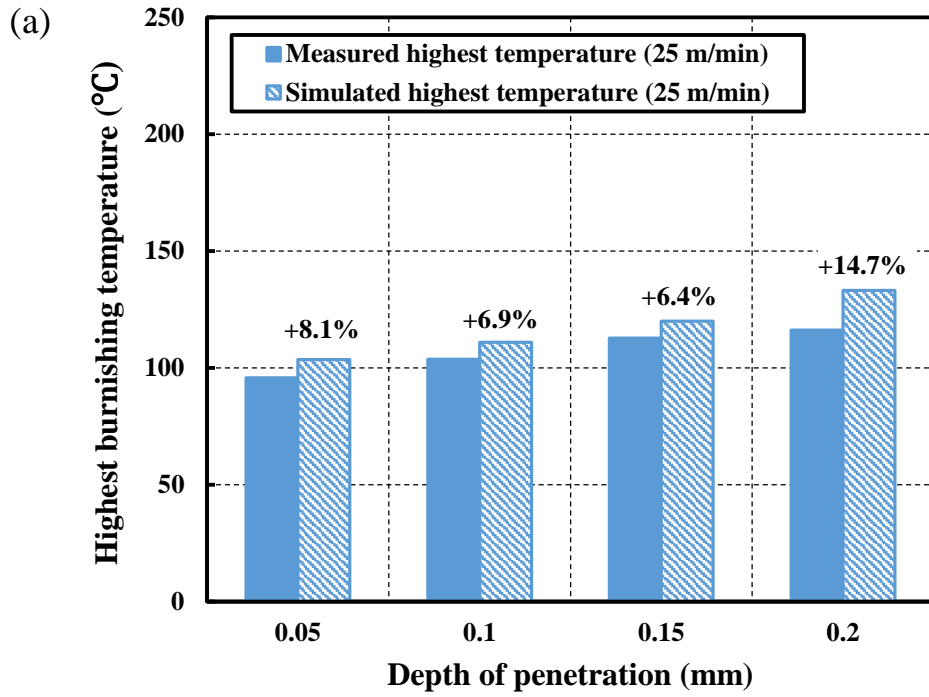


Figure 6.9: Comparison between predicted and experimental tangential forces in cryogenic burnishing: (a) burnishing speed of 25 m/min; (b) burnishing speed of 50 m/min; and (c) burnishing speed of 100 m/min.

The highest burnishing temperature measured in the contact zone between the work material and burnishing tool, was also simulated by using the modified Johnson-Cook model before DRX, and the constitutive equations describing the flow stress after DRX. The experiments of dry burnishing provided the highest temperature results measured from the infrared thermal imaging discussed in the previous chapter. However, the highest temperatures obtained in cryogenic burnishing could not be measured due to the rapid cooling effect of liquid nitrogen that decreased the temperature in a relatively short time which was beyond the capability of the infrared camera and the mist of liquid nitrogen coming out of the nozzle also affecting the measurement accuracy of the infrared camera.

A total of 12 sets of temperature results were of good quantity to validate the accuracy of the numerical FEM model. The comparison between the predicted and experimental temperatures is shown in Figure 6.10. The differences were found to be larger than the ones of burnishing forces. The burnishing conditions with the highest and lowest depths of penetrations had approximately 15% difference, but most of the simulation results exhibited a reasonable prediction in which less than 10% difference was achieved. Considering the overall prediction results from the points of burnishing force and temperature, the calibrated burnishing model should be ready to conduct the subsequent simulation for the depth of SPD layer induced by cryogenic burnishing. And, a more elaborate procedure shown in the next section will give the idea how the depth of SPD layer is predicted.



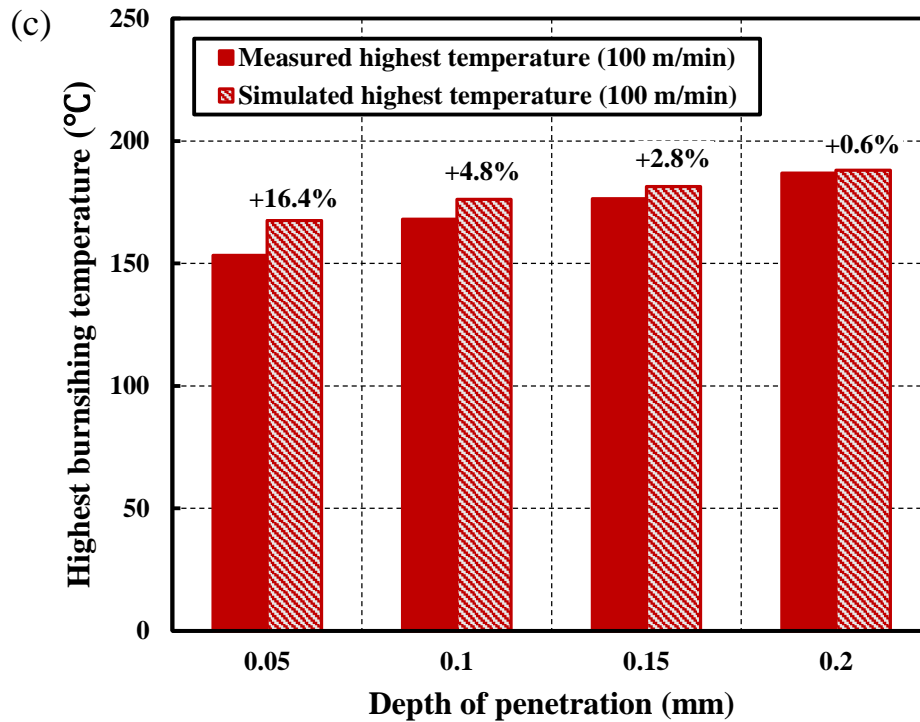


Figure 6.10: Comparison between predicted and experimental highest temperatures in dry burnishing: (a) burnishing speed of 25 m/min; (b) burnishing speed of 50 m/min; and (c) burnishing speed of 100 m/min.

6.4 Prediction of depth of SPD layer induced by cryogenic burnishing

In order to predict the depth of SPD layer accurately, calibration of grain size was made to validate the grain size model. DRX is assumed to occur when the critical strain is reached. For *Al 7050-T7451* alloys, Eqn. (5) determining the critical strain was mentioned in the previous section. In this grain size model, if the strain induced by burnishing is equal or greater than the critical strain under certain strain-rate and temperature, DRX is considered to happen at this moment in the burnishing simulation.

The newly generated recrystallized grain size can be calculated by the following equation:

$$d = d_0 \cdot \alpha \cdot Z^M \quad (11)$$

This method has been successfully applied by previous researchers to predict the recrystallized grain size (Yanagimoto et al., 1998; Caruso et al., 2011; Yang, 2012). In this equation, d represents the recrystallized grain size, d_0 is the initial grain size of *Al 7050-T7451* alloys with near-UFG structure processed by FSP. Z is the Zener-Hollomon parameter mentioned in Eqn. (10). α and M are the material constants, and these two parameters need to be obtained through the calibration procedure as shown in the flow chart in Figure 6.11, it is very important to acquire proper values for these two material constants in order to achieve more accurate prediction results for the SPD layer depth.

Through calibration, strain-rate and temperature could be derived as the output parameters, and they are plugged into the equation by which the critical strain is calculated. If the critical strain is smaller than or equal to the effective strain extracted from the simulation as one output parameter, DRX is considered to occur. Then, the predicted grain size is calculated and compared with the grain size in the refined layer measured by using AFM. If the agreement is achieved, the calibration ends. Otherwise, the modification of the two material constants α and M is made iteratively until the predicted grain size agrees with the experimental results.

The predicted grain size in the refined layer was 39.9 nm through the simulation when the two material constants α and M were 9.2 and -0.1, respectively, determined by the calibration, compared with the average grain size of 38.9 ± 3.3 nm measured from the AFM image. Therefore, the calibrated grain size model should be applicable to predict the depths of SPD layer for all the conditions in cryogenic burnishing where three

burnishing speeds and four depths of penetration are used. All simulation results are shown and compared with the experimental measurements for the purpose of verifying the accuracy of this numerical model to predict the grain refinement and severe plastic deformation induced by cryogenic burnishing.

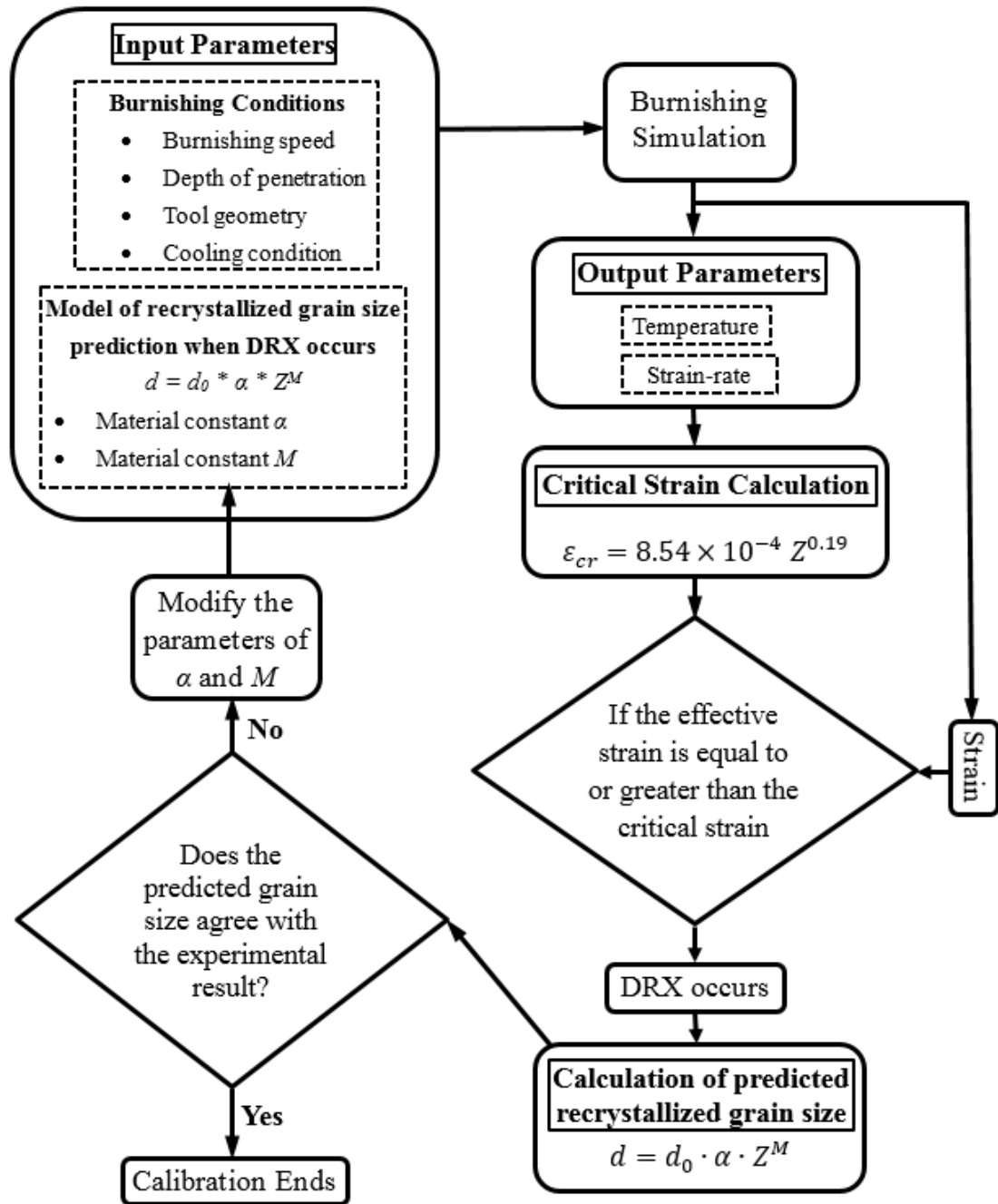


Figure 6.11: Calibration of the recrystallized grain size model.

The figures of the simulation for the SPD layers are in contrast to microstructure images measured from microscopic methods. The depth of SPD layer is to consider the layer with the grain size of less than 1.8 μm . The definition of SPD layer also includes the burnishing-influenced layer with a sweeping pattern plus the refined layer with the featureless nano grains. Under this standard, the depths of SPD layers predicted by the FEM-based numerical model are in the range of 91.3 - 141.2 μm , when the depth of penetration is 0.2 mm.

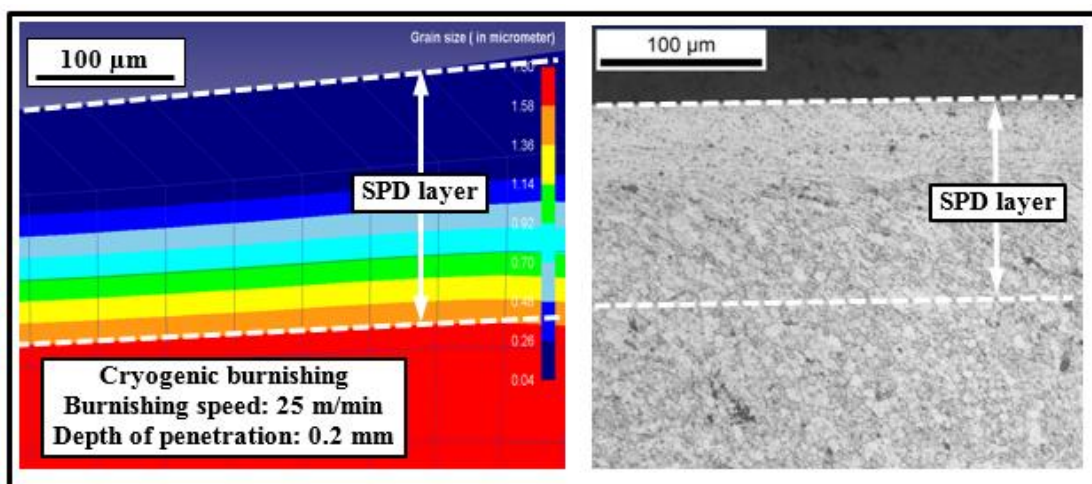
The elaborate simulation figures of the refined layers and the comparison between predicted and experimental data are shown in Figures 6.12 and 6.13, respectively. Both the predicted and experimental depths of SPD layers show a decreasing trend when the burnishing speed increased under most of the burnishing conditions at all four depths of penetration. The SPD layer was also influenced by depth of penetration, reflected by an increasing trend along with increased depth of penetration. However, burnishing speed played a more important role in the variation of SPD layer, which was clearly shown in the two figures.

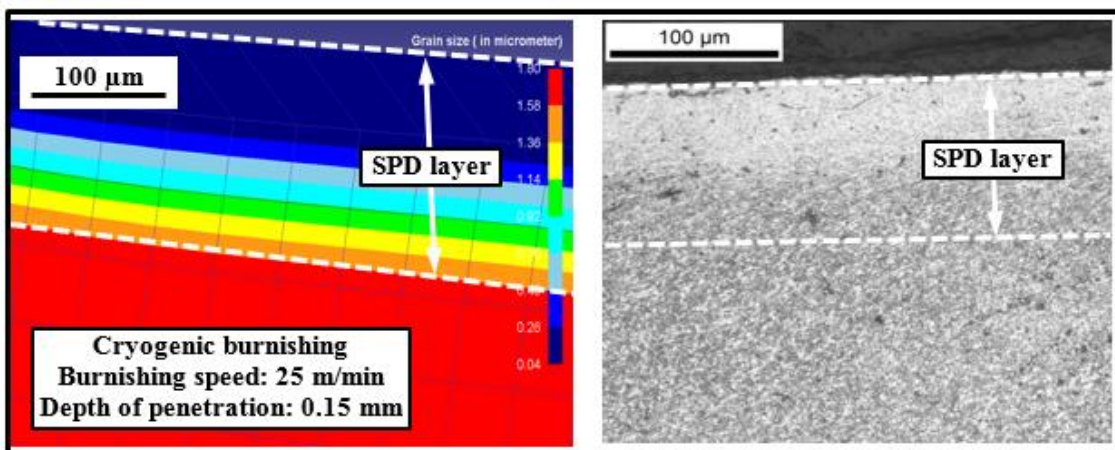
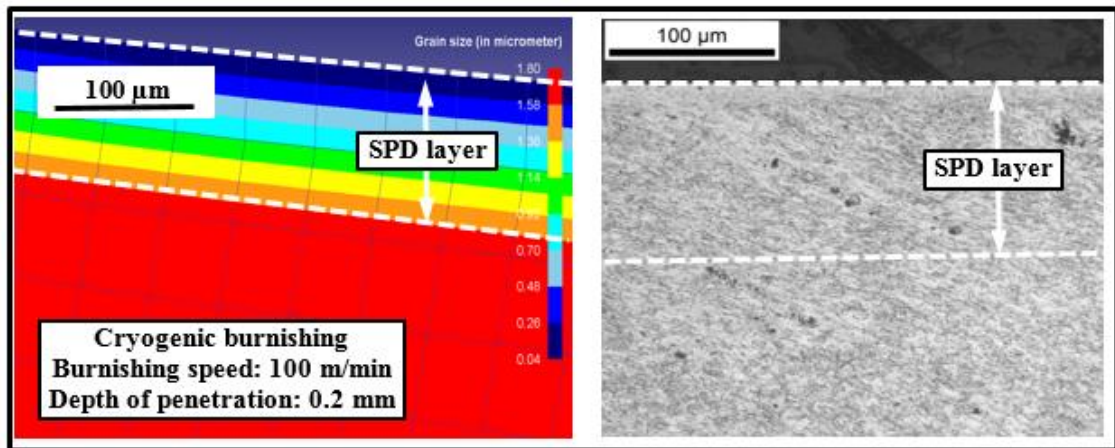
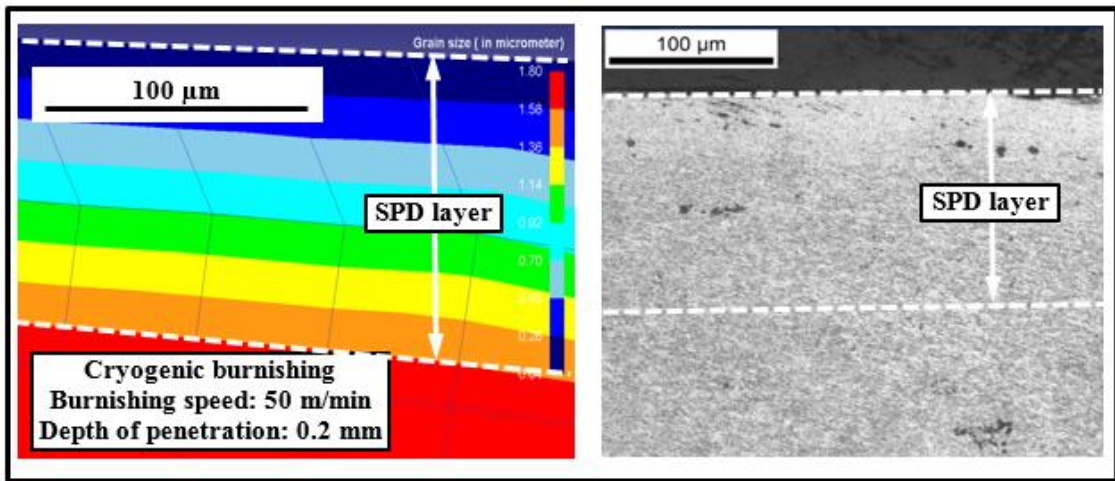
For most of conditions in cryogenic burnishing, a difference of less than 15% was achieved between the experimental and predicted results of SPD layer depth, and it was within a reasonable range. But, when using a lower burnishing speed of 25 m/min, the simulation results became less accurate. The reduced accuracy was also found when a lower depth of penetration of 0.05 mm was employed in the numerical model.

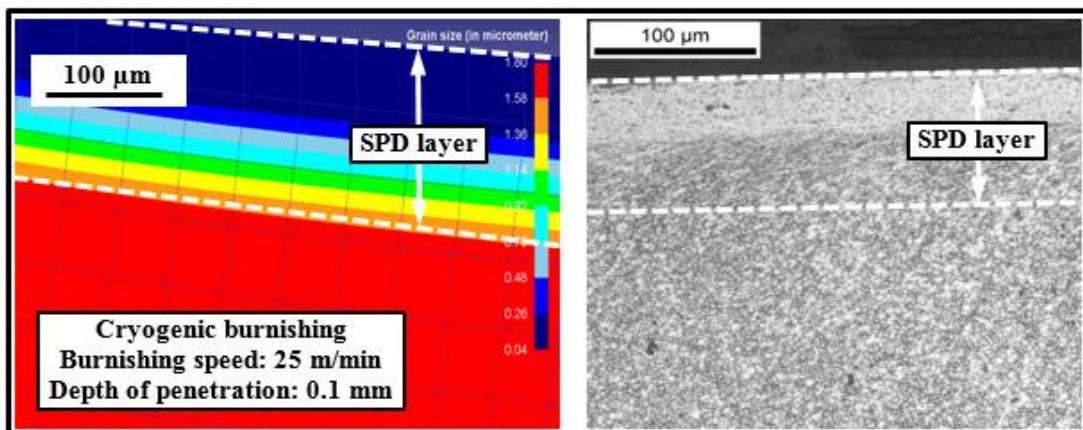
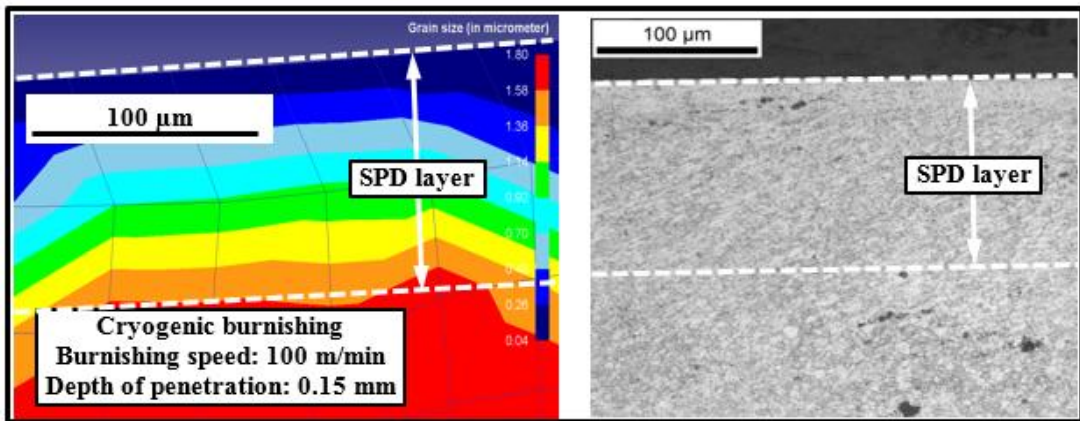
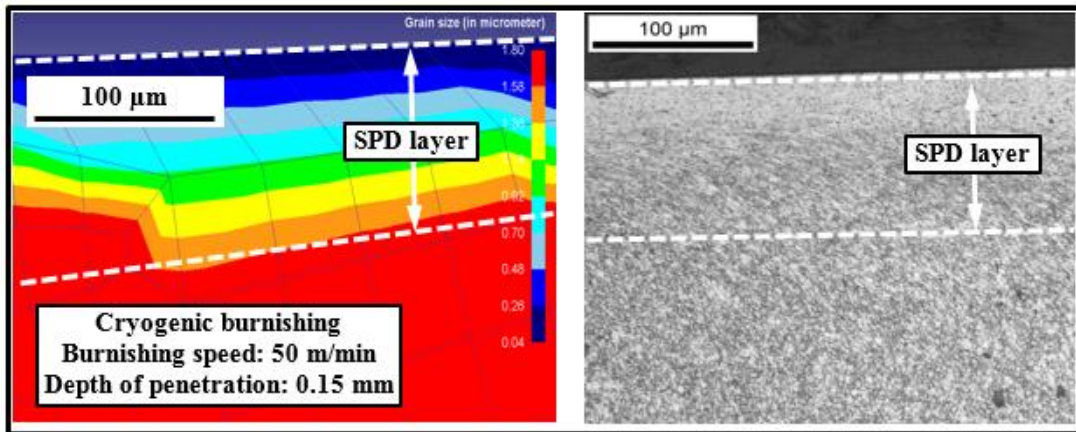
The first reason to explain the inaccuracy of this model, to some extent, is that no grain growth after DRX is considered in the model, and the grains are assumed to be fully

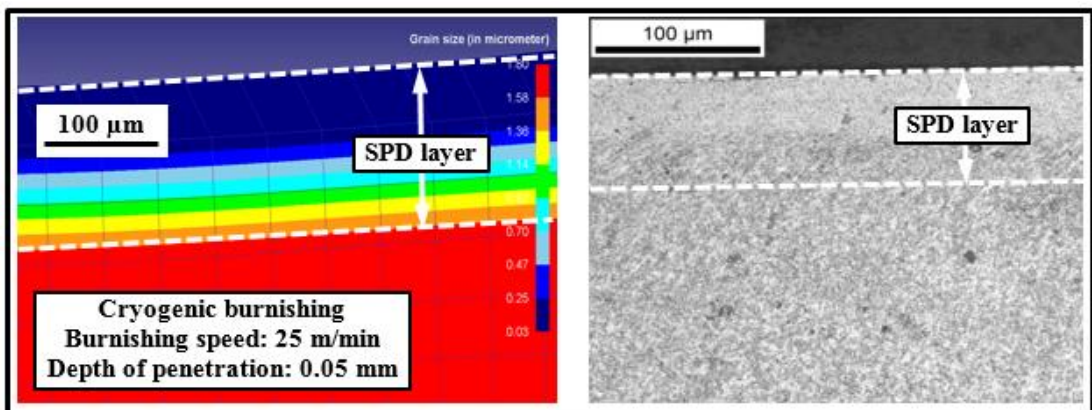
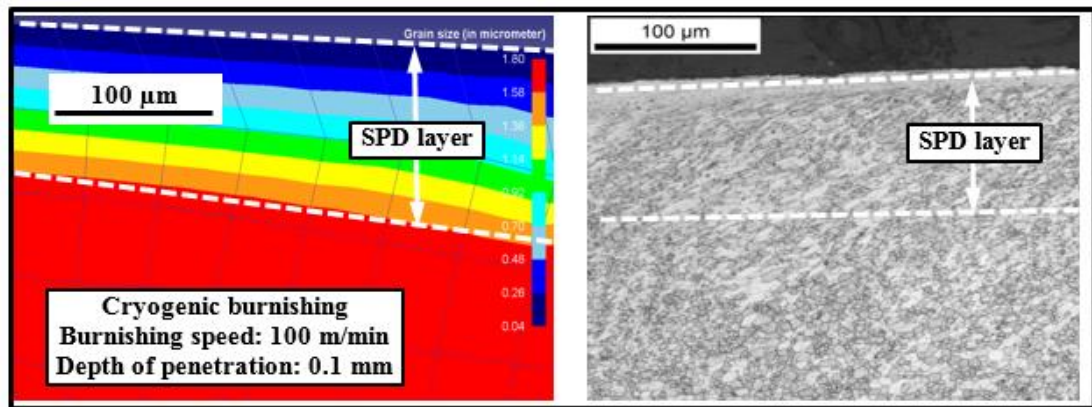
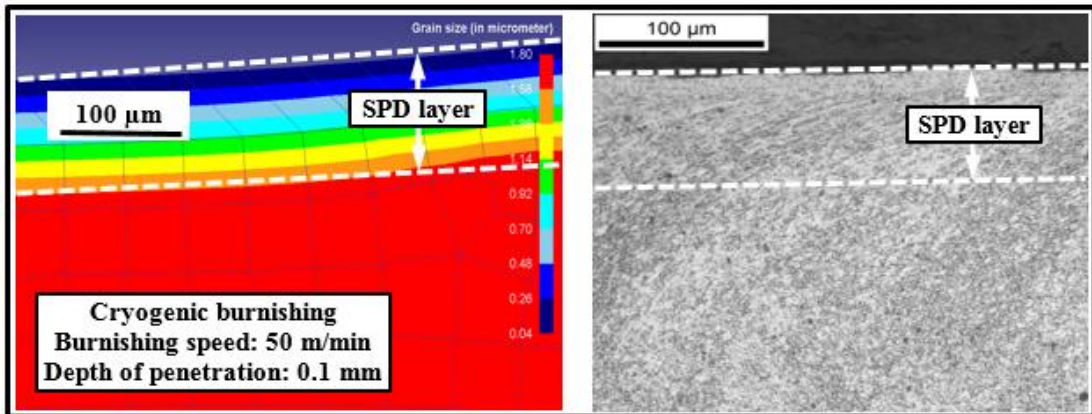
recrystallized which means partial recrystallization of the grains are not taken into consideration in the simulation. And, lack of tests on material properties is another reason to influence the accuracy of the model to predict the SPD layer induced by cryogenic burnishing. Borrowing the data and constitutive equations and then using them in the model, will not completely reflect the actual material behavior of *Al 7050-T7451* alloys used in this study as there are some variations in the material properties provided by different material manufacturers. A smaller mesh size may also help to improve the accuracy of the simulation results.

Another thing noticed here is that only one pass of burnishing process was used in the simulation, however, in the practical application of burnishing, multiple passes were applied in order to achieve the desired burnishing effects on the manufactured components. Multiple passes should be used in the numerical model to provide more accurate results, particularly in the simulation of SPD layer depth.









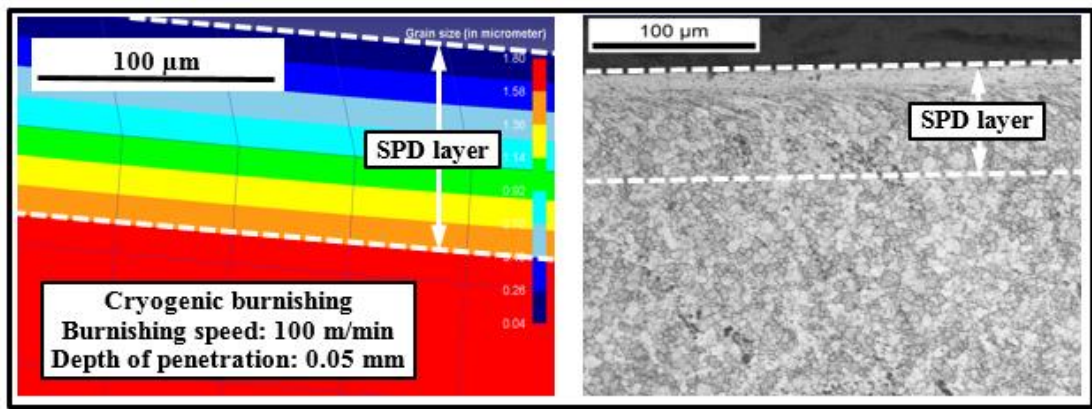
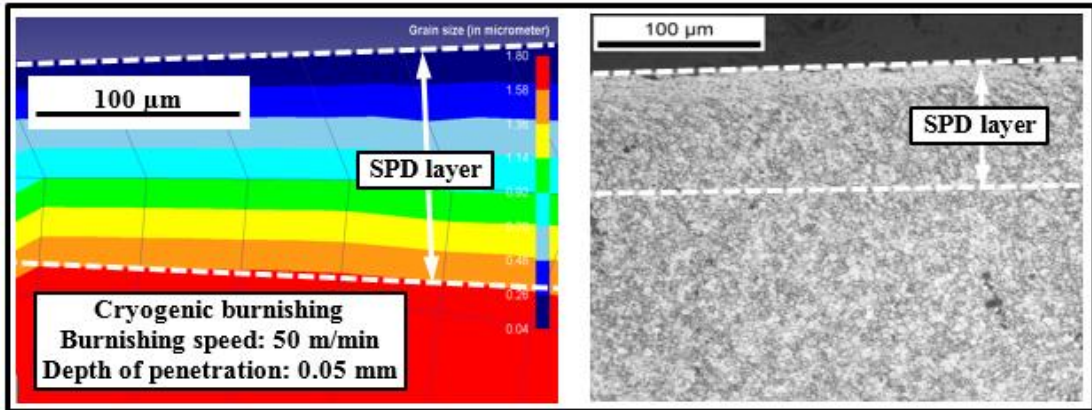
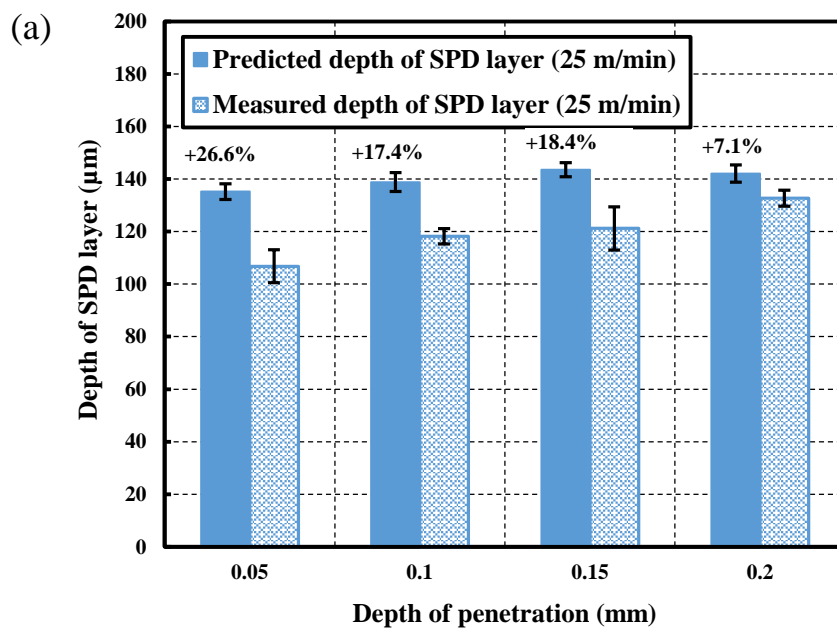


Figure 6.12: Simulation images of SPD layers induced by cryogenic burnishing and the comparison with the corresponding microstructure images: (a) burnishing speed of 25 m/min; (b) burnishing speed of 50 m/min; and (c) burnishing speed of 100 m/min.



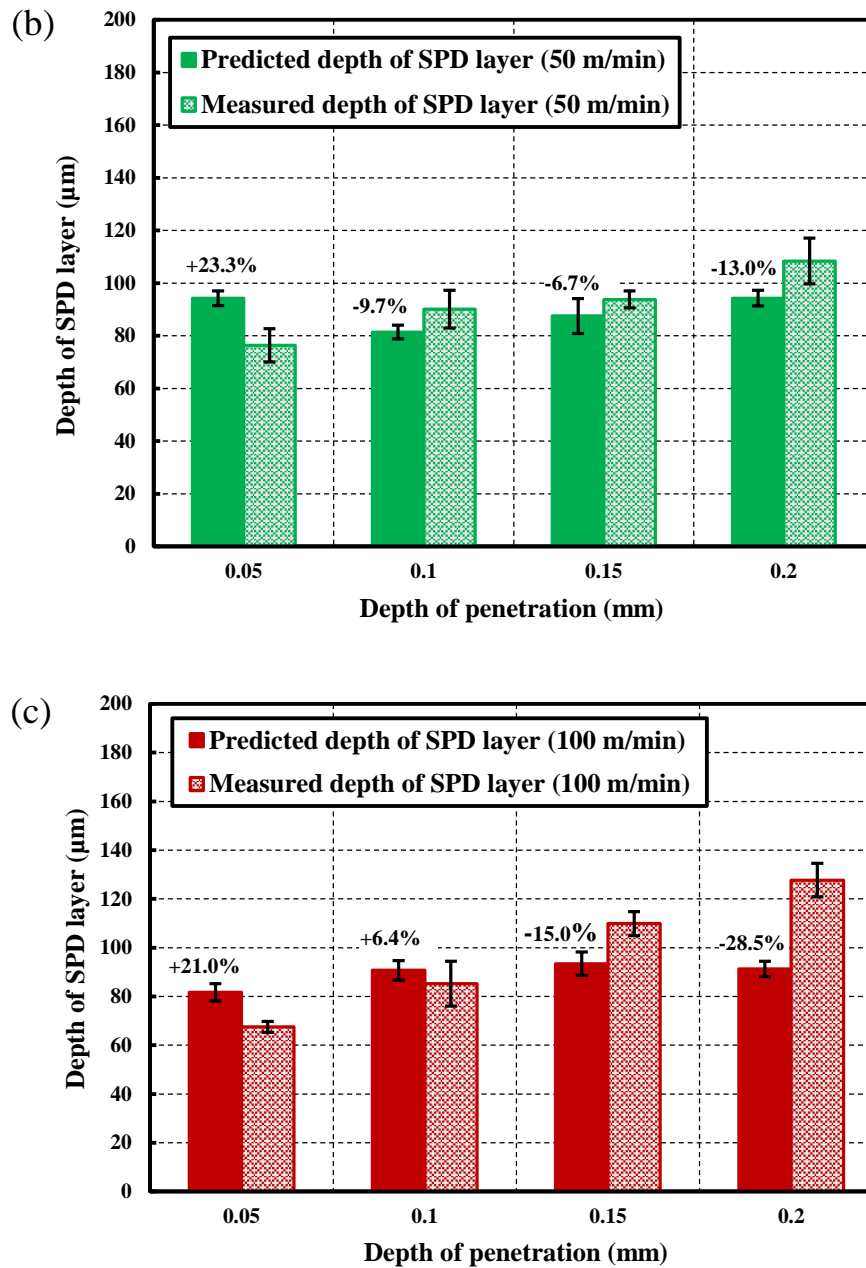


Figure 6.13: Comparison between the predicted and measured SPD layers induced by cryogenic burnishing by showing the error bars: (a) burnishing speed of 25 m/min; (b) burnishing speed of 50 m/min; and (c) burnishing speed of 100 m/min.

6.5 Chapter conclusion

In this chapter, a numerical FEM-based model is developed to predict the burnishing force, temperature and depth of SPD layer in burnishing process. In order to describe the material behavior of *Al 7050-T7451* alloys before and after DRX, a modified

Johnson-Cook model and a series of material constitutive equations are used, respectively. Through the calibrations, the material constants A , B and shear friction coefficient are determined first, and then applied in this numerical model to predict the burnishing force and temperature. Also, two material constants, α and M are determined by the calibration of grain size in the refined layer, and then the grain size model including the two material constants is used to predict the depth of SPD layer under the conditions of three burnishing speeds and four depths of penetration in cryogenic burnishing. The major findings from the simulation results obtained from this numerical FEM-based model are as follows:

- Less than 10% error was found when comparing the predicted and experimental burnishing forces in both dry and cryogenic burnishing. However, for dry burnishing, the model provided more accurate simulation in contrast to cryogenic burnishing.
- Less accurate predicted results of tangential forces were found in the simulation of dry and cryogenic burnishing, in comparison with experimental results. The difference was 10% to 20% in dry burnishing. However, for cryogenic burnishing, the variation observed was 20% to 30%.
- In dry burnishing, the highest burnishing temperature was predicted by the numerical model. The differences between the experimental and predicted results were less than 10% for most of the cases.
- For the prediction of depth of SPD layer induced by cryogenic burnishing, the simulation showed reasonable results compared to the microscopic measurements.

However, future work needs to be performed to improve the accuracy of this model for the prediction of SPD layers.

In conclusion, the developed numerical model for the simulation of burnishing process is capable of predicting the burnishing force and temperature with less than 10% error under most of the conditions in dry and cryogenic burnishing. However, the model needs to be modified in the future research to make sure that a better accuracy can be achieved for the predictions of tangential burnishing force and SPD layer.

CHAPTER 7

CONCLUSIONS AND FUTURE WORK

7.1 Conclusions

In this chapter, the primary findings obtained from the experimental and numerical work are summarized. These conclusions are summarized in the sequential order from Chapter 3 to Chapter 6 for cryogenic processing of *Al 7050-T7451* alloy for improved surface integrity as follows:

- *Al 7050-T7451* alloy with near-UFG structure was achieved by dry and cryogenic FSP. Homogeneous and equiaxed grains with the size less than 2 μm were produced by cryogenic FSP when a low rotational speed of 19.2 m/min was used. However, the grain size of 2-3 μm was obtained for most of FSP conditions under four different rotational speeds. More homogeneous and smaller grains were distributed in the microstructures acquired by cryogenic FSP compared with dry FSP, due to the rapid cooling effect resulting by liquid nitrogen suppressing the grain growth after DRX.
- Approximately 10% increase could be observed from the hardness measurement from the samples processed by cryogenic FSP, in contrast to dry FSP.
- The texture change could be achieved by FSP for *Al 7050-T7451* alloy. The transformation from *Al (200)* to *Al (111)* was found in all the samples processed by dry and cryogenic FSP. Better material properties of *Al (111)* with the most densely packed plane of FCC-based aluminum alloys exhibiting lower surface energy, indicated that FSP could be a potential technology to broaden the application of

aluminum alloys by changing the texture.

- An average value of approximate 250 N was found in the cutting and thrust force measurements from dry and cryogenic machining of *Al 7050-T7451* alloys with near-UFG structure under four different cutting speeds. The highest cutting temperature was reduced by up to 44.7% due to the cooling effect of liquid nitrogen in cryogenic machining compared with dry machining.
- Slightly smaller grains with the size of about 1.6 μm were produced in the machined surface of the samples processed by cryogenic machining, which demonstrated that DRX occurred and marginally smaller grains were obtained from near-UFG structure.
- Hardness in the surface and sub-surface of cryogenically-machined samples was higher than the dry one, particularly at low cutting speeds of 50 m/min and 100 m/min, because work hardening effect was more dominant compared with the thermal softening effect where the heat could be taken away in a relatively short time during cryogenic machining.
- Another evidence of chip microstructure showed that DRX did occur in the machined surfaces produced by dry and cryogenic machining. The average grain size of about 1.2 μm was seen from the microstructures measured from the samples processed by dry and cryogenic machining. While hardness values of chips produced by dry and cryogenic machining were approximately 41.8% higher than initial hardness of work materials prepared by FSP, due to higher strain and strain-rate induced by more severe plastic deformation in the primary deformation zone.

- In dry and cryogenic burnishing processes, an increasing trend of burnishing forces was observed when a higher depth of penetration was used because more work hardening effect with high strain and strain-rate induced by burnishing. As the burnishing speed increased, the measurements showed less burnishing forces due to more thermal softening effect reflected by the measurements of burnishing temperatures where the highest burnishing temperature increased with the increase of depth of penetration and burnishing speed. While cryogenic burnishing produced higher radial burnishing forces because the work materials became harder due to the cryogenic cooling effect, compared with dry burnishing.
- The microstructure images demonstrated the formation of refined layers and burnishing-influenced layers in the burnished surface and sub-surface induced by cryogenic burnishing. Average depths of refined layers were approximately 50, 26, 19 μm measured from the microstructure images acquired in cryogenic burnishing under the burnishing speeds of 25, 50 and 100 m/min, respectively. Up to 35.4% hardness increase was achieved within the layer depth of 200 μm in the burnished surface introduced by cryogenic burnishing, while dry burnishing only resulted in hardness increase up to 14.7%.
- Less than 10% difference between the experimental and predicted burnishing forces was achieved by the FEM-based numerical burnishing model developed to simulate the burnishing process of *Al 7050-T7451* alloy for most of the cases when four different depths of penetration and three burnishing speeds were used. Good agreement was also reached in the temperature prediction where the difference of

less than 10% was acceptable.

- The current numerical model was less capable of predicting depth of SPD layer and tangential burnishing force, compared with the predictions of radial burnishing force and temperature. However, the simulation shows reasonable results of SPD layers, compared to the microscopic measurements for cryogenic burnishing.

7.2 Future work

In general, cryogenic processing technologies including FSP, machining and burnishing in sequential order, can be used to process *Al 7050-T7451* alloy to obtain more homogeneous microstructure and improved surface integrity characteristics. The major findings presented above will provide good information to the academic and industry communities in certain degrees due to the novelty and scientific contribution of this work. Nonetheless, there is a need for more future work that need to be done in order to extend the current research of cryogenic processing to fill the voids of the unfinished work existing in this dissertation. Detailed future work that can be done are shown as below:

- The best combination of rotational speed and feed needs to be optimized in order to acquire the best possible grain refinement, hardness and homogeneity of the materials in dry and cryogenic FSP. More experiments regarding materials test are necessary to be performed, such as tensile test which is a very important method for determining the material properties for the application of superplastic forming in which the materials processed by FSP are commonly used.

- The wear and corrosion tests are very helpful to identify the wear and corrosion resistance of the processed materials. The refined layer with higher hardness in which nano-grains are produced, provides the benefit to improve these two properties, however this needs to be verified by experiments.
- Compressive residual stresses are induced in the surface and sub-surface of the work materials produced by cryogenic machining and burnishing, and it is very beneficial to improve the fatigue life of the manufactured components. The measurement of residual stresses is very critical to verify the effects of cryogenic machining and burnishing of *Al 7050-T7451* alloy.
- For the modeling work in burnishing, the material constants used in the models of flow stress, friction and grain size calculation, need to be determined directly from the effective material tests in order to minimize or eliminate the calibrations between experimental and predictive results for a more reliable and accurate simulation, especially for the predications of tangential force and depth of SPD layer induced by cryogenic burnishing. The consideration of multi-pass burnishing will also reflect the practical application of burnishing process and improve the accuracy of the numerical FEM-based burnishing model.

REFERENCES

- Alcoa, 2012. Alloy 7050 plate and sheet. www.millproducts-alcoa.com.
- Aldajah, S.H., Ajayi, O.O., Fenske, G.R., David, S., 2009. Effect of friction stir processing on the tribological performance of high carbon steel. *Wear*, 267: 350-355.
- Alidokht, S.A., Abdollah-Zadeh, A.A., Soleymani, S., Saeid, T., Assadi, H., 2012. Evaluation of microstructure and wear behavior of friction stir processed cast aluminum alloy. *Materials Characterization*, 63: 90-97.
- Atkins, 2012. View of the internal face of a starboard wing skin panel. www.atkinsglobal.com.
- Azizieh, M., Kokabi, A.H., Abachi, P., 2010. Effect of rotational speed and probe profile on microstructure and hardness of $AZ31/Al_2O_3$ nanocomposites fabricated by friction stir processing. *Materials & Design*, 32 (4): 2034-2041.
- Azushima, A., Kopp, R., Korhonen, A., Yang, D.Y., Micari, F., Lahoti, G.D., Groche, P., Yanagimoto, J., Tsuji, N., Rosochowski, A., Yanagida, A., 2008. Severe plastic deformation (SPD) processes for metals. *CIRP Annals - Manufacturing Technology*, 57: 716-735.
- Balland, P., Tabourot, L., Degre, F., Moreau, V., 2013. An investigation of the mechanics of roller burnishing through finite element simulation and experiments. *International Journal of Machine tools & Manufacture*, 65: 29-36.
- Balyanov, A., Kutnyakova, J., Amirhanova, N.A., Stolyarov, V.V., Valiev, R.Z., Liao, X.Z., Zhao, Y.H., Jiang, Y.B., Xu, H.F., Lowe, T.C., Zhu, Y.T., 2004. Corrosion resistance of ultra fine-grained *Ti*. *Scripta Materialia*, 51: 225-229.
- Bao, R., Zhang, X., 2010. Fatigue crack growth behavior and life prediction for 2324-T39 and 7050-T7451 aluminum alloys under truncated load spectra. *International Journal of Fatigue*, 32: 1180-1189.
- Barmouz, M., Givi, M.K.B., Seyfi, J., 2011. On the role of processing parameters in producing *Cu/SiC* metal matrix composites via friction stir processing: Investigating microstructure, microhardness, wear and tensile behavior. *Materials Characterization*, 62: 108-117.
- Baro, M.D., Kolobov, Y.R., Ovidko, I.A., Schaefer, H.E., Straumal, B.B., Valiev, R.Z., Alexandrov, I.V., Ivanov, M., Reimann, K., Reizis, A.B., Surinach, S., Zhilyaev, A.P., 2001. Diffusion and related phenomena in bulk nanostructured materials. *Reviews on Advanced Materials Science*, 2: 1-43.
- Black, A.J., Kopalinsky, E.M., Oxley, P.L.B., 1997. Analysis and experimental investigation of a simplified burnishing process. *International Journal of Mechanical Sciences*, 39(6): 629-641.

- Bork, C.A.S., Gonçalves, J.F.S., Gomes, J.O., 2015. The jatropha curcas vegetable base soluble cutting oil as a renewable source in the machining of aluminum alloy 7050-T7451. *Industrial Lubrication and Tribology*, 67(2): 181-195.
- Bougharriou, A., Bouzid, W., Saï, K., 2014. Analytical modeling of surface profile in turning and burnishing. *Journal of Advanced Manufacturing Technology*, 75: 547-558.
- Brandão, L.C., Coelho, R.T., Rodrigues, A.R., 2008. Experimental and theoretical study of workpiece temperature when end milling hardened steels using (TiAl) N-coated and PcBN-tipped tools. *Journal of Material Processing Technology*, 99: 234-244.
- Brown, R., Tang, W., Reynolds, A.P., 2009. Multi-pass friction stir welding in alloy 7050-T7451: Effects on weld response variables and on weld properties. *Materials Science and Engineering A*, 513-514: 115-121.
- Campbell, C.E., Bendersky, L.A., Boettinger, W.J., Ivester, R., 2006. Microstructural characterization of Al-7075-T651 chips and work pieces produced by high-speed machining. *Materials Science and Engineering A* 430: 15-26.
- Caruso, S., Di Renzo, S., Umbrello, D., Jayal, A.D., Dillon Jr, O.W., Jawahir, I.S., 2011. Finite element modeling of microstructural changes in hard turning. *Advanced Materials Research*, 223: 960-968.
- Carvalho, A.L.M., Voorwald, H.J.C., 2007. Influence of shot peening and hard chromium electroplating on the fatigue strength of 7050-T7451 aluminum alloy. *International Journal of Fatigue*, 29: 1282-1291.
- Carvalho, A.L.M., Voorwald, H.J.C., 2009. The surface treatment influence on the fatigue crack propagation of Al 7050-T7451 alloy. *Materials Science and Engineering A*, 505: 31-40.
- Caudill, J., Huang, B., Arvin, C., Schoop, J., Meyer, K., Jawahir, I.S., 2014. Enhancing the surface integrity of Ti-6Al-4V alloy through cryogenic burnishing. *Procedia CIRP*, 13: 243-248.
- Charit, I., Mishra, R.S., 2003. High strain rate superplasticity in a commercial 2024 Al alloy via friction stir processing. *Materials and Engineering A*, 359: 290-296.
- Chen, W.C., Ferguson, D.E., Ferguson, H.S., Mishra, R.S., Jin, Z., 2001. Development of ultrafine grained materials using the MAXStrain® technology. *Materials Science Forum*, 357-359: 425-430.
- Clark, D.A., Johnson, W.S., 2003. Temperature effects on fatigue performance of cold expanded holes in 7050-T7451 aluminum alloy. *International Journal of Fatigue*, 25: 159-165.
- Coelho, R.T., de Souza, A.F., Roger, A.R., Rigatti, A.M.Y., de Lima Ribeiro, A.A., 2010. Mechanistic approach to predict real machining time for milling free-form geometries applying high feed rate. *International Journal of Advanced Manufacturing Technology*, 46:1103-1111.

- Davies, M.A., Burns, T.J., 2011. Thermomechanical oscillations in material flow during high-speed machining. *Philosophical Transactions of the Royal Society of London. Series A: Mathematical, Physical and Engineering Sciences* 359 (1781): 821-846.
- Deng, Y., Yin, Z., Huang, J., 2011. Hot deformation behavior and microstructural evolution of homogenized 7050 aluminum alloy during compression at elevated temperature. *Materials Science and Engineering A*, 528:1780-1786.
- Dhar, N.R., Nanda Kishore, S.V., Paul, S., Chattopadhyay, A.B., 2002. The effects of cryogenic cooling on chips and cutting forces in turning *AISI 1040* and *AISI 4320* steels. *Proceedings of the Institution of Mechanical Engineers, Part B: Journal of Engineering Manufacture*, 216(5): 713-724.
- Dixit, M., Mishra, R.S., Sankaran, K.K., 2008. Structure-property correlations in *Al 7050* and *Al 7055* high-strength aluminum alloys. *Material Science and Engineering A*, 478: 163-172.
- Dupuy, L., Blandin, J., 2002. Damage sensitivity in a commercial al alloy processed by equal channel angular extrusion. *Acta Materialia*, 50: 3251-3264.
- Elmadagli, M., Perry, T., Alpas, A.T., 2007. A parametric study of the relationship between microstructure and wear resistance of *Al-Si* alloys. *Wear* 2007, 262:79-92.
- El-Axir, M.H., Othman, O.M., Abodiena, A.M., 2008. Improvements in out-of-roundness and microhardness of inner surfaces by internal ball burnishing process. *Journal of Materials Processing Technology*, 196: 120-128.
- El-Khabeery, M.M., El-Axir, M.H., 2001. Experimental techniques for studying the effects of milling roller-burnishing parameters on surface integrity. *International Journal of Machine Tool & Manufacturing*, 41: 1705-1719.
- Estrin, Y., Vinogradov, A., 2013. Extreme grain refinement by severe plastic deformation: A wealth of challenging science. *Acta Materialia*, 61: 782-817.
- Fang, N., Wu, Q., 2005. The effects of chamfered and honed tool edge geometry in machining of three aluminum alloys. *International Journal of Machine Tools & Manufacture*, 45: 1178-1187.
- Fang, G., Zhou, J., Duszczyk, J., 2009. Extrusion of 7075 aluminium alloy through double-pocket dies to manufacture a complex profile. *Journal of Materials Processing Technology*, 209: 3050-3059.
- Feng, A.H., Ma, Z.Y., 2007. Enhanced mechanical properties of *Mg-Al-Zn* cast alloy via friction stir processing. *Scripta Materialia*, 56: 397-400.
- Feng, X.L., Liu, H.J., Lippold, J.C., 2013. Microstructure characterization of the stir zone of submerged friction stir processed aluminum alloy 2219. *Materials Characterization*, 82: 97-102.

- Friction stir link Inc., 2011. Friction stir welding. <http://www.frictionstirlink.com/desc.html>.
- Fu, X.L., Wang, H., Wan, Y., Wang, X.Q., 2010a. Material constitutive model in machining 7050-T7451 by orthogonal machining experiments. *Advanced Materials Research*, 97-101:713-716.
- Fu, X.L., Pan, Y.Z., Wan, Y., Ai, X., 2010b. Research on predictive model surface roughness in high speed milling for aluminum alloy 7050-T7451. 2010 International Conference on Computing, Control and Industrial Engineering, 165: 186-189.
- Fuller, C.B., Mahoney, M.W., Calabrese, M., Micono, L., 2010. Evolution of microstructure and mechanical properties in naturally aged 7050 and 7075 Al friction stir welds. *Materials Science and Engineering A*, 527: 2233-2240.
- Gao, N., Wang, C.T., Wood, R.J.K., Langdon, T.G., 2012. Tribological properties of ultrafine-grained materials processed by severe plastic deformation. *Journal of Materials Science*, 47:4779–4797.
- García-Bernal, M.A., Mishra, R.S., Verma, R., Hernández-Silva, D., 2009. High strain rate superplasticity in continuous cast Al-Mg alloys prepared via friction stir processing. *Scripta Materialia*, 60: 850-853.
- Gleiter, H., 2001. Nanostructured materials: Basic concepts and microstructure. *Acta Materialia*, 48:29.
- Grzesik, W., Żak, K., 2012. Modification of surface finish produced by hard turning using superfinishing and burnishing operations. *Journal of Materials Processing Technology*, 212: 315-322.
- Guo, Y., Saldana, C., Compton, W.D., Chandrasekar, S., 2011. Controlling deformation and microstructure on machined surfaces. *Acta Materialia*, 59: 4538-4547.
- Hamilton, C., Dymek, S., Sommers, A., 2008. A thermal model of friction stir welding in aluminum alloys. *International Journal of Machine Tools & Manufacture*, 48: 1120-1130.
- Hamilton, C., Sommers, A., Dymek, S., 2009. A thermal model of friction stir welding applied to Sc-modified Al-Zn-Mg-Cu alloy extrusions. *International Journal of Machine Tool & Manufacture*, 49: 230-238.
- Hassan, A.M., 1997. The effects of ball- and roller-burnishing on the surface roughness and hardness of some non-ferrous metals. *Journal of Materials Processing Technology*, 72: 385-391.
- Hill, M.R., Panontin, T.L., 2002. Microstructural modeling of fracture initiation in 7050 aluminum. *Engineering Fracture Mechanics*, 69: 2163-2186.
- Hofmann, D.C., Vecchio, K.S., 2005. Submerged friction stir processing (SFSP): An improved method for creating ultra-fine-grained bulk materials. *Materials Science and Engineering A*, 402: 234-241.

- Hong, S.Y., Markus, I., Jeong, W.C., 2001a. New cooling approach and tool life improvement in cryogenic machining of titanium alloy *Ti-6Al-4V*. *International Journal of Machine Tool & Manufacture*, 41: 2245-2260.
- Hong, S.Y., Ding, Y.C., 2001b. Cooling approaches and cutting temperatures in cryogenic machining of *Ti-6Al-4V*. *International Journal of Machine Tool & Manufacture*, 41: 1407-1437.
- Hsu, C.J., Kao, P.W., Ho, N.J., 2005. Ultrafine-grained *Al-Al₂Cu* composite produced in situ by friction stir processing. *Scripta Materialia*, 53: 341-345.
- Izadi, H., Gerlich, A.P., 2012. Distribution and stability of carbon nanotubes during multi-pass friction stir processing of carbon nanotube/aluminum composites. *Carbon*, 50: 4744-4749.
- Jata, K.V., Sankaran, K.K., Ruschau, J.J., 2000. Friction-stir welding effects on microstructure and fatigue of aluminum alloy *7050-T7451*. *Metallurgical and Materials Transactions A*, 31A: 2181-2192.
- Jawahir, I.S., Brinksmeier, E., M'Saoubi, R., Aspinwall, D.K., Outeiro, J.C., Meyer, D., Umbrello, D., Jayal, A.D., 2011. Surface integrity in material removal processes: recent advances. *CIRP Annals-Manufacturing Technology*, 60: 603-626.
- John, R., Jata, K.V., Sadananda, K., 2003. Residual stress effects on near-threshold fatigue crack growth in friction stir welds in aerospace alloys. *International Journal of Fatigue*, 25: 939-948.
- Johnson, G.R., Cook, W.H., 1985. A constitutive model and data for metals subjected to large strains, high rates and high temperatures. *Proceedings of the Seventh International Symposium on Ballistics*, The Netherlands: The Hague, 541-547.
- Kamp, N., Reynolds, A.P., Robson, J.D., 2009. Modelling of *7050* aluminum alloy friction stir welding. *Science and Technology of Welding and Joining*, 14(7): 589-596.
- Kaynak, Y., Karaca, H.E., Noebe, R.D., Jawahir, I.S., 2013. Tool-wear analysis in cryogenic machining of *NiTi* shape memory alloys: A comparison of tool-wear performance with dry and MQL machining. *Wear*, 306: 51-63.
- Kaynak, Y., 2014. Evaluation of machining performance in cryogenic machining of Inconel *718* and comparison with dry and MQL machining. *Journal of Advanced Manufacturing Technology*, 72: 919-933.
- Kaynak, Y., Lu, T., Jawahir, I.S., 2014a. Cryogenic machining-induced surface integrity: a review and comparison with dry, MQL and flood-cooled machining. *Machining Science and Technology*, 18: 149-198.
- Kaynak, Y., Tobe, H., Karaca, H.E., Noebe, R.D., Jawahir, I.S., 2014b. Machining-induced thermo-mechanical properties of *NiTi* shape memory alloys. *Scripta Materialia*, 74: 60-63.

- Kim, W.J., Sa, Y.K., 2006. Micro-extrusion of ECAP processed magnesium alloy for production of high strength magnesium micro-gears. *Scripta Materialia*, 54: 1391-1395.
- Klocke, F., Bäcker, V., Wegner, H., Zimmermann, M., 2011. Finite element analysis of the roller burnishing process for fatigue resistance increase of engine components. *Proceedings of the Institution of Mechanical Engineers, Part B: Journal of Engineering Manufacture*, 225(1): 2-11.
- Korzynski, M., 2009. A model of smoothing slide ball-burnishing and an analysis of the parameter interaction. *Journal of Materials Processing Technology*, 209: 625-633.
- Lalpoor, M., Eskin, D.G., Katgerman, L., 2009. Cold-cracking assessment in AA7050 billets during direct-chill casting by thermomechanical simulation of residual thermal stresses and application of fracture mechanics. *Metallurgical and Materials Transactions A*, 40A: 3304-3313.
- Langdon, T.G., 2011. Processing by severe plastic deformation: Historical developments and current impact. *Materials Science Forum*, 667-669: 9-14.
- Lapovok, R., Molotnikov, A., Levin, Y., Bandaranayake, A., Estrin, Y., 2012. Machining of coarse grained and ultra-fine grained titanium. *Journal of Materials Science*, 47: 4589-4594.
- Lashgari, H.R., Zangeneh, S., Shahmir, H., Saghafi, M., Emamy, M., 2010. Heat treatment effect on the microstructure, tensile properties and dry sliding wear behavior of A356-10%B4C cast composites. *Materials & Design*, 31: 4414-4422.
- Lee, C.J., Huang, J.C., Hsieh, P.J., 2006. Mg based nano-composites fabricated by friction stir processing. *Scripta Materialia*, 54:1415-1420.
- Li, L., Duszczek, J., 2004. Prediction of temperature evolution during the extrusion of 7075 aluminum alloy at various ram speeds by means of 3D FEM simulation. *Journal of Materials Processing Technology*, 145: 360-370.
- Li, C., Wan, Y., Zhang, R.R., Liu, Z.Q., 2012. Effect of milling speed and feed on surface residual stress of 7050-T7451 aluminum alloy. *Key Engineering Materials*, 499: 217-222.
- Li, F.L., Xia, W., Zhou, Z.Y., Zhao, J., Tang, Z.Q., 2012. Analytical prediction and experimental verification of surface roughness during the burnishing process. *International Journal of Machine Tools & Manufacture*, 62: 67-75.
- Li, F.X., Liu, Y.Z., Jiang, Y., Xia, L., 2013. Effect of processing parameters on the relative density of spray rolling 7050 aluminum alloy strip. *International Journal of Advanced Manufacturing Technology*, 67: 2771-2778.
- Liu, Q., Yang, C.H., Ding, K., Barter, S.A., Ye, L., 2007. The effect of laser power density on the fatigue life of laser-shock-peened 7050 aluminum alloy. *Fatigue & Fracture of Engineering Materials & Structures*, 30: 1110-1124.

- Liu, Z.Y., Xiao, B.L., Wang, W.G., Ma, Z.Y., 2014. Analysis of carbon nanotube shortening and composite strengthening in carbon nanotube/aluminum composites fabricated by multi-pass friction stir processing. *Carbon*, 69: 264-274.
- Lloyd, D.J., Kenny, D., 1980. The structure and properties of some heavily cold worked aluminum alloys. *Acta Materialia*, 28: 639-649.
- Long, T., Tang, W., Reynolds, A.P., 2007. Process response parameter relationships in aluminum alloy friction stir welds. *Science and Technology of Welding and Joining*, 12(4): 311-317.
- Lu, D., Li, J.F., Rong, Y., Grevstad, A., Usui, S., 2007. Temperature and Stress Analysis in Micro-cutting of *Ti-6Al-4V* and *Al 7050-T6* with AdvantEdge, ASPE Annual Meeting, Oct. 14-19, 2007, Dallas, TX.
- Lu, H.E., Zhen, L., Yang, L., Shao, W.Z., Zhang, B.Y., 2008. Deformation behavior and microstructure evolution of 7050 aluminum alloy during high temperature deformation. *Materials Science and Engineering A*, 488: 64-71.
- Luo, H.Y., Liu, J.Y., Wang, L.J., Zhong, Q.P., 2006. The effect of burnishing parameters on burnishing force and surface microhardness. *International Journal of Advanced Manufacturing Technology*, 28: 707-713.
- Luo, H., Liu, J., Wang, L., Zhong, Q., 2006. Investigation of the burnishing force during the burnishing process with a cylindrical surfaced tool. *Proceedings of the Institution of Mechanical Engineers, Part B: Journal of Engineering Manufacture*, 220(6): 893-904.
- Luong, H., Hill, M.R., 2010. The effects of laser peening and shot peening on high cycle fatigue in 7050-T7451 aluminum alloy. *Materials Science and Engineering A*, 527: 699-707.
- Lyman, T., 1967. *Metals Handbook 2*, 8th edition. American Society for Metals, Ohio: 270-272.
- Ma, Z.Y., Mishra, R.S., Mahoney, M.W., 2002. Superplastic deformation behavior of friction stir processed 7075Al alloy. *Acta Materialia*, 50: 4419-4430.
- Ma, Z.Y., Mishra, R.S., Mahoney, M.W., 2004. Superplasticity in cast A356 induced via friction stir processing. *Scripta Materialia*, 50: 931-935.
- Ma, Z.Y., Sharma, S.R., Mishra, R.S., 2006a. Effect of friction stir processing on the microstructure of cast A356 aluminum. *Material Science Engineering A*, 433: 269-278.
- Ma, Z.Y., Mishra, R.S., Mahoney, M.W., 2006b. Superplastic deformation behavior of friction stir processed 7075Al alloy. *Acta Materialia*, 50: 4419-4430.
- Ma, Z.Y., Sharma, S.R., Mishra, R.S., 2006c. Microstructural modification of as-cast Al-Si-Mg alloy by friction stir processing. *Metallurgical and Materials Transactions A*, 37A: 3323-3336.

- Ma, Z.Y., Sharma, S.R., Mishra, R.S., 2006d. Effect of multiple-pass friction stir processing on microstructure and tensile properties of a cast aluminum–silicon alloy. *Scripta Materialia*, 54: 1623-1626.
- Magnusen, P.E., Bucci, R.J., Hinkle, A.J., Brockenbrough, J.R., Konish, H.J., 1997. Analysis and prediction of microstructural effects on long-term fatigue performance of an aluminum aerospace alloy. *International Journal of Fatigue*, 19(1): S275-S283.
- Mahoney, M.W., Rhodes, C.G., Flintoff, J.G., Spurling, R.A., Bingel, W., 1998. Properties of friction-stir-welded 7075 T651 aluminum. *Metallurgical and Materials Transactions A*, 29A: 1955-1964.
- Mamedov, A., Layegh, S.E.K., Lazoglu, I., 2013. Machining forces and tool deflections in micro milling. *Procedia CIRP* 8: 147-151.
- Wen, C., Mudawar, I., 2004. Emissivity characteristics of roughened aluminum alloy surfaces and assessment of multispectral radiation thermometry (MRT) emissivity models. *International Journal of Heat and Mass Transfer*, 47: 3591-3605.
- Meyer, D., 2012. Cryogenic deep rolling-An energy based approach for enhanced cold surface hardening. *CIRP Annals-Manufacturing Technology*, 61: 543-546.
- Military handbook, 1994. *Metallic materials and elements for aerospace vehicle structures (MIL-HDBK-5G)*. Washington, DC: US Department of Defense.
- Miles, M.P., Mahoney, M.W., Fuller, C.B., 2006. Prediction of bending limits in friction-stir-processed thick plate aluminum, *Metallurgical and Materials Transactions A*, 37A: 399-404.
- Mohammadi, F., Sedaghati, R., Bonakdar, A., 2014. Finite element analysis and design optimization of low plasticity burnishing process. *Journal of Advanced Manufacturing Technology*, 70: 1337-1354.
- Mohammed, A., 2012. Achieving ultrafine grains in *Mg AZ31B-O* Alloy by cryogenic friction stir processing and machining, Master thesis, University of Kentucky.
- Morehead, M., Huang, Y., Hartwig, K.T., 2007. Machinability of ultrafine-grained copper using tungsten carbide and polycrystalline diamond tools. *International Journal of Machine Tool & Manufacture*, 47: 286-293.
- Morisada, Y., Fujii, H., Nagaoka, T., Fukusumi, M., 2006. Effect of friction stir processing with SiC particles on microstructure and hardness of *AZ31*. *Materials Science Engineering A*, 433:50-54.
- M'Saoubi, R., Outeiro, J.C., Chandrasekaran, H., Dillon Jr, O.W., Jawahir, I.S., 2008. A review of surface integrity in machining and its impact on functional performance and life of machined products. *International Journal of Sustainable Manufacturing*, 1: 203-236.

- Mueller, L.N., 1985. ALCOA aluminum alloy 7050, Green Letter No. 220. ALCOA Center, PA: Aluminum Company of America.
- Murayama, M., Horita, Z., Hono, K., 2001. Microstructure of two-phase *Al-1.7* at % *Cu* alloy deformed by equal-channel angular pressing. *Acta Materialia*, 49: 21-29.
- Nakata, K., Kim, Y.G., Fujii, H., Tsumura, T., Komazaki, T., 2006. Improvement of mechanical properties of aluminum die casting alloy by multi-pass friction stir processing. *Materials Science and Engineering A*, 437: 274-280.
- Nam, C.Y., Han, J.H., Chung, Y.H., Shin, M.C., 2003. Effect of precipitates on microstructural evolution of 7050 *Al* alloy sheet during equal channel angular rolling. *Materials Science and Engineering A*, 343: 253-257.
- Némat, M., Lyons, A.C., 2000. An investigation of the surface topography of ball burnished mild steel and aluminum. *International Journal of Advanced Manufacturing Technology*, 16: 469-473.
- Ni, D.R., Xiao, B.L., Ma, Z.Y., Qiao, Y.X., Zheng, Y.G., 2010. Corrosion properties of friction stir processed cast *NiAl* bronze. *Corrosion Science*, 52: 1610-1617.
- OTTO FUCHS KG, 2012. Components made of *Al 7050-T7451* alloys: Fuselage frame and front fitting for aircrafts. www.otto-fuchs.com.
- Pao, P.S., Gill, S.J., Feng, C.R., Sankaran, K.K., 2001. Corrosion-fatigue crack growth in friction stir welded *Al 7050*. *Scripta Materialia*, 45: 605-612.
- Ponge, D., 2011. Structural materials-steels. [Http://materialsknowledge.org/docs/Steels %20Ponge%20Marie-Curie%20Summer%20School.pdf](http://materialsknowledge.org/docs/Steels%20Ponge%20Marie-Curie%20Summer%20School.pdf).
- Prevéy, P.S., Cammett, J.T., 2004. The influence of surface enhancement by low plasticity burnishing on the corrosion fatigue performance of *AA7075-T6*. *International Journal of Fatigue*, 26: 975-982.
- Prime, M.B., Gnäupel-Herold, T., Baumann, J.A., Lederich, R.J., Bowden, D.M., Sebring, R.J., 2006. Residual stress measurements in a thick, dissimilar aluminum alloy friction stir weld. *Acta Materialia*, 54: 4013-4021.
- Pu, Z., Yang, S., Song, G.L., Dillon Jr., O.W., Puleo, D.A., Jawahir, I.S., 2011. Ultrafine-grained surface layer on *Mg-Al-Zn* alloy produced by cryogenic burnishing for enhanced corrosion resistance. *Scripta Materialia*, 65: 520-523.
- Pu, Z., Outeiro, J.C., Batista, A.C., Dillon Jr, O.W., Puleo, D.A., Jawahir, I.S., 2012. Enhanced surface integrity of *AZ31B* Mg alloy by cryogenic machining towards improved functional performance of machined components. *International Journal of Machine Tool & Manufacture*, 56: 17-27.
- Pu, Z., 2012. Cryogenic machining and burnishing of *AZ31B* magnesium alloy for enhanced surface integrity and functional performance, Doctoral Dissertation, University of Kentucky.

- Pusavec, F., Hamdi, H., Kopac, J., Jawahir, I.S., 2011. Surface integrity in cryogenic machining of nickel based alloy-Inconel 718. *Journal of Materials Processing Technology*, 211: 773-783.
- Qiao, X.G., Gao, N., Moktadir, Z., Kraft, M., Starink, M.J., 2010. Fabrication of MEMS components using ultrafine-grained aluminium alloys. *Journal of Micromechanics and Microengineering*, 20: 045029 (9p).
- Ramesh, K.N., Pradeep, S., Pancholi, V., 2012. Multipass friction-stir processing and its effect on mechanical properties of aluminum alloy 5086. *Metallurgical and Materials Transactions A*, 43A: 4311-4319.
- Reynolds, A.P., Tang, W., Khandkar, Z., Khan, J.A., Lindner, K., 2005. Relationships between weld parameters, hardness distribution and temperature history in alloy 7050 friction stir welds. *Science and Technology of Welding and Joining*, 10(2): 190-199.
- Rhodes, C.G., Mahoney, M.W., Bingel, W.H., Calabrese, M., 2003. Fine-grain evolution in friction-stir processed 7050 aluminum. *Scripta Materialia*, 48: 1451-1455.
- Richert, M., 1997. Changes of structure and properties due to severe plastic deformation. *Materials Engineering*, 2: 59-69.
- Rotella, G., Lu, T., Settineri, L., Dillon Jr, O.W., Jawahir, I.S., 2011. Dry and cryogenic machining: comparison from the sustainability perspective, sustainable manufacturing-shaping global value creation: 95-100.
- Salahshoor, M., Guo, Y.B., 2013. Process mechanics in ball burnishing biomedical magnesium-calcium alloy. *Journal of Advanced Manufacturing Technology*, 64: 133-144.
- Salehi, M., Farnoush, H., Heydarian, A., Mohandesi, J.A., 2014. Improvement of mechanical properties in the functionally graded aluminum matrix nanocomposites fabricated via a novel multistep friction stir processing. *Metallurgical and Materials Transactions B*, 46B: 20-29.
- Salishchev, G.A., Murzinova, M.A., Zherebtsov, S.V., Afonichev, D.D., Malysheva, S.P., 2001. Influence of reversible hydrogen alloying on formation of SMC structure and superplasticity of titanium alloys. *Materials Science Forum*, 357-359: 315-320.
- Sánchez, J.M., Rubio, E., Álvarez, M., Sebastián, M.A., Marcos, M., 2005. Microstructural characterization of material adhered over cutting tool in the dry machining of aerospace aluminum alloys. *Journal of Materials Processing Technology*, 164-165: 911-918.
- Sanders, P.G., Eastman, J.A., Weertman, J.R., 1997. Elastic and tensile behavior of nanocrystalline copper and palladium. *Acta Materialia*, 45 (10): 4019-4025.
- Sandstrom, D.R., Hodowany, J.N., 1998. Modeling the physics of metal cutting in high-speed machining. *Machining Science and Technology*, 2(2): 343-353.

- Santos, T.G., Miranda, R.M., Vilaça, P., Teixeira, J.P., 2011. Modification of electrical conductivity by friction stir processing of aluminum alloys. *International Journal of Advanced Manufacturing Technology*, 57: 511-519.
- Sanusi, K.O., Makinde, O.D., Oliver, G.J., 2012. Equal channel angular pressing technique for the formation of ultra-fine grained structures. *South African Journal of Science*, 108 (9/10).
- Sarkar, A, Chakravartty, J.K., Paul, B., Suri, A.K., 2011. Kinetics of dynamic recrystallization in cobalt: A study using the Avrami relation. *Physical Status Solidi a-Applications and Materials Science*, 208(4): 814-818.
- Sayahi, M., Sghaier, S., Belhadjsalah, H., 2013. Finite element analysis of ball burnishing process: comparisons between numerical results and experiments. *Journal of Advanced Manufacturing Technology*, 67: 1665-1673.
- Schubbe, J.J., 2009. Fatigue crack propagation in *7050-T7451* plate alloy. *Engineering Fracture Mechanics*, 76: 1037-1048.
- Seniw, M.E., Conley, J.G., Fine, M.E., 2000. The effect of microscopic inclusion locations and silicon segregation on fatigue lifetimes of aluminum alloy *A356* castings. *Materials Science Engineering A*, 285:43-48.
- Sergueeva, A.V., Stolyarov, V.V., Valiev, R.Z., Mukherjee, A.K., 2002. Superplastic behaviour of ultrafine-grained *Ti-6Al-4V* alloys. *Materials Science Engineering, A323*: 318-325.
- Shafiei-Zarghani, A., Kashani-Bozorg, S.F., Zarei-Hanzaki, A., 2009. Microstructures and mechanical properties of *Al/Al₂O₃* surface nano-composite layer produced by frictions stir processing. *Materials Science and Engineering A*, 500: 84-91.
- Shafiei-Zarghani, A., Kashani-Bozorg, S.F., Zarei- Hanzaki, A., 2011. Wear assessment of *Al/Al₂O₃* nano-composite surface layer produced using friction stir processing. *Wear*, 270: 403-412.
- Shankar, M.R., Chandrasekar, S., King, A.H., Compton, W.D., 2005. Microstructure and stability of nanocrystalline aluminum *6061* created by large strain machining. *Acta Materialia*, 53: 4781-4793.
- Sharma, S.R., Ma, Z.Y., Mishra, R.S., 2004. Effect of friction stir processing on fatigue behavior of *A356* alloy. *Scripta Materialia*, 51: 237-241.
- Sharp, P.K., Clark, G., 2001. The effect of peening on the fatigue life of *7050* aluminum alloy. *Defense Science & Technology Organisation, Australia, DSTO-RR-0208*.
- Skalski, K., Morawski, A., Przybylski, W., 1995. Analysis of contact elastic-plastic strains during the process of burnishing. *International Journal of Mechanical Science*, 37: 461-472.
- Strasik, M., Hull, J.R., Mittleider, J.A., Gonder, J.F., Johnson, P.E., McCrary, K.E., McIver, C.R., 2010. An overview of Boeing flywheel energy storage systems

- with high-temperature superconducting bearings. *Superconductor Science and Technology*, 23: 034021 (5pp).
- Slemp, W.C., Bird, R.K., Kapania, R.K., Havens, D., Norris, A., Olliffe, R., 2011. Design, optimization and evaluation of integrity stiffened *Al 7050* panel with curved stiffeners. NASA/TP-2011-217178.
- Su, J.Q., Nelson, T.W., Mishra, R., Mahoney, M., 2003. Microstructural investigation of friction stir welded *7050-T651* aluminum. *Acta Materialia*, 51: 713–729.
- Su, J.Q., Nelson, T.W., Sterling, C.J., 2005. Friction stir processing of large-area bulk UFG aluminum alloy. *Scripta Materialia*, 52: 135-140.
- Su, G.S., Liu, Z.Q., 2014. Experimental study on specific shear energy in high-speed machining *7050-T7451*. *Key Engineering Materials*, 589-590: 8-12.
- Substech, 2013. Burnishing. <http://www.substech.com/dokuwiki/doku.php?id=burnishing>.
- Surekha, K., Murty, B.S., Rao, K.P., 2008. Microstructural characterization and corrosion behavior of multipass friction stir processed *AA2219* aluminum alloy. *Surface & Coatings Technology* 202, 4057-4068.
- Tang, Z.T., Liu, Z.Q., Pan, Y.Z., Wan, Y., Ai, X., 2009. The influence of tool flank wear on residual stress induced by milling aluminum alloy. *Journal of Materials Processing Technology*, 209: 4502-4508.
- Tang, K.Y., Zhou, L.H., Song, L., 2012. Investigation of the milling performance about *7050-T7451* aluminum alloy based on orthogonal experiment. *Applied Mechanics and Materials*, 121-126:1431-1435.
- Thomas, W.M., Nicholas, E.D., Needham, J.C., Murch, M.G., Temple Smith, P., Dawes, C.J.: G.B. Application No. 9125978.8, 1991, U.S. Patent No. 5460317, 1995.
- Tikhonovsky, M., 2011. Ultrafine-grained tantalum, titanium and stainless steel for medical and other applications. National Science Center “Kharkiv Institute of Physics & Technology .www.stcu.int/documents/reports/distribution/tpf/.../hannover%2024.pdf.
- Tian, Y.W., Xu, F., Li, W.Y. and Tang, Z.B., 2011. Nonuniformity of Mechanical Property in the Weld Zone of Friction Stir Welded *7050* Aluminum Alloy Joint, *Advanced Materials Research*, 189-193: 3560-3563.
- Topping, T.D., Ahn, B., Li, Y., Nutt, S.R., Lavernia, E.J., 2012. Influence of process parameters on the mechanical behavior of an ultrafine-grained *Al* alloy. *Metallurgical and Materials Transactions A*, 43A: 505-519.
- Umbrello, D., 2004. FE-analysis of machining processes: innovative experimental techniques for results assessing. PhD dissertation, University of Calabria, Italy.

- Umbrello, D., Micari, F., Jawahir, I.S., 2012. The effects of cryogenic cooling on surface integrity in hard machining: A comparison with dry machining. *CIRP Annals-Manufacturing Technology*, 61: 103-106.
- Upadhyay, P., Reynolds, A.P., 2010. Effects of thermal boundary conditions in friction stir welded AA7050-T7 sheets. *Materials Science and Engineering A*, 527: 1537-1543.
- Valiev, R.Z., Islamgaliev, R.K., Alexandrov, I.V., 2000. Bulk nanostructured materials from severe plastic deformation. *Progress in Materials Science*, 45: 103-189.
- Valiev R.Z., 2003. Paradoxes of severe plastic deformation. *Advanced Engineering Materials*, 5(5): 296-300.
- Valiev, R.Z., 2004. Nanostructuring of metals by severe plastic deformation for advanced properties. *Natural Materials*, 3: 511-516.
- Valiev, R.Z., Estrin, Y., Horita, Z., Langdon, T.G., Zehetbauer, M.J., Zhu, Y.T., 2006. Producing bulk ultrafine-grained materials by severe plastic deformation. *Journal of the Minerals*, 58(4): 33-39.
- Valiev, R.Z., Semenova, I.P., Latysh, V.V., Rack, H., Lowe, T.C., Petruzelka, J., Dluhos, L.M., Hrusak, D., Sochova, J., 2008. Nanostructured titanium for biomedical applications. *Advanced Engineering Materials*, 10: B15-B17.
- Wang, W., Shi, Q.Y., Liu, P., Li, H.K., Li, T., 2009. A novel way to produce bulk SiCp reinforced aluminum metal matrix composites by friction stir processing. *Journal of Materials Processing Technology*, 209:2099-2103.
- Wang, Z.Q., Li, J.F., Sun, J., Jiang, F., Zhou, J., 2010. Flow stress determination of aluminum alloy 7050-T7451 using inverse analysis method. *Key Engineering Materials*, 431-432: 174-177.
- Wang, F.Z., Sun, J., Sun, P.Q., Zhou, J., 2012. Finite element model and analysis for micro-cutting of aluminum alloy 7050-T7451. *International Journal of Materials and Mechanics Engineering*, 566: 650-653.
- Wikipedia, 2011. Lockheed Martin F-35 Lightning. http://en.wikipedia.org/wiki/Lockheed_Martin_F-35_Lightning_II.
- Wu, B., Li, M.Q., Ma, D.W., 2012. The flow stress behavior and constitutive equations in isothermal compression of 7050 aluminum alloy. *Materials Science and Engineering A*, 542: 79-87.
- Xu, C.L., Wei, B.Q., Ma, R.Z., Liang, J., Ma, X.K., Wu, D.H., 1999. Fabrication of aluminum-carbon nanotube composites and their electrical properties. *Carbon*, 37:855-858.
- Xu, Y., Wang, J.C., Guo, S.J., Li, X.T., Xue, G.X., 2011. Effects of water-restricted panel on the casting process of high strength aluminum alloy ingots. *Journal of Materials Processing Technology*, 211: 78-83.

- Yan, J., Reynolds, A.P., 2009. Effect of initial base metal temper on mechanical properties in AA7050 friction stir welds. *Science and Technology of Welding and Joining*, 14(4): 282-287.
- Yanagimoto, J., Karhausen, K., Brand, A.J., Kopp, R., 1998. Incremental formulation for the prediction of flow stress and microstructural change in hot forming. *Journal of Manufacturing Science and Engineering-Transactions of the ASME*, 120(2): 316-322.
- Yang, S., Puleo, D.A., Dillon Jr, O.W., Jawahir, I.S., 2011. Surface layer modifications in *Co-Cr-Mo* biomedical alloy from cryogenic burnishing. *Procedia Engineering*, 19: 383-388.
- Yang, S., 2012. Cryogenic burnishing of *Co-Cr-Mo* biomedical alloy for enhanced surface integrity and improved wear performance, Doctoral Dissertation, University of Kentucky.
- Yang, S., Dillon Jr., O.W., Puleo, D.A., Jawahir, I.S., 2013. Effect of cryogenic burnishing on surface integrity modifications of *Co-Cr-Mo* biomedical alloy. *Journal of Biomedical Materials Research Part B: Applied Biomaterials*, 101B: 139-152.
- Yang, S., Umbrello, D., Dillon Jr., O.W., Puleo, D.A., Jawahir, I.S., 2015. Cryogenic cooling effect on surface and subsurface microstructural modifications in burnishing of *Co-Cr-Mo* biomaterial. *Journal of Materials Processing Technology*, 217: 211-221.
- Yen, Y.C., Sartkulvanich, P., Altan, T., 2005. Finite element modeling of roller burnishing process. *CIRP Annals-Manufacturing Technology*, 54(1): 237-240.
- Žak, K., Grzesik, W., Prażmowski, M., 2014. Investigation of sequential cryogenic hard turning and ball burnishing processes. *Journal Metalurgija*, 53(4): 521-525.
- Zhang, B., Poirier, D.R., Chen, W., 1999. Microstructural effects on high-cycle fatigue-crack initiation in A356.2 casting alloy. *Metallurgical Materials Transaction A*, 30: 2659-2966.
- Zhang, L.H., Yu, J., Zhang, X.M., 2010. Effect of ultrasonic power and casting speed on solidification structure of 7050 aluminum alloy ingot in ultrasonic field. *Journal of Cent. South Univ. Technol.*, 17: 431-436.
- Zhao, Z., Hong, S.Y., 1992. Cooling strategies for cryogenic machining from a materials viewpoint. *Journal of Materials Engineering and Performance*, 1(5): 669-678.
- Zhong, R., Cong, H., Hou, P., 2003. Fabrication of nano-*Al* based composites reinforced by single-walled carbon nanotubes. *Carbon*, 41(CO1):848-851.
- Zhou, J., Li, J.F., Sun, J., Xu, Z.P., 2008. The influence of tool edge radius on size effect in orthogonal micro-cutting process of 7050-T7451 aluminum alloy. *Key Engineering Materials*, 375-376: 31-35.

- Zhou, J., Li, J.F., Sun, J., 2010a. Experimental study on the chip geometry and shear angle in micro-cutting aluminum *7050-T7451*. *Key Engineering Materials*, 443: 657-662.
- Zhou, J., Li, J.F., Sun, J., 2010b. Finite element analysis of micro-cutting aluminum *7050-T7451* with the tool edge radius considered. *Key Engineering Materials*, 443:663-668.

VITA

Name

Bo Huang

Place of Birth

Shenyang, Liaoning Province, China

Education

B.S. in Mechanical Engineering, Dalian Polytechnic University, Liaoning, China

July, 2007

M.S. in Mechanical Engineering, Dalian University of Technology, Liaoning, China

December, 2009

Experience

Editorial Assistant (01/2015 ~ 05/2016), Machining Science and Technology, Taylor & Francis

Research Assistant (06/2012 ~ 05/2016), Institute for Sustainable Manufacturing, University of Kentucky, Lexington, KY

Teaching Assistant (08/2009 ~ 05/2012), Department of Mechanical Engineering, University of Kentucky, Lexington, KY

Publications:

Journal Papers:

Huang, B., Kaynak, Y., Arvin, C., Jawahir, I.S., 2015. Improved surface integrity from cryogenic machining of *Al 7050-T7451* alloy with ultrafine-grained structure. *Advances in Materials and Processing Technologies*, 1(3-4): 361-374.

Huang, B., Kaynak, Y., Khraisheh, M.K., Sun, Y., Jawahir, I.S., Enhanced thermo-mechanical properties in cryogenic friction stir processing of *Al 7050-T7451* alloy (under review).

Huang, B., Sun, Y., Kaynak, Y., Jawahir, I.S., Surface layer modification by cryogenic burnishing of *Al 7050-T7451* alloy with ultra-fine grained structure (under review).

Conference Papers:

Huang, B., Kaynak, Y., Sun, Y., Jawahir, I.S., 2015. Surface layer modification by cryogenic burnishing of *Al 7050-T7451* alloy and validation with FEM-based burnishing model. *Procedia CIRP*, 31: 1-6.

Sun, Y., **Huang, B.**, Puleo, D.A., Jawahir, I.S., 2015. Enhanced machinability of *Ti-5553* alloy from cryogenic machining: comparison with MQL and Flood-cooled machining and modeling. *Procedia CIRP*, 31: 447-482.

Caudill, J., **Huang, B.**, Arvin, C., Schoop, J., Meyer, K., Jawahir, I.S., 2014. Enhancing the surface integrity of *Ti-6Al-4V* alloy through cryogenic burnishing. *Procedia CIRP*, 13: 243-248.